

# **Processing, microstructure, properties and performance of thermal sprayed ceramic coatings from powder, suspension and solution precursor**

By

**Daniel Tejero Martín**

Supervisor: Professor Tanvir Hussain

Co-supervisor: Associate Professor Chris Bennett



**University of  
Nottingham**  
UK | CHINA | MALAYSIA

Department of Mechanical, Materials and Manufacturing

Faculty of Engineering

**January 2022**

# Table of Contents

Acknowledgements.....	6
Abstract.....	7
List of publications presented in this thesis .....	9
List of publications related to this thesis.....	10
Chapter 1: Introduction .....	12
1.1. Project background .....	12
1.2. Aim and objectives .....	15
1.3. Thesis structure .....	17
Chapter 2: Literature review .....	20
2.1. Solution precursor thermal spray .....	24
2.1.1. In-flight transformation.....	24
2.1.2. Niobium-doped TiO <sub>2</sub> .....	28
2.1.3. Current status and future research.....	32
2.2. Porosity measurement on thermal sprayed coatings.....	33
2.2.1. Neutron/x-ray scattering .....	35
2.2.2. Image analysis.....	36
2.2.3. Current status and future research.....	37
2.3. Environmental barrier coatings.....	39
2.3.1. Development of environmental barrier coatings.....	44
2.3.1.1. Yttrium silicates.....	50

2.3.1.2.	Ytterbium silicates .....	51
2.3.2.	Corrosion mechanisms .....	55
2.3.2.1.	Steam degradation .....	56
2.3.2.2.	CMAS corrosion.....	66
2.3.3.	Current status and future research.....	79
Chapter 3: Splat Formation and Microstructure of Solution Precursor Thermal Sprayed Nb-doped Titanium Oxide Coatings .....		
		81
Abstract.....		81
3.1.	Introduction.....	82
3.2.	Experimental methods .....	84
3.2.1.	Materials and coating deposition .....	84
3.2.2.	Characterisation .....	86
3.3.	Results and discussion .....	88
3.3.1.	Microstructure and phase evolution in SP-HVOF .....	88
3.3.2.	Elemental distribution.....	90
3.3.3.	Phase evolution .....	92
3.3.4.	In-flight transformation.....	97
3.3.5.	Swipe test.....	101
3.3.6.	Deposition mechanisms of Nb-TiO <sub>2</sub> particles .....	104
3.4.	Conclusions.....	109
3.5.	Acknowledgements.....	110

Chapter 4: Evolution of Porosity in Suspension Thermal Sprayed YSZ Thermal Barrier Coatings through Neutron Scattering and Image Analysis Techniques ..... 111

Abstract..... 111

4.1. Introduction..... 112

4.2. Experimental methods ..... 115

    4.2.1. Materials and coating deposition ..... 115

    4.2.2. Neutron scattering..... 116

    4.2.3. Material characterisation..... 117

    4.2.4. Image analysis..... 118

4.3. Results..... 120

    4.3.1. Porosity measurements ..... 120

    4.3.2. Phase composition ..... 128

4.4. Discussion..... 137

    4.4.1. Porosity measurement: neutron scattering versus image analysis techniques . 137

    4.4.2. Porosity evolution ..... 139

    4.4.3. Phase transformation..... 141

4.5. Conclusions..... 145

4.6. Appendix A..... 145

4.7. Acknowledgements..... 148

Chapter 5: Interaction of CMAS on Thermal Sprayed Ytterbium Disilicate Environmental Barrier Coatings: A Story of Porosity..... 149

Abstract..... 149

5.1.	Introduction.....	150
5.2.	Experimental methods .....	152
5.2.1.	Free-standing coatings .....	152
5.2.2.	CMAS exposure.....	153
5.2.3.	Material characterisation.....	154
5.3.	Results.....	155
5.3.1.	Powder and coating characterisation .....	155
5.3.2.	1 h CMAS exposure.....	159
5.3.3.	48 h CMAS exposure.....	164
5.4.	Discussion.....	170
5.5.	Conclusions.....	176
5.6.	Acknowledgements.....	177
Chapter 6: Steam Degradation of Ytterbium Disilicate Environmental Barrier Coatings: Effect of Composition, Microstructure and Temperature..... 179		
	Abstract.....	179
6.1.	Introduction.....	180
6.2.	Experimental methods .....	182
6.2.1.	Materials and steam exposure.....	182
6.2.2.	Materials characterisation .....	184
6.3.	Results.....	185
6.3.1.	Powder and coating characterisation .....	185
6.3.2.	Steam exposure to 1350 °C.....	192

6.3.3. Steam exposure at 1400 °C.....	196
6.4. Discussion.....	202
6.5. Conclusions.....	207
6.6. Acknowledgements.....	208
Appendix.....	209
Chapter 7: General discussion .....	212
7.1. Solution precursor HVOF thermal spray .....	213
7.2. Porosity measurement of SP-HVOF thermal sprayed coatings.....	215
7.3. Performance testing of novel EBCs.....	216
Chapter 8: General conclusions and Future work.....	219
8.1. General conclusions .....	219
8.2. Future work.....	222
References.....	223

## **Acknowledgements**

I would like to thank the Engineering and Physical Sciences Research Council (EPSRC) and the Centre for Doctoral Training in Innovative Metal Processing (IMPACT) for funding my research. I truly appreciate the opportunity that Dr Tanvir Hussain, my supervisor, granted me. During this time, he always made an effort to support my work and me, and it is thanks to his assistance that I have become the researcher that I am today. I would also like to thank Dr Chris Bennett, my co-supervisor, for his assistance.

The work presented in this thesis would have not be possible without the help of the technical team at Wolfson and the Nanoscale and Microscale Research Centre (nmRC). I will always be grateful to Rory Sreaton, John Kirk, Hannah Constantin, Beth Steer and Richard Homer.

The same can be said about all the colleagues that I had the pleasure to work with. Every single one of the members of the Coatings and Surface Engineering team, and other teams working at Wolfson, has been nothing but fantastic. They all provided me with their knowledge and friendship, and these years would have been very different without them.

My family will always have a special place in my heart. They supported me, and believed in me throughout the years, allowing me to follow my passion.

Finally, I can only express my deepest gratitude to my wife, Dr Maria York, who always believed in me and taught me how a real scientist should be. I cannot imagine a better person to share this journey with.

## **Abstract**

Ceramic coatings are applied in many sectors, ranging from functional coatings to high temperature coatings for aerospace engines. Typically, the deposition technique chosen represents a compromise between the required properties and the economic restraints. Over the years, thermal spraying has proven itself as a reliable and cost-efficient method for the deposition of a multitude of compositions. For instance, thermal sprayed ceramic coatings are essential for the current and future generations of aerospace engines. Nickel-based superalloys are typically coated with thermal sprayed thermal barrier coatings (TBCs). Even the potential replacement, ceramic matrix composites (CMCs), require thermal sprayed environmental barrier coatings (EBCs) to protect them. In this context, this Ph.D. thesis is framed, working with the study of thermal sprayed coatings from powder, suspension and solution precursor.

The introduction of liquid feedstocks was developed to overcome the limitations presented by powder, such as flowability with sub-micron particles, and the complexity of introducing doping elements. This thesis first presents a thorough study of the use of a novel solution precursor feedstock to produce coatings where the composition can be modified to produce functional coatings with improved properties. Taking niobium doped  $\text{TiO}_2$  as an example material, homogeneously doped coatings were produced, proving the capabilities of this solution precursor route. In addition to the chemical modification, porosity was controlled through the spraying parameters, showing that microstructure can be easily tailored to the final application. In order to provide a comprehensive view accounting for the differences observed, a model detailing the evolution of the liquid feedstock as it turns into solid material during its transformation in-flight was presented.

The importance of porosity, already realised in the previous stage, is the centre of the next step in the research. Conventional powder feedstock tends to produce coatings with porosity with a

minimum range of tens of microns. However, this limitation is not present when suspension thermal spraying is used. To properly study this new range of pores, techniques such as image analysis are ill suited. Instead, this thesis proposes the use of more advanced techniques, such as neutron scattering techniques performed at large neutron facilities. Using yttria-stabilised zirconia, a standard TBC (where porosity has severe implications on lifetime and thermal conductivity), neutron scattering was proven as a powerful, non-destructive technique capable of accessing pores with a size of 1 nm. As a proof of concept, the evolution of porosity during heat treatment was studied and a detailed evolution study was conducted.

Finally, the work in this thesis focuses on the performance of EBCs under simulated corrosive environments. As these protective coatings are expected to limit the ingress of corrosive species into the CMC substrates, porosity again plays a key role. In order to investigate this scenario, low and high porosity content EBCs were exposed to molten calcium magnesium aluminosilicates (CMAS) and superheated steam (1350 °C and 1400 °C) to assess their performance. The results show that both the low and high porosity EBCs behaved similarly, particularly during longer exposures (48 h), where inter-splat boundaries become the preferential path for access, instead of the porosity, as suggested by the literature review here presented. No evidence of failure could be detected in any of the EBCs, presenting a promising result for the development of abradable environmental barrier coatings.

The work presented in this thesis represents the foundation for further research into solution precursor and suspension thermal sprayed EBCs, with both composition and porosity levels easily tailored to the end application. The new framework here discussed will ensure adequate measurement of the porosity in such coatings, accounting for sub-micron pores if using a suitable technique. Finally, these novel EBCs would require performance assessment under simulated service conditions. CMC coated samples, including high porosity abradable EBCs, would represent the natural progression of this research.

## List of publications presented in this thesis

[1] D. Tejero-Martin, Z. Pala, S. Rushworth, T. Hussain, Splat formation and microstructure of solution precursor thermal sprayed Nb-doped titanium oxide coatings, *Ceram. Int.* 46 (2020) 5098–5108. <https://doi.org/10.1016/j.ceramint.2019.10.253>.

Daniel Tejero Martin deposited and analysed the coatings and wrote the manuscript. Zdenek Pala performed the Rietveld refinement and provided assistance with the phase content and transformation. Simon Rushworth proofread the manuscript. Tanvir Hussain supervised the experiments, assisted with the analysis and proofread the manuscript.

[2] D. Tejero-Martin, C. Bennett, T. Hussain, A review on environmental barrier coatings: History, current state of the art and future developments, *J. Eur. Ceram. Soc.* 41 (2021) 1747–1768. <https://doi.org/10.1016/j.jeurceramsoc.2020.10.057>.

Daniel Tejero Martin wrote the review paper. Chris Bennett proofread the review. Tanvir Hussain assisted with the structuring of the review and proofread it.

[3] D. Tejero-Martin, M. Bai, J. Mata, T. Hussain, Evolution of porosity in suspension thermal sprayed YSZ thermal barrier coatings through neutron scattering and image analysis techniques, *J. Eur. Ceram. Soc.* 41 (2021) 6035–6048. <https://doi.org/10.1016/j.jeurceramsoc.2021.04.020>.

Daniel Tejero Martin deposited the coatings, performed the porosity measurements, analyse the results and wrote the manuscript. Mingwen Bai performed the Rietveld refinement, assisted with the phase content and transformation discussion and proofread the manuscript. Jitendra Mata assisted with the neutron scattering measurements, analysis of the data and proofread the manuscript. Tanvir Hussain provided assistance with the data analysis and proofread the document.

[4] D. Tejero-Martin, A. R. Romero, R. G. Wellman, T. Hussain, Interaction of CMAS on thermal sprayed ytterbium disilicate environmental barrier coatings: a story of porosity, *Ceram. Int. Article in press* <https://doi.org/10.1016/j.ceramint.2021.12.033>

Daniel Tejero Martin performed the experiments, prepared the samples, analyse the data and wrote the manuscript. Acacio Rincon Romero assisted with the data analysis, general discussion and proofread the document. Richard Wellman provided the coatings used, assisted with the general discussion and proofread the manuscript. Tanvir Hussain provided assistance with the data analysis and proofread the document.

[5] D. Tejero-Martin, M. Bai, A. R. Romero, R. G. Wellman, T. Hussain, Steam degradation of ytterbium disilicate environmental barrier coatings: effect of composition, microstructure and temperature. *Manuscript submitted for publication. Pre-print accessible at* <https://engrxiv.org/xj3s7/>

Daniel Tejero-Martin performed the experiments, prepared the samples, analysed the data and wrote the manuscript. Mingwen Bai performed the Rietveld analysis, assisted with the phase content and transformation discussion and proofread the manuscript. Acacio Rincon Romero assisted with the data analysis, general discussion and proofread the manuscript. Richard Wellman provided the coatings used, assisted with the general discussion and proofread the manuscript. Tanvir Hussain provided assistance with the data analysis and proofread the document.

## **List of publications related to this thesis**

[6] D. Tejero-Martin, M. Rezvani Rad, A. McDonald, T. Hussain, Beyond Traditional Coatings: A Review on Thermal-Sprayed Functional and Smart Coatings, *J. Therm. Spray Technol.* 28 (2019) 598–644. <https://doi.org/10.1007/s11666-019-00857-1>.

Daniel Tejero Martin wrote the review paper with the exception of the section “Resistive Heating”. Milad Rezvani Rad wrote the section “Resistive Heating”. Andre McDonald proofread the review and provided assistance. Tanvir Hussain proofread the review and provided assistance.

# Chapter 1: Introduction

## 1.1. Project background

Ceramic coatings have been successfully applied in a plethora of fields, such as, but not limited to aerospace and electricity production, becoming an essential component of today's industry [1]. The focus of this thesis is thermal sprayed ceramic coatings for high temperature applications for aerospace applications, with a brief introduction to this application outlined here. Although the specific design for the different gas turbine engines available nowadays can vary widely, the underlying mechanism is the same. Atmospheric air enters the gas turbine engine, being compressed to higher pressure. Fuel is mixed into the air and combusted, generating a flow of high temperature gases, which enters the turbine. After passing through the gas turbine engine, the flow of gases exits the engine producing thrust. At the so-called hot section, schematically represented in Figure 1, high temperature gases are present, reaching temperatures as high as 1500 °C [2], requiring materials capable of withstanding such conditions. The current generation of gas turbines rely on nickel-based superalloys as the material of choice for components in the hot section, such as combustors, high pressure turbine (HPT) vanes and blades.

# HOT SECTION PARTS

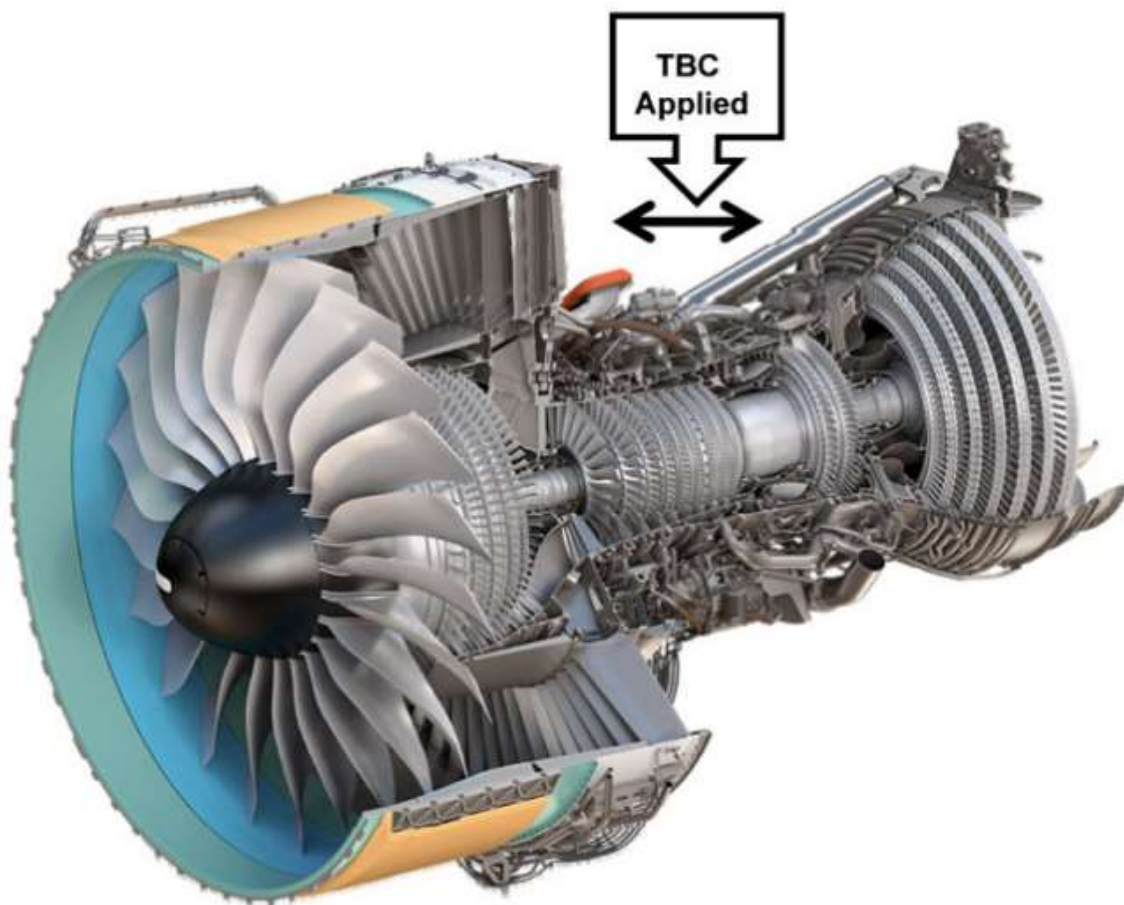
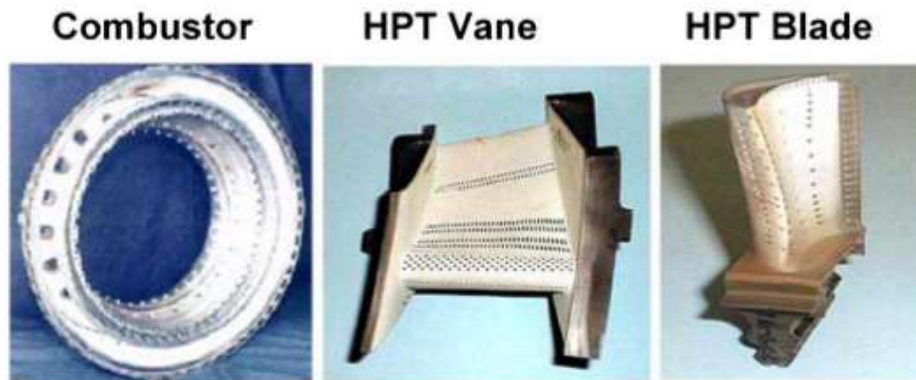


*Figure 1: Examples of components present in the hot section of a traditional gas turbine engine, with a cross section of a gas turbine engine [3]*

Gas turbine engines for aerospace and energy generation represent the cornerstone of a rapidly growing sector, with an estimation of 2 trillion USD for the cumulative sales of gas turbine engines in the 2017–2031 period [4]. Due to this considerable economic presence, there is a

great interest for the development of better performing components. Despite the merits of nickel-based superalloys, their innate high temperature properties are not enough to provide the level of efficiency required for modern gas engine turbines [5]. To achieve such ambitious goals, high temperature ceramic coatings are applied in conjunction with active cooling to effectively reduce the temperature experienced by the nickel-based superalloy component, as represented in Figure 2.

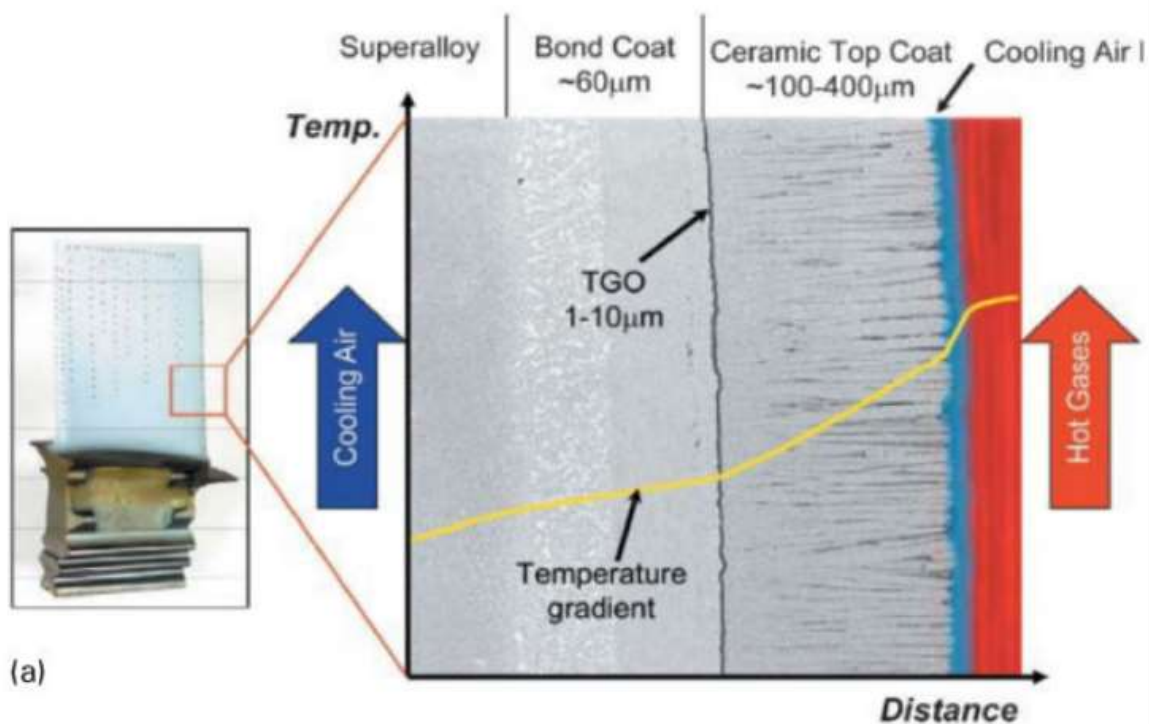


Figure 2: A nickel-based superalloy HPT blade coated with a ceramic coating and bond coat, with the addition of active cooling, showing the temperature gradient experienced during service [3]

Yttria-stabilised zirconia has been the reigning material for the production of protective coatings applied on top of nickel-based superalloy components used in the hot section [6]. Despite its successful implementation, the application of active cooling and protective coatings is reaching their performance limit, which has driven considerable research into finding a replacement for nickel-based superalloys. Ceramic matrix composites have been postulated as the next generation of high temperature materials for gas turbine engines, presenting improved

high temperature characteristics and reduced weight [7]. As with nickel-based superalloys, ceramic matrix composites will only see wide implementation if an effective protective coating is developed and applied, ensuring reliability and consistency under the noxious environment experienced during service. With this goal in mind, environmental barrier coatings have been investigated and slowly introduced into service [8], research showing that ytterbium disilicate is a promising candidate.

One of the key aspects of ceramic coatings is that their properties are dependent on the deposition technique. This characteristic can be exploited to benefit the performance of the deposited coatings. Two main techniques are being considered for the deposition of high temperature ceramic coatings for gas turbine engines: electron-beam physical vapour deposition (EB-PVD) [9,10] and thermal spraying [11–13]. Thermal spraying has been present for over a century, being greatly refined and optimised during this time. It has become nowadays a reliable and cost-efficient method to deposit thick coatings with a wide variety of feedstock materials and substrates. Due to its popularity and inherent flexibility, new developments are continuously being proposed. In order to ensure that these new developments, both in terms of coating compositions and deposition techniques, are successfully implemented by the final industry users, extensive research is required. A deep understanding of the relationship between the initial processes, including spraying parameters, the microstructure of the produced coating and the performance under simulated operating condition is needed.

## **1.2. Aim and objectives**

The aim of this thesis was to investigate the processing-microstructure-properties-performance relationships of a range of feedstocks: powder, suspension and solution precursor for the production of ceramic coatings using thermal spraying techniques. In order to achieve this aim,

high velocity oxy-fuel (HVOF) thermal spraying and air plasma spraying (APS) were used to produce a range of ceramic coatings. In addition to feedstock, different spraying parameters were chosen to investigate their effect on the coating microstructure. The deposited coatings were then extensively analysed using analytical techniques such as scanning electron microscopy, x-ray diffraction (with Rietveld refinement) and porosity measurement techniques (including neutron scattering) to precisely determine the characteristics of the coating. Finally, corrosion investigations were conducted under simulated operating conditions to assess the performance under commonly encountered corrosive species, such as high temperature steam or calcium-magnesium-alumino silicates (CMAS).

More in detail, several objectives were determined as milestones for the achievement of the aim of the thesis. As a summary, the objectives were:

- Evaluation of the solution precursor HVOF technique for the production of doped functional ceramic coatings with tailored microstructures, such as different levels of porosity. Additionally, the transformation from liquid feedstock into solid material deposited onto a substrate was to be thoroughly investigated, presenting a coherent model accounting for the in-flight evolution
- Acknowledging the importance of porosity in thermal barrier coatings, an investigation into porosity measurement techniques for suspension thermal sprayed coatings was planned. The goal was to apply neutron scattering to determine the porosity level and size distribution of suspension thermal sprayed thermal barrier coatings, aiming to capture sub-micron porosity, not measured with traditional techniques such as image analysis
- Finally, the performance of thermal sprayed environmental barrier coatings was to be investigated. Aiming to establish a better understanding of the effects of porosity under typical service conditions, two sets of samples were considered. The first one, with low

porosity levels, would resemble traditional environmental barrier microstructure. The second set, with high porosity, would represent abradable coatings. Both sets would be investigated under CMAS attack and steam degradation, to evaluate the performance of different levels of porosity

The original aim of the project was to focus the research on environmental barrier coatings (EBC) produced via various feedstock and altering their composition to evaluate their potential. Nevertheless, difficulties within the coating deposition process, as well as the cease of all in-person research activities caused due to the on-going pandemic, caused the focus of this project to shift towards ceramic coatings with applications beyond EBCs, with particular emphasis on the correlation between feedstock, spraying parameters and the resulting microstructure, including how to best characterise the coatings.

### **1.3. Thesis structure**

This thesis is submitted based on Thesis by Papers format. With this goal in mind, the different aspects of the research were conducted and published, corresponding to the following chapters:

- Chapter 1, the current chapter, introduces the context of the thesis, the overall goal, objectives and the thesis structure
- Chapter 2 presents a comprehensive literature review of the topics investigated during this thesis. First, a look at the solution precursor thermal spraying technique is presented, focusing on the current knowledge for the in-flight transformation, current state of the art and research opportunities detected. Secondly, porosity and the associated measurement techniques available for thermal sprayed coatings are presented. An overall view is given, before a more detailed introduction to the two main techniques applied in this thesis: neutron scattering and image analysis. A summary, including the current research landscape and gaps in the literature, is also given. The

last section of the literature review deals with environmental barrier coatings, including the main compositions nowadays being considered, and the two main corrosion mechanisms detected in the current generation. As before, this section ends with a summary stating the current state of the art of the field and several future lines of research

- Chapter 3 evaluates the use of solution precursor HVOF spraying to produce Nb-doped TiO<sub>2</sub> coatings. The objective was, first, to study the capability of SP-HVOF to produce TiO<sub>2</sub> coatings with homogenous Nb doping levels. Secondly, to study the effect that different flame powers had on the microstructure of the coating, as well as provide a more detailed understanding of the in-flight transformation of the solution precursor
- Chapter 4 deals with the measurement of porosity on suspension thermal sprayed thermal barrier coatings. Two techniques were applied to evaluate their merits, image analysis (IA) and neutron scattering (NS). Whereas IA is widely applied for powder feedstock thermal sprayed coatings, it presents limitations when the feedstock particle size is reduced, as seen in suspension thermal spraying. NS is a less common technique, requiring advanced facilities and complex data analysis, but it presents benefits regarding pore size studied and information obtained
- Chapter 5 makes use of free-standing ytterbium disilicate coatings to investigate the corrosion resistance against CMAS, without the influence of bond coat or substrate. Different compositions, thicknesses and porosity levels were studied, aiming to provide insight into the corrosion mechanism and the influence of the coating microstructure
- Chapter 6 studies the interaction between heated steam and free-standing ytterbium disilicate coatings at different temperatures, once more using coatings with different composition and porosity levels, to evaluate the resistance to prolonged exposure under corrosive environments. In addition to the effects of composition, microstructure and

temperature, observations are gathered regarding the use of alumina tubes in the furnace simulating operating conditions

- An Appendix is also included, providing more details into the thermal spray system used of the deposition of coatings using SHVOF and SP-HVOF thermal spray
- Chapter 7 provides a discussion of the work presented in this thesis, connecting the results providing in the experimental chapters and detailing the novelty of the results
- Chapter 8 presents the general conclusions of this thesis, detailing the scientific contributions produced during the duration of the project, in addition to suggestions for future lines of research that could use the advancement presented here as their foundation

## **Chapter 2: Literature review**

This chapter will present the necessary background preceding the experimental chapters. First, a general introduction to thermal spray is given, to put into context the process used in this thesis to produce the coatings. Then, a more in-depth view to the solution precursor thermal spraying is presented, detailing the inner mechanisms behind coating deposition, common applications and identified gaps in the literature. The second section of this chapter will deal with the current techniques commonly used for the measurement of porosity on thermal sprayed coatings. This section will briefly present the main advantages and disadvantages of the most used techniques, before taking a more detailed look at the two techniques used in this thesis: neutron scattering and image analysis. Current use for both techniques, as well as identified limitations are discussed. Finally, a literature review for environmental barrier coatings is presented. In this final section, the need for environmental barrier coatings is explained, as well as the characteristics that define a successful environmental barrier coating. A more detailed look at the current compositions of rare earth silicates used is then presented, with a short description of the achievement of each compositions, and their limitations. As a final section, the two main corrosion mechanisms that environmental barrier coatings as expected to face during service (namely calcium, magnesium, alumina-silicates and steam) are investigated. To sum everything up, the identified gaps in the current knowledge are presented.

Thermal spraying processes incorporate those technologies on which metallic or non-metallic coatings are deposited through the same principle. A heat source melts the feedstock material and a jet is used to impart kinetic energy to the molten particles. They then impinge the substrate surface and rapidly cool down to form a solid splat, continuously building up the desired thickness [14,15]. A basic schematic of the thermal spray process can be seen in Figure 3. The flexibility on thermal sources and jet configurations give rise to a plethora of different

deposition technologies, as presented in Figure 4, each one producing coatings with different microstructures and physical properties.

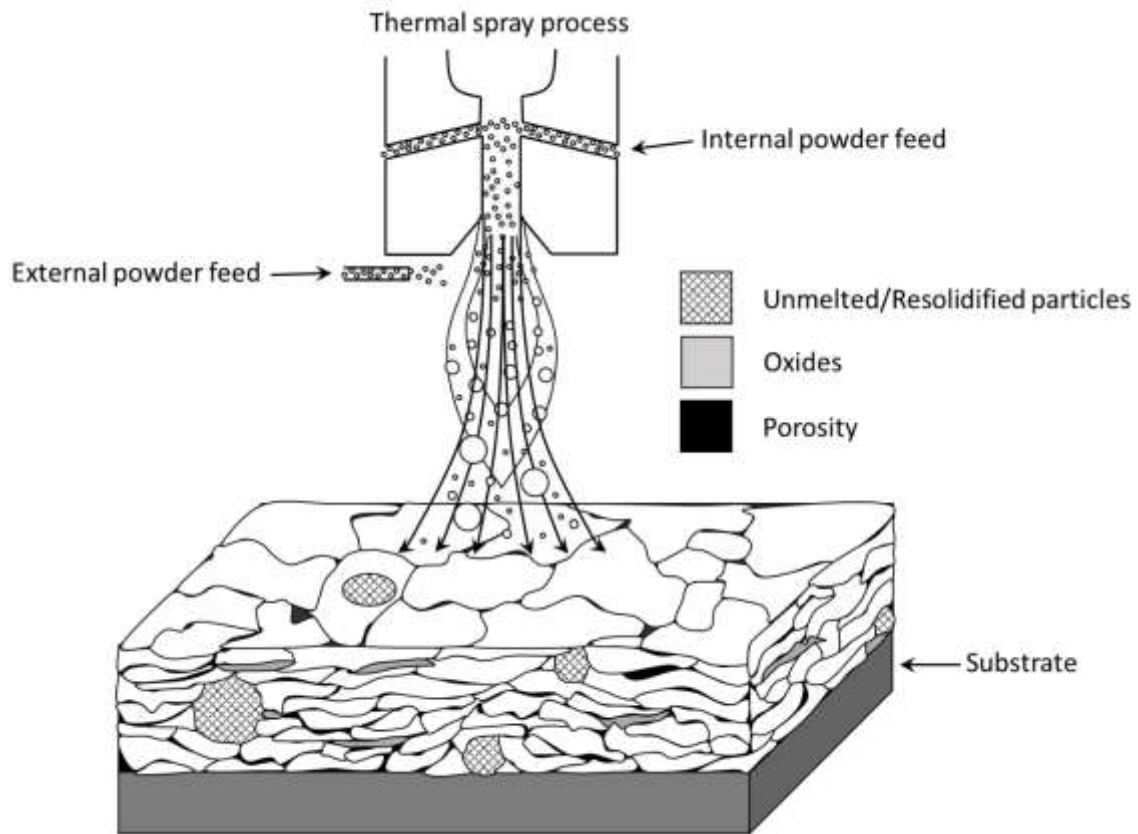


Figure 3: Schematic representation of a thermal spraying process with the two main components, a heat source and a jet, and the main features of the produced coatings. Redrawn from [16].

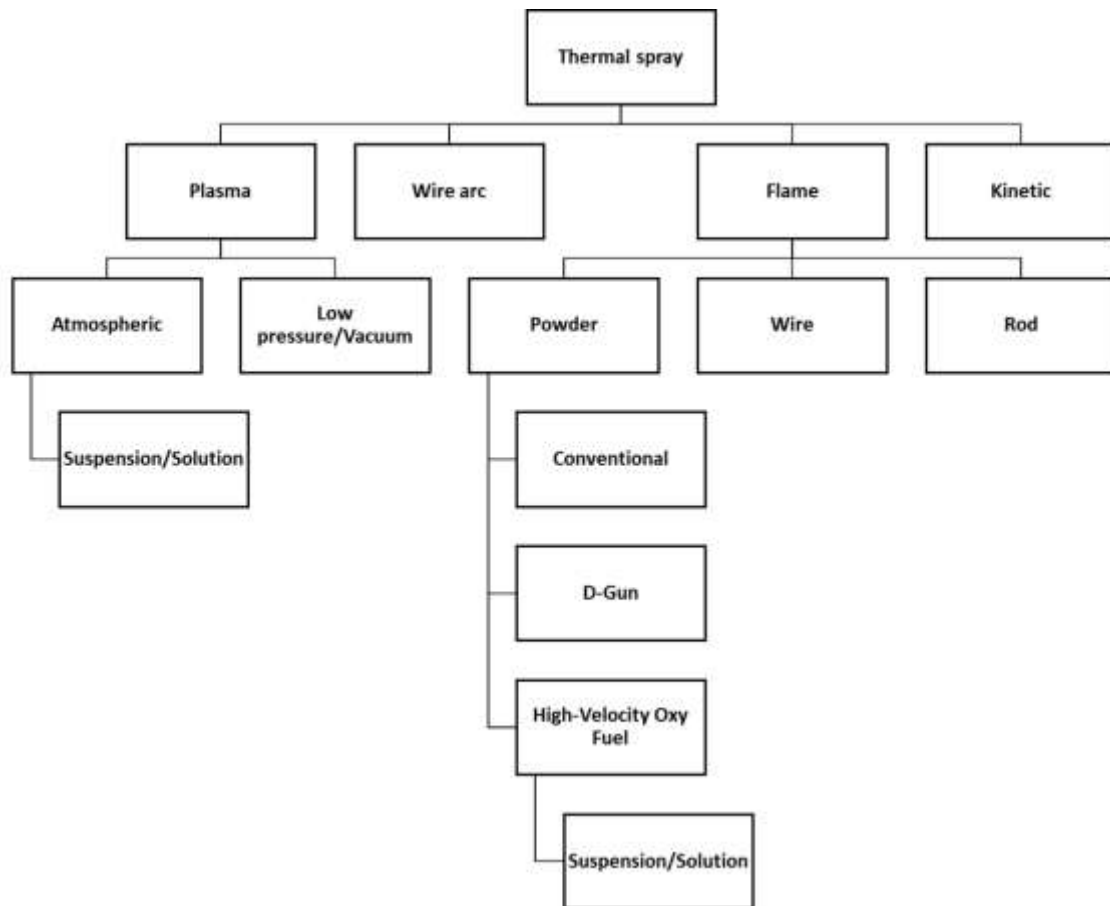


Figure 4: Classification of the thermal spray family of deposition techniques. Redrawn from [15].

The development of thermal spraying processes has been central to the evolution of functional and smart coatings [1], allowing new materials to be deposited and new substrates to be coated, broadening the range of accessible possibilities. As a summary, Figure 5 give an overview of the physical conditions for each of the main thermal spraying technologies:

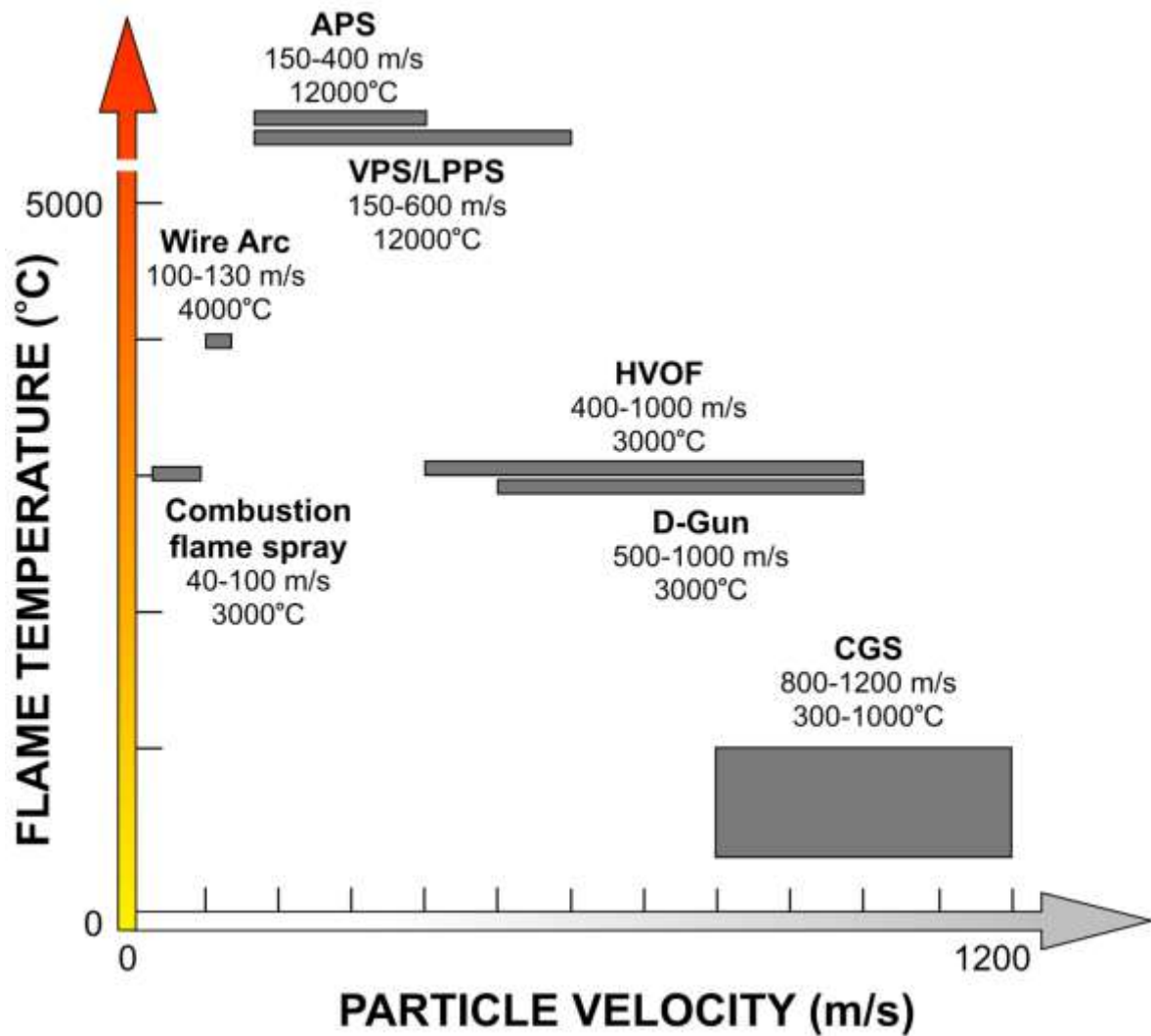


Figure 5: Schematic representation of the typical flame temperature and particle velocity for atmospheric plasma spray (APS), vacuum/low pressure plasma spray (VPS/LPPS), wire arc, conventional flame spray, high velocity oxy-fuel (HVOF), detonation gun (D-gun) and cold gas spray (CGS) [17]

Of particular interest is the use of solution precursor as the feedstock for thermal spraying, aiming to overcome some of the shortcomings present when using powder feedstock. A detailed literature review is presented in the next section.

## **2.1. Solution precursor thermal spray**

Adequate flowability of the feedstock powder presents a limitation to traditional thermal spraying methods. Generally speaking, particles with an approximate lower limit size of 10 – 100  $\mu\text{m}$  [18,19] must be employed to ensure proper flowability and deposition efficiency. In order to allow the use of sub-micron powders, different approaches have been developed as an alternative to the traditional injection of powder. The use of suspensions and solution precursors as the injection medium has been developed for several thermal spraying techniques. The differentiation factor between the two methods is that suspension thermal spraying relies on a liquid medium, generally water or alcohol, to carry the powder particles [20–22]. The liquid medium evaporates during the combustion, as is not expected to modify the chemistry of the feedstock. On the other hand, solution precursor thermal spraying is based on liquid precursors that will react during the combustion phase of the spraying, forming the desired composition in-flight [20,22–25]. One factor to be taken into account when choosing suspension and solution precursor feedstock is the cooling of the flame caused by the evaporation of the liquid and heating of the vapour. For this reason, thermal spray techniques with higher enthalpies involved, such as HVOF or plasma spraying, are preferred [26].

### **2.1.1. In-flight transformation**

Solution precursor thermal spray processes are inherently more complicated than their powder or suspension counterparts. In addition to the physical evolution of the feedstock, traditionally being molten powder or evaporation of the suspension medium, solution precursor adds an additional layer of complexity with the chemical processes taking place in-flight. As Pawlowski [27] described, there are several common steps that all solution precursor thermal spraying techniques generally adhere to, also being illustrated in Figure 6.

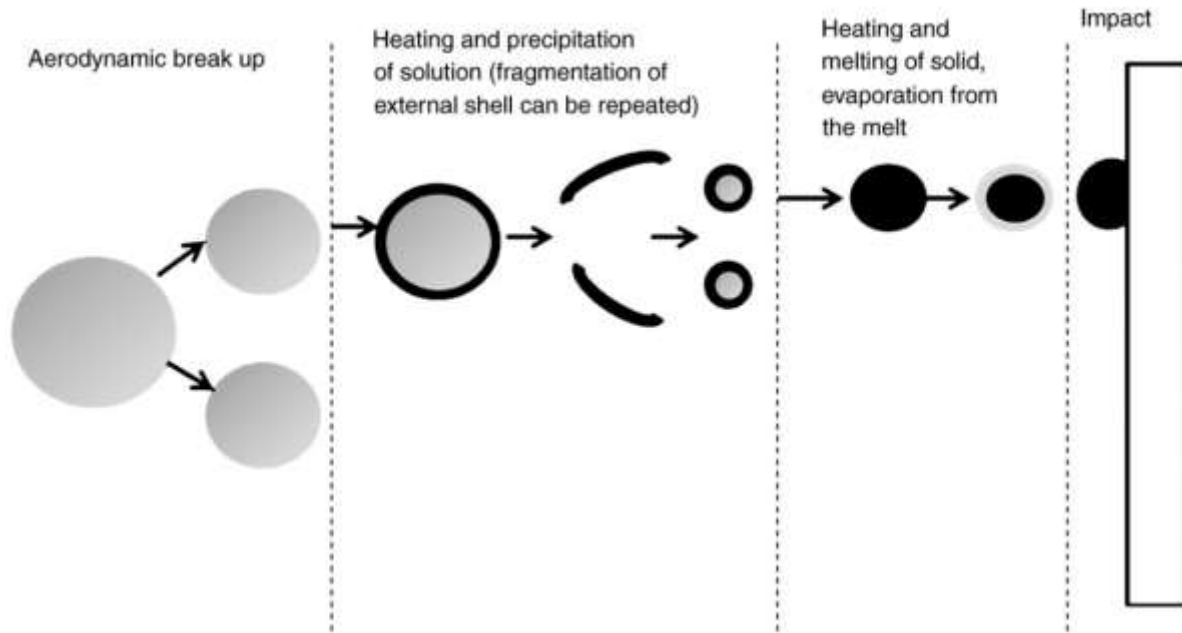


Figure 6: Evolution of a solution precursor droplet during thermal spraying

The general steps observed during solution precursors, as shown in Figure 6, can be described as:

1. **Aerodynamic break up.** Regardless of the method chosen for the injection of the solution precursor into the thermal spray equipment (injection or atomisation, as well as axial or radial injection), the difference in the average velocity between the combustion gases and the solution precursor will cause the liquid jet to break up into droplets. The specific evolution and morphology of the produced droplets are dependent on the physical properties of the liquid and the interaction with the gas. Generally speaking, the two dimensionless values of the Weber number ( $We$ ) and the Reynolds number ( $Re$ ), shown in Equations 1 and 2, are used to study this phenomenon [28].

$$We = \frac{\rho v_{rel}^2 d}{\sigma} \quad (1)$$

$$Re = \frac{\rho v_{rel} d}{\mu} \quad (2)$$

In the previous equations,  $\rho$  is the density of the solution,  $v_{rel}$  is the initial relative velocity between ambient and the droplet,  $d$  is the initial diameter,  $\sigma$  is the surface tension and  $\mu$  is the dynamic viscosity.

2. **Heating, vaporisation and internal precipitation.** As the droplets travel further within the flame, heat transfer causes the evaporation of the solvent, reducing the size of the droplets. This also causes the appearance of internal precipitation within the droplet, as a condensed solid content is formed. From this point, the evolution of the droplet will be dependent on two competing phenomena. If the rate of solvent vaporisation is greater than the diffusion of the solvent, an external supersaturated layer will be formed. On the contrary, if the rate of solvent vaporisation is slower than the diffusion of solvent, the solid content will diffuse until solid particles are formed. A schematic of these alternatives is shown in Figure 7.

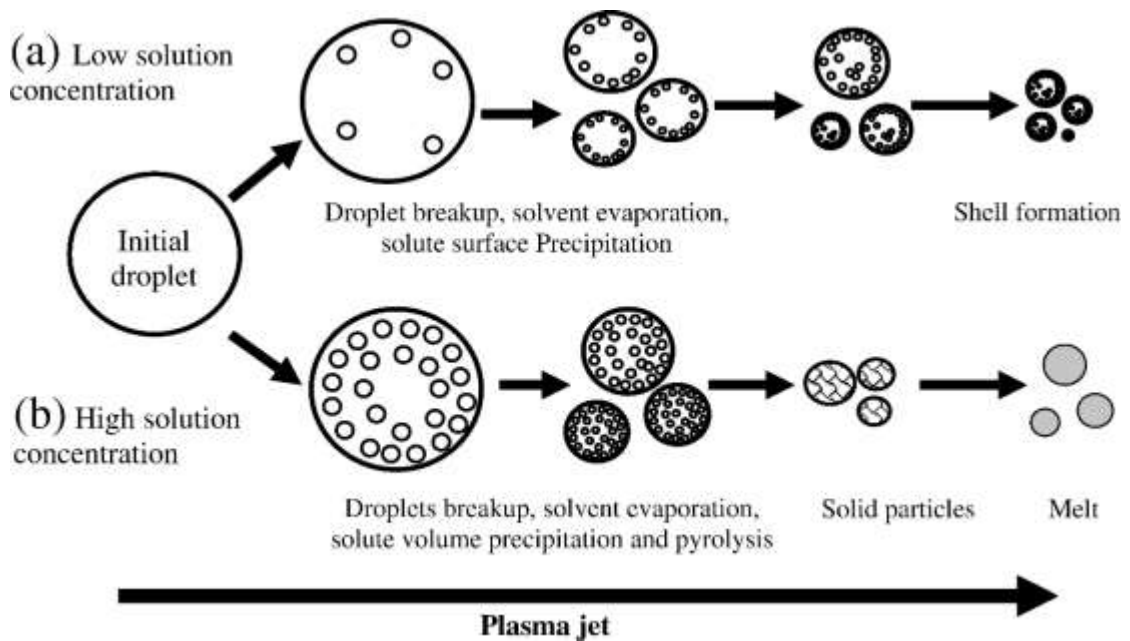


Figure 7: Schematic of the different evolution paths for a droplet during solution precursor thermal spray depending on the initial solution concentration [29]

3. **Internal pressurisation and droplet break up.** Assuming that solid shell does indeed form, the continuous heat transfer will cause the vaporisation of the liquid content inside the droplet, followed by an internal climb up of the pressure. If the vapour pressure becomes greater than the strength of the solid shell, a break up of the shell will occur.
4. **Solid particle heating and melting.** The solid content formed in-flight, both due to the solid content formed due to high diffusion rates and due to the rupture of the solid shells, will continue to heat up during its time in the flame. If the flame conditions allow it, namely high enough flame temperature and long in-flame residence times, the solid content will melt. This can cause additional fragmentation if the melt is severely affected by the conditions of the flame, further reducing the size of the final splats.
5. In cases of particularly high flame temperatures and low particle velocity (leading to longer residence times in the flame), such as those experience during plasma thermal spraying, the melt can experience further vaporisation, causing the loss of material and the reduction of the size of the droplets. This reduction in size can have detrimental consequences, as particles too small will follow the gas path instead of reaching the substrate at the adequate angle, as exemplified in Figure 8.

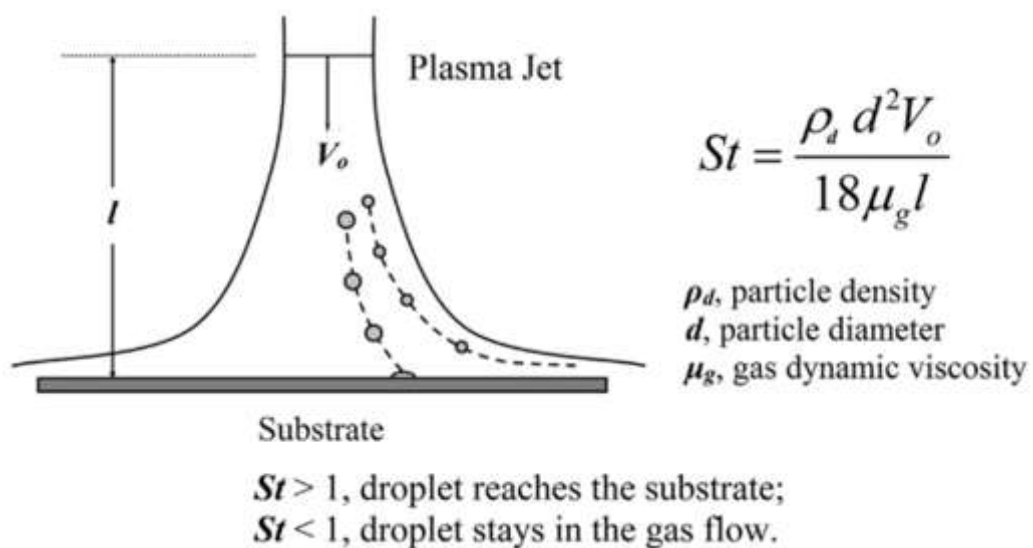


Figure 8: In-flight particle path depending on the Stokes number (greatly influenced by particle size)

6. **Impact with the substrate.** As the final step, the molten splats and solid content reach the substrate to be coated, causing the formation of a coating if the spraying conditions permit it.

### **2.1.2. Niobium-doped TiO<sub>2</sub>**

The study of a deposition technique does not only require knowledge and proper preparation of the technique itself, but a careful consideration of the material to be used. The goal is to find a material that is capable of being used with the chosen technique, allowing enough flexibility to ensure that the different phenomenon occur, while avoiding unwanted issues that could mask the potential of the technique.

TiO<sub>2</sub> is a widespread material that has been used in a plethora of fields owing to its inherent properties. An early example can be found in 1972 when Fujishima and Honda [30] reported the use of TiO<sub>2</sub> to decompose H<sub>2</sub>O into oxygen and hydrogen making use of the photocatalytic properties presented by TiO<sub>2</sub>, as schematically represented in Figure 9.

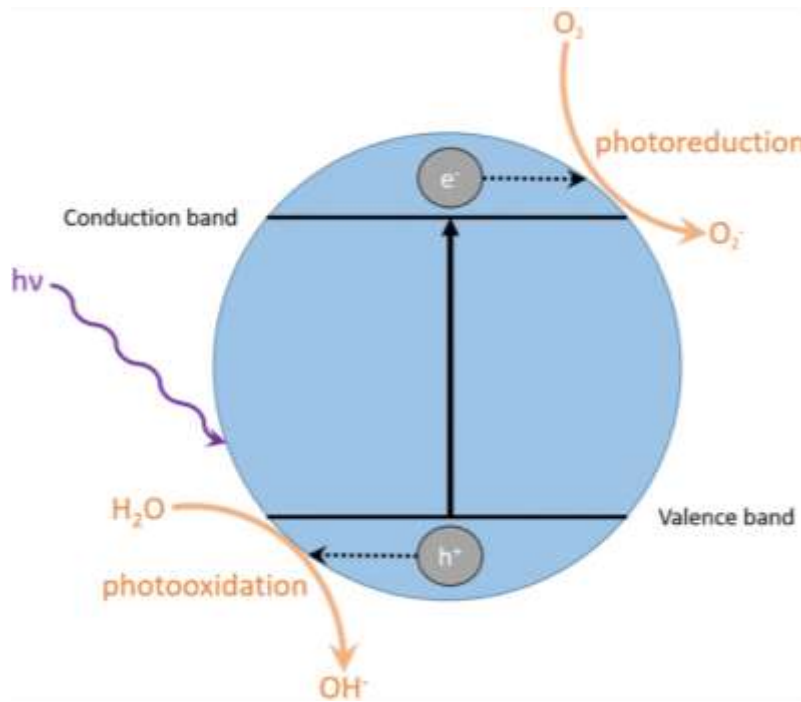


Figure 9: Schematic of the photocatalytic effect in  $\text{TiO}_2$ , with the production of free hydroxyl ( $\text{OH}^-$ ) upon illumination [1]

The photocatalytic effect of  $\text{TiO}_2$  seen in Figure 9 has been since then applied, for instance, for the production of antimicrobial coatings. Upon illumination with a light source producing photons carrying energy equal or greater than the gap band of  $\text{TiO}_2$ , electron-holes are created, which have a probability to interact with the water molecules and produce  $\text{O}_2^-$  and  $\text{OH}^-$  radicals. These radicals have been proven to present biocidal properties against numerous bacteria [31,32].

Another interesting property of  $\text{TiO}_2$  that has been exploited is its coherent change in electrical conductivity when exposed to reducing gases [33]. The change of conductivity can be easily measured on thick films, providing a suitable platform for solid state gas sensors use, for example, to track pollutants. As a proof-of-concept, Carrota *et al.* [34] produced nanostructured  $\text{TiO}_2$  sensors calibrated to measure CO concentration in real conditions. The results, presented in Figure 10, show excellent capabilities when compared to commercially available sensors.

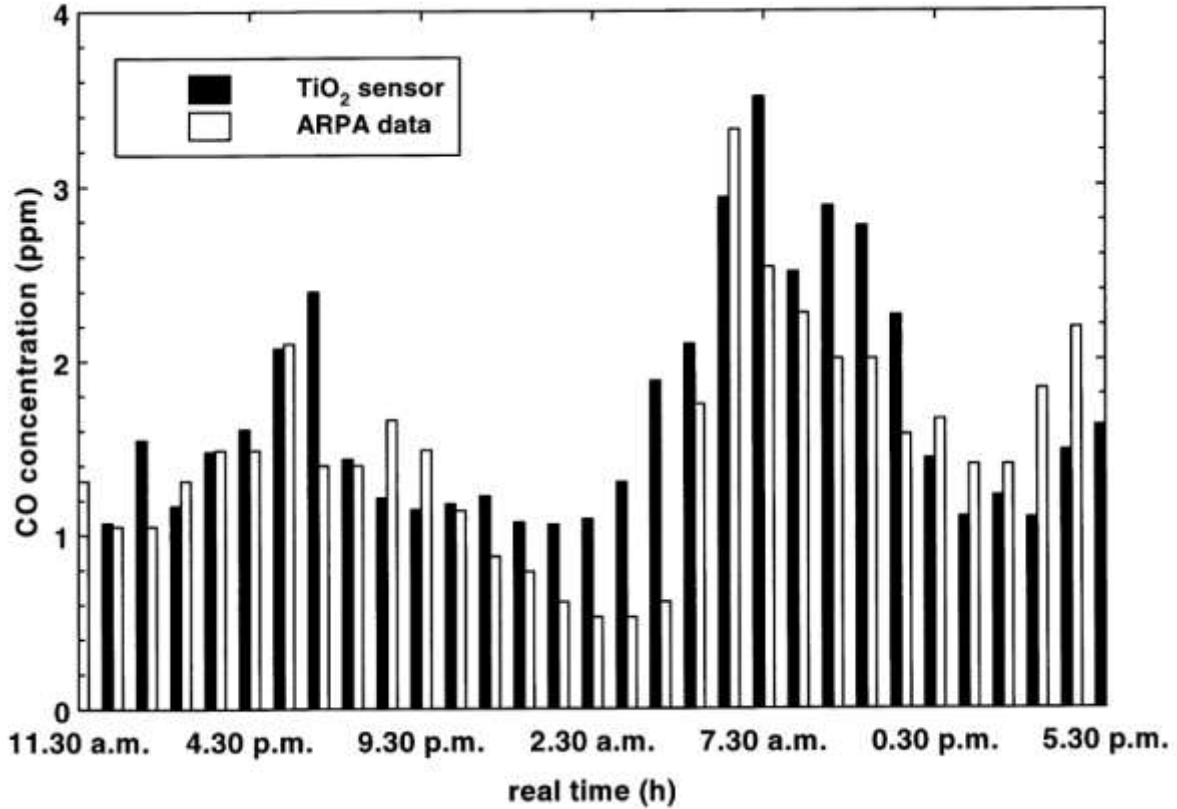


Figure 10: Comparison between the CO levels measured in real time by a TiO<sub>2</sub> sensor (black columns) and a commercially available sensor (white columns) [34]

The last example of the flexibility and applications of TiO<sub>2</sub> is the production of transparent conductive oxide (TCO) films. The current standard for the industrial production of TCO, a key element in liquid-crystal displays, OLEDs and touchscreens, is Sn-In<sub>2</sub>O<sub>3</sub>, which presents serious problems in the short and medium long term due to limited resources and continuous increasing cost [35]. Considerable research is being conducted, aiming to produce transparent and conductive TiO<sub>2</sub> coatings that can replace Sn-In<sub>2</sub>O<sub>3</sub> [36].

Despite the clear beneficial properties of TiO<sub>2</sub>, its behaviour can be tailored to the specific application in mind. Doping with elements such as Nb has been a proven route to modify the properties of TiO<sub>2</sub>, particularly increasing the electrical conductivity and improving its electrochemical properties [37,38]. Directly relating to the examples given above, the addition of Nb doping helps stabilise the anatase phase at high temperatures [39], being considered the

most beneficial phase for sensing applications. In addition to the phase stabilisation properties, Nb doping has also been proven as an effective route to control grain growth and improve the overall electrical conductivity of  $\text{TiO}_2$  [40], which is desirable when producing gas sensors and conductive oxide films.

Regarding production of  $\text{TiO}_2$  and Nb- $\text{TiO}_2$  coatings, a plethora of techniques have been successfully applied. Examples include flame spray pyrolysis [40,41], sputtering [36,42,43], pulsed laser deposition [44,45], atomic layer deposition [46], spin-coating [47] or aerosol-assisted chemical vapour deposition [48]. At the same time, thermal spraying deposition of titanium oxide has been thoroughly studied before; using powder, suspensions and solution precursors as feedstock material [49–52].  $\text{TiO}_2$  coatings have been produced using HVOF and APS [49], as well as SPPS [51,52], proving that thermal spraying is a suitable technique for its deposition. Particularly interesting is the work of Chen *et al.* [51,52] producing  $\text{TiO}_2$  with different porosity levels using in both cases SPPS, as presented in Figure 11.

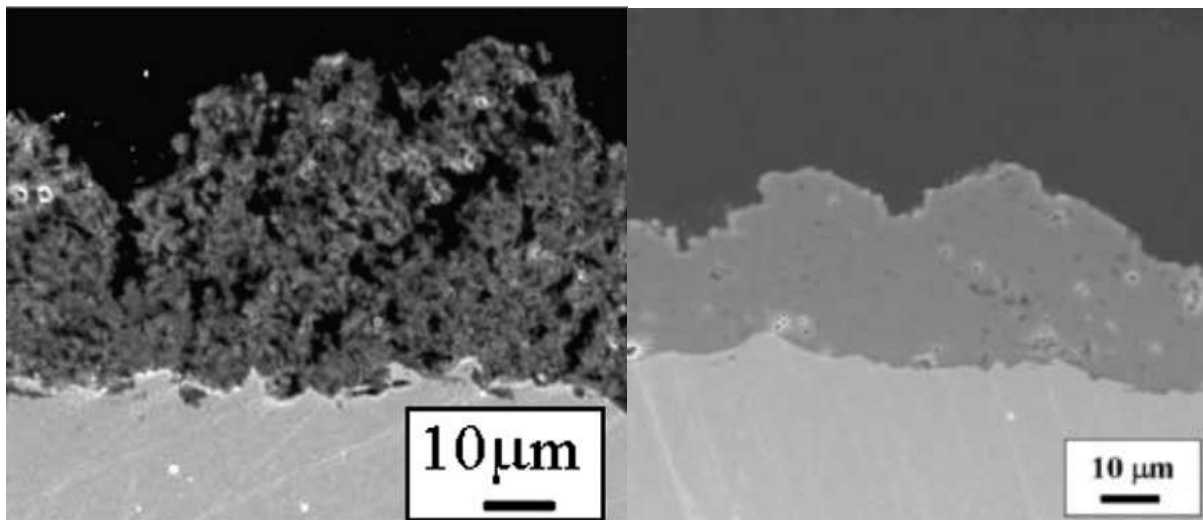


*Figure 11: Cross-section images of two different  $\text{TiO}_2$  coatings produced using SPPS with different levels of porosity [51,52]*

The ability of solution precursor thermal spraying to produce coatings with varying microstructure is one of the strengths of the feedstock that will play a role in its industrial

implementation. Since the majority of the research has been conducted using SPPS, as mentioned before, it is worth noting that a detailed understanding of the deposition mechanism for SP-HVOF will be beneficial to tailor the microstructure of the deposited coating to the desired application, although more research is needed. Given the flexibility that SP-HVOF allows when dealing with the chemical modification of the initial feedstock in order to produce doped ceramic coatings, the potential of SP-HVOF as the deposition technique for Nb-TiO<sub>2</sub> is clear, with more research needed to evaluate the level and distribution of the doping element within the deposited coating.

### **2.1.3. Current status and future research**

The use of solution precursor thermal spraying has been particularly prolific in the field of plasma spraying (SPPS). As noted by Gell *et al.* [53], since the first report of a SPPS sprayed material in the early 2000s, extensive research has taken place, aiming to overcome the limitations that powder feedstock imparted to the coatings. In particular, the field of thermal barrier coatings has seen considerable application of SPPS for the production of optimised protective coatings [54]. The reason for this success lies in the capability of SPPS to produce coatings with uniformly distributed porosity and evenly spaced cracks, which helped to reduce the overall residual stress and the thermal properties of the coating [55–57]. A detailed review by Fan and Bai [54] presents a more detailed view of the merits of this technique for the deposition of thermal barrier coatings.

Despite the success that SPPS has had on thermal barrier coatings, plasma spraying is not the only thermal spraying technique that can benefit from this feedstock presentation, nor are thermal barrier coatings the only application where success can be obtained. As previously mentioned, deposition techniques with higher enthalpies are preferred when using solution precursor, making HVOF, in addition to plasma spraying, a suitable candidate. Although

detailed studies regarding the suitability of solution precursor HVOF (SP-HVOF) have been published [24], efforts have been focused on SPPS. This makes SP-HVOF an ideal ground for further research and study, in order to better understand its capabilities and properly assess whether it can be applied with success to solve the industry's needs.

## **2.2. Porosity measurement on thermal sprayed coatings**

Porosity, encompassing the total level of porosity, the morphology of the pores and the size distribution, is one of the key microstructural features present in thermal sprayed coatings. During the deposition of thermal sprayed coatings, size distribution of the feedstock particles (or particles formed in-flight in the case of solution precursor) plays an essential role in determining the porosity present within the coating. The presence of unmelted or semi-molten particles, as well as the gaps present in between splats, are directly correlated to the content and shape of pores [58]. The reason why porosity is critical to the performance of thermal sprayed coatings can be explained through the direct association that porosity has with several physical and thermal properties [59,60].

Despite the utmost importance of porosity, the task of actually measuring the porosity level, along with the pore morphology and size distribution, is a challenge in itself that requires significant amount of consideration and planning. Figure 12 presents a myriad of techniques currently available to measure porosity.

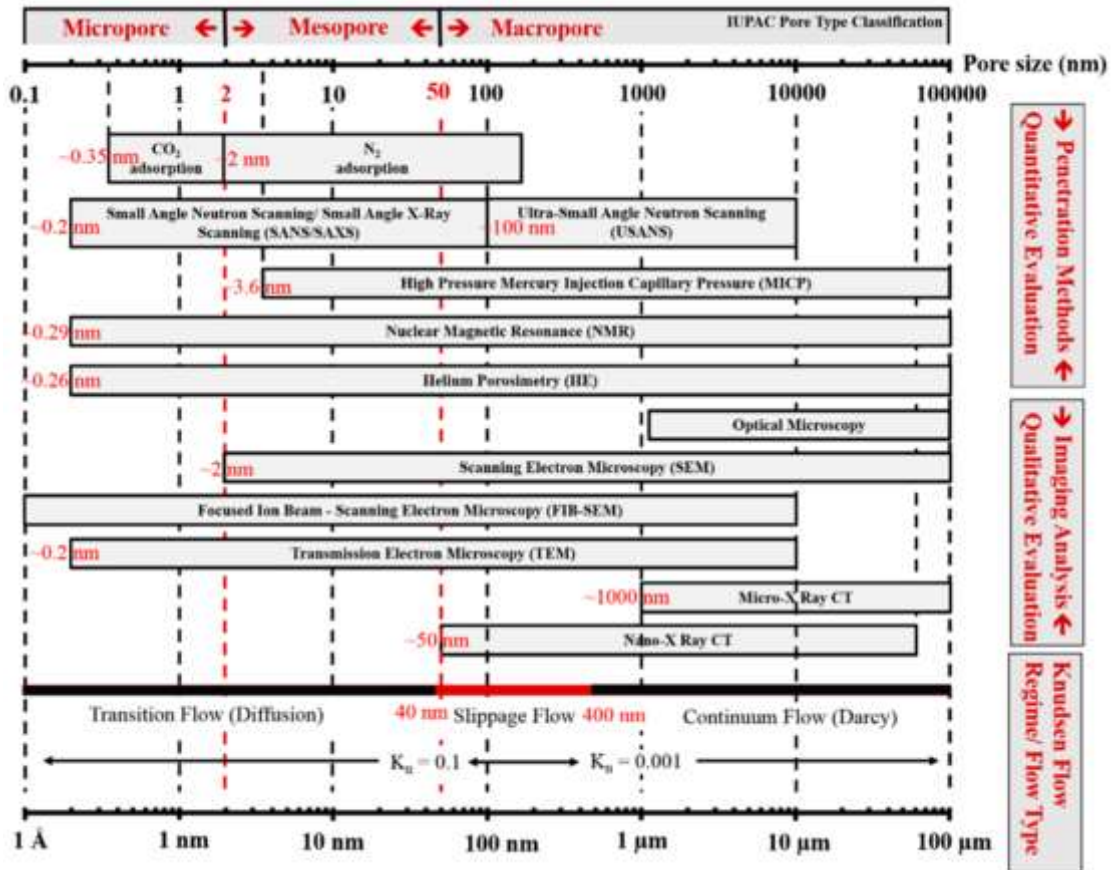


Figure 12: Overview of some of the different techniques available to measure porosity, along with the approximate pore size range measurable [61]

As exemplified in Figure 12, the pore size range that needs to be investigated is the first consideration when deciding which technique is the most suitable. In addition to different measurable pore size ranges, each technique has different advantages and disadvantages. For instance, mercury intrusion porosimetry (MIP) is a destructive technique with no possibility to reuse the samples for alternative testing. In addition, since mercury needs to access the pore in order to measure it, only open porosity (pores connected to the surface) are measured, providing a partial picture of the porosity state of the coating. A more detailed look at neutron (as well as x-ray, due to the similarities of the mechanism) scattering and image analysis, the two porosity measurement techniques used in this thesis, can be found in the next section.

### 2.2.1. Neutron/x-ray scattering

Small-angle neutron/x-ray scattering (SANS/SAXS) techniques are based on the elastic scattering of a monochromatic beam of neutrons or x-ray with the sample to be investigated. Details and mathematical justification for the technique can be found in section 4.6 “Appendix A”. A schematic of the set-up for a SANS measurement is presented in Figure 13.

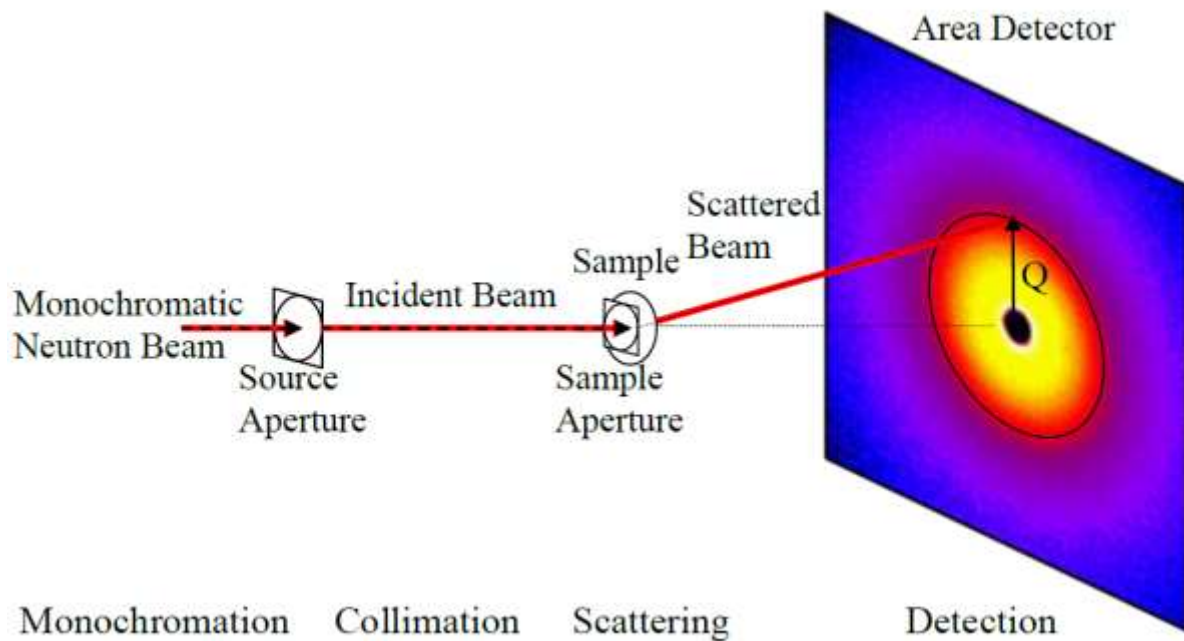


Figure 13: Schematic of the SANS technique [62]

The main advantage offered by neutrons is that since they are particles without charge, their penetration depth is higher when compared to x-ray, allowing for samples with the typical thickness observed in thermal sprayed coatings (up to  $\sim 500 \mu\text{m}$ ). This penetration depth also allows for non-destructive testing where the same sample can be investigated using different techniques, feature not present with other porosity measurement techniques. Furthermore, the addition of complementary techniques such as ultra-small-angle neutron/x-ray scattering (USANS/USAXS) can effectively provide a measurable pore size range between  $\sim 1 \text{ nm}$  up to  $\sim 50 \mu\text{m}$  [59].

On the other hand, one of the main disadvantages that these techniques present is the need for highly specialised facilities (neutron facilities for SANS and synchrotron for SAXS) which are difficult to access. In addition, data analysis is a complex process that requires detailed information for it to be successful. The scattering length density (SLD) of the material needs to be known, as well as the morphology of the pores, in order to simulate the pore size distribution based on the measurements obtained.

### **2.2.2. Image analysis**

Analysis of microscopy images can provide adequate information regarding the total porosity, pore morphology and size distribution of thermal sprayed coatings, one of the most common techniques at present [63]. The technique is relatively straightforward, starting with a digital image of the cross section of the coating, properly mounted and polished [64], being imaged using a microscopy technique. The resolution achieved will be dependent on the imaging technique chosen, and the magnification used. For larger pores, optical microscopy might be suitable and sufficient, but smaller pores might require more advanced techniques, such as scanning electron microscopy or even transmission electron microscopy. Once the coating has been appropriately imaged, ensuring that all the relevant features have been included and enough images have been captured to fully represent the porosity in the coating, the software can be used to translate the images into black and white maps, as represented in Figure 14.

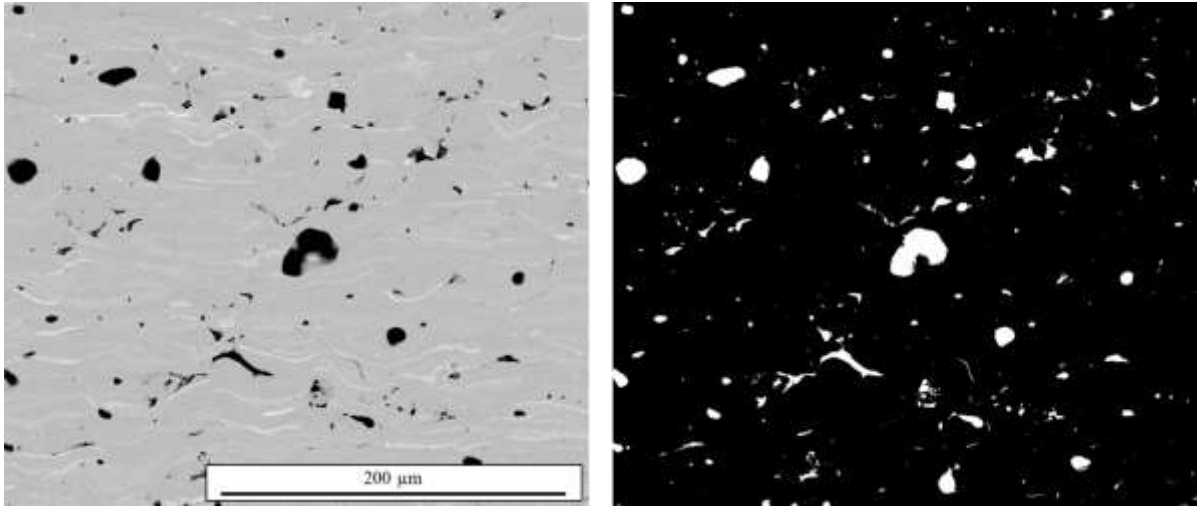


*Figure 14: Image on the left shows a BSE image of a thermal sprayed ceramic coating with the presence of porosity. Image on the right shows the same image after treatment with a software to translate it into a black and white map*

From the black and white map shown in Figure 14, information regarding the porosity level of the coating, morphology of the pores and size distribution can be extracted. Image analysis is a very useful technique as it allows the operator to gain both quantitative and qualitative knowledge regarding the porosity within the coating. On the other hand, samples need to be cut, mounted and polished for imaging, making this technique a destructive one. Additionally, there is some degree of subjectivity as the operator must choose the areas to be imaged and then the processing parameters in the desired software, which can affect the final results. Contrary to neutron/x-ray scattering techniques, it does not require specialised facilities, as a simple optical microscope might be enough for porosity measurements, making this technique also quite accessible.

### **2.2.3. Current status and future research**

Due to the importance of porosity in thermal sprayed coatings, several techniques are commonly applied to measure both the total porosity content and the morphology of the pores. As mentioned above, image analysis is a prevalent technique due the simplicity of the

measurement and the wide availability of optical or electron microscopes. This popularity is reflected in the use of this technique for the ASTM International Standard E2109 – 01 “Standard Test Methods for Determining Area Percentage Porosity in Thermal Sprayed Coatings” [64]. Porosity measurements via image analysis have been applied for powder-based thermal sprayed coatings (i.e. APS and HVOF) for almost 20 years now, and most recent publications still rely to some degree on measurements produced using this technique [63].

Several other techniques, namely mercury intrusion porosimetry (MIP) and neutron scattering, have also been studied and applied with success. For instance, Ilavsky *et al.* [65] reported back in 1997 the benefits and disadvantages of applying MIP to plasma sprayed coatings. Despite the ability of the MIP technique to provide detailed information regarding the porosity within the coating, the underlying mathematical model is based on the equivalent diameter of the pore, which might be considerable different from the actual diameter of the pore. This effect is caused as the method effectively measures the largest available entrance to the pore. In the case of pores closely resembling a cylinder this approximation is very accurate, but this is not always the case. Another disadvantage of the use of MIP is that in order for the mercury to intrude the pores, these must be connected to the surface, or open as they are traditionally called. Closed pores, or pores without a connection to the surface, cannot be measured using MIP.

The popularisation of liquid-based thermal spraying techniques, such as SPS/SPPS or SHVOF/SP-HVOF requires a careful consideration when considering the best approach to measure the porosity. The current framework for the measurement of the porosity was established years ago, when powder was the primary feedstock presentation. Work by Deshpande *et al.* [66] comparing image analysis and neutron scattering for APS coatings was instrumental, but it does not take into account the nano-sized porosity associated with suspension thermal spray. It is clear that in order to safely apply image analysis for porosity measurements of suspension thermal sprayed coating, more research is needed to evaluate the

discrepancy acceptable, evaluating the pros and cons of this technique with others presenting a wider measurable pore size, such as neutron scattering.

### **2.3. Environmental barrier coatings**

The main body of this section is reproduced from the paper:

*D. Tejero-Martin, C. Bennett, T. Hussain, A review on environmental barrier coatings: History, current state of the art and future developments, J. Eur. Ceram. Soc. 41 (2021) 1747–1768. <https://doi.org/10.1016/j.jeurceramsoc.2020.10.057>*

Gas turbine engines for aerospace and energy generation represent the cornerstone of a rapidly growing sector, with an estimation of 2 trillion USD for the cumulative sales of gas turbine engines in the 2017-2031 period [4]. Due to this considerable economic presence, there is a great interest for the development of better performing components. Ni-based super-alloys have been for the past decades the norm for components in the hot section of gas turbine engines. Improvements on thermal barrier coatings and cooling mechanisms have allowed the industry to increase the gas inlet temperatures up to 1500 °C [2,5], driving upwards the thermal efficiency, the thrust-to-weight ratio and reducing the emission of noxious by-products. Nevertheless, this strategy is approaching the intrinsic limit imposed by the melting point of Ni-based super-alloys, and novel strategies will be needed to further increase the gas inlet temperature. A new approach is required for the next breakthrough in jet engines, and SiC/SiC ceramic matrix composites are the most promising material to fulfil the role. When compared to Ni-based super-alloys, CMCs provide an increased service temperature and superior strength at high temperature, as can be seen in Figure 15.

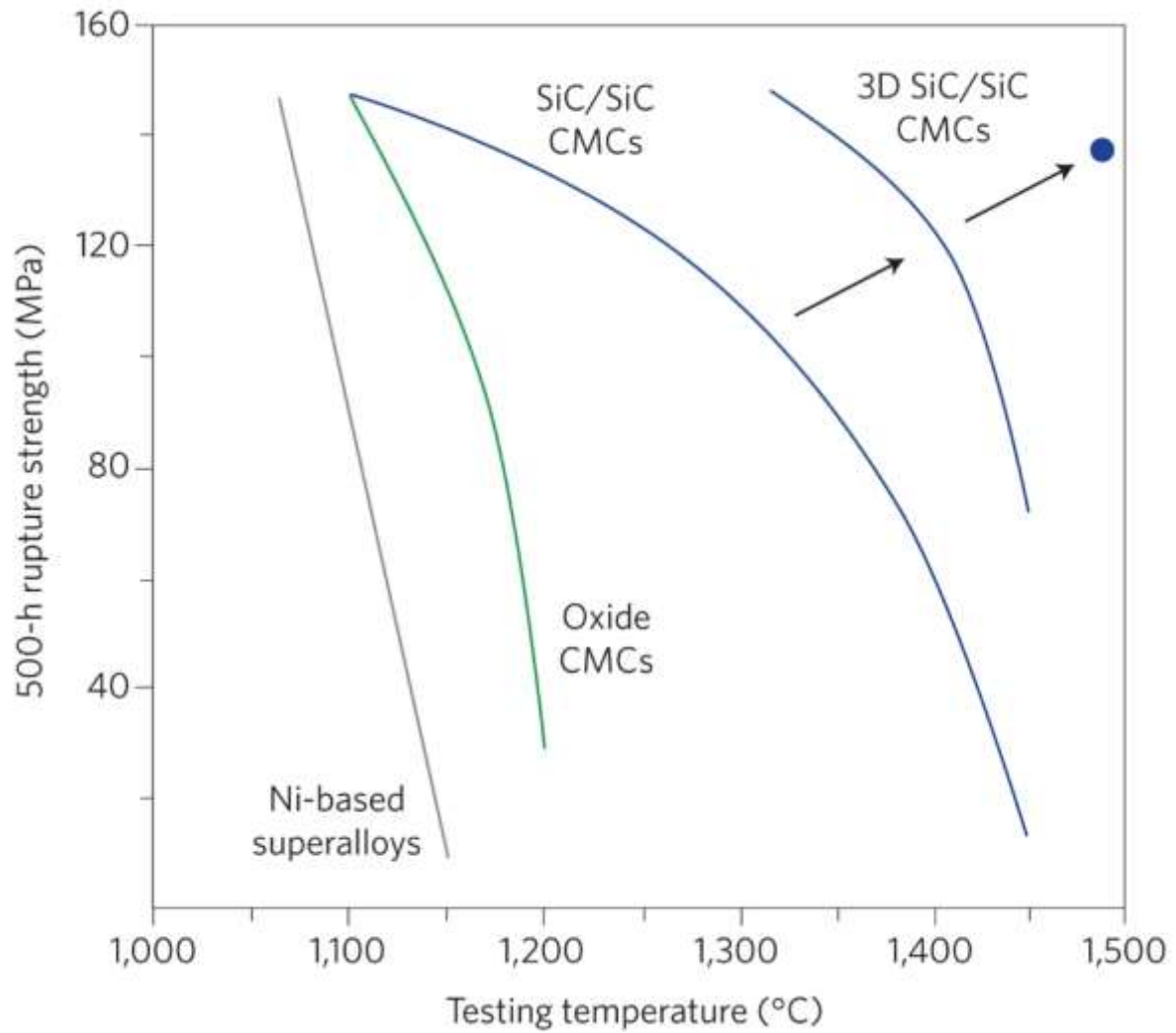
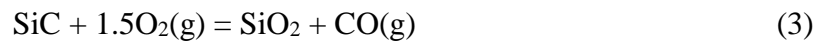


Figure 15: Rupture strength after 500 h of continuous exposure versus testing temperature of Ni-based super-alloys, oxide CMCs and various SiC/SiC CMCs. The blue point is the 300 h rupture strength [5]

Under clean, dry oxygen atmosphere, SiC-based CMCs present excellent oxidation resistance attributed to the formation of a protective silica layer. Al Nasiri *et al.* [67] reported the oxidation kinetics of SiC/SiC CMCs exposed at 1200 – 1400 °C for up to 48 h in air, showing a parabolic mass gain and oxide layer thickness growth that was caused by a decrease in the oxidation rate associated with the diffusion of oxygen through the oxide layer, with an activation energy of 619 kJ/mol. Nevertheless, under the presence of steam (a common combustion reaction product) or corrosive species (caused by the ingestion of debris with the intake air during take-

off and landing, such as sand or ingestion of volcanic ash during in-flight, generally labelled as CMAS, or present as fuel impurities [68,69]) accelerated degradation of the otherwise protective silica layer takes place, compromising the integrity of the CMC [70–74]. The effect of steam on CMCs has been extensively studied over the past decades, since it was realised early in their development that an increase in the steam content led to an accelerated oxidation rate. In the late twentieth century Opila *et al.* [70] first studied the precise mechanism behind silica volatilisation, establishing an additional step following the reaction of SiC with O<sub>2</sub> to form silica, shown in Equation 3 in which the silica further reacted with H<sub>2</sub>O to form gaseous Si-O-H species, such as Si(OH)<sub>4</sub> [71] as shown in Equation 4, therefore causing the mentioned silica volatilisation.



This volatilisation process would be accompanied by a recession of the surface of the component, which has been calculated to be as high as ~1 μm/h under normal gas turbine operating conditions (temperature of 1350 °C, gas velocity of 300 m/s, steam partial pressure of 0.1 atm and total pressure of 1 atm) [75]. Such a recession rate would imply an unacceptable level of corrosion for components that are expected to operate without maintenance for at least 30,000 h.

On the other hand, the negative effect of molten salts has also been extensively studied for decades. Contrary to the case of steam, salt degradation can be caused by a wide range of chemical compounds, making its study and prevention more challenging. In the early 1990s, reports were coming in regarding the effect of the ingestion of volcanic material by planes flying near volcanic plumes [76]. This promoted a shift from the previously studied hot corrosion by Na<sub>2</sub>SO<sub>4</sub> to a different corrosion mechanism coming from a more generalised

family of compositions, being labelled as CaO-MgO-Al<sub>2</sub>O<sub>3</sub>-SiO<sub>2</sub> or CMAS [77,78]. Therefore, as summarised above, the early realisation of the deleterious effect of steam and corrosive compounds (such as alkali salts or debris) on the longevity of CMCs prompted the desire to develop a protective coating that would prevent the environmental attack of SiC components. With this goal in mind, environmental barrier coatings were first introduced as a solution to the exacerbated corrosion experienced by CMCs under typical service environments. As mentioned above, EBCs are expected to fulfil a set of requirements to be considered fit for service, being the five main characteristics shown in Figure 16.

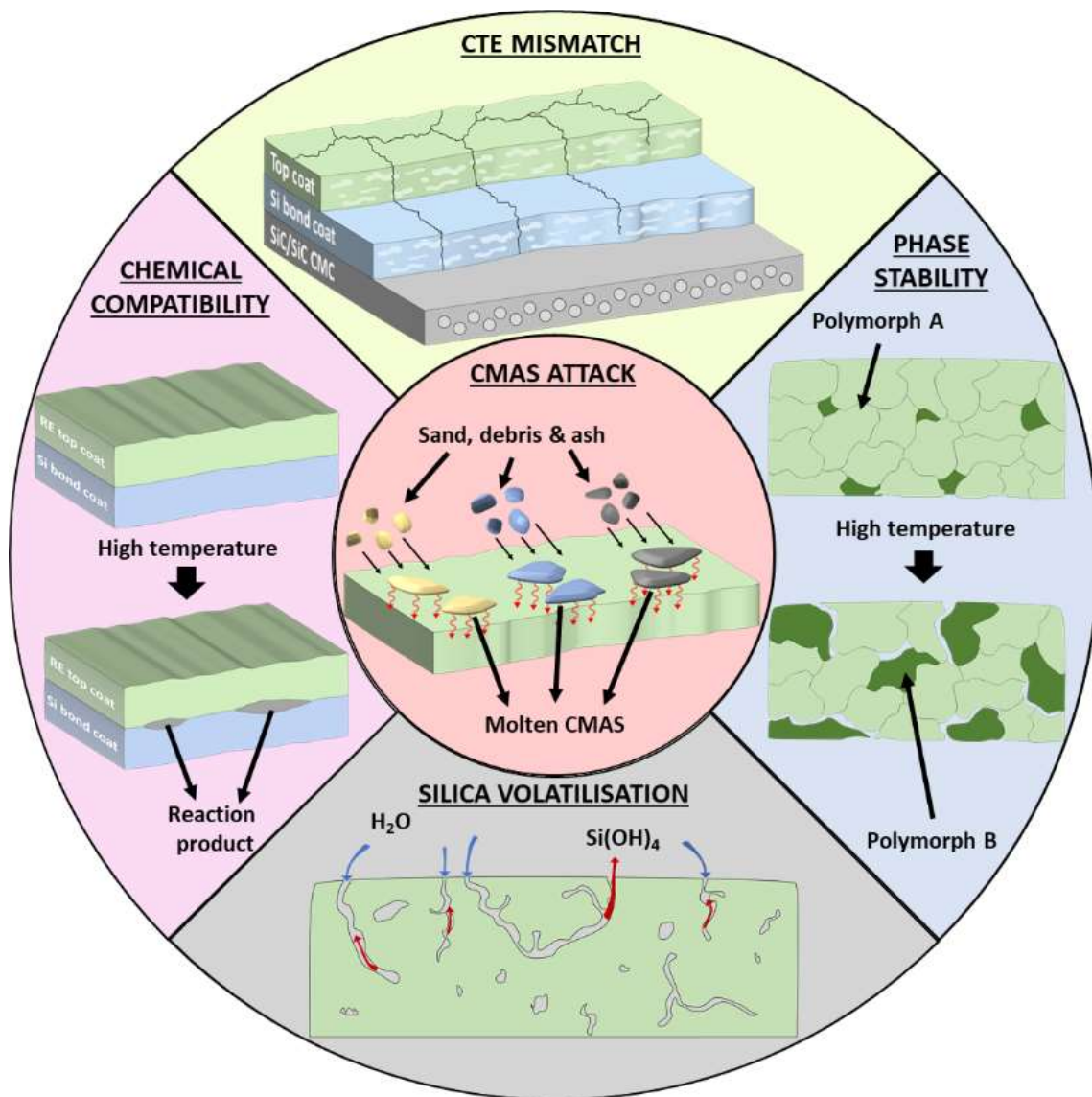


Figure 16: Schematic of the main five requirements that any successful EBC is expected to fulfil

As it can be seen in Figure 16, high temperature induces a series of phenomena that determine whether the EBC will remain protective and fulfil its role, or fail. At the top, a representation of the effects of a mismatch in the CTE is shown. Due to the presence of heating and cooling cycles during service, thermal expansion and contraction will take place for each of the components of the EBC. If the magnitude of their CTE is too different from each other, the thermal stresses induced will lead to the formation of cracks. On the right sector, it can be seen how the presence of polymorphs can affect. The as-deposited coating might show a majority of polymorph A, but at high temperatures, there might be a phase transformation into polymorph B, which can be accompanied by a noticeable volume contraction (or expansion), causing cracking and defects such as porosity. At the bottom, the process of silica volatilisation is presented. The presence of steam at high temperatures induces the formation of silica containing gases, such as  $\text{Si(OH)}_4$ , producing the recession of the material. On the left, the chemical compatibility between the layers present is shown. Materials that at room temperature might show good compatibility and stability might become reactive and produce unwanted by-products when exposed to high temperatures for extended periods of time. Finally, in the middle, the presence of various debris and impurities leads to molten deposits of corrosive species (generalised under the term CMAS,  $\text{CaO-MgO-Al}_2\text{O}_3\text{-SiO}_2$ ) that can have detrimental effects on the coating. As it can be seen, the development of a successful EBC is a complex task that has required, and still requires to this day, extensive research. As with any challenge, many unsuccessful approaches have been tried for the field to move forward. This never-ending search for more optimised solutions is represented in Figure 17, where a timeline with the evolution of the most notable compositions for EBCs is shown.

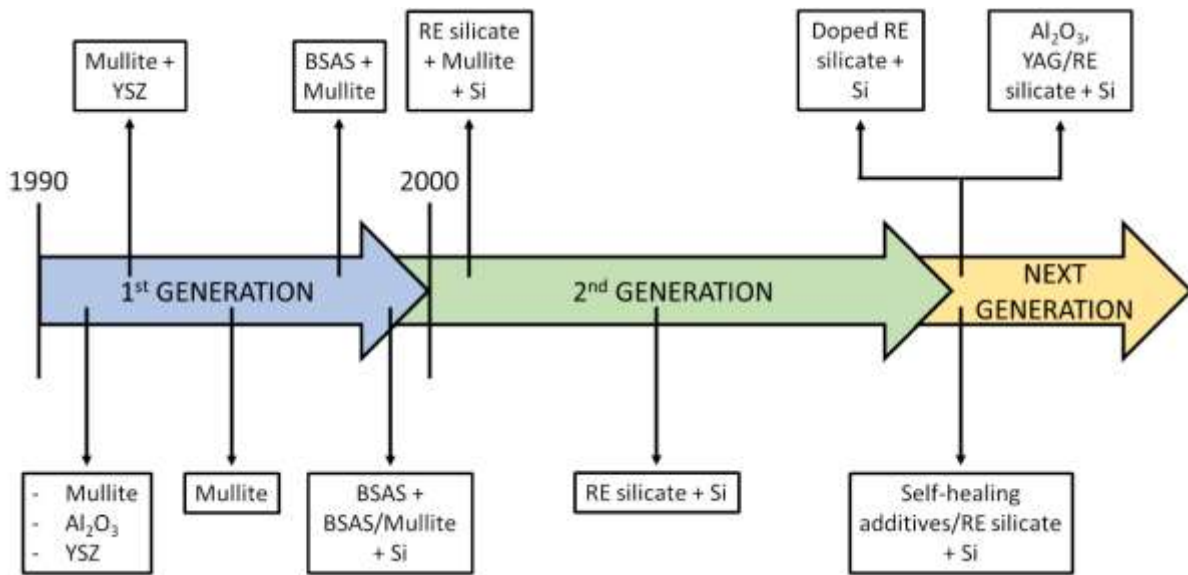


Figure 17: Timeline of the evolution in the design of EBCs, including some of the major compositions used

In this section, an overview of the development of EBCs is first presented, with a particular focus on the process that established the actual requirement for state-of-the-art EBC compositions. A detailed review of the current most promising candidates is presented, referring to the specifications mentioned above, and their behaviour under the most common environments (steam oxidation and CMAS corrosion).

### 2.3.1. Development of environmental barrier coatings

As it was shown in Figure 16, the development of EBCs is generally categorised into different generations based on the main composition being used. In this section, a more detailed review of the second (and current) generation is presented, with a particular focus on the capabilities and disadvantages.

Despite the great advancements achieved since the first iteration of EBCs, it was soon realised that mullite and BSAS based systems would not live up to the expectations. The path towards a new composition was made possible by the knowledge gained during the initial experimental and theoretical work. To summarise the requirements identified at the end of the 1990s, a

successful EBC system had to present the following characteristics. Firstly, a close CTE match between the forming layers and the SiC substrate is required to avoid thermal stresses and the appearance of cracks. Next, it is expected that the coating does not undergo any phase transformations during high temperature exposure, or at least that if a phase transformation does occur, the CTE of the involved polymorphs is close in value, and there is minimal volume change. Thirdly, an EBC must be characterised by a low silica activity under a variety of conditions, such as dry or wet environments. Finally, highlighted by the experimental evidence that multi-layered systems would be required, chemical compatibility must exist between the involved compositions of the different layers, in order to avoid the formation of unwanted and detrimental reaction products at the interfaces, risking the structural integrity of the EBC and altering its protective capabilities.

Therefore, once it was realised that mullite and BSAS were not ideal candidates for the ambitious goals in mind, and with a clear set of requirements for the next generation of EBCs, a research program was launched at NASA in 1999. The initiative, named the ultraefficient engine technology (UEET) programme, had the goal to conduct extensive research and screening tests to identify the prime materials capable of withstanding a temperature of 1316 °C (2400 °F) at the EBC – SiC substrate interface and 1482 °C (2700 °F) at the EBC surface for thousands of hours [79]. This programme identified a new family of compositions with promising properties, being categorised under the name of rare earth silicates. Within rare earth silicates, two main compositions are present, namely rare earth monosilicates ( $\text{RE}_2\text{SiO}_5$ , being RE a rare earth element) and rare earth disilicates ( $\text{RE}_2\text{Si}_2\text{O}_7$ ). Among the rare earth silicates identified as suitable candidates were those with rare elements such as scandium (Sc), lutetium (Lu), ytterbium (Yb), yttrium (Y) and erbium (Er) [80].

As mentioned before, the first condition that any potential composition has to fulfil in order to be considered for its use as EBC is a close CTE match with the SiC substrate. Table 1 shows

the CTE of a selected range of rare earth silicates along with that of SiC and silicon, in addition to the space group categorisation according to the Felsche classification in the case of rare earth silicates [81].

Table 1: Space group and average CTE for several rare earth silicates considered for its use as EBCs

Composition	Space group	Average CTE ( x 10 <sup>-6</sup> K <sup>-1</sup> )	Reference
SiC		4.5 – 5.5	[82]
Si		3.5 – 4.5	[82]
$\beta$ - Sc <sub>2</sub> Si <sub>2</sub> O <sub>7</sub>	<i>C2/m</i>	5.4	[83]
Lu <sub>2</sub> SiO <sub>5</sub>	<i>I2/a</i>	6.7	[84]
$\beta$ - Lu <sub>2</sub> Si <sub>2</sub> O <sub>7</sub>	<i>C2/m</i>	4.2	[83]
Yb <sub>2</sub> SiO <sub>5</sub>	<i>I2/a</i>	7.1 – 7.4	[84]
Yb <sub>2</sub> SiO <sub>5</sub>	<i>P2<sub>1</sub>/c</i>	---	
$\beta$ - Yb <sub>2</sub> Si <sub>2</sub> O <sub>7</sub>	<i>C2/m</i>	3.6 – 4.5	[83]
X1 - Y <sub>2</sub> SiO <sub>5</sub>	<i>P2<sub>1</sub>/c</i>	8.7	[84]
X2 - Y <sub>2</sub> SiO <sub>5</sub>	<i>I2/a</i>	6 – 7.7	[84]
$\alpha$ - Y <sub>2</sub> Si <sub>2</sub> O <sub>7</sub>	<i>P<math>\bar{1}</math></i>	8	[85]
$\beta$ - Y <sub>2</sub> Si <sub>2</sub> O <sub>7</sub>	<i>C2/m</i>	3.6 – 4.5	[83,85]
$\gamma$ - Y <sub>2</sub> Si <sub>2</sub> O <sub>7</sub>	<i>P2<sub>1</sub>/c</i>	3.9	[85]
$\delta$ - Y <sub>2</sub> Si <sub>2</sub> O <sub>7</sub>	<i>Pnam</i>	8.1	[85]
Er <sub>2</sub> SiO <sub>5</sub>	<i>I2/a</i>	5 - 7	[84]
$\beta$ - Er <sub>2</sub> Si <sub>2</sub> O <sub>7</sub>	<i>C2/m</i>	3.9	[83]

A closely matched CTE is not the only requirement for an EBC, and as it can be seen in Table 1, several rare earth silicates present polymorphs. This will produce a phase transformation at high temperatures, as shown in Figure 18, which in most cases is undesirable due to a potential abrupt change in the CTE.

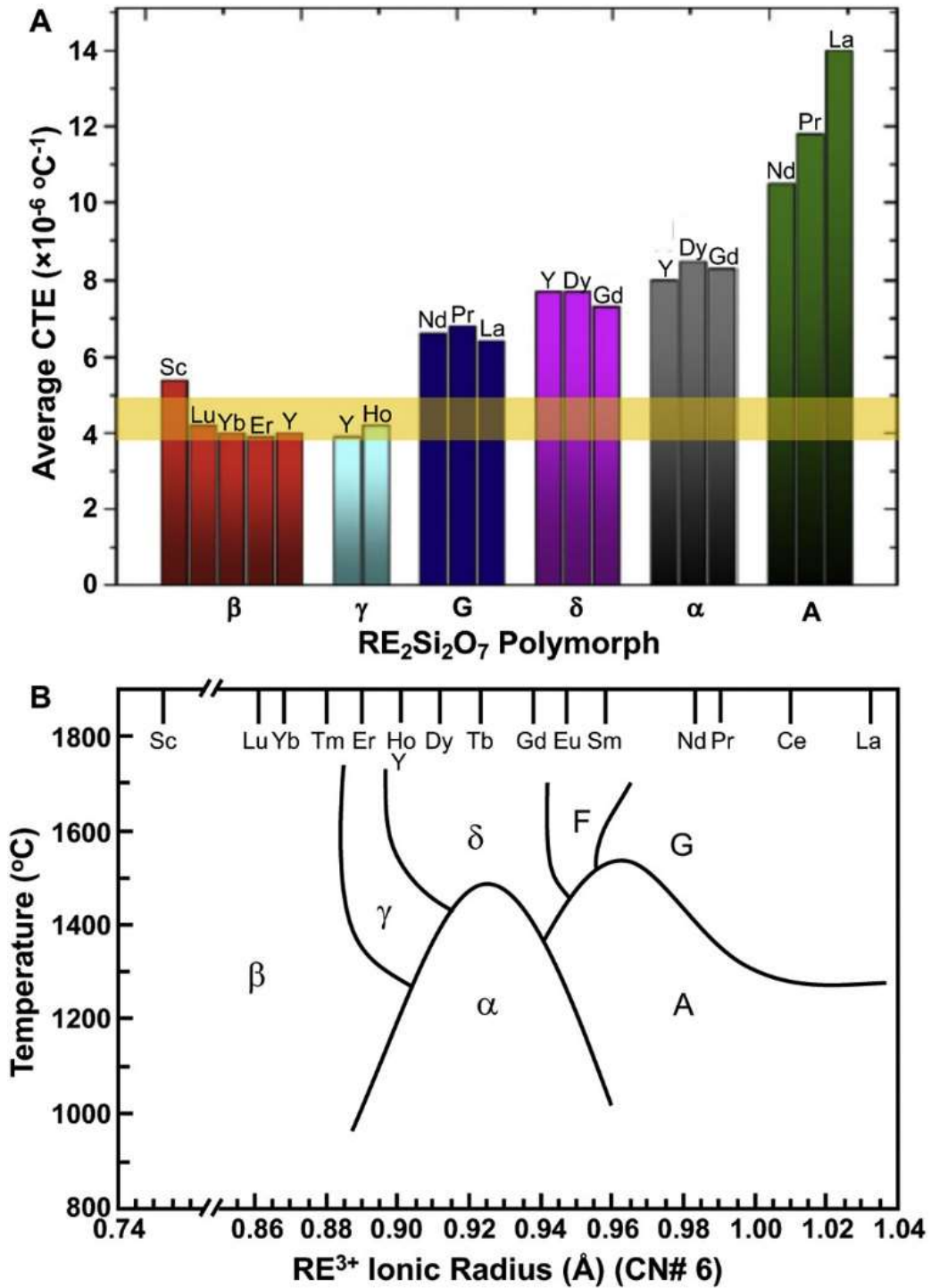


Figure 18: (A) Average CTE of rare earth disilicates polymorphs. The horizontal band indicates the range of CTE values for SiC CMCs. (B) Diagram of the different polymorphs present within rare earth disilicates according to temperature [86]

When studying the silica activity of rare earth silicates, it is assumed that only Si(OH)<sub>4</sub> is removed as a gaseous sub-product, being the rest of the EBC components rapidly disintegrated

[87]. In that case the volatilisation rate can be linked to the removal of SiO<sub>2</sub> from the rare earth silicate in the form of gaseous Si(OH)<sub>4</sub>, as it was shown in Equation 4. The total recession suffered by the system is then directly proportional to the silica activity  $a_{SiO_2}$  of the otherwise protective top coat. The higher the silica activity, the higher the level of volatilisation, which eventually will lead to unacceptable recession levels on components that are expected to provide protection for up to 30,000 h, as indicated before for industrial gas turbines. This relationship is described in Equations 5 and 6 below, where the weight loss rates ( $k$ ) for silica volatilisation in the case of laminar and turbulent flow conditions are shown:

$$k_{laminar} = a_{SiO_2} \cdot \exp\left(-\frac{E}{RT}\right) \cdot v^{1/2} \cdot (P_{H_2O})^n \cdot P^{-1/2} \quad (5)$$

$$k_{turbulent} = a_{SiO_2} \cdot \exp\left(-\frac{E}{RT}\right) \cdot v^{4/5} \cdot (P_{H_2O})^n \cdot P^{-1/5} \quad (6)$$

Where  $E$  is the activation energy,  $R$  is the gas constant,  $T$  is the temperature,  $v$  is the gas velocity,  $P_{H_2O}$  is the steam partial pressure,  $n$  is the steam partial pressure exponent and  $P$  is the total pressure. Due to this direct connection between the silica activity and the recession rate, a reliable database containing the  $a_{SiO_2}$  values of the main EBC candidates would be an invaluable tool; however, testing and measuring this is not a trivial task. As it can be seen, the flow conditions of the gas (laminar vs turbulent), the flow velocity, steam partial pressure and total pressure also play a role, which makes reliably measuring  $a_{SiO_2}$  quite a challenge. Measurements performed at specific test conditions might not be entirely comparable to others performed under different conditions, and lab-based testing systems might differ greatly from the expected conditions during service, as shown in Figure 19 for the recession rate of SiC. In addition to the intrinsic problematic nature of the task, external considerations such as the material of the furnace tube should be taken into account. If fused quartz (SiO<sub>2</sub>) tubes are used, the hot steam will corrode the tube, artificially increasing the level of Si(OH)<sub>4</sub> experienced by

the samples. Whereas, if alumina ( $\text{Al}_2\text{O}_3$ ) tubes are used, contamination will be produced through  $\text{Al}(\text{OH})_3$ , promoting the formation of compositions otherwise not expected [4,80,88].

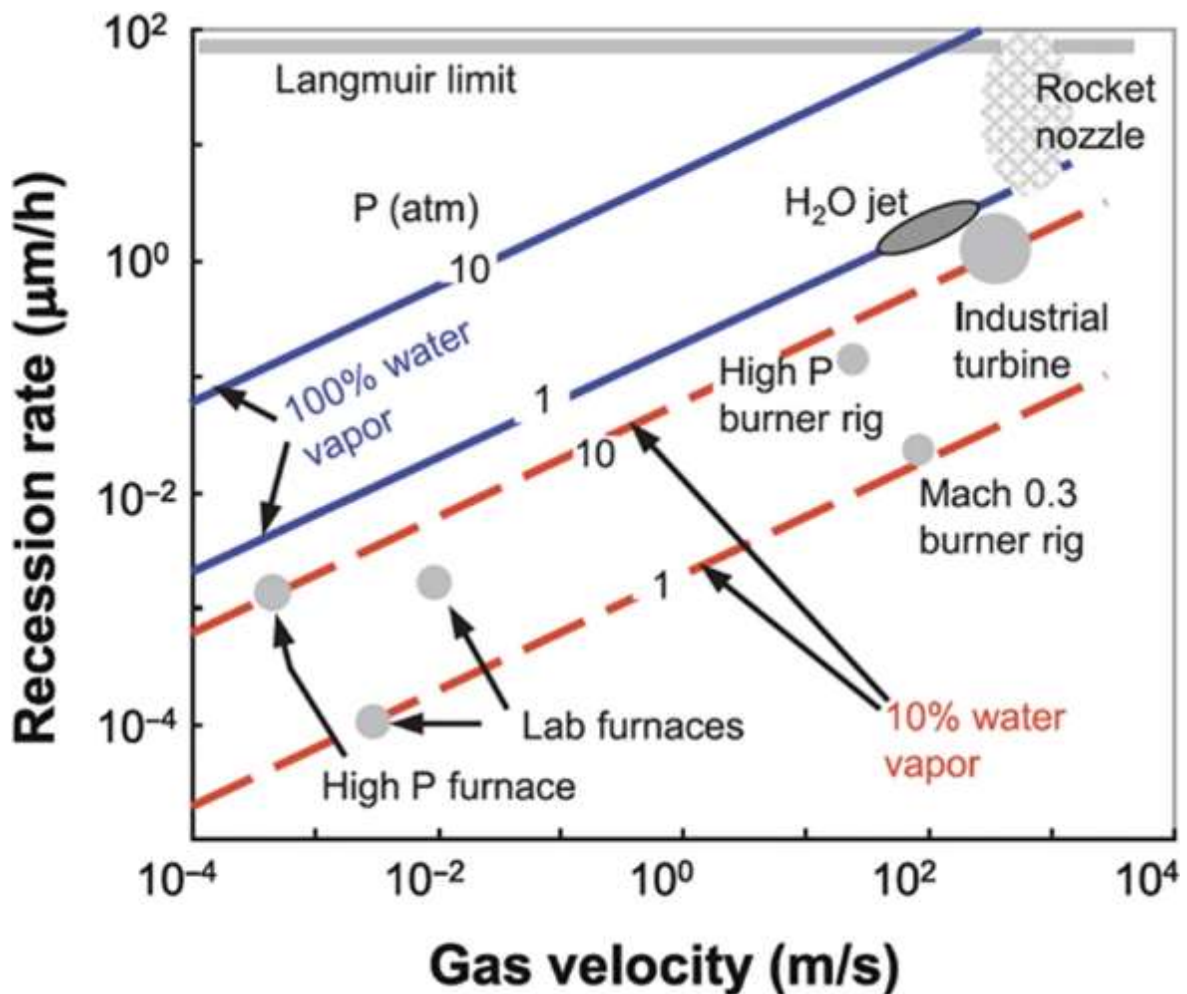


Figure 19: Recession rate for SiC under different conditions, in all cases being the temperature 1316 °C and assuming linear flow [4]

Despite these challenges, considerable effort (both experimental and computational) has been put into developing reliable testing methodologies to assess the volatility of different materials under high temperature, high velocity steam flow [75,89,90]. Providing specific values for the silica volatility of rare earth silicates may not yet be possible, as theoretical calculations and experimental measurements still differ too much. Worth mentioning is the work of Jacobson [91] and Costa and Jacobson [92] in the measurement of the silica activity and calculation of the theoretical values for the recession of the  $\text{Y}_2\text{O}_3\text{-SiO}_2$  and  $\text{Yb}_2\text{O}_3\text{-SiO}_2$  systems, showing

good agreement with some experimental values reported in the literature for YDS-YMS and YbDS-YbMS coatings, respectively. Nevertheless, there is still too much variability in the volatilisation rate of rare earth silicates to definitively validate the theoretical calculations. As a general conclusion, however, it is agreed that the volatility of monosilicates is lower than its disilicate counterpart, measured under identical conditions, although the CTE of the latter tends to be closer to that of SiC and Si. Finally, no evidence of chemical incompatibility between rare earth silicates and the rest of the layers commonly applied in an EBC system has been reported, which seems to indicate that this family of materials is an ideal candidate for its use as an EBC.

#### 2.3.1.1. Yttrium silicates

Yttrium silicates were among the first rare earth silicates to be studied, with a brief mention in the literature that a yttrium silicate coating deposited using thermal spray had been tested for 500 h of cyclic steam testing at 1200 °C [93], although limited details were disclosed due to patents in the same system being granted [94]. Although the presence of multiple polymorphs for both YMS and YDS, as shown in Table 2, could be a limiting factor for the application of Y-based EBCs, some authors have reported that the  $\gamma$ -Y<sub>2</sub>Si<sub>2</sub>O<sub>7</sub> polymorph is stable between ~1320 °C and temperature above 1600 °C, showing a sluggish transformation kinetics down to 1200 °C [88,95]. Regarding the two YMS polymorphs, X1-YMS and X2-YMS, there have been reports of transformation between the low temperature X1 to the high temperature X2 polymorph after exposure to 100% steam to 1100 °C and 1200 °C for up to 16 h with gas flow of 2 m<sup>3</sup>/h and gas velocity of 5 m/s [96]; however, exposure to 1300 °C caused the coating to decompose, with only Y<sub>2</sub>O<sub>3</sub> being detected, which represents a clear failure for a material expected to withstand thousands of hours at high temperatures. No such decomposition has been reported by other authors, although the high CTE value of YMS (around  $8 \times 10^{-6} \text{ K}^{-1}$  for both polymorphs, compared to  $\sim 5 \times 10^{-6} \text{ K}^{-1}$  for SiC) and a slightly higher silica activity when

compared to other rare earth silicates [88] and the presence of a multitude of polymorphs for YDS has made yttrium silicate lose momentum against ytterbium silicates when it comes to potential candidates for EBC applications.

In summary, yttrium silicates have some attractive properties that could have made them ideal candidates for EBC systems; however, they add additional degrees of complexity to the design of a protective multilayer solution. The presence of several polymorphs with a wide range of CTE values in the case of disilicates, despite the reports of sluggish phase transformation and potential high temperature stability, represents another variable that should be taken into account and prevented during operation. In the case of monosilicates, contradictory reports exist regarding its high temperature stability, but phase transformation between its two polymorphs seems well documented, which is certainly a disadvantage. Seeing that the general trend in the design of EBC is the simplification of the system (with the removal of the mullite layer, favouring just a rare earth silicate top coat and Si bond coat) makes the choice of yttrium silicates quite difficult to argue for.

#### 2.3.1.2. Ytterbium silicates

Initial efforts were focused on ytterbium monosilicate (YbMS -  $\text{Yb}_2\text{SiO}_5$ ) as a promising EBC candidate due to its lower silica volatility. The research carried by Richards *et al.* [97,98] on the deposition of rare earth silicates top coat + mullite diffusion barrier + Si bond coat using plasma spraying (APS) and the study of the characteristics of the deposited coatings before and after thermal cycling in water environment, provided great insights into the failure mechanisms [99,100]. Drawing from the knowledge on the mullite transformation at high temperatures, both the mullite diffusion layer and the rare earth silicate top coat were deposited using atmospheric air plasma with the substrate heated to 1200 °C inside a box furnace. Despite the use of this improved deposition procedure, the defects and porosities present in the coating, combined with the CTE mismatch between the layers, produced the failure of the system

through the appearance of vertical cracks (mud cracks), as shown in Figure 20, after annealing in air at 1300 °C for 20 h. Those same mud cracks were partially responsible for the poor performance of the coating under steam cycling conditions (1 atm pressure, flow velocity of 4.4 cm/s, 90% H<sub>2</sub>O/10% O<sub>2</sub> environment, 60 min at 1316 °C and 10 min at 110 °C), presenting spallation after less than 200 cycles. It was concluded that despite the considerable efforts concerning the optimisation of the deposition method, the characteristics of the deposited coating and the adherence between the layers, the CTE mismatch was too great to produce a successful EBC. Vertical cracks would appear during the heat treatments, as it can be seen in Figure 20, providing a preferential path for the ingress of oxidisers, which then reacted with the Si bond coat, producing the failure of the EBC.

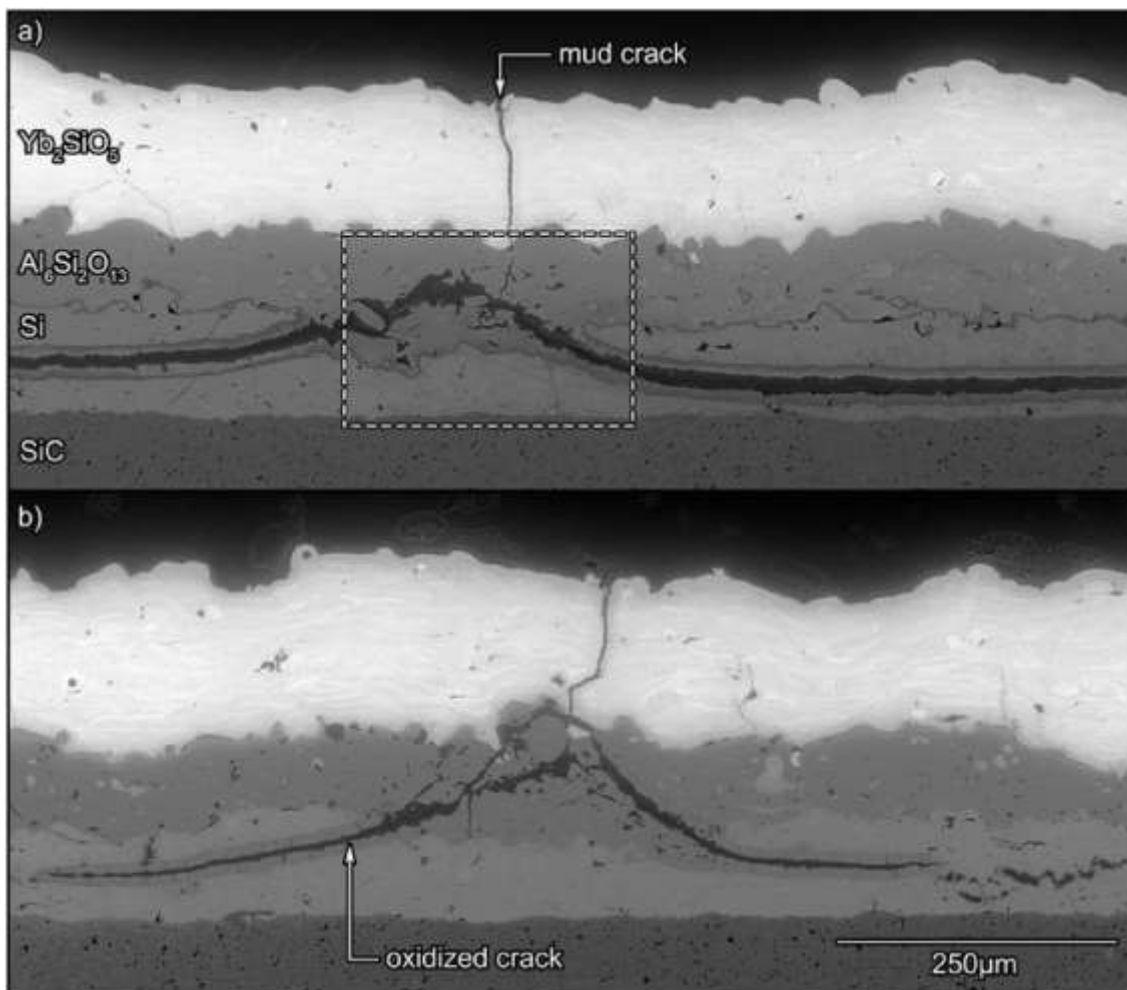


Figure 20: SEM images of the cross section of the failed coating after 250 1-h steam cycles [100]

Seeing that CTE match still represents one of the main challenges when selecting a potential material, the attention was shifted towards rare earth disilicates, which despite having a slightly higher silica activity, tend to present a better matched CTE with the SiC substrate. Ytterbium disilicate (YbDS –  $\text{Yb}_2\text{Si}_2\text{O}_7$ ) has been primarily studied as a potential candidate for its use as an EBC. The preferential volatilisation of YbDS versus YbMS was also found by Bakan *et al.* [101] when studying the oxidation behaviour under steam conditions (1 atm pressure, flow velocity of 100 m/s, partial pressure of steam of 0.15 atm, temperature of 1200 °C and up to 200 h of exposure) of APS deposited coatings with different YbDS/YbMS ratio. The coating deposited at higher plasma power resulted in a lower YbDS content (36 wt.%) due to the increased  $\text{SiO}_2$  loss during spraying, whereas a lower plasma power produced a coating with a higher YbDS (62 wt.%). The YbDS content was directly correlated to the mass loss and severity of the corrosion during the test, showing better performance in the case of low YbDS content. Nevertheless, phase content is not the only factor that should be considered. Microstructure, particularly porosity and pore connectivity also play an essential role. Bakan *et al.* [102] reported the corrosion of APS deposited coatings with YbDS content of 70 wt.% compared to sintered bodies with YbDS content of 92 wt.%. Their results show that weight loss and the thickness of the  $\text{SiO}_2$  depleted layer was smaller in the case of the sintering body, due to the reduced porosity level and lower pore connectivity.

Therefore, the focus of this section will be in thermal sprayed coatings, as they better represent the characteristics and performance of the final product. Initial reports showed that the deposition of YbDS using thermal spray could yield low-porosity, mud-crack-free coatings [98], providing an exciting new candidate. Further investigations on the deposition of YbDS using thermal spray techniques have been conducted [103,104], being worth noting the work of Garcia *et al.* [105] on the effect of different  $\text{SiO}_2$  content in the feedstock powder and plasma power when using APS to achieve the desired composition. The different rates of volatilisation

of SiO<sub>2</sub> affect the viscosity of the splats and phase composition of the coating, modifying the initial state of the as sprayed coatings. Their work highlighted the importance that crystallisation and phase transformation have in the integrity of the coatings. Crystallisation, since the APS deposited coatings will present an amorphous state in the as sprayed condition, due to the rapid cooling involved in the process [106], and will crystallise once heat treated. Phase transformation as continued exposure to high temperatures will promote the conversion of *P2<sub>1</sub>/c* Yb<sub>2</sub>SiO<sub>5</sub> into the *I2/a* polymorph, accompanied by a volume expansion. The combination of SiO<sub>2</sub> volatilisation during spraying (and the associated appearance of Yb<sub>2</sub>SiO<sub>5</sub>), volume contraction due to crystallisation, volume expansion due to phase transformation, thermal stresses arising from CTE mismatch, changes in porosity and formation of a thermal grown oxide at the top coat/Si bond coat interface deepens the complexity of designing a successful EBC system.

Despite the availability of several thermal spraying deposition techniques, efforts have been currently focused on the use of APS, although several techniques have been preliminarily considered. An example is the work of Bakan *et al.* [107,108] on the deposition of YbDS coatings using APS, suspension plasma spray (SPS), high velocity oxy-fuel (HVOF) spray and very-low pressure plasma (VLPPS) spray. Their work shows how the different melting levels of the splats achieved with each technique, as well as the subsequent cooling rate of the coated samples, affect the degree of crystallinity and the structural integrity of the coatings. High temperature techniques, such as APS and SPS, produced highly amorphous coatings that cracked during the post-deposition cooling to room temperature. HVOF sprayed samples presented a higher degree of crystallinity, due to the presence of semi-molten and non-molten particles as confirmed by electron backscatter diffraction [108], and higher porosity levels. The reduced thermal stresses related to a lower flame temperature, and the increased presence of porosity, key elements to a better strain tolerance, resulted in crack-free coatings. Regarding

VLPPS, the ability to maintain the substrates heated to a temperature close to 1000 °C prior to spraying and the use of the plasma flame to reduce the post-deposition cooling rate gave rise to highly crystalline coatings with no visible cracks. Despite being VLPPS the technique that produced better results, its application for real sized components might not be achievable in terms of operations cost and size limitations of the vacuum chamber. Therefore, HVOF thermal spray might be an interesting alternative for future EBC developments.

Of all the rare earth silicate top coats presented in this work, ytterbium compositions seem to have currently the advantage in terms of favourable properties for its application by the industry. Further research is still needed, particularly in suitable deposition techniques that fulfil the requirements needed for a successful EBC while presenting a realistic technique applicable on a large scale on components of large dimensions and complex shapes. Although this preference for ytterbium silicates is based on its inherent properties and high temperature behaviour, there is still room for improvement, and future research into more complex compositions with ytterbium silicates as a base might represent the future of the field.

### **2.3.2. Corrosion mechanisms**

During the development of better performing EBCs, steam and molten corrosive species were early identified as the main challenges presented in terms of corrosion encounter during service. A brief description of the deleterious effects of both corrodents have been presented in the previous sections; however, a more detailed review of the fundamentals for both steam and molten corrosive species is presented here. For the sake of brevity, this comprehensive summary will only cover the corrosion mechanisms and effects reported in rare earth silicate EBCs.

#### 2.3.2.1. Steam degradation

When considering the effect that flowing steam at high temperature has on EBC systems it is necessary to remember that an EBC is expected to behave as a gas-tight layer, reducing the penetration of oxidisers to the substrate underneath. Nevertheless, as it has been shown before, several factors can affect the physical integrity of the EBC, in which case the coating loses its gas-tight characteristic, causing the system to experience a shortened effective life. Two main mechanisms can be identified as the cause for the structural failure of the coatings. First, as described before, flowing steam at elevated temperatures will induce the volatilisation of silica from the rare earth silicate top coat. Even in the ideal scenario of a homogenous material removal from the coating, this mass loss will eventually lead to the failure of the coating, leaving exposed the unprotected component beneath. On top of this, material removal due to silica volatilisation is rarely a homogenous process in coatings. Differences in the phase content, porosity level and surface roughness cause hot spots for volatilisation and erosion due to the flowing steam, producing accelerated material removal, as reported by Bakan *et al.* [101] and shown in Figure 21.

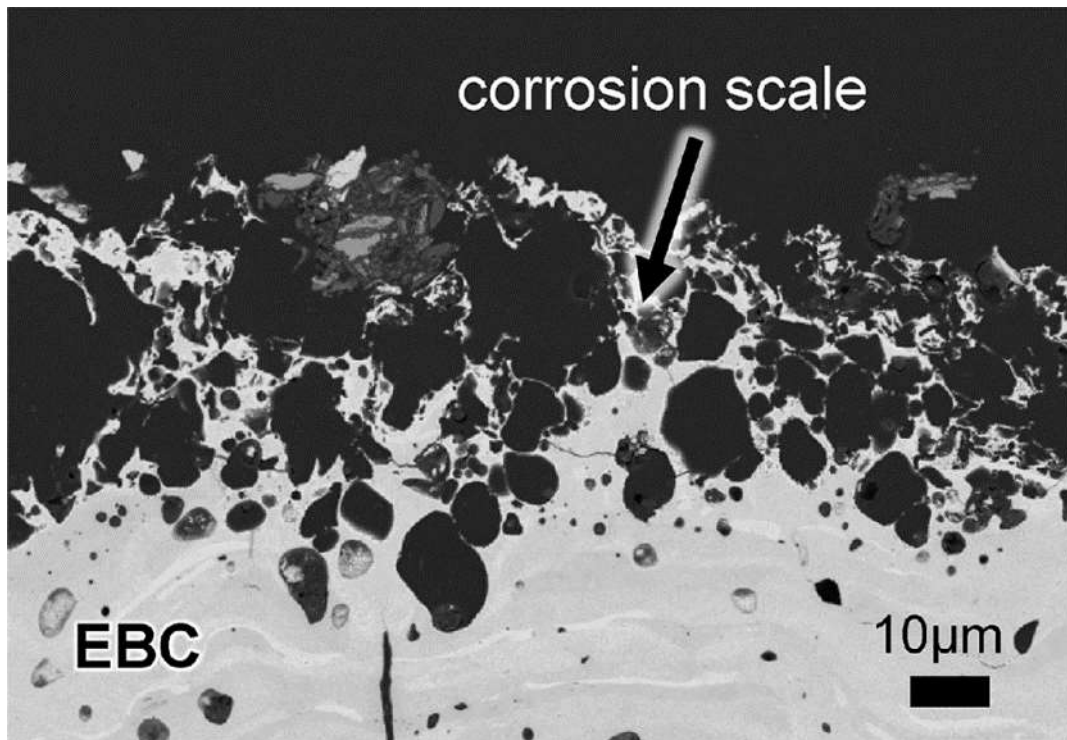


*Figure 21: BSE SEM image of the cross section of a ytterbium disilicate coating deposited using APS and exposed to steam corrosion (temperature: 1200 °C, gas flow velocity: 100 m/s,  $P_{H_2O} = 0.15$  atm,  $P_{total} = 1$  atm, time = 200 h) [101]*

For the purpose of comparison, Table 2 shows a summary of the corrosion under steam conditions of rare earth silicates measured so far, including the maximum mass loss, the volatility rate (if available) and the deposition method. A few details should be taken into consideration when consulting Table 2. First, the deposition method (including whether the test was performed on a single layer or on a coating deposited onto a substrate), the phase composition as deposited and after the test, and the porosity are provided (if reported) as this factors will greatly affect the volatilisation. Secondly, the maximum corrosion experienced (whether mass weight gained or lost) at the end of the testing time is indicated as a measure of the total damage experienced, although this value is hardly comparable between different reports for the reasons previously mentioned. A volatilisation rate is provided, which is a better value for comparison. This volatilisation rate is expressed as reported from the literature,

calculated if the volatilisation at different time points was reported and linear behaviour was observed or estimated from the maximum corrosion if linear behaviour was observed.

Material	Deposition method	As deposited phase composition	Post-testing phase composition	Porosity	Testing conditions	Max volatilisation	Volatilisation rate	Reference
Y <sub>2</sub> SiO <sub>5</sub> (YMS)	Uniaxial cold pressing (50 MPa) + sintering at 1580 °C for 3 h	YMS: at least 85 wt. %	---	2 %	Temperature: 1350 °C. Flow rate: 40 ml/min. Composition: 90% H <sub>2</sub> O/10% O <sub>2</sub> . Testing up to 166 h	-0.404 mg/cm <sup>2</sup> after 166 h	-0.00258 mg/cm <sup>2</sup> ·h	[109]
	Hot pressing at 1500 °C/27.6 MPa in vacuum	YMS. Traces of Y <sub>2</sub> O <sub>3</sub> and YDS	YMS. Traces of Al <sub>2</sub> Y <sub>4</sub> O <sub>9</sub>	---	Temperature: 1500 °C. Flow velocity: 4.4 cm/s. Composition: 50% H <sub>2</sub> O/10% O <sub>2</sub> . Testing up to 100 h	0.3 & 0.6 mg/cm <sup>2</sup> after 100 h	0.003 & 0.006 mg/cm <sup>2</sup> ·h	[80]
	Magnetron sputtering on top of substrate + annealing at 1100 °C for 3 h in vacuum	X1- and X2-YMS polymorphs. Traces of Y <sub>4.69</sub> (SiO <sub>4</sub> ) <sub>3</sub> O	Y <sub>2</sub> O <sub>3</sub>	---	Temperature: 1300 °C. Flow rate: 2 m <sup>3</sup> /h. Flow velocity: 5 m/s. Composition: 100% H <sub>2</sub> O. Testing up to 1 h	-1.22 mg/cm <sup>2</sup> after 1 h	---	[96]
			X2-YMS and YDS	---	Temperature: 1200 °C. Flow rate: 2 m <sup>3</sup> /h. Flow velocity: 5 m/s. Composition: 100% H <sub>2</sub> O. Testing up to 16 h	-1.18 mg/cm <sup>2</sup> after 16h		
	Sol-gel + calcination at 1000 °C for 10 h	YMS	YMS, Y <sub>3</sub> Al <sub>2</sub> (AlO <sub>4</sub> ) <sub>3</sub> , Y <sub>4.67</sub> (SiO <sub>4</sub> ) <sub>3</sub> O, YDS	---	Temperature: 1400 °C. Flow velocity (cold zone): 5 cm/s. PH <sub>2</sub> O = 50 kPa, Ptotal = 100 kPa. Testing up to 300 - 310 h	0.6 mg/cm <sup>2</sup> after 310 h	---	[110]
	Sol-gel + calcination at 1000 °C for 10 h + sintering at 1400 °C for 5 h			---		0.7 mg/cm <sup>2</sup> after 310 h		
	Sol-gel + calcination at 1000 °C for 10 h + sintering at 1500 °C for 5 h			---		0.45 mg/cm <sup>2</sup> after 310 h		
	Milling and compacting powders, no sintering	Y <sub>2</sub> O <sub>3</sub> , SiO <sub>2</sub>	YMS, Y <sub>3</sub> Al <sub>2</sub> (AlO <sub>4</sub> ) <sub>3</sub> , Y <sub>4.67</sub> (SiO <sub>4</sub> ) <sub>3</sub> O	---		1.45 mg/cm <sup>2</sup> after 300 h		
	Milling and compacting powders + sintering at 1400 °C for 5 h	YMS, Y <sub>2</sub> O <sub>3</sub>		---		0.6 mg/cm <sup>2</sup> after 310 h		
	Milling and compacting powders + sintering at 1500 °C for 5 h	YMS		---		0.9 mg/cm <sup>2</sup> after 300 h		
Y <sub>2</sub> Si <sub>2</sub> O <sub>7</sub> (YDS)	Cold pressing + sintering at 1500 °C for 2 h in Ar atmosphere	YDS, some YMS	YDS, decreased content of YMS	---		Temperature: 1400 °C. Composition: 50% H <sub>2</sub> O/50% O <sub>2</sub> . Testing up to 400 h		
	Cold pressing + sintering at 1400 - 1600 °C	>99 wt. % YDS	---	30 %	Temperature: 1500 °C. Flow rate: ~290 l/h. Flow velocity: 13 cm/s. Composition 30% H <sub>2</sub> O/70% air. PH <sub>2</sub> O = 0.3 bar, Ptotal = 0.1 MPa. Testing up to 310 h	-0.898 mg/cm <sup>2</sup> after 310 h	-0.00192 mg/cm <sup>2</sup> ·h	[88]
	Sol-gel + calcination at 1000 °C for 10 h	YDS	YDS	---	Temperature: 1400 °C. Flow velocity (cold zone): 5 cm/s. PH <sub>2</sub> O = 50 kPa, Ptotal = 100 kPa. Testing up to 300 - 310 h	-2.5 mg/cm <sup>2</sup> after 310 h	---	[110]
	Sol-gel + calcination at 1000 °C for 10 h + sintering at 1400 °C for 5 h					-1.8 mg/cm <sup>2</sup> after 310 h		
	Sol-gel + calcination at 1000 °C for 10 h + sintering at 1500 °C for 5 h					-2.1 mg/cm <sup>2</sup> after 310 h		
	Milling and compacting powders, no sintering	Y <sub>2</sub> O <sub>3</sub> , SiO <sub>2</sub>	YDS, Y <sub>3</sub> Al <sub>2</sub> (AlO <sub>4</sub> ) <sub>3</sub>			-0.1 mg/cm <sup>2</sup> after 300 h		
	Milling and compacting powders + sintering at 1400 °C for 5 h	YDS, Y <sub>2</sub> O <sub>3</sub>				-0.5 mg/cm <sup>2</sup> after 310 h		
Milling and compacting powders + sintering at 1500 °C for 5 h	YDS	-0.25 mg/cm <sup>2</sup> after 300 h						

Material	Deposition method	As deposited phase composition	Post-testing phase composition	Porosity	Testing conditions	Max volatilisation	Volatilisation rate	Reference
Gd <sub>2</sub> SiO <sub>5</sub> (GdMS)	Uniaxial cold pressing (50 MPa) + sintering at 1580 °C for 3 h	GdMS: 95 wt.% / GdDS: 5 wt.%	---	2 %	Temperature: 1350 °C. Flow rate: 40 ml/min. Composition: 90% H <sub>2</sub> O/10% O <sub>2</sub> . Testing up to 166 h	-2.3 mg/cm <sup>2</sup> after 166 h	-0.01576 mg/cm <sup>2</sup> ·h	[109]
Er <sub>2</sub> SiO <sub>5</sub> (ErMS)	Uniaxial cold pressing (50 MPa) + sintering at 1580 °C for 12 h	ErMS: at least 85 wt.%	---	5 %		-0.502 mg/cm <sup>2</sup> after 166 h	-0.00353 mg/cm <sup>2</sup> ·h	
Er <sub>2</sub> SiO <sub>5</sub> (ErMS)	Hot pressing at 1500 °C/27.6 MPa in vacuum	ErMS. Traces of Er <sub>2</sub> O <sub>3</sub> and ErDS	ErMS. Traces of Al <sub>10</sub> Er <sub>6</sub> O <sub>24</sub>	---	Temperature: 1500 °C. Flow velocity: 4.4 cm/s. Composition: 50% H <sub>2</sub> O/10% O <sub>2</sub> . Testing up to 100 h	-0.1 mg/cm <sup>2</sup> after 100 h	Not linear	[80]
Yb <sub>2</sub> SiO <sub>5</sub> (YbMS)	Uniaxial cold pressing (50 MPa) + sintering at 1580 °C for 3 h	YbMS: 85 wt.% / YbDS: 15 wt.%	---	6 %	Temperature: 1350 °C. Flow rate: 40 ml/min. Composition: 90% H <sub>2</sub> O/10% O <sub>2</sub> . Testing up to 166 h	-0.347 mg/cm <sup>2</sup> after 166 h	-0.00213 mg/cm <sup>2</sup> ·h	[109]
	Hot pressing at 1500 °C/27.6 MPa in vacuum	YbMS. Traces of Yb <sub>2</sub> O <sub>3</sub> and YbDS	YbMS. Traces of Al <sub>5</sub> Yb <sub>3</sub> O <sub>12</sub>	---	Temperature: 1500 °C. Flow velocity: 4.4 cm/s. Composition: 50% H <sub>2</sub> O/10% O <sub>2</sub> . Testing up to 100 h	0.05 mg/cm <sup>2</sup> after 100 h	Not linear	[80]
	Dip coating CMC substrate + heat treatment at 1350 °C for 50 h	> 90 wt.% YbMS, < 10 wt.% YbDS, Yb <sub>2</sub> O <sub>3</sub>	Mainly YbDS	~ 10 %	Temperature: 1350 °C. Flow rate: 0.67 cm <sup>3</sup> /s. Composition: 90% H <sub>2</sub> O/10% O <sub>2</sub> . Testing up to 150 h	0.55 mg/cm <sup>2</sup> after 150 h	0.00277 mg/cm <sup>2</sup> ·h	[112]
Yb <sub>2</sub> Si <sub>2</sub> O <sub>7</sub> (YbDS)	Hot pressing at 1500 °C/27.6 MPa in vacuum	YbDS. Traces of YbMS	YbDS. Traces of YbMS and Al <sub>5</sub> Yb <sub>3</sub> O <sub>12</sub>	---	Temperature: 1500 °C. Flow velocity: 4.4 cm/s. Composition: 50% H <sub>2</sub> O/10% O <sub>2</sub> . Testing up to 100 h	-0.2 & -0.4 mg/cm <sup>2</sup> after 100 h	-0.002 mg/cm <sup>2</sup> ·h (second measurement not linear)	[80,92]
	Oxidation bonded by reaction sintering Si <sub>3</sub> N <sub>4</sub> substrate at 1500 °C for 2 h in Ar atmosphere	---	---	---	Temperature: 1500 °C. Flow rate: 175 ml/min. Flow velocity: 0.046 cm/s. Composition: 30% H <sub>2</sub> O/70% O <sub>2</sub> . Testing up to 50 h	---	0.004688 mg/cm <sup>2</sup> ·h	[113]
	Cold pressing + sintering at 1600 °C for 12 h in air	---	---	---	Temperature: 1500 °C. Flow rate: 175 ml/min. Flow velocity: 0.046 cm/s. Composition: 30% H <sub>2</sub> O/70% O <sub>2</sub> . Testing up to 50-100 h	---	-0.75 mg/cm <sup>2</sup> ·h	[114]
	Cold pressing + sintering at 1400 - 1600 °C	> 99 wt.% YbDS	---	< 5%	Temperature: 1500 °C. Flow rate: ~290 l/h. Flow velocity: 13 cm/s. Composition 30% H <sub>2</sub> O/70% air. PH <sub>2</sub> O = 0.3 bar, Ptotal = 0.1 MPa. Testing up to 310 h	-0.616 mg/cm <sup>2</sup> after 310 h	Not linear	[88]
	Si bond coat and YbDS top coat deposited using air plasma spraying on top of SiC substrates	YbDS: 62 wt.% / YbMS: 38%	YbDS: 32 wt.% / YbMS: 68 wt.%	2 %	Temperature: 1200 °C. Flow velocity: 100 m/s. PH <sub>2</sub> O = 0.15 atm, Ptotal = 1 atm. Testing up to 200 h	-0.1 μm/h	---	[101]
	Air plasma spraying + heat treatment in air at 1500 °C for 40 h	YbDS: 70 wt.% / YbMS: 30 wt.%	YbDS: 5 wt.% / YbMS: 95 wt.%	7 %	Temperature: 1400 °C. Flow velocity: 90 m/s. PH <sub>2</sub> O = 0.15 atm, Ptotal = 1 atm. Testing up to 200 h	-0.3 mg/cm <sup>2</sup> after 200 h	Not linear	[102]
	Spark plasma sintering at 1650 °C/50 MPa in vacuum	YbDS: 92 wt.% / YbMS: 8 wt.%	YbDS: 14 wt.% / YbMS: 86 wt.%	< 2%		-0.1 mg/cm <sup>2</sup> after 200 h	0.0005 mg/cm <sup>2</sup> ·h	

Material	Deposition method	As deposited phase composition	Post-testing phase composition	Porosity	Testing conditions	Max volatilisation	Volatilisation rate	Reference
Lu <sub>2</sub> SiO <sub>5</sub> (LuMS)	Uniaxial cold pressing (50 MPa) + sintering at 1580 °C for 3 h	LuMS: 88 wt.% / LuDS: 12 wt.%	---	1 %	Temperature: 1350 °C. Flow rate: 40 ml/min. Composition: 90% H <sub>2</sub> O/10% O <sub>2</sub> . Testing up to 166 h	-0.859 mg/cm <sup>2</sup> after 166 h	-0.00596 mg/cm <sup>2</sup> ·h	[109]
	Hot pressing at 1500 °C/27.6 MPa in vacuum	LuMS	LuMS. Traces of Al <sub>5</sub> Lu <sub>3</sub> O <sub>12</sub>	---	Temperature: 1500 °C. Flow velocity: 4.4 cm/s. Composition: 50% H <sub>2</sub> O/10% O <sub>2</sub> . Testing up to 100 h	0.3 & 0.65 mg/cm <sup>2</sup> after 100 h	0.003 & 0.0065 mg/cm <sup>2</sup> ·h	[80]
	Dip coating CMC substrate + heat treatment at 1350 °C for 50 h	> 90 wt.% LuMS, < 10 wt.% LuDS, Lu <sub>2</sub> O <sub>3</sub>	Mainly LuDS	~10%	Temperature: 1350 °C. Flow rate: 0.67 cm <sup>3</sup> /s. Composition: 90% H <sub>2</sub> O/10% O <sub>2</sub> . Testing up to 150 h	0.69 mg/cm <sup>2</sup> after 150 h	0.00256 mg/cm <sup>2</sup> ·h	[112]
Lu <sub>2</sub> Si <sub>2</sub> O <sub>7</sub> (LuDS)	Oxidation bonded by reaction sintering Si <sub>3</sub> N <sub>4</sub> substrate at 1500 °C for 2 h in Ar atmosphere	LuDS	---	---	Temperature: 1500 °C. Flow rate: 175 ml/min. Flow velocity: 0.046 cm/s. Composition: 30% H <sub>2</sub> O/70% O <sub>2</sub> . Testing up to 50 h	---	0.002218 mg/cm <sup>2</sup> ·h	[113]
	Cold pressing + sintering at 1600 °C for 12 h in air	---	---	---	Temperature: 1500 °C. Flow rate: 175 ml/min. Flow velocity: 0.046 cm/s. Composition: 30% H <sub>2</sub> O/70% O <sub>2</sub> . Testing up to 50-100 h	---	-0.0042 mg/cm <sup>2</sup> ·h	[114]
	Cold pressing + sintering at 1400 - 1600 °C	> 99 wt.% LuDS	---	< 5 %	Temperature: 1500 °C. Flow rate: ~290 l/h. Flow velocity: 13 cm/s. Composition 30% H <sub>2</sub> O/70% air. PH <sub>2</sub> O = 0.3 bar, Ptotal = 0.1 MPa. Testing up to 310 h	-0.156 mg/cm <sup>2</sup> after 310 h	-0.00009 mg/cm <sup>2</sup> ·h	[88]
	Hot pressing at 1600 °C/20 MPa for 3 h in Ar atmosphere	LuDS and LuMS	LuDS, LuMS and Lu <sub>2</sub> O <sub>3</sub>	---	Temperature: 1300 °C. Flow rate: 175 ml/min. Composition: 30% H <sub>2</sub> O/70% air. Testing up to 100 h	---	-0.001427 mg/cm <sup>2</sup> ·h	[115]
Sc <sub>2</sub> Si <sub>2</sub> O <sub>7</sub> (ScDS)	Hot pressing at 1500 °C/27.6 MPa in vacuum	ScDS. Traces of SiO <sub>2</sub>	ScDS	---	Temperature: 1500 °C. Flow velocity: 4.4 cm/s. Composition: 50% H <sub>2</sub> O/10% O <sub>2</sub> . Testing up to 100 h	-0.4 & -0.45 mg/cm <sup>2</sup> after 100 h	Not linear	[80]

Table 2: Summary of the volatilisation of different rare earth silicates. The maximum volatilisation was approximated from plots where no explicit data was available. Volatilisation rate was calculated where no explicit rate was provided, assuming linear behaviour

The fact that different test conditions were used in most of the experiments summarised in Table 2 makes it difficult to draw conclusions directly from the volatilisation rates. It should be kept in mind that this rate is dependent of the temperature, steam velocity, steam partial pressure and total pressure, as indicated by Equations 5 and 6. In order to provide a more comparable quantity, which could be used to assess the resistance to steam volatilisation of different compositions, several approaches have been taken. First, as it was previously mentioned, considerable effort has been placed into developing a theoretical model that can predict this effect [90–92]. This line of work has provided some interesting results, for instance, showing confirmation that as a general characteristic, rare earth monosilicates tend to experience lower volatility rates than their disilicate counterparts. Nevertheless, the current state of the research does not provide a detailed description of the volatility rates to be expected for different compositions at different test conditions, which complicates the comparison. Another approach has been proposed recently, based on more fundamental chemical concepts. Optical basicity (OB or  $\Lambda$ ) was first introduced by Duffy and Ingram [116] aiming to classify the chemical activity of oxides in glass, being defined as the ability of oxygen anions to donate electrons, which depends on the polarizability of the metal cations [117]. This chemical criterion has been suggested as a potential quantity useful for comparison between different compositions, as higher optical basicity values correlate to lower steam-induced volatility [4]. This correlation has not yet been confirmed, making comparison of experimental data, such as the one presented in Table 2, still a valuable insight into the volatility of different rare earth silicates.

This volatilisation not only removes material from the top coat, reducing the time required for oxidisers to diffuse to the silicon bond coat, but also can cause the appearance of connected porosity, which represents a preferential pathway for the ingress of oxidisers. This phenomenon, reported by Richards *et al.* [118] on a APS deposited YbDS top coat with a Si

bond layer, tested under steam cycling conditions (total pressure of 1 atm, oxygen partial pressure of 0.1 atm, flow velocity of 4.4 cm/s, 90% H<sub>2</sub>O/10% O<sub>2</sub> environment, 60 min at 1316 °C and 10 min at 110 °C for up to 2000 h), is shown below in .

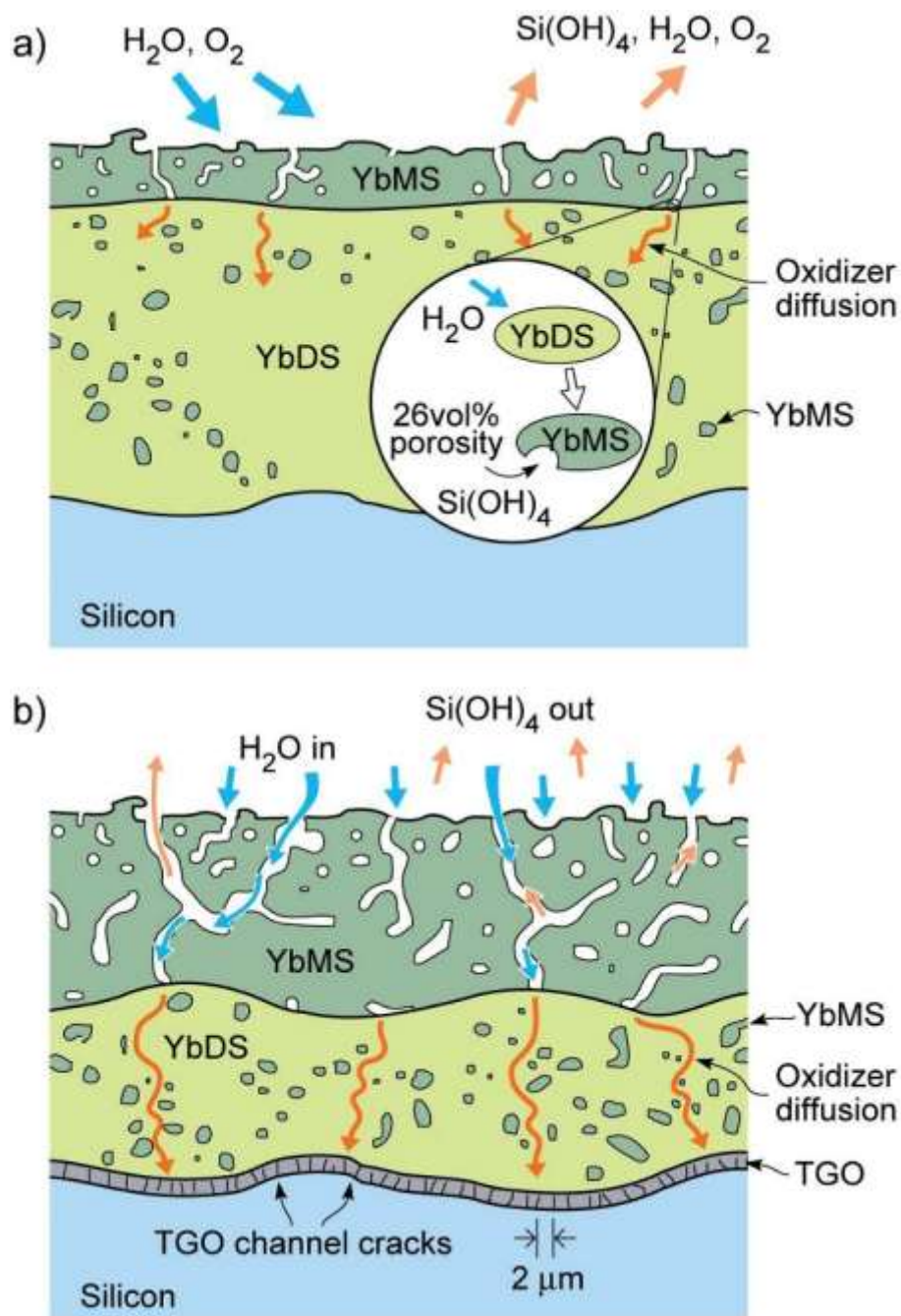
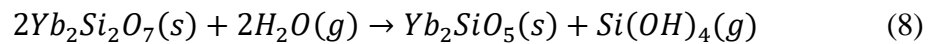


Figure 22: Schematic representation of the volatilisation of silica from the initial YbDS and formation of YbMS. (a) shows the initial stage of the process, while (b) shows the late stages [118]

Assuming that the only volatile product produced is  $\text{Si(OH)}_4$ , the transformation from YbDS into YbMS, described in Equation 8, implies a volume reduction of 26%. This coupled with the increased content of YbMS (which has a higher CTE when compared to SiC) produced a CTE mismatch that induced thermal stresses upon cycling testing, producing vertical cracks and facilitating the access of oxidisers to the silicon bond coat. This preferential access of oxidisers to the silicon bond coat produced a quick growth of the TGO.



On the other hand, the formation of a monosilicate layer on top of the disilicate can act as passivation barrier, due to the lower volatilisation of monosilicates when compared to disilicates, associated with a lower silica activity. Although this passivation layer can reduced the volatility rate of the coating, excessive formation of porosity and high steam flow velocities can cause the erosion of these layers, effectively increasing the mass loss rate [101].

In addition to the volatilisation of the rare earth silicate, failure of EBCs exposed to steam containing environments can take place due to the appearance of vertical cracks and spallation. Regarding vertical cracks, they can be formed due to CTE mismatch between the initial compositions of the different layers, as mentioned before, or due to the formation of a new phase with a different CTE value. This situation may arise in the case of top layers made of rare earth silicates with several polymorphs. The newly formed cracks allow the access of oxidisers to the silicon bond coat, inducing the rapid growth of a  $\beta$ -cristobalite TGO. Upon cooling below  $\sim 220$  °C, this  $\beta$ -cristobalite  $\text{SiO}_2$ , transforms to the  $\alpha$ -phase, process accompanied by a volume reduction of approximately 4.5% [99,100]. This process promotes the formation of cracks parallel to the interface, which eventually lead to the coating spallation, as shown in Figure 23a. Figure 23b shows the mentioned change of the CTE of cristobalite with temperature, seeing a sharp change around  $\sim 220$  °C ( $\sim 500$  K).

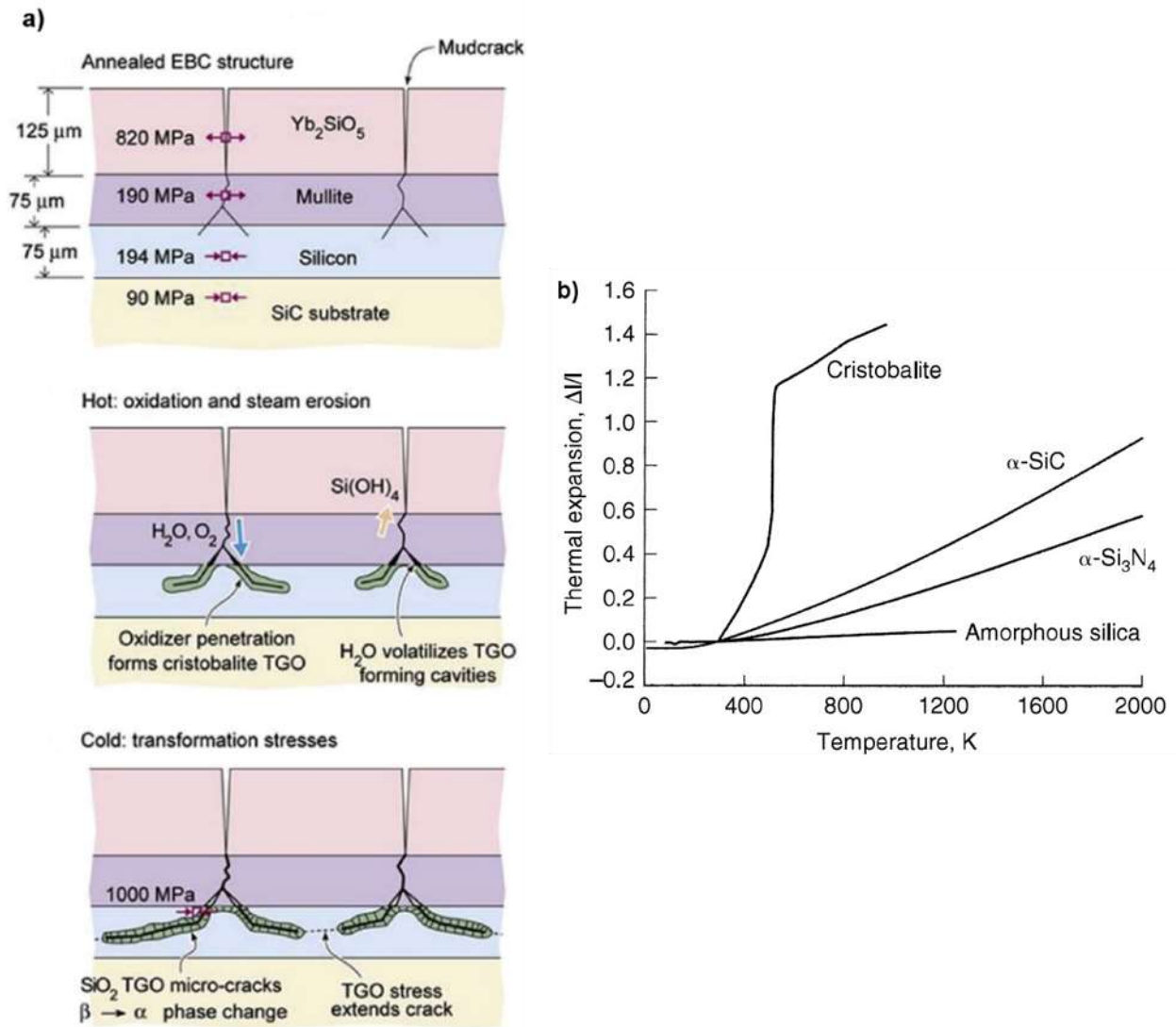


Figure 23: a) Schematic of the spallation process induced on multilayer EBC systems due to the formation of  $\beta$ -cristobalite TGO and the transformation to  $\alpha$ -phase upon cooling, causing cracking. b)

Change of the coefficient of thermal expansion with temperature on cristobalite, SiC,  $\text{Si}_3\text{N}_4$  and amorphous silica [100] [74]

The results presented in this section support the idea that the design and study of the performance of EBCs should be approached as a multifaceted problem. A low volatilisation rate is not enough for a composition to be considered as the optimal EBC top coat, since CTE matching, chemical stability and phase transformation at high temperature also play an essential role. Results coming from approximate models, such as sintered bodies, will still

provide useful knowledge, but if a successful transition to real world applications is to be achieved, further testing with production-like deposition methods and testing is required to understand the fundamental mechanisms of steam corrosion on EBC. Even when realistic coatings are produced and tested under the appropriate conditions, attention should be paid not only to one single phenomenon involved in the failure of the coating. That is not to say that single phenomenon should not be thoroughly investigated, as a deeper understanding of the causes will allow for better performing coatings, but it should be kept in mind that a compromise between the requirements is needed for proper performance during service. Top coat volatilisation is, undoubtedly, a serious issue, but it is only one of the potential failure modes. Cracking due to CTE mismatch and oxidation of the Si bond coat, leading to detrimental phase transformation within the TGO are also important occurrences that need to be considered when designing the test methodology. Finally, although the isolation of the effect that steam has on EBCs is needed to understand the basis of its attack, it should not be forgotten that steam is not the only component present in the environment experienced by EBCs during service. Molten corrosive species, or CMAS, as it is discussed in the next section, represent a severe challenge for the current iteration of EBCs, and steam protection alone will not suffice for the successful application of rare earth silicates.

#### 2.3.2.2. CMAS corrosion

During the early development of first generation of EBCs, the main concern was the degradation suffered by the SiC CMC substrates by molten corrosive species. Due to the variability in specific compositions, the term CMAS (CaO-MgO-Al<sub>2</sub>O<sub>3</sub>-SiO<sub>2</sub>) will be used to denote the multitude of impurities that represent a threat when ingested by the engine or turbine. As previously mentioned in this work, that focus shifted towards steam once it was realised that steam presented also a considerable threat to the performance and service life of SiC components. Nevertheless, CMAS was, and still is, a crucial obstacle that any potential EBC

system must surpass, and research has continued in this regard trying to understand the interaction between molten CMAS and EBCs. In this work only research done on rare earth silicates will be presented.

One of the particularities of the interaction of CMAS with coatings is that temperature plays a critical role. Not by accident, in this work the description of corrosive species or CMAS has been always accompanied by “molten”. In its many configurations, CMAS does not represent a problem as long as it remains in solid form. Although the exact melting point for CMAS varies with the precise composition used, the commonly agreed melting point for CMAS is  $\sim 1200$  °C, well below the service temperature at which EBCs are expected to operate, of  $\sim 1500$  °C. The problem is not new, as CMAS has been a thoroughly investigated topic in relation to YSZ coatings for thermal barrier coating (TBC) applications [119–123]. The corrosion pathways are, however, different in the case of rare earth silicates, requiring of additional research. This provides an additional challenge, as the CMAS composition is highly variable, as mentioned previously, and different compositions have been demonstrated to present different reactions [124,125], as shown in Figure 24.

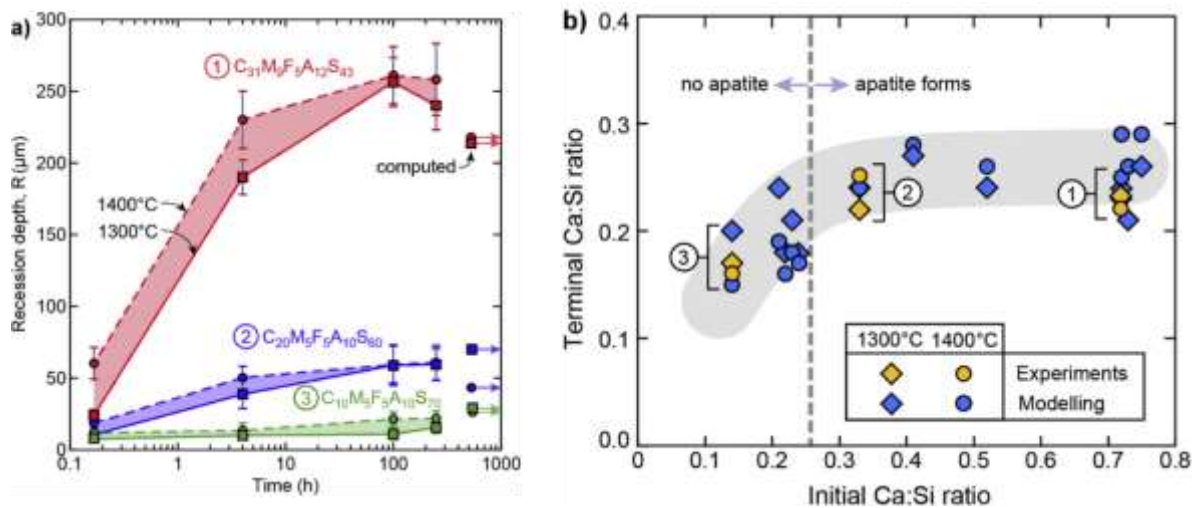
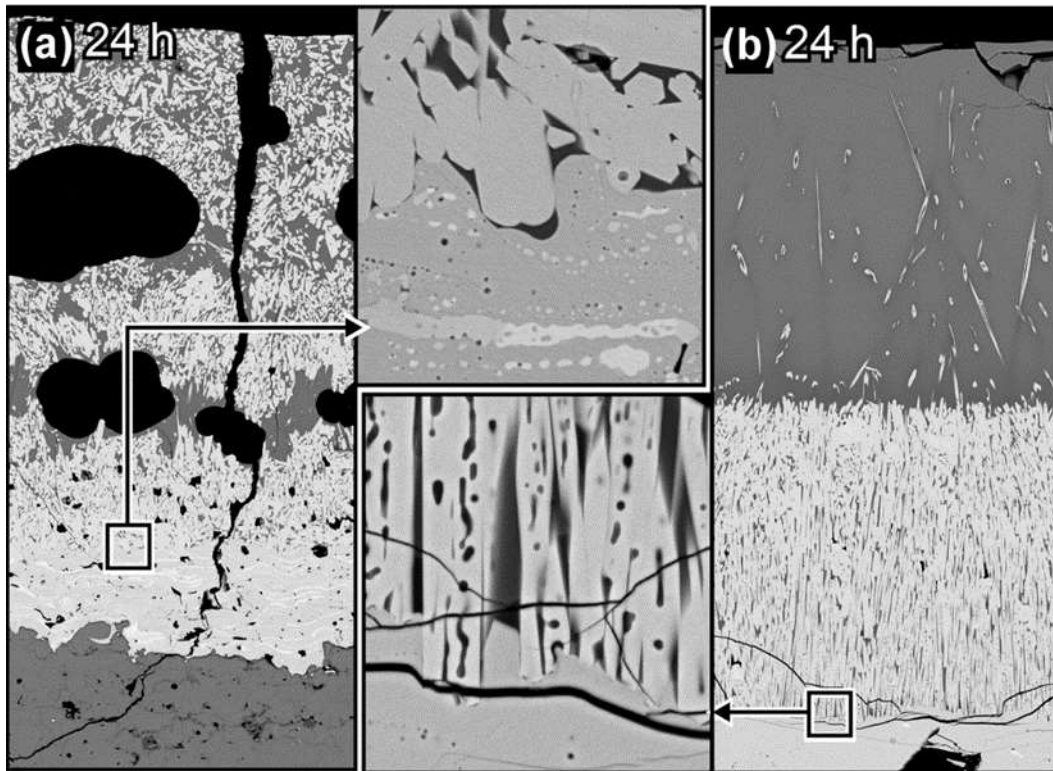


Figure 24: a) Experimental data on recession depth of the YDS surface after CMAS attack with different compositions. Theoretically derived values are represented to the right as “computed” (1) indicates a CaO rich composition, (2) an intermediate CaO composition and (3) a CaO lean composition. b) Terminal Ca:Si ratio versus initial Ca:Si after heat treatment of YDS for two temperatures and three CMAS compositions, both from theoretical calculations and experimental results. The dashed grey line represents the minimum initial Ca:Si ratio discovered for the formation of apatite precipitates [126]

Another factor that should be considered is that the majority of the studies regarding rare earth silicates and CMAS have been reported on sintered pellets or bulk material. Sintered bodies or bulk materials, as discussed with the steam interaction, can provide useful information, but should be treated carefully if conclusions are to be extracted regarding coatings produced through thermal spraying, as required per many sectors of the industry. Additionally, these studies tend to be performed in phase-pure fully crystalline materials, which does not accurately represent the reality of deposited coatings. The differences between tests performed on sprayed coatings and sintered bodies are clearly represented in Figure 25.



*Figure 25: YDS and CMAS interaction after 24 h at 1300 °C in air where an APS-deposited coating (a) is shown versus a sintered body (b). The same CMAS composition and testing conditions were used in both cases. Modified from [127]*

Although the degradation suffered by EBCs due to CMAS is highly variable depending on the testing temperature, the composition of the CMAS used, the deposition method chosen and the composition of the EBC top coat (pure phase or mixed phases), as mentioned above, several common aspects have been discovered when studying the interaction of rare earth silicates and CMAS at high temperatures. Two main degradation mechanisms have been identified, with examples being shown in Figure 26. The first interaction observed involves the reaction between the molten CMAS and the EBC top coat. Such mechanism has been reported for  $Y_2SiO_5$  and  $Y_2Si_2O_7$  [78,124,126,128–132], in which the reaction with the CMAS produces the dissolution of the EBC followed by the recrystallisation of yttrium monosilicate and Y-Ca-Si apatite in solid solution, forming characteristic needle-like structures, as it can be seen in Figure 26a. The second possibility is based not on the reaction between CMAS and the top

coat, but on the penetration of the CMAS material along grain boundaries, reaching deeper layers of the EBC and causing “blister” damage, as seen in Figure 26b for  $\text{Yb}_2\text{Si}_2\text{O}_7$ , due to the dilatation gradient caused by the slow penetration of CMAS.

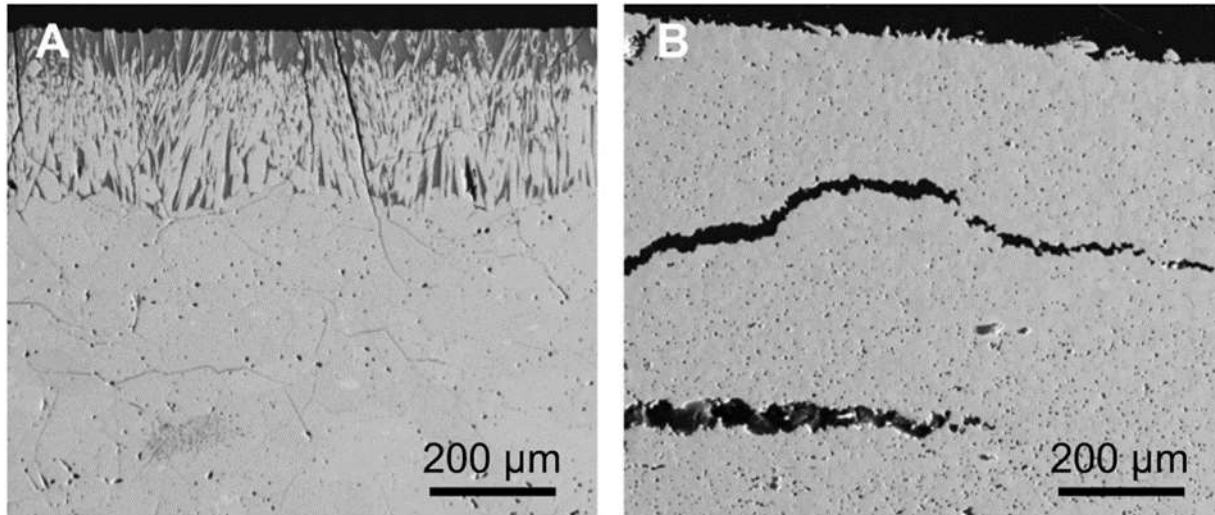


Figure 26: Cross-section SEM images of rare earth silicates pellets exposed to CMAS at 1500 °C for 24 h. Image A corresponds to  $\text{Y}_2\text{Si}_2\text{O}_7$  and image B to  $\text{Yb}_2\text{Si}_2\text{O}_7$ . Adapted from [86]

In addition to the chemical composition of the EBC top coat, the morphology of the coating (due to the deposition method chosen) and the presence of a mixture of phases also affects the degradation mechanism present. For instance, for  $\text{Yb}_2\text{SiO}_5$  and  $\text{Yb}_2\text{Si}_2\text{O}_7$  [124,128,129,133–138], there seems to be a difference in the mechanism involved when the EBC is exposed to CMAS attack at high temperatures depending on whether the testing involves sintered bodies or thermal sprayed coatings. Some authors report minimal reaction between the Yb mono- and di-silicate pellets, rather showing intensive penetration of CMAS along grain boundaries. Nevertheless, several studies on thermal sprayed coatings have shown extensive dissolution of the ytterbium silicate and the precipitation of needle-like apatite structures, much like with yttrium silicates, as it can be seen in the schematic proposed by Zhao *et al.* [135] for the mechanism taking place, shown in Figure 27. Both this work, and the ones conducted by Stolzenburg *et al.* [136] and Poerschke *et al.* [127] deserve special attention as they were

performed on APS deposited coatings, which provides a unique perspective not fully captured with sintered pellets studies.

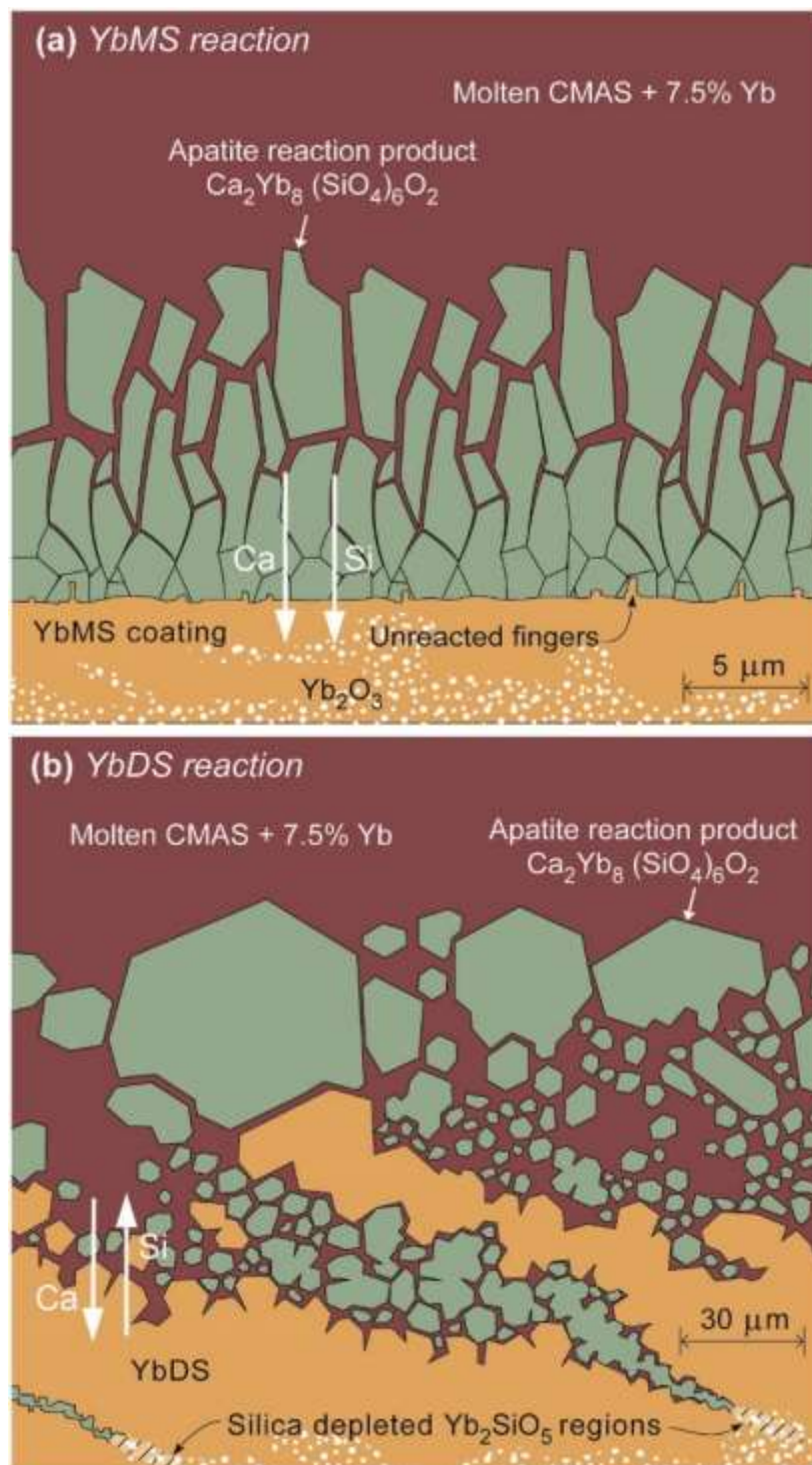


Figure 27: Schematic of the proposed interaction mechanism between YbMS (top) and YbDS (bottom) when exposed to CMAS at 1300 °C [135]

The mechanism shown in Figure 27a) for YbMS is based in the discussed dissolution of the monosilicate and posterior precipitation as needle-like apatite grains with areas of intercalated residual CMAS, forming the already seen reaction layer. In the case of YbDS, shown in Figure 27b), the initial apatite grains are coarser and larger in size, with an irregular reaction layer where no clear reaction front can be determined. As the corrosion continues, molten CMAS preferentially attacks the YbMS-rich areas of the coatings. Due to the lamellar structure of the plasma deposited coatings, the YbMS-rich splats are elongated and parallel to the surface, which produces a rapid advance of the reaction in this direction. The precipitation of the apatite grains creates a “cleft” effect, as it can be seen in the schematic.

This effect is one of the most clear examples reported of the different corrosion attacks mechanism that can be shown in deposited coatings versus sintered bodies, since the latter tends to be a pure phase without presence of splats or enriched and leaner areas. This variability depending of the experimental methods applied and the testing conditions is presented in Table 3, where a summary of different CMAS corrosion experiments is presented, attending to the deposition techniques for both the substrate and the CMAS, the specific CMAS composition used and the testing conditions (such as temperature, CMAS mass loading or high temperature exposure time).

Material	CMAS composition (mol %)	CMAS preparation	Test material preparation	Testing conditions	Corrosion effects	Ref.
Yb <sub>2</sub> SiO <sub>5</sub> (YbMS)	35CaO-10MgO-7AlO <sub>1.5</sub> -48SiO <sub>2</sub>	CMAS + ethanol applied as paste	Hot pressing at 1500 °C/103 MPa in vacuum	~40 mg/cm <sup>2</sup> 1500 °C for 50h	Preferential attack at grain boundaries. 4 mm CMAS penetration. Reaction layer with hexagonal-shaped apatite grains	[129]
	33CaO-9MgO-13AlO <sub>1.5</sub> -45SiO <sub>2</sub>	100 °C for 10 h + 1200 °C for 24 h + cold pressing + sintering at 1200 °C for 2 h	Sol-gel + cold pressing + sintering at 1500 °C for 10 h in air	1200 °C for 4 h 50% H <sub>2</sub> O/50% O <sub>2</sub>	Reaction layer at the CMAS/YbMS interface, with the presence of Yb-doped CaAl <sub>2</sub> Si <sub>2</sub> O <sub>8</sub>	[139]
		1200 °C for 20 h + cold pressing	Air plasma sprayed YbMS/mullite/Si on SiC substrates + 1300 °C for 20 h	1300 °C for 250 h	Apatite reaction layer after 1 minute with vertical needle-like grains. Thicker reaction layer and grain coarsening with increasing time. EBC fully penetrated after 250 h, layers reacted forming large pores	[135]
		1550 °C for 4 h twice. CMAS and YbMS powders mixed 70:30 wt.%	Commercially available	1300 °C for 96 h	YbMS phase content dropped to 27% after 1 minute, dropping to 7% after 96 h. Apatite appears in its place forming needle-like hexagonal precipitates	[133]
		1550 °C for 4 h twice. Placed on a well on the bulk YbMS	Not reported	~35 mg/cm <sup>2</sup> 1300 °C for 96 h	Extensive reaction between the bulk YbMS and the molten CMAS to form needle-like hexagonal apatite precipitates dispersed along the residual CMAS	[133]
Yb <sub>2</sub> Si <sub>2</sub> O <sub>7</sub> (YbDS)	33CaO-9MgO-13AlO <sub>1.5</sub> -45SiO <sub>2</sub>	100 °C for 10 h + 1200 °C for 24 h + cold pressing + 1200 °C for 2 h	Sol-gel + cold pressing + 1500 °C for 10 h	~314 mg/cm <sup>2</sup> 1400 °C for 10 h 50% H <sub>2</sub> O/50% O <sub>2</sub>	Preferential attack at grain boundaries. 1.5 - 2 μm CMAS penetration. Formation of large pores	[128]
	39.2CaO-5.2MgO-4.1AlO <sub>1.5</sub> -51.5SiO <sub>2</sub>	1550 °C for 4 h twice. CMAS + ethanol applied as paste	Spark plasma sintering at 1600 °C/75 MPa + 1500 °C for 1 h	~15 mg/cm <sup>2</sup> 1500 °C for 24 h	Dense CMAS glass layer with apatite grains after 1 h, both hexagonal and needle-like. After 24 h severe blister damage is seen, almost no presence of apatite. CMAS penetrating through grain boundaries	[130]
	30.7CaO-8.2MgO-12.8AlO <sub>1.5</sub> -48.3SiO <sub>2</sub> 24.8CaO-9.1MgO-14.2AlO <sub>1.5</sub> -51.7SiO <sub>2</sub> 6.7CaO-8.9MgO-14.2AlO <sub>1.5</sub> -70.1SiO <sub>2</sub>	850 °C for 10 h + 1500 °C for 1 h + water quenching. 50:50 mol% EBC:CMAS	Commercially available + 1500 °C for 10 h	1200 °C, 1300 °C and 1400 °C for 1 h	At the highest CaO content there was formation of apatite at all three temperatures, YbDS still present. At 1200 °C there is little presence of needle-like apatite	[124]
	33CaO-9MgO-13AlO <sub>1.5</sub> -45SiO <sub>2</sub>	1200 °C for 20 h + cold pressing	Air plasma sprayed YbDS/mullite/Si on SiC substrates + 1300 °C for 20 h	1300 °C for 250 h	For lower CaO contents, YbDS was produced at all temperatures along with cristobalite	[135]
		1550 °C for 4 h twice. CMAS and YbMS powders mixed 70:30 wt.%	Commercially available	1300 °C for 96 h	Irregular apatite reaction layer after 1 h with coarse grains. No clear reaction front seen, CMAS preferentially reacted with YbMS-rich areas, creating quickly advancing fronts acting as clefts	[133]
		1550 °C for 4 h twice. Placed on a well on the bulk YbDS	Not reported	~35 mg/cm <sup>2</sup> 1300 °C for 96 h	YbDS phase content dropped to 30% after 96 h. No apatite is detected after 96 h, some dissolution of the YbDS	[133]

Material	CMAS composition (mol %)	CMAS preparation	Test material preparation	Testing conditions	Corrosion effects	Ref.
Y <sub>2</sub> SiO <sub>5</sub> (YMS)	33CaO-9MgO-13AlO <sub>1.5</sub> -45SiO <sub>2</sub>	1200 °C for 24 h + cold pressing + 1220 °C for 2 h	Pellets provided by industrial partner	~13 mg/cm <sup>2</sup> 1300 °C for 100 h	80 µm of recession after 100 h. Needle-like apatite grains reaction layer	[78]
		100 °C for 10 h + 1200 °C for 24 h + cold pressing + 1200 °C for 2 h	Sol-gel + cold pressing + 1500 °C + 10 h	1200 °C for 4 h 50% H <sub>2</sub> O/50% O <sub>2</sub>	Reaction layer at the CMAS/YMS interface, with the presence of Y-doped CaAl <sub>2</sub> Si <sub>2</sub> O <sub>8</sub>	[139]
Y <sub>2</sub> Si <sub>2</sub> O <sub>7</sub> (YDS)	35CaO-10MgO-7AlO <sub>1.5</sub> -48SiO <sub>2</sub>	CMAS + ethanol applied as paste	Hot pressing 1500 °C/103 MPa	~40 mg/cm <sup>2</sup> 1500 °C for 50h	Preferential attack at grain boundaries. 4 mm CMAS penetration. Reaction layer with apatite needle-like grains and Si-rich areas	[129]
	33CaO-9MgO-13AlO <sub>1.5</sub> -45SiO <sub>2</sub>	100 °C for 10 h + 1200 °C for 24 h + cold pressing + 1200 °C for 2 h	Sol-gel + cold pressing + 1500 °C + 10 h	~314 mg/cm <sup>2</sup> 1400 °C for 10 h 50% H <sub>2</sub> O/50% O <sub>2</sub>	Dense apatite reaction layer with minimal CMAS penetration	[128]
	39.2CaO-5.2MgO-4.1AlO <sub>1.5</sub> -51.5SiO <sub>2</sub>	1550 °C for 4 h twice. CMAS + ethanol applied as paste	1600 °C for 4 h + spark plasma sintering at 1600 °C/75 MPa + 1500 °C for 1 h	~15 mg/cm <sup>2</sup> 1500 °C for 24 h	300 µm apatite reaction zone after 24 h with 2 layers: (1) needle-like grains and CMAS and (2) dense apatite grains	[130]
	25.2CaO-2.6MgO-8.2AlO <sub>1.5</sub> -59.8SiO <sub>2</sub> -1.6FeO <sub>1.5</sub> -1.5K <sub>2</sub> O	Placed on a well on the bulk YDS	Commercially available + hot pressing 1500 °C/27.6 MPa for 2 h	~35 mg/cm <sup>2</sup> 1200 °C, 1300 °C, 1400 °C and 1500 °C for 20 h	~215 µm of penetration at 1500 °C for 20 h, reaction zone with 2 layers: (1) apatite grains and CMAS (2) needle-like apatite grains with new pores. Grains in (1) transition to needle-like with increasing temperature	[140]
	30.7CaO-8.2MgO-12.8AlO <sub>1.5</sub> -48.3SiO <sub>2</sub> 24.8CaO-9.1MgO-14.2AlO <sub>1.5</sub> -51.7SiO <sub>2</sub> 6.7CaO-8.9MgO-14.2AlO <sub>1.5</sub> -70.1SiO <sub>2</sub>	850 °C for 10 h + 1500 °C for 1 h + water quenching. 50:50 mol% EBC:CMAS	Commercially available + 1500 °C for 10 h	1200 °C, 1300 °C and 1400 °C for 1 h	For the highest CaO content, formation of apatite, grain size increases with temperature. For reduced CaO content, unreacted YDS and cristobalite are detected. For the lowest CaO content, no apatite detected, only crystallised CMAS	[124]
	31CaO-9MgO-5FeO <sub>1.5</sub> -12AlO <sub>1.5</sub> -43SiO <sub>2</sub>	~50 °C below melting point for 24 h + cold pressing + 1100 °C for 12 h	Powder provided by industrial partner + field-assisted sintering at ~1500 °C/~100 MPa + 1400 °C for 24 h	~15 mg/cm <sup>2</sup> 1300 °C for 24 h	Recession of 25 µm with ~15 µm reaction layer with needle-like apatite grains after 10 min. After 4 h recession is 180 µm with thicker reaction layer and cristobalite. After 24 h recession is 220 µm with thicker reaction layer due to growth and formation of needle-like apatite grains	[127]
			Air plasma sprayed YDS /Si on CMC substrates provided by industrial partner + 1325 °C for 10 h	~15 mg/cm <sup>2</sup> 1300 °C for 100 h	Recession of 60 µm with coarse apatite grains after 10 min. After 4 h recession is 150 µm with needle-like grains, CMAS with pores and dispersed apatite grains. After 24 h recession is 200 µm with coarser grains and more pores and grains in the CMAS. Cracks reaching substrate appear. After 100 h recession is ~250 µm	
31CaO-9MgO-5FeO <sub>1.5</sub> -12AlO <sub>1.5</sub> -43SiO <sub>2</sub> 20CaO-5MgO-5FeO <sub>1.5</sub> -10AlO <sub>1.5</sub> -60SiO <sub>2</sub> 10CaO-5MgO-5FeO <sub>1.5</sub> -10AlO <sub>1.5</sub> -70SiO <sub>2</sub>	~50 °C below melting point for 24 h + cold pressing + 1100 °C for 12 h	Field-assisted sintering at 1470 °C/100 MPa + 1400 °C for 24 h	~18 mg/cm <sup>2</sup> 1300 °C and 1400 °C for 250 h	For intermediate and lowest CaO content CMAS shows large pores after 10 min. Recession was maximum after 100 h at 1300 °C, being ~248, 59 and 16 µm from higher to lower CaO content. Slightly faster recession but similar final values for 1400 °C	[126]	

Material	CMAS composition (mol %)	CMAS preparation	Test material preparation	Testing conditions	Corrosion effects	Ref.
Lu <sub>2</sub> SiO <sub>5</sub> (LuMS)	33CaO-9MgO-13AlO <sub>1.5</sub> -45SiO <sub>2</sub>	100 °C for 10 h + 1200 °C for 24 h + cold pressing + 1200 °C for 2 h	Sol-gel + cold pressing + 1500 °C for 10 h	1200 °C for 4 h 50% H <sub>2</sub> O/50% O <sub>2</sub>	Reaction layer at the LuMS/CMAS interface, presence of Lu-doped CaAl <sub>2</sub> Si <sub>2</sub> O <sub>8</sub>	[139]
Lu <sub>2</sub> Si <sub>2</sub> O <sub>5</sub> (LuDS)				~314 mg/cm <sup>2</sup> 1400 °C for 10 h 50% H <sub>2</sub> O/50% O <sub>2</sub>	Preferential attack at grain boundaries, 2 μm CMAS penetration after 10 h. Formation of large pores	[128]
La <sub>2</sub> SiO <sub>5</sub> (LaMS)				1200 °C for 4 h 50% H <sub>2</sub> O/50% O <sub>2</sub>	Reaction layer at the LaMS/CMAS interface with dendritic, tree-like precipitates. La <sup>3+</sup> cations diffuse easily into CMAS	[139]
La <sub>2</sub> Si <sub>2</sub> O <sub>5</sub> (LaDS)				~314 mg/cm <sup>2</sup> 1400 °C for 10 h 50% H <sub>2</sub> O/50% O <sub>2</sub>	Formation of branch shaped, tree-like crystals. Presence of Ca <sub>3</sub> La <sub>6</sub> (SiO <sub>4</sub> ) <sub>6</sub> and Ca <sub>3</sub> La <sub>8</sub> (SiO <sub>4</sub> ) <sub>6</sub> O <sub>2</sub>	[128]
Gd <sub>2</sub> SiO <sub>5</sub> (GdMS)				1200 °C for 4 h 50% H <sub>2</sub> O/50% O <sub>2</sub>	Reaction layer at the GdMS/CMAS interface with presence of dendritic, tree-like precipitates	[139]
Gd <sub>2</sub> Si <sub>2</sub> O <sub>7</sub> (GdDS)				30.7CaO-8.2MgO-12.8AlO <sub>1.5</sub> -48.3SiO <sub>2</sub> 24.8CaO-9.1MgO-14.2AlO <sub>1.5</sub> -51.7SiO <sub>2</sub> 6.7CaO-8.9MgO-14.2AlO <sub>1.5</sub> -70.1SiO <sub>2</sub>	850 °C for 10 h + 1500 °C for 1 h + water quenching. 50:50 mol% EBC:CMAS	Commercially available + cold pressing + 1580 °C for 10 h
	1400 °C for 1 h	At the lowest CaO content there is apatite precipitates along with cristobalite. Highest CaO content produces needle-like apatite precipitates	[125]			
Eu <sub>2</sub> SiO <sub>5</sub> (EuMS)	33CaO-9MgO-13AlO <sub>1.5</sub> -45SiO <sub>2</sub>	100 °C for 10 h + 1200 °C for 24 h + cold pressing + 1200 °C for 2 h	Sol-gel + cold pressing + 1500 °C for 10 h	1200 °C for 4 h 50% H <sub>2</sub> O/50% O <sub>2</sub>	Reaction layer at the EuMS/CMAS interface with dendritic, tree-like precipitates	[139]
Eu <sub>2</sub> Si <sub>2</sub> O <sub>7</sub> (EuDS)				~314 mg/cm <sup>2</sup> 1400 °C for 10 h 50% H <sub>2</sub> O/50% O <sub>2</sub>	Dense apatite reaction layer with the presence of clefts or blister damage that could lead to spallation	[128]
Sc <sub>2</sub> Si <sub>2</sub> O <sub>7</sub> (ScDS)				39.2CaO-5.2MgO-4.1AlO <sub>1.5</sub> -51.5SiO <sub>2</sub>	1550 °C for 4 h twice. CMAS + ethanol applied as paste	1600 °C for 4 h + spark plasma sintering at 1600 °C/75 MPa + 1500 °C for 1 h
	~15 mg/cm <sup>2</sup> 1500 °C for 24 h	Dense residual CMAS glass with scattered apatite grains after 1 h. After 24 h sever blister damage with no presence of apatite. Reaction between ScDS and CMAS, with Sc-doped CMAS penetrating through grain boundaries	[130]			
Dy <sub>2</sub> Si <sub>2</sub> O <sub>7</sub> (DyDS)	30.7CaO-8.2MgO-12.8AlO <sub>1.5</sub> -48.3SiO <sub>2</sub> 24.8CaO-9.1MgO-14.2AlO <sub>1.5</sub> -51.7SiO <sub>2</sub> 6.7CaO-8.9MgO-14.2AlO <sub>1.5</sub> -70.1SiO <sub>2</sub>	850 °C for 10 h + 1500 °C for 1 h + water quenching. 50:50 mol% EBC:CMAS	Commercially available + cold pressing + 1580 °C for 10 h	1400 °C for 1 h	Formation of apatite with different stoichiometries and cristobalite presence for all CaO contents. Highest CaO content produces needle-like apatite grains	[125]
Er <sub>2</sub> Si <sub>2</sub> O <sub>7</sub> (ErDS)						
Nd <sub>2</sub> Si <sub>2</sub> O <sub>7</sub> (NdDS)						

Table 3: Summary of the CMAS corrosion experimental results reported in the literature for different rare earth silicates

Despite the wide range of effects described in Table 3, accounting for the variability in rare earth silicates tested, the different CMAS compositions and testing conditions, some general features can be observed. First of all, if reaction between the rare earth silicate and the CMAS does occur, precipitation of RE-Ca-Si apatite is the most common product, with the appearance in occasions of  $\beta$ -SiO<sub>2</sub> cristobalite. This reaction will produce the recession of the coating and appearance of defects such as cracks or porosity. However, reaction with CMAS is not always guaranteed, and penetration of CMAS can also take place without almost interaction, particularly for lower Ca-containing CMAS compositions. This infusion of CMAS into the EBC is undoubtedly undesirable, as it can lead to blister damage as shown in Figure 26b. Secondly, as mentioned before, the CaO content present in the chosen CMAS composition plays a key effect in the corrosion mechanism observed and its severity. Higher CaO contents will have a more nefarious interaction with the top coat in terms of recession rates and precipitation of apatite. On the other hand, lean CaO compositions are still highly undesired due to the potential switch from silicate-CMAS reaction to CMAS penetration, as shown in Figure 24b.

As with the case of steam volatilisation, there is an interest to draw comparison between different rare earth silicate compositions and their experienced CMAS corrosion in order to assess which one might be optimal for the application desired. The use of optical basicity, first introduced in this work for the steam volatilisation, has also been suggested as a rough screening parameter for CMAS resistance [130,137]. The basis behind this criterion is the reduced reactivity between a crystalline oxide ceramic and an oxide glass if their respective OB values are close in value. Although this consideration have value in the initial stages of the EBC design, aiding to choose a composition that in theory could present improved resistance against CMAS corrosion, still presents a rough criterion, which should not be considered to withstand under all conditions and CMAS compositions. Particularly, regarding CMAS

compositions, Krause *et al.* [122] reported how the OB values can vary with the specific CMAS compositions, with values ranging between 0.49 to 0.75. This provides another degree of complexity, as debris ingested by engines during service might have different sources, and therefore different interaction with the EBC.

Despite considerable research being conducted regarding the interaction between CMAS and EBC at high temperatures, the fundamental mechanisms that control the interaction are not fully understood yet. One of the reasons, as previously highlighted, is the difference in materials employed and testing protocols. A standardised protocol involving the deposition method used, the acceptable ranges for the phases present in the coating and the deposited microstructure would be needed to fully determine which potential candidate has the best characteristics to provide reliable protection to SiC CMC coated components during operation that involves the ingestion of salt-containing debris. It should be taken into account, however, that a standardised CMAS composition and testing protocol will only be useful for comparison purposes, since the industry might still request specific CMAS compositions, more suited to the debris involved when operating in different areas. A great example of this is the extensive research that was conducted after the eruption in 2010 of the volcano Eyjafjallajökull in Iceland [141–143], representing an unique challenge for aviation in the European air space.

Perhaps, as it was mentioned in the case of the steam corrosion of rare earth silicates, it is too ambitious to expect the same top coat composition to provide effective protection against steam at high flow speeds while showing appropriate CMAS corrosion against a wide range of compositions. To this end, different alternatives are being considered [134,144], and some of them are borrowed from the previous knowledge gathered in the field of TBC, as it is shown in Figure 28.

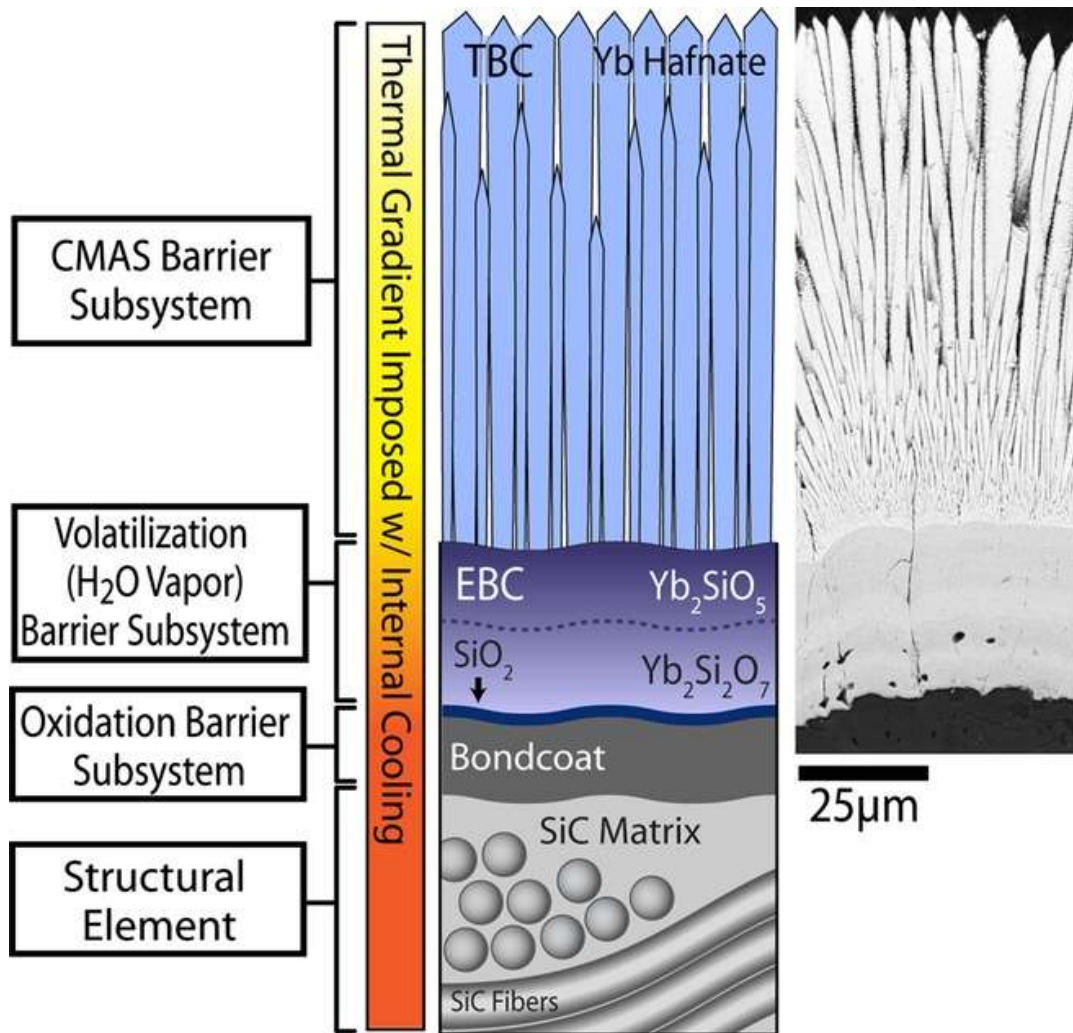


Figure 28: Schematic structure of an EBC sharing features of a thermal barrier coatings (TBC), being mixed TBC/EBC systems aiming to provide protection against steam and CMAS attack [134]

The incorporation of an additional layer to the EBC system might be the way forward to provide complete protection to the component underneath, both from the environment (which could have steam, salt-containing debris or a mixture of both) and from the high temperatures required for a benefit in efficiency. A clear point can be concluded from the current information on CMAS: molten corrosive species represent a formidable challenge that still cannot be tackled with the current generation of EBCs. Recession rates and penetration depths comparable to the standard thickness of EBC systems are observed after a few hundred hours, which is unacceptable if the same situation were to be encountered during service. On top of

that, the majority of the reported experiments were conducted with a single application of CMAS, whereas during operation, engines might ingest salt-containing debris continuously, adding fresh molten CMAS to the reaction zone, and preventing the hindering of the nefarious effects due to exhaustion of the components.

### **2.3.3. Current status and future research**

The current generation of environmental barrier coatings can be considered to be in a mature stage, both in terms of requirements identified and compositions proposed. Despite this, testing and further research is still needed to verify and optimised the microstructure and characteristics of the coatings. Due to the lack of a standardised testing protocol, both for steam and CMAS degradation, research currently published can be difficult to compare to each other, making it difficult to determine a model that properly describes the underlying mechanisms.

First of all, thermal sprayed coatings should be employed when investigating the properties of current EBCs. Although useful information can be extracted from sintered bodies, it is clear that thermal spray will be a major technique for the deposition of EBC in gas turbine components. Secondly, to limit the number of variables involved in the testing protocol, free-standing coatings would be preferable, at least in the initial stages. The presence of a Si bond coat and a CMC or SiC substrate, although needed for late stages of research, might not be beneficial yet. The goal should be to achieve a deep understanding of the mechanism governing the steam and CMAS corrosion with the rare-earth top layer. Finally, the different parameters involved should be carefully considered. For instance, temperature, in both steam and CMAS testing, has been traditionally kept below 1400 °C. This is to avoid complications with temperatures too close to the melting point of the Si bond coat (~1390 °C, or below if impurities are present). But the role of the Si bond coat is nowadays being questioned as research progresses, and higher temperatures should be included in the testing protocols. In addition to

temperature, porosity, a key parameter on ceramic coatings, has been kept as low as possible for EBC applications, to limit the ingress of corrosive species. However, as discussed in section 2.3.2 “Corrosion mechanisms”, grain boundaries seem to be of greater importance when considering the preferred ingress path. Since higher levels of porosity are required for specific applications, such as abradable coatings, in order to be eroded and allow the turbine blades to create a tight seal without risking damage due to friction [145], coatings with varying levels of porosity should be added to the testing protocols.

## **Chapter 3: Splat Formation and Microstructure of Solution Precursor Thermal Sprayed Nb-doped Titanium Oxide Coatings**

The main body of this section is reproduced from the paper:

*D. Tejero-Martin, Z. Pala, S. Rushworth, T. Hussain, Splat formation and microstructure of solution precursor thermal sprayed Nb-doped titanium oxide coatings, Ceram. Int. 46 (2020) 5098–5108. <https://doi.org/10.1016/j.ceramint.2019.10.253>*

### **Abstract**

Solution precursor thermal spray can become a breakthrough technology for the deposition of coatings with novel chemistries; however, the understanding of the process that the feedstock material undergoes is still poorly when compared to more traditional presentations (i.e. powder and suspension). In this paper, niobium-doped TiO<sub>2</sub> coatings were deposited by solution precursor high velocity oxy-fuel spraying, studying its microstructure and phase. It was reported that a lower flame temperature produced a highly porous coating, while the porosity was reduced at higher flame temperature. Investigation of the phase content showed that, contrary to our current understanding, a higher flame power implied an increase of the anatase phase content for solution precursor spray. Three methods were used: Rietveld refinement, peak height and peak area of the x-ray diffraction patterns. Additionally, single splats were analysed, showing that as the precursor travels through the flame, pyrolysis and sintering takes place to form the solid material. These results were used to derive a model of the physico-chemical transformation of the solution precursor. This work proves that solution precursor thermal spray is a promising technique for the deposition of doped ceramic coatings, being the microstructure and phase content controllable through the spraying parameters.

### 3.1. Introduction

Titanium oxide coatings are widely used in a number of fields owing to its unique properties, such as a prominent photocatalytic effect [30], its electrochemical activity [146], its coherent change in electrical conductivity under gas exposure [33] or its ability to produce transparent coatings [147,148]. Nevertheless, the properties of titanium oxide (also known as titania) can be tailored to be more beneficial through doping [40,149–153]. Among those elements, niobium presents some desirable properties that makes it a suitable candidate for the formation of doped titanium oxide coatings. It effectively increases the electrical conductivity which, in addition to the favourable electrochemical properties of TiO<sub>2</sub> (such as high capacity and low volume expansion during ion charge/discharge [37,38,154]), makes it a viable option as an anode material for high-power Li-ion batteries. The ability to produce transparent coatings has increased its interest regarding its use as a transparent conductive oxide (TCO) coating. In the recent years there has been a growing demand for a replacement of the current TCO industrial reference, Sn-In<sub>2</sub>O<sub>3</sub>, due to limited resources and increasing costs [35]. An increase of the coating conductivity, coupled with high transmittance in the visible range, positions Nb-doped TiO<sub>2</sub> as a viable candidate for the next generation of TCOs [43,48,155]. In addition to the improvement in electrical conductivity, Nb-doped TiO<sub>2</sub> coatings have also found application as sensors, as the niobium limits the grain growth and inhibits the anatase to rutile phase transformation to temperatures up to 650 °C [156], being the rutile phase traditionally considered detrimental for sensing applications [34,40,41,157,158].

Due to the plethora of applications present, production of niobium-doped TiO<sub>2</sub> has been reported in the literature using techniques such as flame spray pyrolysis [40,41], sputtering [36,42,43], pulsed laser deposition [44,45], atomic layer deposition [46], spin-coating [47] or aerosol-assisted chemical vapour deposition [48]. At the same time, thermal spraying deposition of titanium oxide has been thoroughly studied before; using powder, suspensions

and solution precursors as feedstock material [49–52]. In thermal spray, a heat source is used to melt the feedstock material while a jet carries the molten particles towards the piece to be coated [14]. In the case of high velocity oxy-fuel (HVOF) thermal spraying, the flame is produced via the combustion of mixed oxygen and fuel on a pressurised combustion chamber, which leaves through a nozzle creating a supersonic jet. The traditional presentation of the feedstock material is in powder form; however, that imposes a lower limit to the size of the particles to ensure adequate flowability. Suspension, and more recently, solution precursor thermal spraying have been devised as a route to avoid this limitation. In particular, solution precursor eliminates the need for suspended particles in a liquid medium. Instead, the precursors are mixed in a liquid form and then react in-flight, due to the heat transfer, to form the solid particles, consequently melting and impinging at the substrate surface [159]. The technique opens up new possibilities of microstructural features and chemistries to be explored, as demonstrated by its application in the deposition of thermal barrier coatings [54,159], superhydrophobic coatings [160] or even TiO<sub>2</sub> with different porosity levels [51,52]. Despite these advantages and the plethora of deposition methods reported, and to the best of the author's knowledge, no work has been published on the production of niobium-doped TiO<sub>2</sub> coatings using a solution precursor thermal spray technique.

Although a preference for titanium dioxide coatings with a high anatase content has been the norm, recent studies on the photocatalytic activity of suspension HVOF thermal sprayed titania [161] suggest that the microstructure of the deposited coating and most importantly, the interaction between rutile and anatase regions, plays an essential role in the presence of an enhanced photo-activity at relatively low anatase content (~20%). Therefore, quantitative phase content determination of XRD diffraction pattern of the deposited Nb-TiO<sub>2</sub> has been carried out in this work to better understand the formation of anatase and rutile from solution precursor feedstock.

In this work, a comprehensive study of the deposition process and microstructure of Nb-doped TiO<sub>2</sub> coatings produced using solution precursor high-velocity oxy fuel (SP-HVOF) thermal spray is presented. The process from the original precursor solution into individual droplets when exposed to the flame and the formation of the coating upon impact with the substrate, as well as the characteristics of the deposited coatings, were investigated. Scanning electron microscopy (SEM) was used to determine the morphology of the individual splats and the coatings, and x-ray diffraction was applied to evaluate relationship between the phases present, their content and the spraying parameters used. To analyse the evaporation process and high temperature behaviour of the solution precursor, thermogravimetry (TGA) and differential scanning calorimetry (DSC) analysis were performed.

## **3.2. Experimental methods**

### **3.2.1. Materials and coating deposition**

The solution precursor was provided by EpiValence Ltd. (Cleveland, United Kingdom) and contained a mixture of titanium ethoxide and niobium ethoxide with weight percentages of 15.0 % and 1.35 % respectively, dissolved on 2-isopropoxyethanol. The chemical composition and choice of medium was selected by EpiValence Ltd. to optimise the low temperature printing of Nb-TiO<sub>2</sub>, providing adequate Nb doping, viscosity, air sensitivity, and drying behaviour, as reported elsewhere [35].

The coatings were deposited using a modified GTV TopGun HVOF system with an injector diameter of 0.3 mm directed towards a 22 mm long combustion chamber. A detailed description of the setup can be found elsewhere [162] and in the section “Appendix”, page 209. Two sets of spraying parameters were used, corresponding to a flame power of 25 kW and 75 kW. Flame power was estimated as follows. The percentage of stoichiometry in the process was calculated from the stoichiometry oxygen/hydrogen ratio and the actual ratio used. This

percentage was used to determine, from the initial hydrogen flow, the amount of fuel being combusted. Using the combustion energy of hydrogen ( $1.93 \times 10^6$  J/mol) and the previous estimation of the amount of fuel which is combusted, an approximation for the flame power is achieved.

For the 25 kW flame, the hydrogen flow rate was 78 l/min and the oxygen flow rate was 182 l/min. For the 75 kW flame, the hydrogen flow rate was 229 l/min and the oxygen flow rate was 533 l/min. In both cases the solution precursor flow rate was 50 ml/min, stand-off distance was 85 mm, the carousel rotation speed was 73 rpm (which corresponds to a surface speed of 1 m/s) and the gun traverse speed was 5 mm/s. 10 passes were performed to build up a coating of the desired thickness.

In order to elucidate the transformations that take place once the solution precursor enters the HVOF flame, single splats were collected on stainless steel polished substrates following a swipe test. To do so, the carousel rotation and gun traverse speed were increased to their maximum values (100 rpm and 30 mm/s respectively), while only allowing one pass of the flame. In addition, the spraying was repeated three times maintaining all spraying parameters fixed from the 75 kW spraying, with the exception of the stand-off distances, which were chosen to be 65, 85 and 105 mm, aiming to provide three different snapshots of the evolution of the droplets as they travel along the flame.

The substrates used, with dimensions 60 x 25 x 2 mm, were AISI 304 stainless steel (SS) with nominal composition of Fe–19.0Cr–9.3Ni–0.05C (in wt. %). For the deposition of coatings, the substrates were grit blasted with a blast cleaner from Guyson (Dudley, England) with fine F100 brown alumina (0.125 - 0.149 mm) particles at 3 bar. Following grit blasting, the substrates were cleaned in industrial methylated spirit (IMS) using an ultrasonic bath for up to 10 minutes and blown dry with compressed air. In the case of single splat collection, the surface

of the substrate was ground and polished down to 1  $\mu\text{m}$  finish. The process was done starting with Buehler SiC grinding paper (Esslingen, Germany) grit 220 (P240) until a uniform ground surface was achieved. The process was continued using grinding papers with grit 320 (P400), 400 (P800) and 600 (P1200). The polishing process was carried out using a 6  $\mu\text{m}$  polishing paper, finally moving into 1  $\mu\text{m}$  polishing paper for the final preparation.

### 3.2.2. Characterisation

Cross section of the coatings were prepared cutting a section of the substrate using a SiC cutting wheel (MetPrep Ltd, Coventry, United Kingdom) at a speed of 0.010 mm/s on an Brilliant 220 (ATM GmbH, Mammelzen, Germany) cut-off machine. The cut section was then hot-mounted using Conducto-Mount resin from MetPrep following the recommended standard procedure. The mounted cross section was then grounded and polished down to 1  $\mu\text{m}$  using the same procedure as described above. Briefly, the process was done using SiC grinding papers with grits P240, P400, P800 and P1200 and 6 and 1  $\mu\text{m}$  polishing papers.

A FEI Quanta 600 (FEI Europe, Eindhoven, Netherlands) scanning electron microscope (SEM) was used to image the cross section, surface and single splats of the deposited Nb-TiO<sub>2</sub>, using secondary electron (SE) and backscattered electron (BSE) modes. A spot size of 2.5 nm and an acceleration voltage of 20 kV were used as the imaging parameters. The coatings were also analysed using a Siemens D500 powder X-ray diffractometer in Bragg-Brentano  $\theta - 2\theta$  geometry equipped with copper anode X-ray tube and a scintillation point detector. The  $2\theta$  range scanned by CuK $\alpha$  radiation (with a wavelength of 1.54 Å) was from 20° to 120° with 0.04° step size and 22 s of counting time in each step. Peak identification was performed using the diffracsuite EVA (Bruker Software) and Rietveld refinement procedure was applied to the obtained results using TOPAS V5 software. A split pseudo-Voigt function was used to account for the base broadening of the two anatase and rutile reflections, believed to be caused by

stacking faults on the crystallographic structure and some degree of amorphous content. To account for instrumental broadening effects, the specifics of the XRD instrument, such as source emission profile, detectors and slits, were defined during the refinement process. Structural values for the anatase and rutile were obtained from the inorganic Crystal Structure Database (ICSD). Since both coatings have a thickness below 20  $\mu\text{m}$ , x-ray penetration caused the appearance of peaks from the stainless steel substrate. These peaks were taken into account during the refinement as well, although they were not considered for the total phase quantification.

In addition to Rietveld refinement, two other methods were applied to calculate the phase content of the coatings. The first one, described by Berger-Keller et al. [163] based on data from plasma-sprayed titania from powder feedstock, derives the anatase content according to the relative height of the peaks arising from the (101) reflection of the anatase phase,  $I^{A(101)}$ , and the (110) reflection of the rutile phase  $I^{R(110)}$ , following the formula shown in the Equation 9:

$$C_A = \frac{8 \times I^{A(101)}}{8 \times I^{A(101)} + 13 \times I^{R(110)}} \times 100\% \quad (9)$$

Due to the broadening of XRD peaks when the grain size is smaller than 300 nm [164] the use of the peak height might not be faithfully representative of the anatase content in coatings with nano-sized morphologies. To account for this phenomenon, Yang et al. [165] used the peak area of those same reflections to estimate the anatase content of suspension flame sprayed nano-TiO<sub>2</sub>, using the formula shown in Equation 10.

$$C_A = \frac{A^{A(101)}}{A^{A(101)} + 1.265 \times A^{R(110)}} \times 100\% \quad (10)$$

Thermogravimetric analysis (TGA) and Differential scanning calorimetry (DSC) of the precursor solution were carried out in a TA Instruments SDT-Q600 thermobalance

(Melbourne, Australia). Two temperature profiles of 10 °C/min from room temperature up to 800 °C and 1500 °C were applied with Al<sub>2</sub>O<sub>3</sub> as reference and the material for the initial calibrations (performed in the same conditions with an empty sample crucible). Approximately 10 mg of solution were used for the analysis, performed in an air environment and up to 1500 °C. To produce dried solution for the TGA analysis, the solution precursor was kept at ~100 °C for 24 h, being the produced powder finely crushed using a mortar and pestle. The measurement parameters for the dried solution were a final temperature of 800 °C and heating rates of 10 °C/min.

### **3.3. Results and discussion**

#### **3.3.1. Microstructure and phase evolution in SP-HVOF**

Two different spray runs, with flame powers 25 kW and 75 kW as described in the experimental methods section, were performed. This first set of spraying runs had the purpose of determining the effect of flame power on the microstructure and phase composition of the Nb-doped titanium oxide coatings. As it can be seen on Figure 29, the spraying with 25 kW of flame power produced a highly porous coating with loosely bonded splats. The presence of what could be identified as unpyrolysed material, not fully molten in-flight, provides the coating with numerous voids and cavities. On the other hand, the coating deposited using 75 kW flame power presents a considerably lower porosity, as shown on Figure 29, indicating that the heat transfer in-flight was enough to melt the sintered solid particles. Computational simulations of the process for 25 kW and 75 kW show that the flame at 85 mm stand-off distance reaches a temperature of around 1880 °C and 2480 °C respectively [166]. These numbers support the increased degree of solid TiO<sub>2</sub> material, with a melting point of ~1840 °C, at 25 kW.

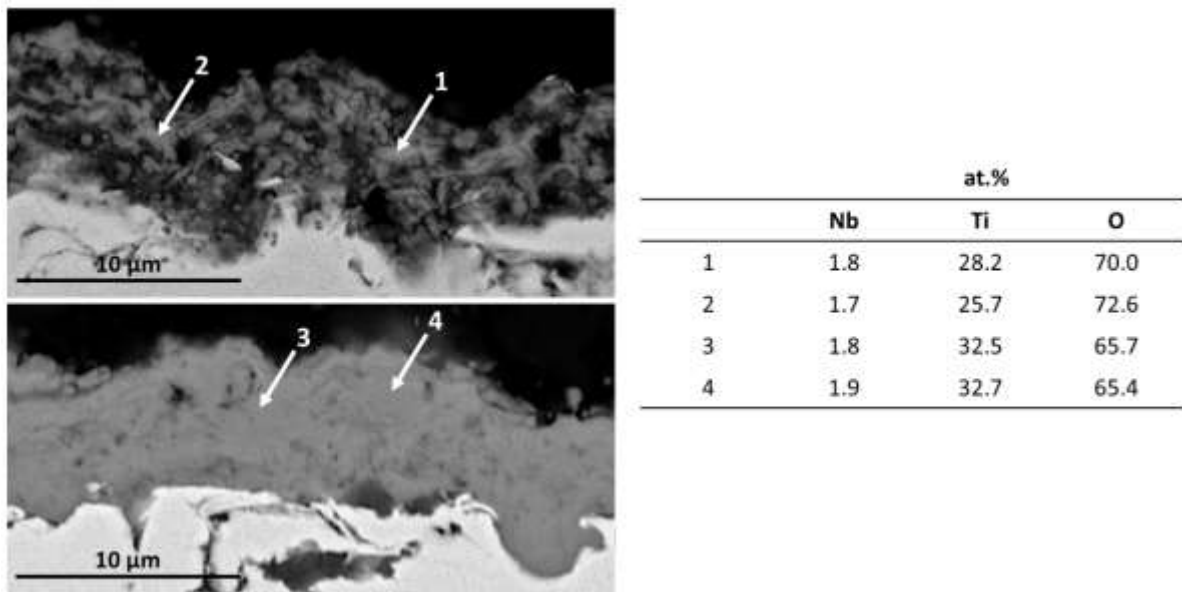


Figure 29: BSE-SEM images of the cross section of the coatings at 25 kW (top) and 75 kW (bottom). The arrows point the spots where EDS measurements were taken, with the element compositions (in atomic weight) being shown in the table

The absence of fully molten splats during the formation of the coating at 25 kW was also confirmed through SEM imaging of the top surface of the coatings, as shown in Figure 30.

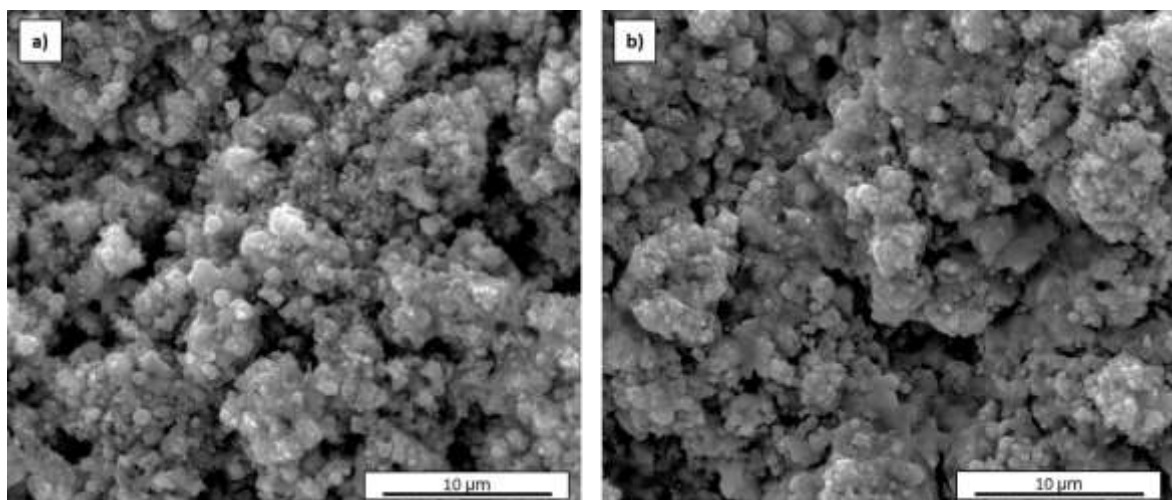


Figure 30: SE-SEM images of the top surface of the coatings at 25 kW (image a) and at 75 kW (image b)

The surface of the 25 kW coating, shown in Figure 30a, presents a limited amount of molten splats. Instead, smaller structures with plenty of crevices could be seen, which contribute to the high porosity. The surface of the 75 kW coating, shown in Figure 30b evidenced a higher percentage of particles completely molten in-flight. This higher degree of melting allowed for a complete coverage the spaces between splats, effectively blocking the inter-splat crevices and producing a denser coating with lower porosity. This combination of molten material with solid particles can be seen on Figure 39b and Figure 39e, showing the swipe test surface of samples sprayed at 75 kW with stand-off distance of 85 mm.

### **3.3.2. Elemental distribution**

In order to understand how the niobium is distributed within the coating, whether it is present as an isolated phase or as a substitutional doping element on the TiO<sub>2</sub> lattice, energy dispersive spectroscopy (EDS) measurements were taken during SEM imaging.

From the BSE images shown in Figure 29, apart from the already mentioned difference in microstructure with flame power, it can be seen that there is only a uniform distribution of Nb-doped TiO<sub>2</sub>, along with porosity. The lack of brighter spots or areas, as one would expect from a heavier element such as Nb, indicates that the addition of such element causes the mentioned substitutional doping. From the EDS values it can be seen that at 25 kW, and due to the presence of unpyrolysed material, there is a larger variance for the titanium and oxygen values across the coating. The content of niobium, however, remains almost constant at 1.8 at.%. To elucidate the distribution of the previously mentioned elements, EDS mapping was also performed on a high magnification BSE image of the 25 kW sample, as seen in Figure 31a. Figure 31b, c and d corresponds to the elemental mapping of oxygen, titanium and niobium, respectively. From the maps, it can be seen that niobium is homogeneously distributed within the coating, being the only differences attributed to crevices or voids, as marked on Figure 31b. The only brighter

phase detected on the BSE image corresponds to debris from the substrate itself, formed due to the pinning effect of the solid material deposited, or during sample preparation.

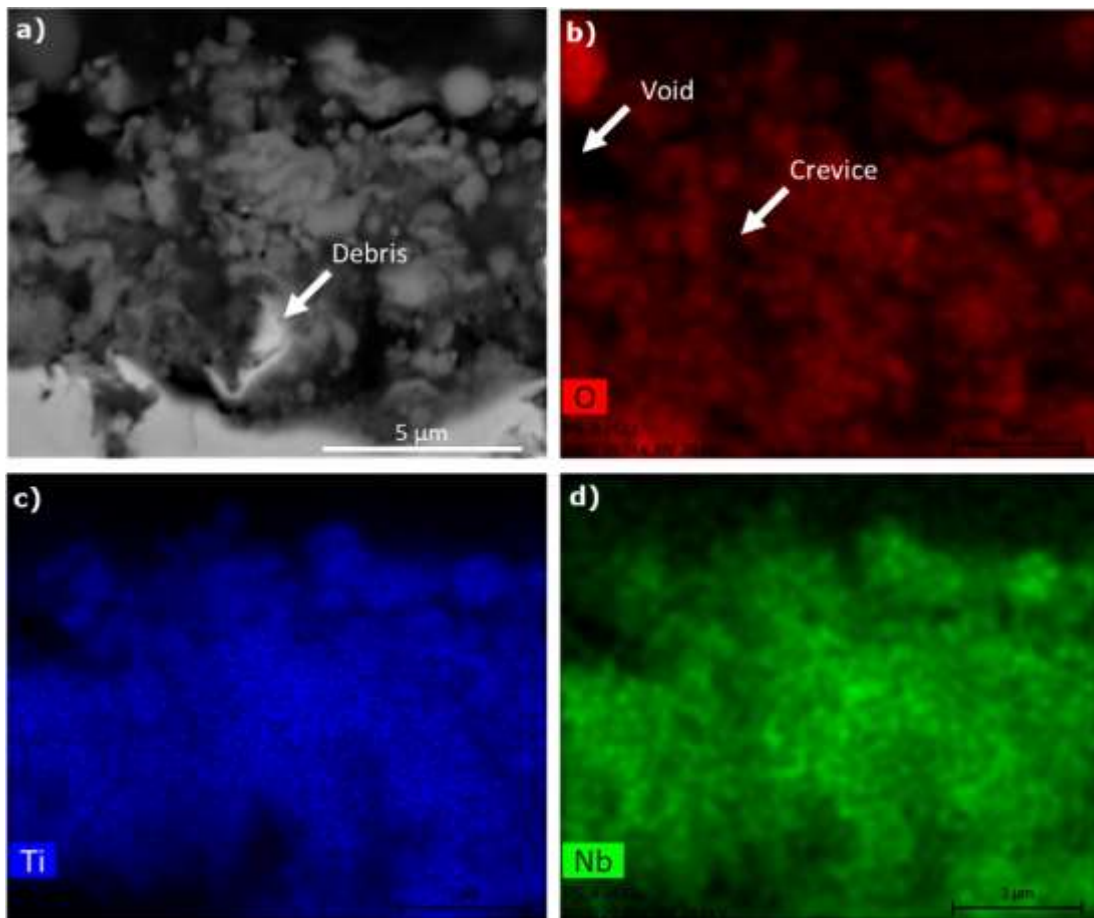


*Figure 31: EDS mapping of the cross section of the coating at 25 kW. Image a) shows the BSE image of the area studied. Image b) corresponds to the oxygen mapping, c) represents titanium mapping and d) shows niobium mapping*

In the case of 75 kW, shown in Figure 32, the appearance is more uniform with no presence of unpyrolysed material. This is also reflected on the titanium and oxygen content, which remains stable at different points of the cross section, matching the stoichiometry ratio of  $\text{TiO}_2$ . No indication of the presence of niobium oxides was present in neither XRD or EDS results.

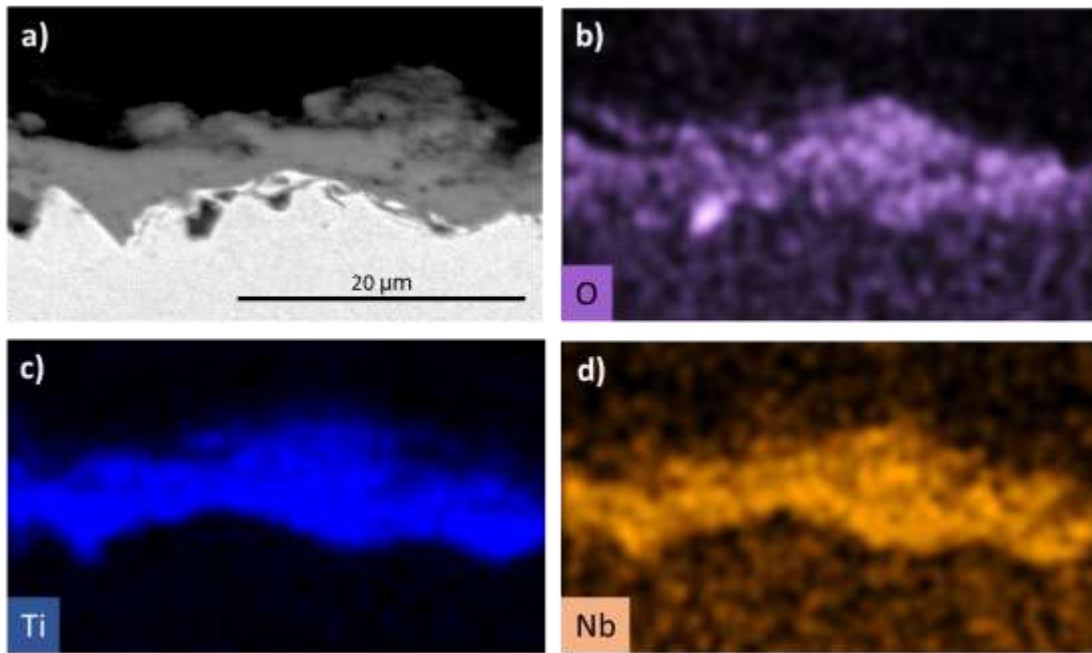


*Figure 32: EDS mapping of the cross section of the coating at 75 kW. Image a) shows the BSE image of the area studied. Image b) corresponds to the oxygen mapping, c) represents titanium mapping and d) shows niobium mapping*

Remarkably, the niobium content also remains almost constant and equivalent to the values seen at 25 kW, which corroborates the proper doping of the TiO<sub>2</sub> with niobium regardless of the flame power and microstructure produced. This could be due to the fact that the niobium doping takes place during the formation of the solid content, stage that both 25 kW and 75 kW fully reach. The successive stages of the physico-chemical in-flight transformation does not affect the niobium content, due to the fact that there is no evidence that niobium reaches its melting point, or takes part into oxidation processes.

### **3.3.3. Phase evolution**

In order to analyse the effect of flame power on the phase content of the Nb-doped TiO<sub>2</sub> coatings, XRD measurements were conducted. The results, shown in Figure 33, indicate the presence of the two distinctive phases: anatase and rutile, along with some peaks corresponding to the stainless steel substrates.

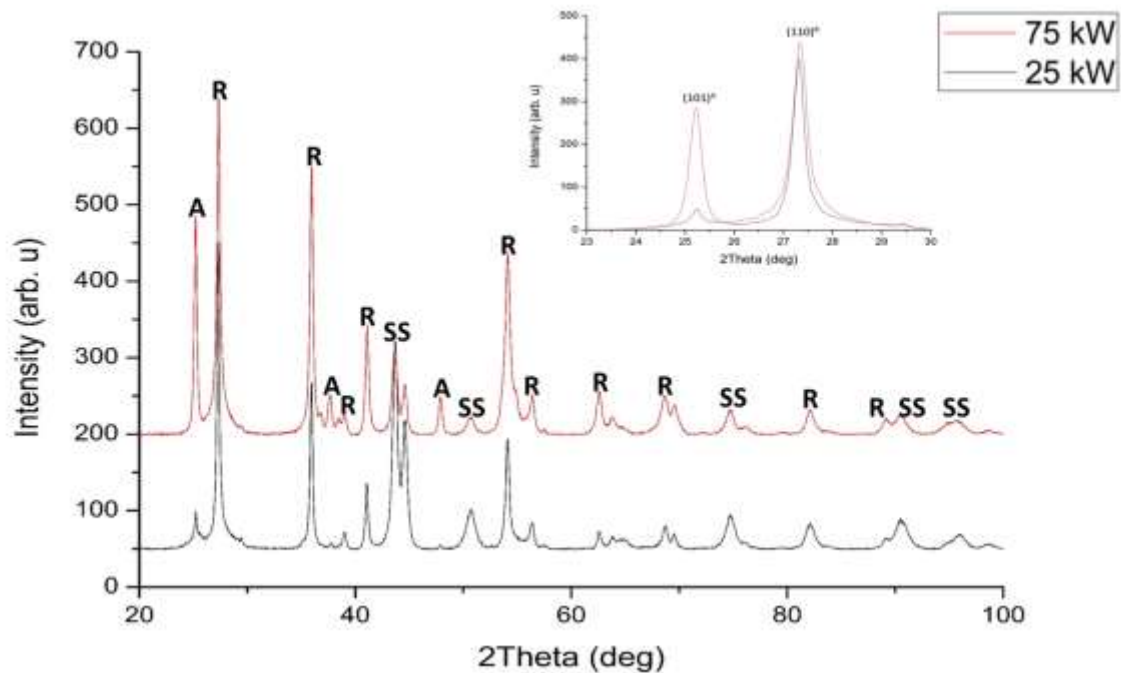


Figure 33: XRD spectra of the coatings deposited at 25 kW (red line) and 75 kW (black line). Each peak has been labelled as corresponding to Nb-TiO<sub>2</sub> rutile phase “R” (PDF card 01-072-7376), TiO<sub>2</sub> anatase phase “A” (PDF card 00-021-1272) and 304 austenite stainless “SS” (PDF card 00-033-0397). The inset shows a detailed view of the two most intense peaks for both rutile and anatase and their corresponding crystal planes

For the peak fitting of the XRD diffraction patterns the star quality PDF entries with reference codes 01-072-7376 (Nb-TiO<sub>2</sub>, rutile phase), 00-021-1272 (TiO<sub>2</sub>, anatase phase) and 00-033-0397 (304 austenite, stainless steel) were used. Unfortunately, no niobium doped anatase XRD diffraction pattern could be found in the database used (PDF-4+ 2018). The XRD spectra already indicates that the 75 kW coating presents a higher content of anatase phase.

Due to the importance of the content of both phases for the physico-chemical properties of the coating, Rietveld refinement was performed, as shown in Figure 34, to obtain the normalised phase content percentage of anatase and rutile.

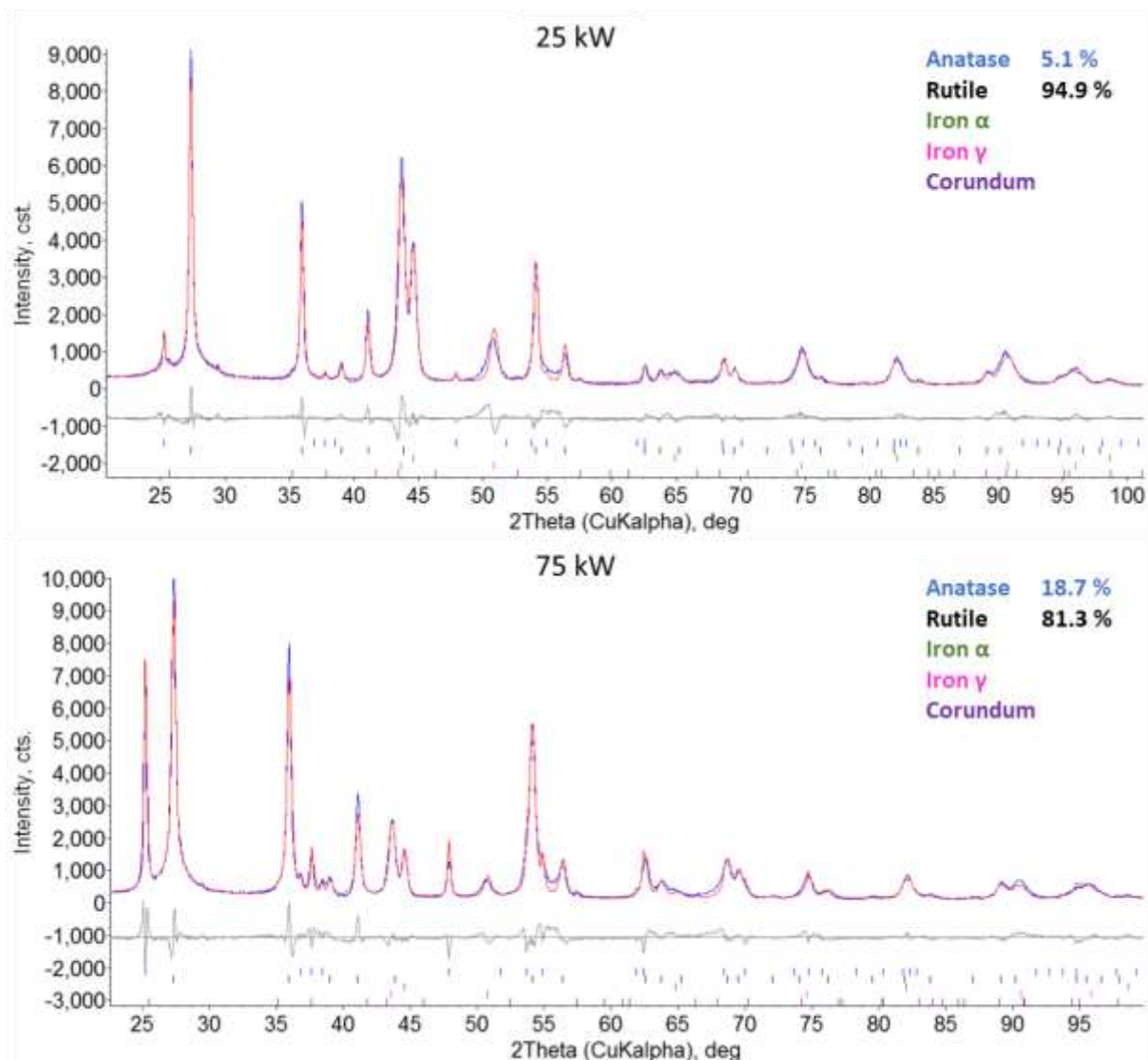


Figure 34: Rietveld refinement of the XRD diffraction patterns with phase quantification

It should be noted that the Rietveld refinement process was carried out including all phases detected in the XRD diffraction patterns: the two titanium phases (anatase and rutile), those associated with the stainless steel substrate (iron  $\alpha$  and iron  $\gamma$ ) as well as a weak signal corresponding to corundum and associated with alumina particles from the grit blasting of the substrate. Since the thickness of the two coatings is not the same, and x-ray penetration on the sample at 25 kW was deemed to be excessive, the values presented in Figure 34 correspond to the normalised values without the substrate contribution. From the results obtained from the Rietveld refinement of both coatings it can be seen that the anatase content increases from 5.1

% to 18.7 % with a higher flame power, while the rutile content decreases from 94.9 % to 81.3 %. Some points should be mentioned regarding the phase content obtained through Rietveld refinement. The process was carried out using the structural values from standard rutile and anatase from ICSD. A slight difference is bound to occur since they correspond to undoped phases. Due to the nature of the niobium doping, entering the titanium oxide structure through substitution of titanium atoms [34], the d101 interplanar spacing in anatase increases [46]. This effect will cause a shift in the position of the anatase XRD peaks that could not be taken into account, since no Nb-doped anatase XRD diffraction could be found in the database used (PDF-4+ 2018). The broadening of the first two anatase and rutile peaks, mentioned in the characterisation section, could be caused by stacking faults in the titanium oxide structure [49] and the presence of some amorphous content.

Both the height and the area of the peaks from the (101) reflection of the anatase phase and the (110) reflection of the rutile phase, shown in the inset in Figure 33, were used to calculate the anatase content of the coatings. The results of all three methods are shown summarised in Figure 35.

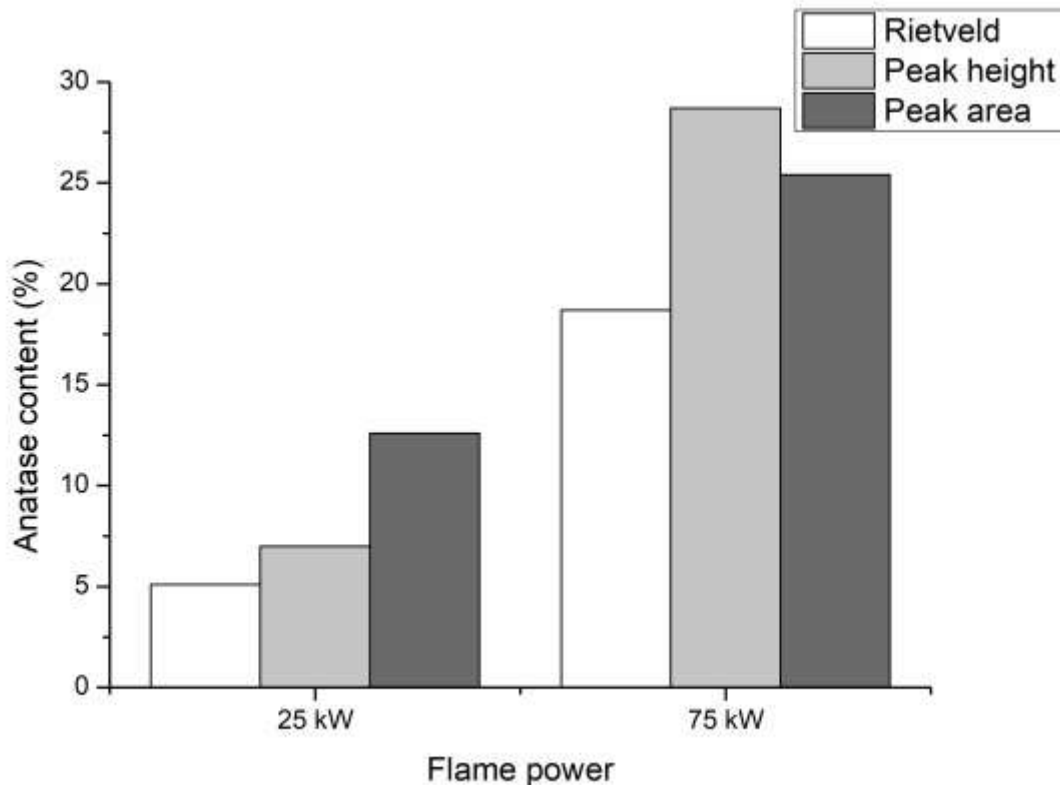


Figure 35: Anatase content of the coatings sprayed at 25 kW (light grey) and 75 kW (dark grey) using three independent methods; Rietveld refinement, peak height and peak area

Although all of the three methods applied in the quantification of the anatase phase have shortcomings, the results shown in Figure 35 clearly indicate that an increase in the flame power results in an increase in the anatase content. This behaviour, contrary to the well-studied anatase-to-rutile phase transformation in titanium oxide at high temperatures [158,167,168], is intriguing. The addition of niobium to titanium oxide hinders the transition from anatase to rutile, which is explained by a reduction in oxygen vacancies when niobium enters substitutionally into  $\text{TiO}_2$  [169]. The reason behind this effect lies in the role of the oxygen vacancies, which act as nucleation sites for the anatase to rutile phase transformation [170]. This feature, that has been exploited to maintain a more favourable phase composition for applications such as sensors [40,41], could be the reason behind the increase in the anatase phase content. However, no evidence or mechanism has been reported that states that the

addition of niobium into titanium oxide causes an alteration in the thermodynamics of the system such that at high temperature the favourable phase transition becomes rutile to anatase. Therefore, the hindering in the anatase to rutile transformation associated with niobium should be considered a reinforcing effect rather than the main reason behind this effect.

A more plausible explanation for this trend would lay in the formation mechanism of the solid content in the coating. At both 25 and 75 kW, the precursor decomposes and forms TiO<sub>2</sub> in-flight. From here, the flame temperature plays an essential role. At 25 kW, the flame temperature is approximately 1880 °C, almost identical to the melting point of TiO<sub>2</sub>. As a consequence, the coating is formed by loosely bounded solid particles formed in-flight, with a mixture of rutile and anatase phases. At 75 kW, the flame temperature rises up to 2480 °C, being enough to melt the material formed in-flight. Due to the presence of air cooling at the substrates during deposition, the liquid droplets experience a high cooling rate upon impact. These conditions favour the nucleation of anatase directly from the molten material, as described by Li and Ishigaki [171], explaining the increase on anatase content.

#### **3.3.4. In-flight transformation**

In order to better understand the in-flight transformation of the solution precursor into solid particles, and consecutively a coating, DSC-TGA analysis was performed to gain insight on the thermodynamic behaviour of the solution. Figure 36 shows the results obtained from the analysis, where both the weight change and the heat flow from room temperature to 1500 °C are presented.

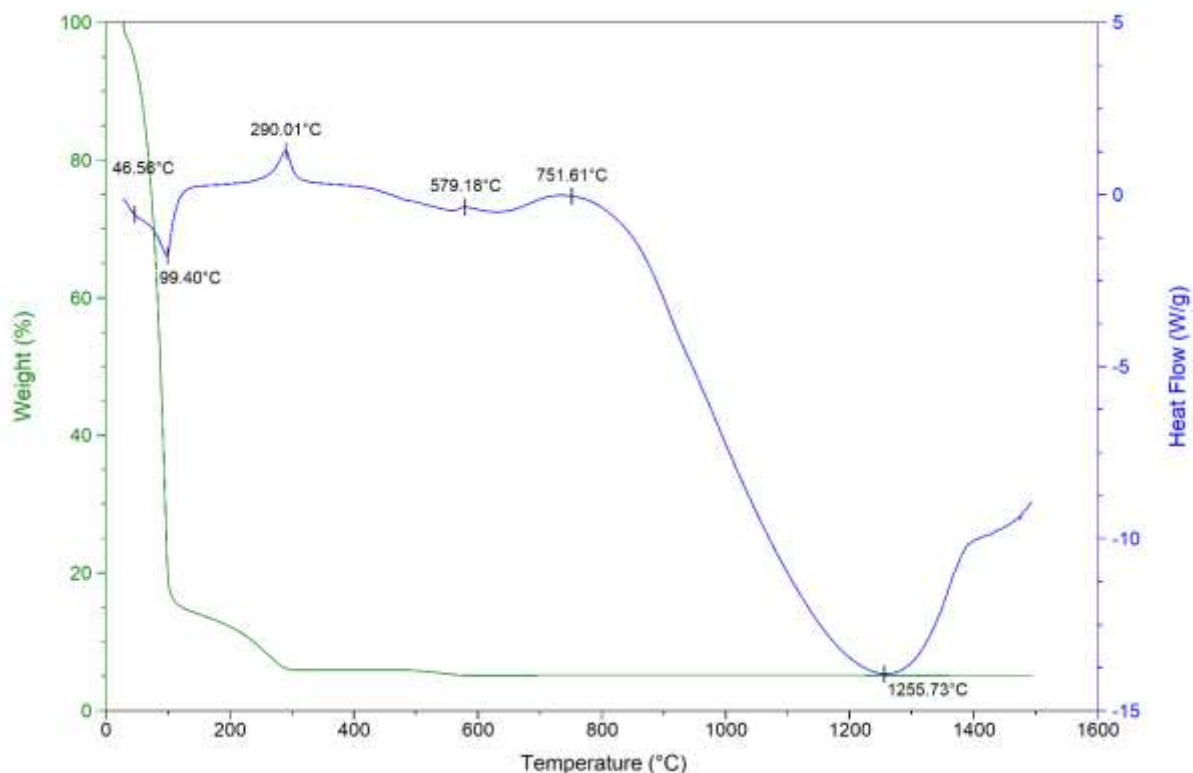


Figure 36: TGA-DSC of the Nb-TiO<sub>2</sub> solution precursor, from room temperature to 1500 °C. The green line represents the weight change in percentage, while the blue shows the heat flow. The temperature of remarkable features in heat flow has been labelled

From the TGA-DSC graph it can be seen that almost 85 % of the weight is lost below 100 °C, which matches the weight proportion correspondent to the solvent. The presence of a sharp endothermic peak at 99 °C also indicates an evaporation process. Within this initial mass loss, two distinctive regions can be seen in the heat flow curve. The first one, with a shallow endothermic peak at 46.56 °C corresponds to the initial, quick evaporation of the medium. The boiling point of 2-isopropoxyethanol is 43 °C at reduced pressure (17 hPa). Due to the standard atmospheric pressure (1013 hPa) used during the TGA-DSC measurements most of the evaporation occurs at a later temperature. The second one, up to 99.40 °C also provides information about the evaporation process. Fleming *et al.* [35] performed dynamic as well as isothermal TGA measurements for the solution precursor used in this work, and found out that temperatures close to 100 °C sustained for as much as 30-35 min were needed to complete the

evaporation of the solvent. This was attributed to a diffusion-limited evaporation process. A further reduction up to 95 % in weight between 100 °C and 300 °C can be seen, ending with a sharp exothermic peak at 290.01 °C. A similar peak was reported by Chen *et al.* [52] on dried precursor titanium oxide powder, being associated with the pyrolysis of the precursor. At 579.18 °C there is another exothermic peak, which matches the end of the detected mass changes by the DSC. The temperature range corresponds to previously reported phase transformation process [51].

From this point on, no distinguishable event can be seen regarding a change in weight. In the case of the heat flow, there are two additional broad peaks present, one exothermic at around 751.61 °C and a final endothermic peak at 1255.73 °C. Since no associated weight change can be detected, the origin of such peaks could be further crystallisation and phase transformation of the remaining titanium oxide dried powder.

To study in detail the pyrolysis and crystallisation of the amorphous Nb-TiO<sub>2</sub>, TGA analysis of the dried solution was performed with a heating rate of 10 °C/min up to 800 °C. The results can be seen in Figure 37.

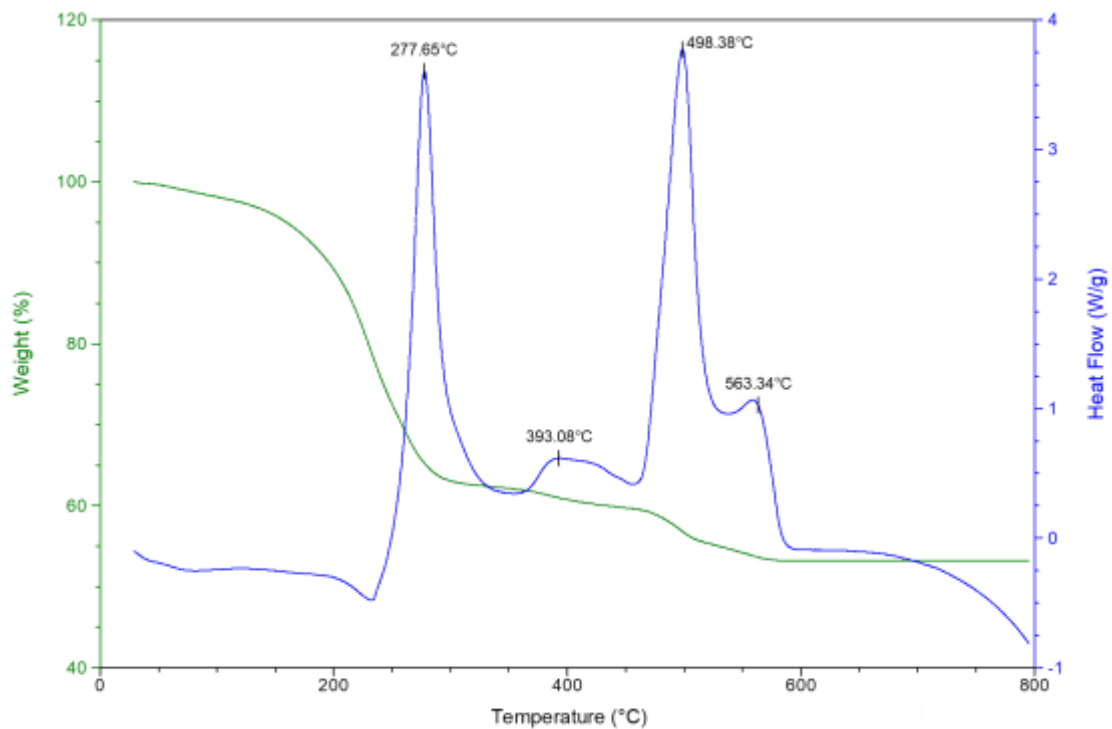
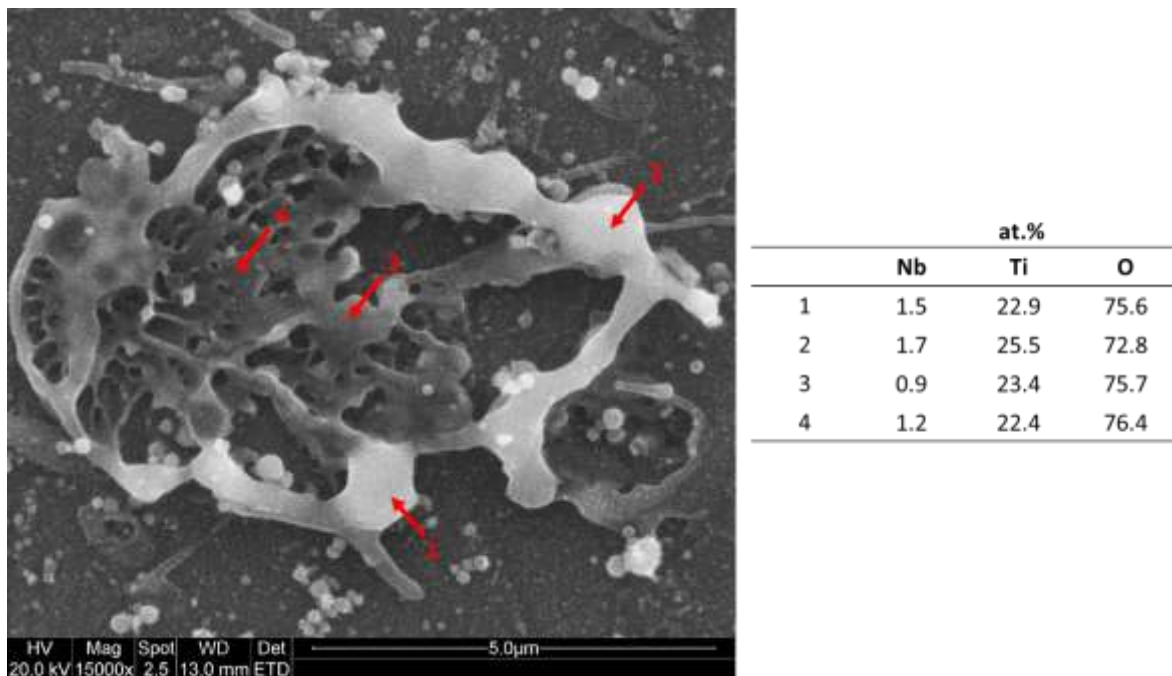


Figure 37: TGA-DSC of the dried Nb-TiO<sub>2</sub> solution precursor, from room temperature to 800 °C

Since the temperature range has been reduced and the thermodynamic contribution of the solvent has been greatly removed, the data in Figure 37 provides a more clear insight into the formation of Nb-doped TiO<sub>2</sub>, its crystallisation and the phase transformation. The first peak, at 277.65 °C, corresponds to the previously identified peak for the pyrolysis of the precursor. The next peak, at 393.08 °C presents a broader aspect, usually associated with a crystallisation process. Nevertheless, the complete crystallisation from amorphous phase takes place at 498.38 °C [52]. The last peak, at 563.34 °C, would correspond to the transformation from anatase to rutile. This anatase to rutile transformation is responsible for the reported trend of increased rutile content with flame power in thermal spraying of powder or suspension feedstock. Nevertheless, when using solution precursor, the solid content must be formed in-flight, adding the possibility of melting in the flame and rapid cooling upon impact with the air cooled substrate, as pointed out for the 75 kW spraying in section 3.3.3 “Phase evolution”.

### 3.3.5. Swipe test

As mentioned in the experimental methods section, swipe tests were performed to study the morphology and presence of single splat at three distinctive stand-off distances: 65 mm, 85 mm and 105 mm. The flame power chosen was 75 kW, as it would ensure enough heat transfer to the solution in order to melt the particles formed in-flight, providing further information on the deposition mechanism. Firstly, the individual splats were analysed to understand their morphology and element composition. To do so, high magnification BSE-SEM images were analysed using EDS to understand the niobium distribution within the splats formed in-flight.



*Figure 38: BSE-SEM image of an individual splat. The arrows mark the points where EDS measurements were performed. The table shows the elemental quantification in atomic weight*

As it can be seen in Figure 38, a liquefied splat has deformed upon impact, while preserving a brighter exterior layer and a darker interior. This difference in brightness is also reflected on the EDS measurements. It should be noticed, however, that the measurements were taken on a non-polished sample, and therefore these values should be used with precaution. Along the four different points measured, the titanium and oxygen contents seem to vary without a very

clear trend, being a potential trend only detected in the case of the niobium content. A qualitative observation can be made combining the increased brightness of the exterior layer on the BSE image, associated with niobium due to the heavier nature of this element, with the suspected increase in niobium shown in the EDS measurements. These results seem to indicate the presence of a supersaturated external layer in the droplet.

The top surface of the substrates, with the produced splats, is shown in Figure 39. Some features can be identified from the images, such as the reduction in deposition efficiency as the stand-off distance is increased. Nevertheless, the surface of the samples at 65 mm is mostly formed by solid particulates with a reduced presence of round, fully molten splats. Such features are more evident at 85 mm, where a mixture of solid particulates and molten splats is present. In the case of stand-off distance of 105 mm, it is considered to be excessive, as the deposition efficiency dramatically drops, without an improvement on the morphological aspect of the splats present. Some fully molten splats are still seen, accompanied by smaller, round particles.

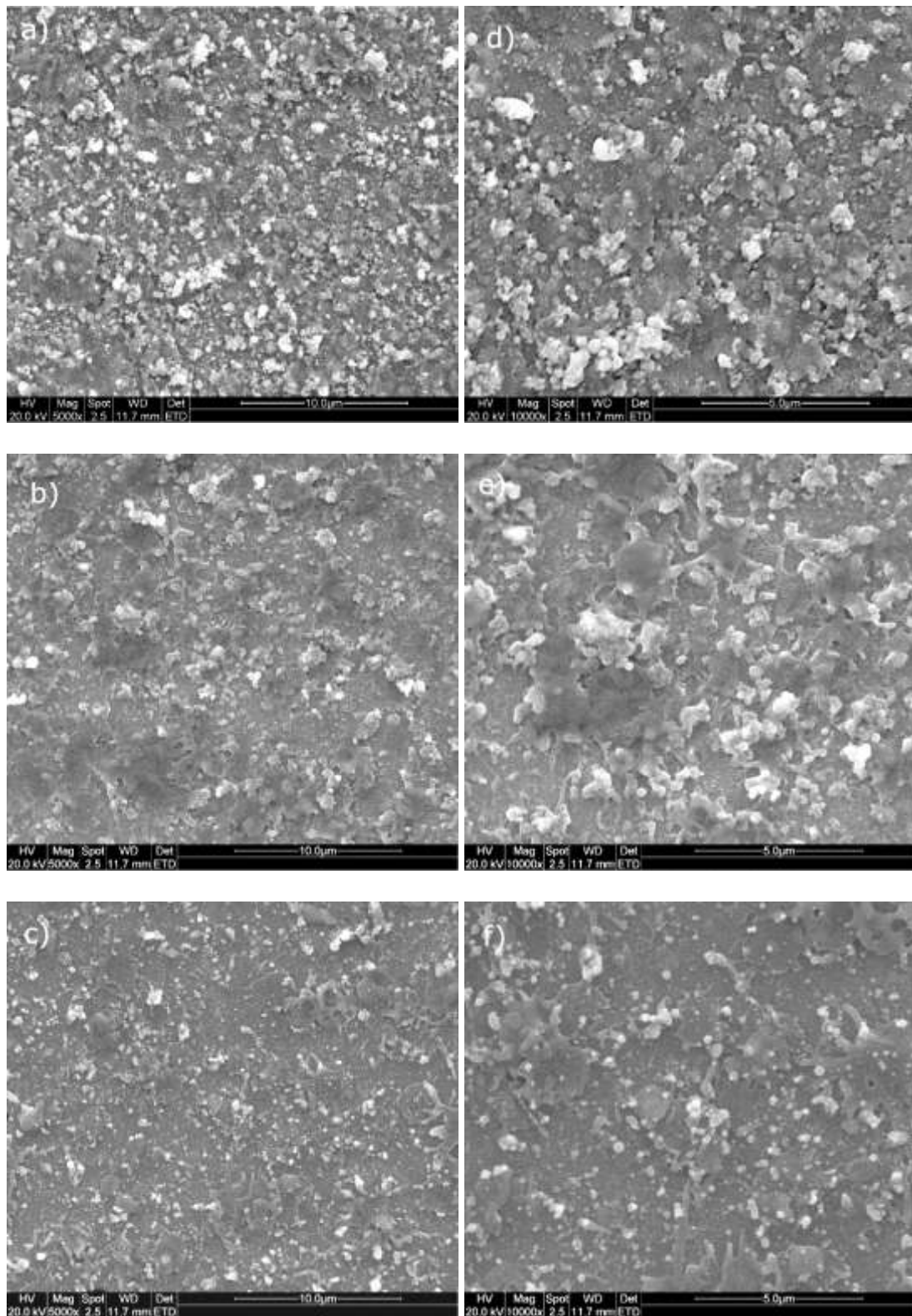


*Figure 39: SE-SEM images of the top surface of the swipe test samples. Images a to c correspond to stand-off distances of 65 mm, 85 mm and 105 mm respectively, being images d to f at high magnification. All images were taken at 20 kV*

These results seem to indicate that in the first stage of the in-flight transformation (evidenced in the samples at 65 mm, Figure 39a) the presence of individual solid particulates is more abundant than fully molten splats, which appear later on. This is due to the pyrolysis and sintering of the solid material formed. A higher content of niobium can be detected on some of the solid material, evidenced by a brighter appearance in the BSE images. The surface of the samples at 85 mm (Figure 39b) shows a higher degree of molten splats, with some agglomerates formed by round, bright particles. Since the solid material has remained longer in the flame, the heat transfer has been higher and more material has been molten. This is also evidenced in a reduction of the bright particles, since the niobium content is now more homogeneously distributed within the molten splats. The size of this splats is also larger than at 65 mm due to the higher viscosity of the heated molten material. As the material travels further down the flame, the amount of molten splats and their size is reduced, as it can be seen in the samples at 105 mm (Figure 39c), indicating an additional tertiary fragmentation process. The amount of solid material is also reduced, which could be attributed to the re-melting of the agglomerates and the reduced deposition efficiency at larger stand-off distances.

From the SEM images in Figure 39, it can be extracted that the amount of bright, nanosized particles is reduced as the solution precursor travels along the flame. On the other hand, the amount of molten material with relation to the solid particles increases with increased stand-off distance. This effect is partially due to the reduced deposition efficiency at larger stand-off distances; however the proportion of solid particles to molten material provides information of the physical transformation of the precursor.

### **3.3.6. Deposition mechanisms of Nb-TiO<sub>2</sub> particles**

A proposed model for the physical transformation that takes place once the solution precursor is injected into the system is here presented, being schematically depicted in Figure 40. The

collection of SE/BSE-SEM images from both the coatings deposited and the swipe test samples was extensively examined, taking into account the various spraying conditions, to come up with a model to show the different stages of the process and the diversity of the splats structures. In the figure, the central schematic shows the proposed model, while the SE-SEM images around it exemplify the features shown. Figure 40a (top surface of the coating, 75 kW) shows the bright dots of the solid phase condensation, as marked with red arrows. Figure 40b (swipe test, 105 mm) shows an individual splat where the supersaturated exterior is visible. Figure 40c (swipe test, 65 mm) represents a crater on the surface. Figure 40d (swipe test, 65 mm) shows the presence of an agglomerate with a solid core, marked with a red circle. In Figure 40e (swipe test, 65 mm) it can be seen an agglomerate formed by smaller, round particles. Figure 40f (swipe test, 105 mm) represents a partially molten agglomerate. Figure 40g (swipe test, 105 mm) shows an individual, fully molten splat.

The model has been developed based on the observations from the SEM images of both the cross section from coatings at different flame power and the top surface after the swipe test, and the previous reports found in the literature [27,56,172].

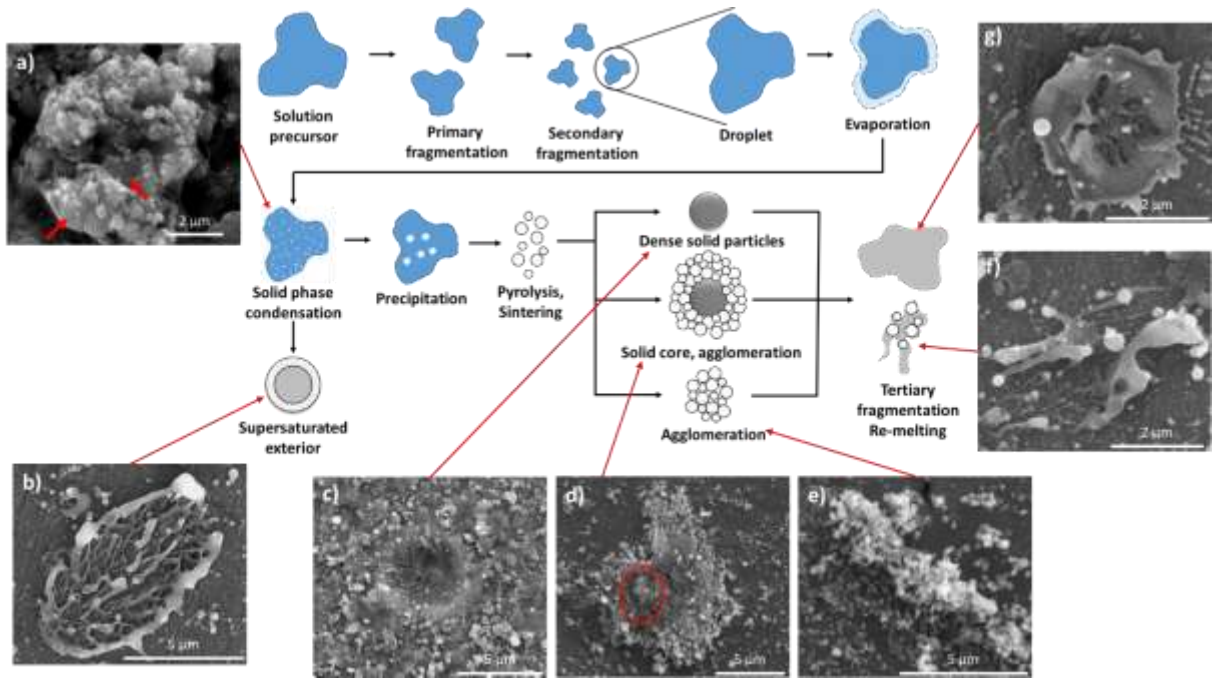


Figure 40: Schematic diagram of the single splat formation in solution precursor HVOF of niobium doped titanium oxide. SE-SEM images correspond to the features explained in the model

In the schematic the process starts when the initial solution precursor is injected into the modified combustion chamber, experiencing primary fragmentation near or at the injector exit. In the case of axial injection, the presence of an annular gaseous stream surrounding the liquid jet produces a breakup into droplets due to the difference in the average velocity of the gas and the liquid [173]. The specific dynamic behaviour is influenced by the dimensionless values of the Weber number ( $We$ ) and the Reynolds number ( $Re$ ), being defined as:

$$We = \frac{\rho v_{rel}^2 d}{\sigma} \quad (11)$$

$$Re = \frac{\rho v_{rel} d}{\mu} \quad (12)$$

Where  $\rho$  is the density of the solution,  $v_{rel}$  is the initial relative velocity between ambient and drop,  $d$  is the initial diameter,  $\sigma$  is the surface tension and  $\mu$  is the dynamic viscosity. These two quantities provide a quantification of the ratio of the fluid inertia to the surface tension ( $We$  number) and the ratio of the fluid inertia to viscosity ( $Re$  number).

Once the mixture of solution precursor and gases comes out through the nozzle, entering the HVOF flame, the droplets experience a secondary fragmentation into smaller structures due to shear deformation from the drag forces [172,174]. This process determines the final size of the droplets, being therefore crucial for the differentiation between the various morphologies, as illustrated in Figure 41. In this case, the  $We$  number is the one mostly responsible for the changes in morphology, as an increase in its value causes the droplets to experience a different secondary fragmentation from Figure 41, being the first morphology associated with lower  $We$  number and the last with higher values.

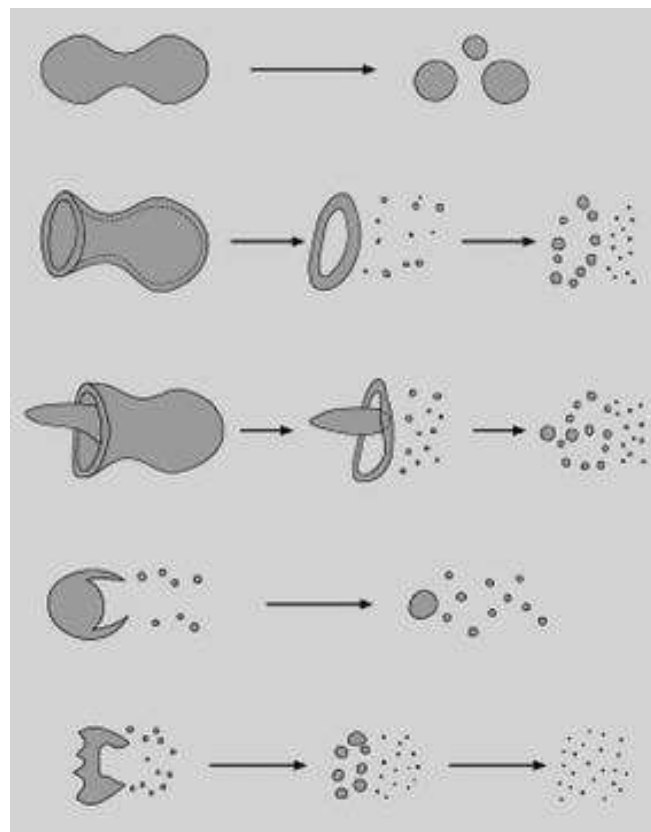


Figure 41: Newtonian drop breakup morphologies [174]

The interfacial tensions and viscous forces counteract the effect of the drag forces, being this equilibrium summarised in the dimensionless Ohnesorge number ( $Oh$ ), defined as:

$$Oh = \frac{\mu}{\sqrt{\rho d \sigma}} \quad (13)$$

Fragmentation is favoured with an increase of the Weber number, occurring the opposite effect as the value of  $Oh$  increases [173].

Due to the elevated temperature of the flame, the solvent starts to evaporate, further reducing the size of the droplets and creating vapours within the flame. Due to the continuous heat transfer from the flame, inside the droplets starts the appearance of a condensed solid phase. This solid phase, present as bright dots within deposited splats visible only at high magnification (visible in Figure 40a, marked with arrows), was confirmed to be niobium-rich phases through energy-dispersive x-ray spectroscopy. The increased niobium content was caused by the segregation of the substitutional niobium present in the lattice of the bulk material [169,175] when exposed to high temperatures.

From the first appearance of the solid phase, two phenomena can occur. If the rate of solvent vaporisation is greater than the diffusion of the solute, a supersaturated external layer will appear surrounding the molten material, as seen in Figure 40b, and confirmed by EDS measurements on the swipe test section. In the opposite case, the condensed phases diffuse to form precipitates. This route starts with the formation of precipitates, which is followed by pyrolysis and sintering, where three morphologies can arise depending on the conditions experienced in-flight by the droplet. In the first case, if a small droplet experiences a low heat rate, a dense solid particle will form. The presence of such solid particles has been observed indirectly, as the surface of some samples from the swipe test at stand-off distance of 65 mm showed multitude of craters such as the one see in Figure 40c, indicating the impact of solid material of micrometric size. The lack of evidence for the presence of solid features on samples with larger stand-off distances indicates that these particles either lose most of its kinetic energy after traveling 65 mm, not creating craters upon impact, or they melt when traveling longer distances. Another possibility arises if the size of the initial droplets is larger or they experience higher heating rates. In this case, the formation of agglomerates of round particles will be

favoured, being an example shown in Figure 40e. These agglomerated structures were more common than the craters from solid material, which provides information on the conditions of the flame and the primary and secondary fragmentation, seemingly favouring large droplets and/or higher heating rates. A third option, with characteristics in between the two previous structures was also identified and can be seen in Figure 40d. In this case, a large agglomerate possesses a solid core, marked with a circle on the BSE-SEM image. The final possible stage of the deposition process takes place when the agglomerates break up into smaller fragments, or if they never reach the critical size to endure the trajectory within the flame without re-melting, as exemplified by the images on Figure 40f and Figure 40g.

### **3.4. Conclusions**

The SP-HVOF deposition technique was used to produce niobium-doped titanium oxide coatings for the first time. The results show that the flame power, chosen in this study to be 25 kW and 75 kW, has critical implications on the microstructural features and phase content of the produced coatings. The effects observed were:

- Flame power was proven an effective way to modify the microstructure of the deposited coatings. Low flame powers induced the sintering of solid material but failed to melt them, producing a coating with porous structure. Higher flame power allows the melting of the solid particles, leading to a lower porosity.
- Three calculation methods confirmed that an increase in flame power equated to an increase in the anatase phase content. This behaviour is believed to be caused by the presence of doped niobium, which hinders the anatase to rutile phase transformation, and the complete melting of the solid content formed in-flight at 75 kW, promoting the anatase phase content.

- In addition to the flame power, three stand-off distances (65, 85 and 105 mm) were used to collect single splats following a swipe test. The features present, as well as the morphologies discovered, were the base for the development of a model of the physico-chemical transformations that the solution precursor experiences. As a summary, in the initial section of the flame, solid content is formed, with limited presence of molten material. As the solution precursor travels further, the amount of solid content is reduced, and it is mostly localised as agglomerates, while fully molten material is seen. In the final section of the flame, the fully molten material experiences a tertiary fragmentation, creating droplets of smaller size, while the solid agglomerates are partially molten, further reducing the amount of solid particles present.

### **3.5. Acknowledgements**

This work was supported by the Engineering and Physical Sciences Research Council (grant number EP/L016206/1). The authors would like to thank Rory Scream and John Kirk for their assistance during the SP-HVOF spray, Sunil Chadha for the computational simulations of the flame temperature and his input on droplet fragmentation, EpiValence Ltd. for providing the solution precursor and to the Nanoscale and Microscale Research Centre (nmRC) at the University of Nottingham for providing access to microscopy facilities.

## **Chapter 4: Evolution of Porosity in Suspension Thermal Sprayed YSZ Thermal Barrier Coatings through Neutron Scattering and Image Analysis Techniques**

The main body of this section is reproduced from the paper:

*D. Tejero-Martin, M. Bai, J. Mata, T. Hussain, Evolution of porosity in suspension thermal sprayed YSZ thermal barrier coatings through neutron scattering and image analysis techniques, J. Eur. Ceram. Soc. 41 (2021) 6035–6048.*

<https://doi.org/10.1016/j.jeurceramsoc.2021.04.020>

### **Abstract**

Porosity is a key parameter on thermal barrier coatings, directly influencing thermal conductivity and strain tolerance. Suspension high velocity oxy-fuel (SHVOF) thermal spraying enables the use of sub-micron particles, increasing control over porosity and introducing nano-sized pores. Neutron scattering is capable of studying porosity with radii between 1 nm and 10  $\mu\text{m}$ , thanks to the combination of small-angle and ultra-small-angle neutron scattering. Image analysis allows for the study of porosity with radii above  $\sim 100$  nm. For the first time in SHVOF 8YSZ, pore size distribution, total porosity and pore morphology were studied to determine the effects of heat treatment. X-ray diffraction and micro-hardness measurements were performed to study the phase transformation, and its effects on the mechanical properties. The results show an abundant presence of nano-pores in the as-sprayed coatings, which are eliminated after heat treatment at 1100  $^{\circ}\text{C}$ ; a transition from inter-splat lamellar to globular pores and the appearance of micro-cracks along with the accumulation of micro-strains associated with the phase transformation at 1200  $^{\circ}\text{C}$ .

## 4.1. Introduction

Yttria-stabilised zirconia (YSZ) currently represents the most used material within thermal barrier coatings (TBC) for gas turbine engine components [3,6]. The main goal of a successful TBC is to provide insulation to the substrate underneath, effectively reducing the experienced temperature and avoiding component degradation due to excessive surface temperature. 8YSZ presents a low thermal conductivity (0.7 – 1.4 W/mK for coatings), good thermal stability (within its temperature application range) and a coefficient of thermal expansion (CTE) close to that of the commonly used Ni-based superalloys ( $\sim 11 \times 10^{-6} \text{ K}^{-1}$  for 8YSZ coatings and  $\sim 14 \times 10^{-6} \text{ K}^{-1}$  for the Ni-based superalloys) [176], making it a sound choice for a TBC topcoat. In addition to its inherent properties, a successful 8YSZ TBC must present a favourable microstructure, in terms of porosity and micro-cracking [177]. For instance, coatings produced using electron-beam physical vapour deposition (EB-PVD) present columnar structure, leading to higher thermal conductivity values, but improved strain tolerance and thermal shock resistance. When atmospheric plasma spraying (APS) is used, the coatings present a splat-based layered structure, with the advantage of a reduced thermal conductivity and production costs when compared to EB-PVD.

Even within APS deposited coatings, the variation of the amount of total porosity and pore size distribution has an effect on the thermomechanical properties of the system, directly affecting properties such as the hardness [178] and the accumulation of thermal stresses [179]. The pore size in a typical APS deposited coating has radii between 0.02 and 1  $\mu\text{m}$  [6]. An increase in the total porosity correlates with a reduction in the density of vertical cracks [180] (also known as segmentation cracks, responsible for an increase in thermal conductivity [181]), a reduction of the residual compression stresses [182]. Thermal insulation in YSZ, at service temperatures of  $\sim 1200 \text{ }^\circ\text{C}$ , is improved by phonon scattering at inhomogeneities (grain boundaries, pores and vacancies) [183]. More porosity provides more scattering sites, effectively lowering the

thermal conductivity of the coating. It is clear then, that a more precise control over the porosity present within the as-deposited coating is desirable when manufacturing TBCs with enhanced properties and performance. Since the porosity in thermal sprayed coatings is strongly correlated to the size distribution of the feedstock particles, mostly due to unmelted feedstock particles and gaps in between adjacent splats [58], there has been a growing interest for sub-micron feedstock particle distribution. Such a reduction in size allows finer grains, higher strength and durability, reduced porosity sizes [184] and enhances the thermal and mechanical properties of the coating [179,185].

Despite the potential shown by the use of nanostructured YSZ powders, APS deposited coatings present a lower limit on the feedstock particle size of around 10 – 100  $\mu\text{m}$  [18,19] to ensure adequate flowability. Aiming to circumvent this issue, suspension thermal spray was developed, where the feedstock material is presented with a size that can be below 1  $\mu\text{m}$  and dispersed in a liquid medium (generally water or ethanol) allowing the use of particles with a smaller size. Such approach has led to the development of novel thermal spraying deposition techniques such as suspension plasma spray (SPS) or suspension high velocity oxy-fuel spray (SHVOF). Suspension thermal spray techniques have been successfully applied to the deposition of YSZ coatings [186], with special focus on the effects on the physical and thermal properties of the deposited coatings [187]. SHVOF thermal spray has been reported in the past as the deposition technique for 8YSZ [184], with higher thermal conductivities than coatings produced using SPS due to the presence of vertical cracks. Nevertheless, we demonstrated that SHVOF thermal spray can be used to deposit crack-free coatings, with the porosity being variable depending on the spraying parameters and suspension medium used [162]. Despite these promising results, no thorough investigation on the porosity of SHVOF thermal sprayed 8YSZ coatings has been reported, particularly aiming at the study of nano-porosity and the microstructural evolution at service temperatures.

Due to the nature of the environment to which TBCs are exposed during service, where temperatures of 1200 °C are expected, the deposited coating will experience several heat-induced phenomena. Microstructural changes are to be expected, such as coalescence of pores (coarsening) or closure of pores (sintering) as well as the appearance of micro-cracks, having a direct impact on the thermal conductivity of the coating. The importance of a deep understanding of the evolution that the porosity on thermal sprayed TBCs undergoes during heat treatment is evidenced by the abundant literature in the topic [162,183,187–193]. Despite the recognised importance and the essential role that porosity plays in TBCs, accurate measurement of the porosity remains a challenging task that should be approached carefully. A plethora of techniques have been developed over the years to measure porosity, with each one of them having its own set of advantages and disadvantages, which should be considered when performing the measurements. One of the key factors is the measurable pore size range of the technique. Scanning electron microscopy (SEM) image analysis is a commonly used technique for the determination of the porosity on thermal sprayed coatings [63], but it is limited to features with a size above ~100 nm [194,195]. Such size limit is inadequate for the study of suspension thermal sprayed coatings, containing pores with radii below 10 nm [196]. X-ray/neutron scattering techniques have already been reported to be effective for the measurement of porosity, both in different materials as here presented [197,198] and in YSZ coatings [199–203]. Such techniques offer access to a wide range of size pores, particularly if the ultra-small-angle variations is combined with small angle, allowing pores with a radii ~1 nm to ~ 20 µm to be studied [204,205].

In this work, a comprehensive study of the evolution of porosity on SHVOF thermal sprayed 8YSZ coatings during heat treatment at 1100 °C, 1200 °C, 1300 °C and 1400 °C for 72 h is presented. Pore size distribution and total porosity were measured using neutron scattering techniques (SANS and USANS) and image analysis (IA). To further understand the effects of

porosity, phase composition and micro-hardness were measured and correlated to the pore size distribution and total porosity measured.

## **4.2. Experimental methods**

### **4.2.1. Materials and coating deposition**

Two commercially available 8YSZ ethanol-based suspension were used in this study, one supplied by Oerlikon Metco (Pfäffikon, Switzerland) being referred to as O-YSZ here, and the other one supplied by Treibacher Industrie AG, (Althofen, Austria), being referred to as T-YSZ. To avoid differences arising from the yttria content or solid content of the suspension, both suspensions had an 8 wt.% yttria content and the solid content of the suspension was 25 wt.% as supplied by the manufacturers. Particle size distribution (PSD) for both suspensions had very similar values, as stated by the manufacturers. O-YSZ had a  $d_{90}$  value of 0.8 – 2.0  $\mu\text{m}$ ,  $d_{50}$  value of 0.3 – 1.0  $\mu\text{m}$  and  $d_{10}$  value of  $\sim 0.1$   $\mu\text{m}$ . T-YSZ had a  $d_{90}$  value of 1.32  $\mu\text{m}$ ,  $d_{50}$  value of 0.60  $\mu\text{m}$  and  $d_{10}$  value of 0.26  $\mu\text{m}$ . In addition, each manufacturer adds a number of undisclosed proprietary additives to improve flow and stability of the suspension, which affects the deposition process and therefore, the microstructure of the as-deposited samples.

The coatings were deposited using a modified GTV TopGun HVOF thermal spray system with direct injection of suspension at the centre of the gas mixing block. The injector had a diameter of 0.3 mm, the length of the combustion chamber was 22 mm and a 110 mm long barrel nozzle was used. A detailed description of the setup can be found elsewhere [12] and in the section “Appendix”, page 209. The suspensions were homogenised for at least 2 hours prior to the spraying using a roller mixer and sealed containers to avoid evaporation of the ethanol. Further homogenisation was provided through the spraying via a mechanical stirrer in the pressurised vessel. Mild steel substrates with dimensions of  $60 \times 25 \times 2$  mm<sup>3</sup> were used, being attached to a carousel with a diameter of 260 mm, a rotation speed of 73 rpm and the gun traverse speed

being set to 5 mm/s, corresponding to a surface speed of 1 mm/s, with a stand-off distance of 85 mm. 40 passes of the gun were completed to deposit the coatings with a thickness of approximately 150  $\mu\text{m}$ . The hydrogen flow rate used for the deposition of both suspensions was 700 l/min and the oxygen flow rate was 300 l/min, providing a theoretical flame power of 99 kW. Before spraying, the substrates were subjected to grit blasting with a blast cleaner (Guyson, UK) using fine F100 brown alumina (0.125 – 0.149 mm) particles at 3 bar. Following grit blasting the substrates were cleaned in industrial methylated spirit using an ultrasonic bath for up to 10 min and dried with compressed air.

Free-standing coatings were produced submerging the coated mild steel substrate in HCl 37 wt.% for 2 – 4 hours, until the coating detached from the substrate. The produced free-standing coatings were subjected to heat treatment using an Elite Thermal Systems Ltd. (Leicestershire, UK) BRF14/5 box furnace at temperatures of 1100 °C, 1200 °C, 1300 °C and 1400 °C, with a heating rate of 10 °C/min in air for 72 h. Once the heat treatments were finished, the samples were allowed to cool down inside the furnace to prevent drastic temperature drops that would induce stresses. Several fragments of the free-standing coatings were placed in the neutron scattering demountable cells, avoiding overlapping of samples to provide uniform sample thickness. This full coverage of the sample provides a good scattering cross section to allow good overlapping of SANS and USANS data. The area measured corresponded to a circle with a diameter of 20 mm for SANS and 40 mm for USANS.

#### **4.2.2. Neutron scattering**

SANS and USANS measurements were performed on free-standing samples using the QUOKKA [206] and KOOKABURRA [207] instruments, respectively, at the Australia's Nuclear Science and Technology Organisation (ANSTO) using the OPAL reactor (Sydney, Australia). For the SANS measurements, an incident neutron beam with wavelengths of 5 Å

and 8.1 Å ( $\Delta\lambda/\lambda = 10\%$ ) were used, with sample-to-detector distance of 1.3 m, 12 m, 20 m (with focussing lens optics in the latter case). The acquired data was corrected for sample transmission, empty cell scattering, detector sensitivity and background scattering. The corrected data was scaled to absolute intensities by comparison to empty beam flux using a package of macros in Igor software (Wavemetric, USA) modified to accept data files from QUOKKA and KOOKABURRA. USANS measurements were carried out using an incident neutron beam with a wavelength of  $\lambda_{\text{Si}(311)} = 2.37 \text{ \AA}$  ( $\Delta\lambda/\lambda = 4\%$ ). An empty cell as a background was subtracted from the USANS data. The USANS data were then desmeared and merged with SANS data. The modelling was done using the SASfit software [208], version 0.94.10. It follows a non-linear least square fitting routine. Spherical shape of the pores and normal Gaussian size distribution for the diameter were assumed for the data analysis. Raw data included the uncertainty of each data point, showing typical values of  $\sim 0.5 - 3.5 \%$  for low scattering angles and  $\sim 10 - 20\%$  for high scattering angles. Due to the data analysis procedure, uncertainty in the raw data did not translate into uncertainty on the obtained volume distribution or total porosity. More details of the neutron scattering techniques and the consequent data analysis is presented in section 4.6 “Appendix A”.

#### **4.2.3. Material characterisation**

Cross-sections of the coatings were prepared by cold mounting a free-standing coating using EpoFix resin and hardener (Struers, Denmark) and cure it for 24 hours. The mounted free-standing was then ground and polished to a 1  $\mu\text{m}$  finish using SiC grinding papers (Buehler, Germany). For the SEM images a Quanta 600 (FEI Europe, Netherlands) scanning electron microscope was used to image the cross-section of the free-standing coatings using backscattered electron (BSE) mode. Imaging parameters were kept constant, with an accelerating voltage of 15 kV, a spot size of 3 and a working distance of 10 mm. A magnification of 1500 $\times$  was used for the IA, taking 5 images on different regions of the coating

which contained representative porosity. The magnification was chosen as a balance between the need to encompass sufficient microstructural features, allowing for valid averaging results, while obtaining high enough resolution to capture detailed features. Due to the brittle nature of the free-standing coatings, macroscopic cracks appeared during the handling of the samples. These “handling cracks” were not included in the SEM images taken for IA; however, neutron scattering does not have the ability to avoid such features. The effect that these “handling cracks” might have in the neutron scattering data is expected to be low, as cracks have lower interfacial surface than pores, lowering its contribution to the scattering.

Phase determination was carried out using a D8 Advance Da Vinci diffractometer (Bruker, Germany) with Cu cathode (wavelength of 1.5406 Å) using transmission mode on free-standing coatings. The angular range investigated was from 20° to 90° for the complete spectra, and from 72° to 76° for detailed measurements. Step size was set to 0.02° and dwell time was 1 s for all the measurements. Rietveld refinement (TOPAS v4.2 software package) was used to determine the  $c/av^2$  parameter, where  $c$  and  $a$  are the unit cell dimensions. Quantitative Rietveld refinement was employed to determine the quantity of each phase ( $t$ -,  $t'$ - and  $c$ -phase), and principles of whole powder pattern modelling (WPPM) were used for crystallite size and micro-strain calculations [209–211]. Micro-hardness measurements were performed on the cold mounted, polished cross-sections using a Vickers micro-hardness indenter (Buehler, USA) using a load of 200 gf and a dwell time of 10 s. Five indentations, approximately in the middle of the cross section and sufficiently spaced in between them were measured to calculate the micro-hardness value, being the error calculated as the standard deviation.

#### **4.2.4. Image analysis**

Five SEM-BSE images were taken at different areas of the centre of cross-section of the coating. All five images per sample were analysed using the open source software ImageJ with

the image processing package “Fiji” [212]. A macro was written for the batch preparation of the images. The macro was written so that first it would set the appropriate scale bar and remove the data bar from the image, then setting a specified threshold converting the image into a binary black and white map, as it is exemplified in Figure 42. It should be noted that the threshold was manually chosen for each set of images after visual inspection of the SEM-BSE images in order to maximise the porosity detected while maintaining noise to a minimum, as indicated by the corresponding ASTM E2109-01 standard [64]. The white and black map was then analysed to measure first the area covered with pores with a size above a determined minimum size to provide the total porosity of the coating. This cut-off minimum size was chosen to filter out single pixel instances, associated with noise rather than physical pores. Then, the area of each individual pore detected in the white and black map was measured and the distribution of all the values was calculated within ImageJ manually setting the size of the bin to  $0.008 \mu\text{m}^2$ . The frequency for each bin was averaged using the value from each of the five SEM-BSE images, being the standard deviation calculated as well. From the area, the radius of the equivalent sphere was calculated. Although not all the pores are expected to be perfect spheres, this criterion was chosen since a similar assumption was made in the analysis of the neutron scattering data.

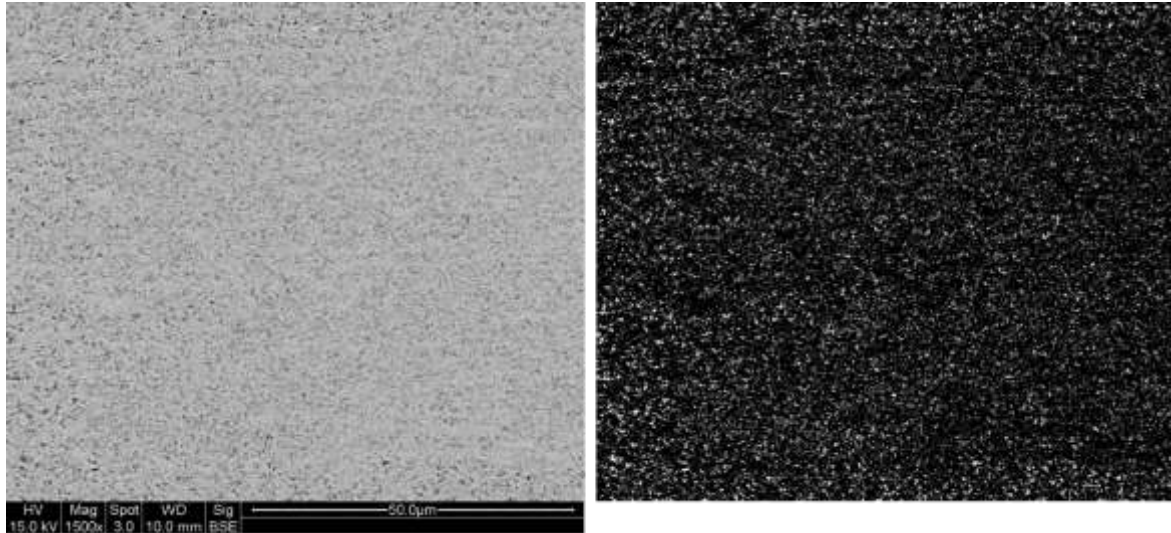


*Figure 42: On the left, one of the SEM images used in this work for the measurement of porosity using IA. On the right, binary black and white mask produced following the protocol described*

### **4.3. Results**

#### **4.3.1. Porosity measurements**

As outlined in the Introduction, the pore size measurable is determined by the technique chosen to measure the porosity. The main purpose of this work is to present a comprehensive study of the evolution of the porosity over a wide pore radii range using neutron scattering and IA. It is evident from the results that the combination of SANS and USANS allows the study of pores with a radius between  $\sim 1$  nm and  $\sim 10$   $\mu\text{m}$ , effectively encompassing the nano-sized features expected from suspension thermal spray and traditional micron-sized features. The overall response to a heat treatment process was in the two samples a striking modification of both the pore volume distribution profile and the total porosity present. Figure 43 presents the information extracted from the neutron scattering data after modelling, where the volume distribution of the porosity present within each coating is shown.

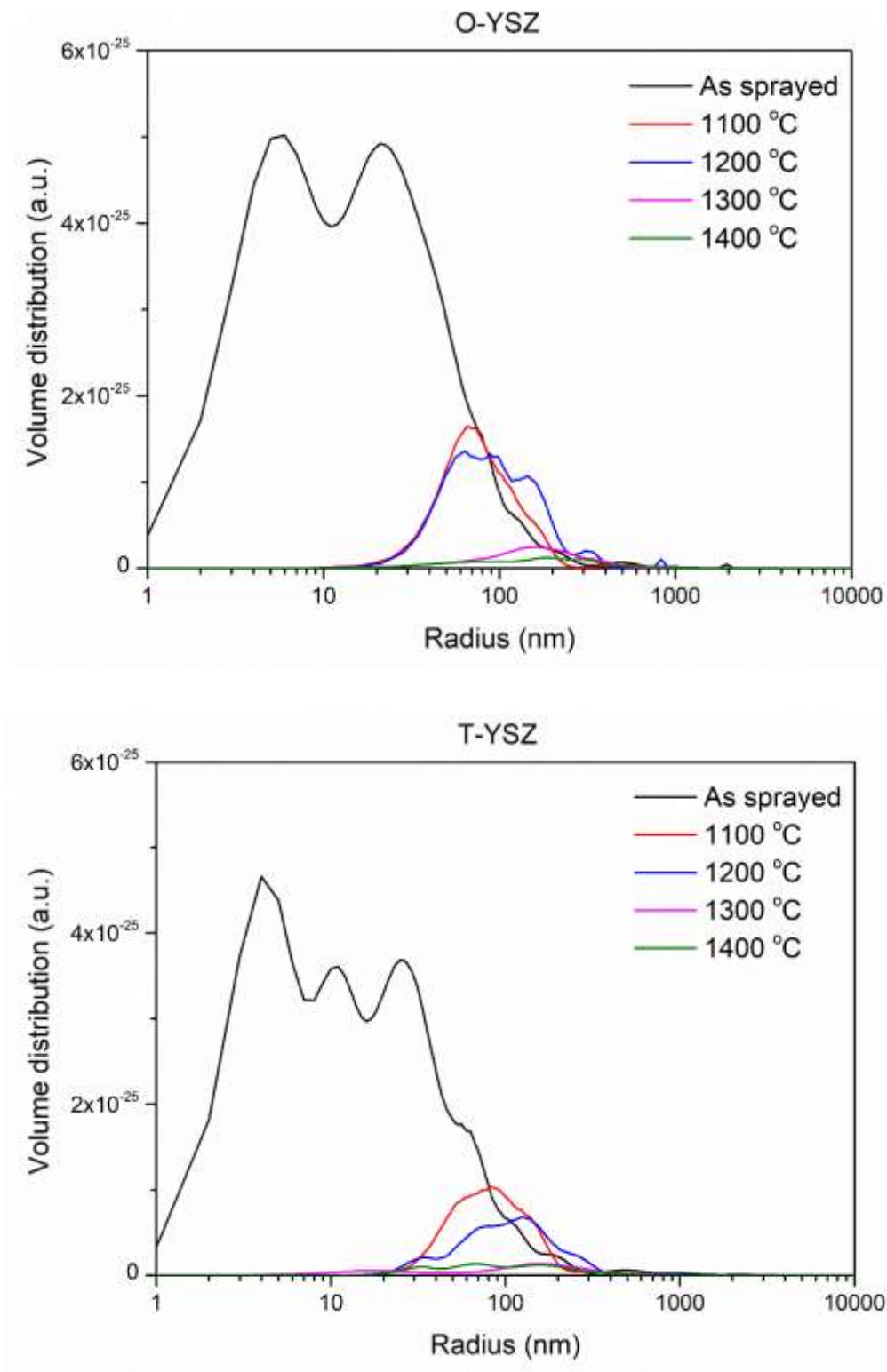
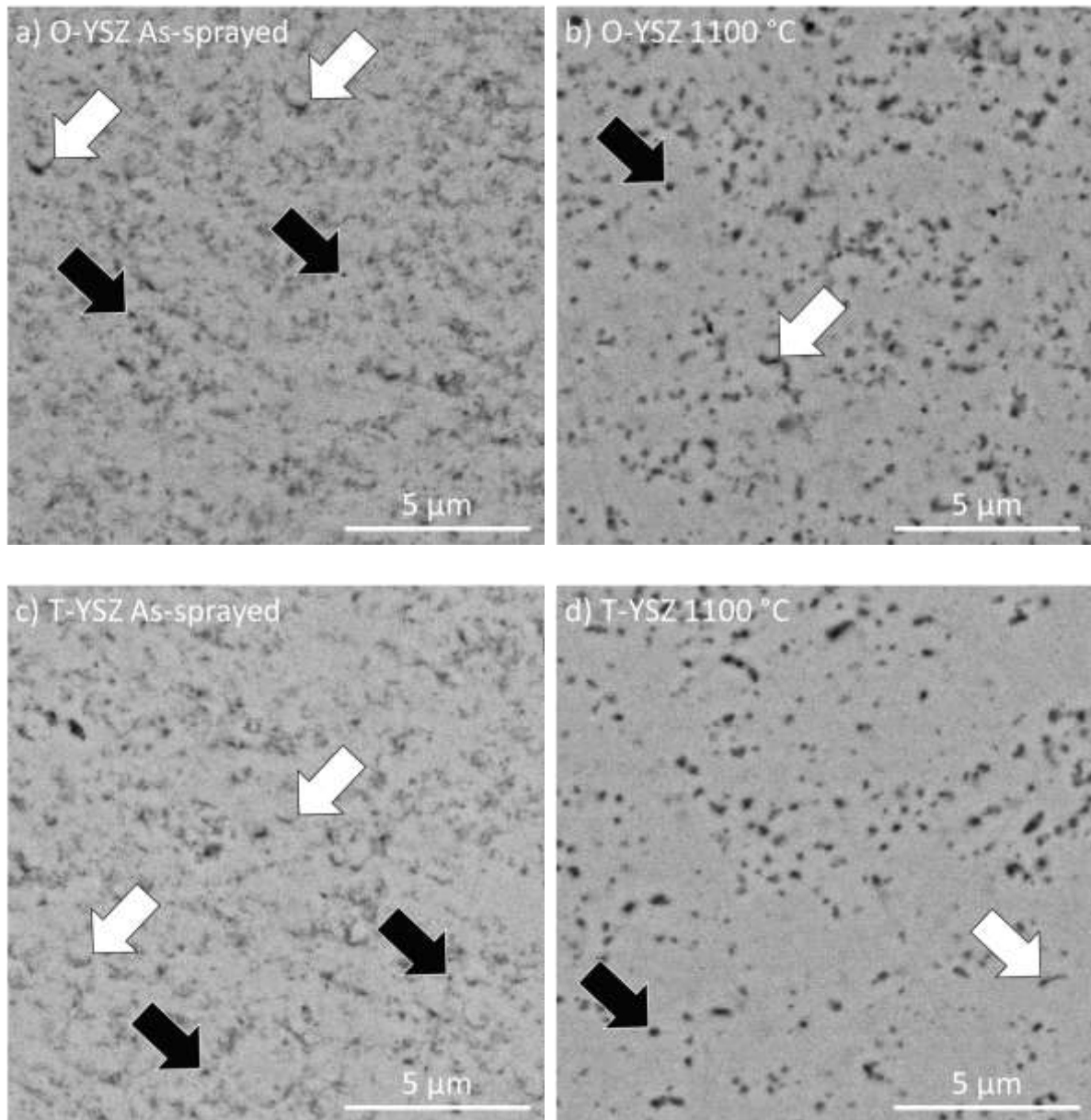


Figure 43: Volume distribution of the porosity of O-YSZ and T-YSZ coatings in as-sprayed condition and after 72 h at various temperatures, measured using SANS and USANS. The results show that porosity with radii below 20 nm is greatly reduced once heat treatment is performed, with an overall reduction in the total porosity as the heat treatment temperature is increased

One immediate observation that can be made from Figure 43 is that for both O-YSZ and T-YSZ coatings, there is a noticeable change between the as-sprayed samples and the samples heat treated at 1100 °C. Both as-sprayed samples have virtually all their porosity located with radii < 300 nm, having most of the pores radius < 100 nm. As it was discussed previously, suspension thermal sprayed coatings present nano-size porosity with radius below 100 nm, outside of the accessible range of IA, making SANS and USANS the appropriate technique. Once a heat treatment is performed, even at the lowest temperature of 1100 °C, the nano-pores with a radius below 10 nm effectively disappears in both coatings. This reduction in nano-sized porosity is accompanied by an overall reduction of the total porosity measured via neutron scattering. Data in Figure 43 suggest that both coatings behave slightly different when heat treated at 1100 °C and 1200 °C. In the case of O-YSZ a small reduction in the porosity with radius below 100 nm can be seen, as well as the appearance of porosity with radius above 100 nm. Additionally, there is the appearance of a small population of pores with radius ~900 nm. Regarding the T-YSZ coating, there is a considerable larger reduction in porosity with radius below 100 nm, with only a minor increase in porosity with a radius above ~200 nm. No signs of populations of pores at larger radii could be observed. The behaviour observed for both samples when heat treated at 1300 °C is fairly similar, with an overall reduction in the total porosity measured and flatter pore volume distributions, showing pore sizes more evenly distributed instead of clearly grouped in populations. The changes related to the samples heat treated at 1400 °C, both O-YSZ and T-YSZ, are less obvious from the pore volume distribution plot, presenting a similar profile to the corresponding samples heat treated at 1300 °C.

SEM-BSE images of polished cross-section of the coatings were taken and analysed to measure the porosity using IA. This technique allows not only for the determination of the total porosity within the coating, but to investigate the microstructure of the coatings in the as-sprayed condition as well as after heat treatment. High magnification images of the as-sprayed and after

heat treatment at 1100 °C cross section of the O-YSZ and T-YSZ coatings can be observed in Figure 44.



*Figure 44: High magnification SEM-BSE images of the cross section of the O-YSZ (images a and b) and T-YSZ (images c and d) in the as-sprayed condition and heat treated at 1100 °C for 72 h. Black arrows mark globular porosity, while white arrows mark non-globular porosity. An overall reduction in the porosity and a transformation from non-globular to globular pores can be appreciated*

As it can be seen, for both coatings the samples in the as-sprayed condition (Figure 44a and c) present higher level of porosity than the heat-treated coatings, with an abundance of inter-splat

porosity, as indicated with white arrows in Figure 44a and c. The morphology of the pores evolves into more globular structures as the heat treatment is conducted, as shown in Figure 45.

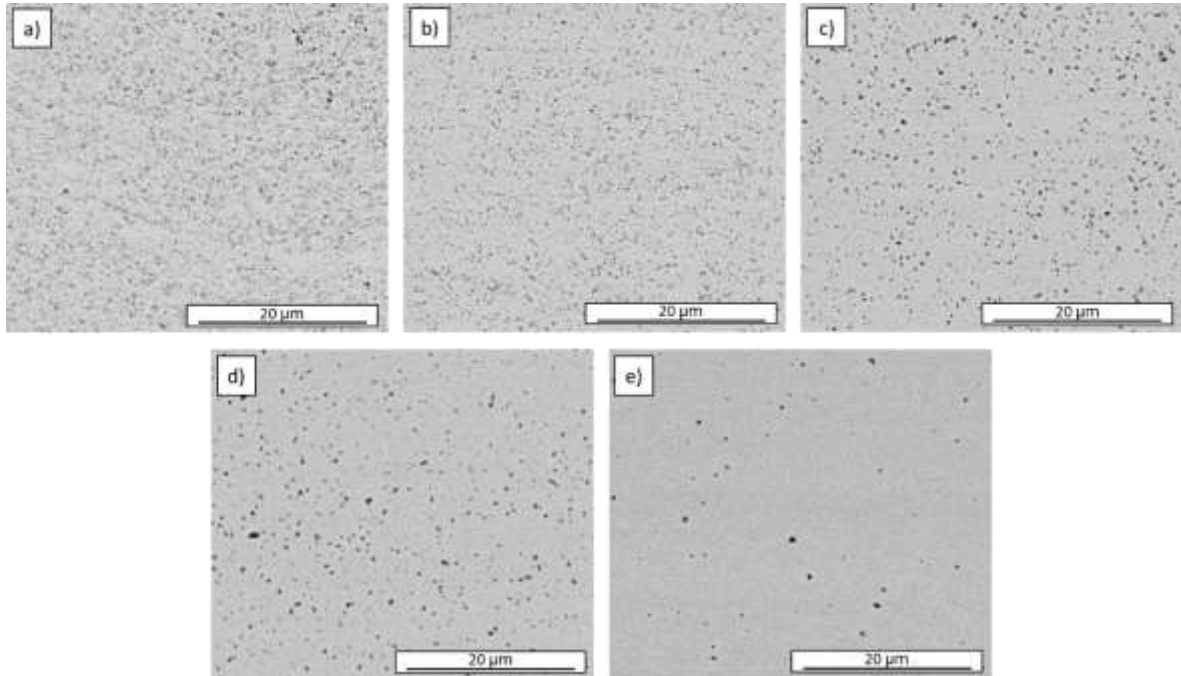


*Figure 45: SEM-BSE images of the cross section of the O-YSZ coatings as-sprayed (image a) and after heat treatment at 1100 °C (b), 1200 °C (c), 1300 °C (d) and 1400 °C (e) for 72 h*

The effect is more predominant the higher the heat treatment temperature is. Additionally, it can be easily appreciated in Figure 45 that the overall level of porosity is reduced as the heat treatment is conducted. An increase of the heat treatment temperature further continued this process, seeing a reduction in the inter-splat porosity with a transformation into spherical pores, and an overall reduction of the total porosity observed.

SEM-BSE cross-section images of the coatings were analysed to determine the apparent pore size distribution. The data can be used for comparison with the pore distribution profiles obtained using neutron scattering, as it is shown in Figure 46.

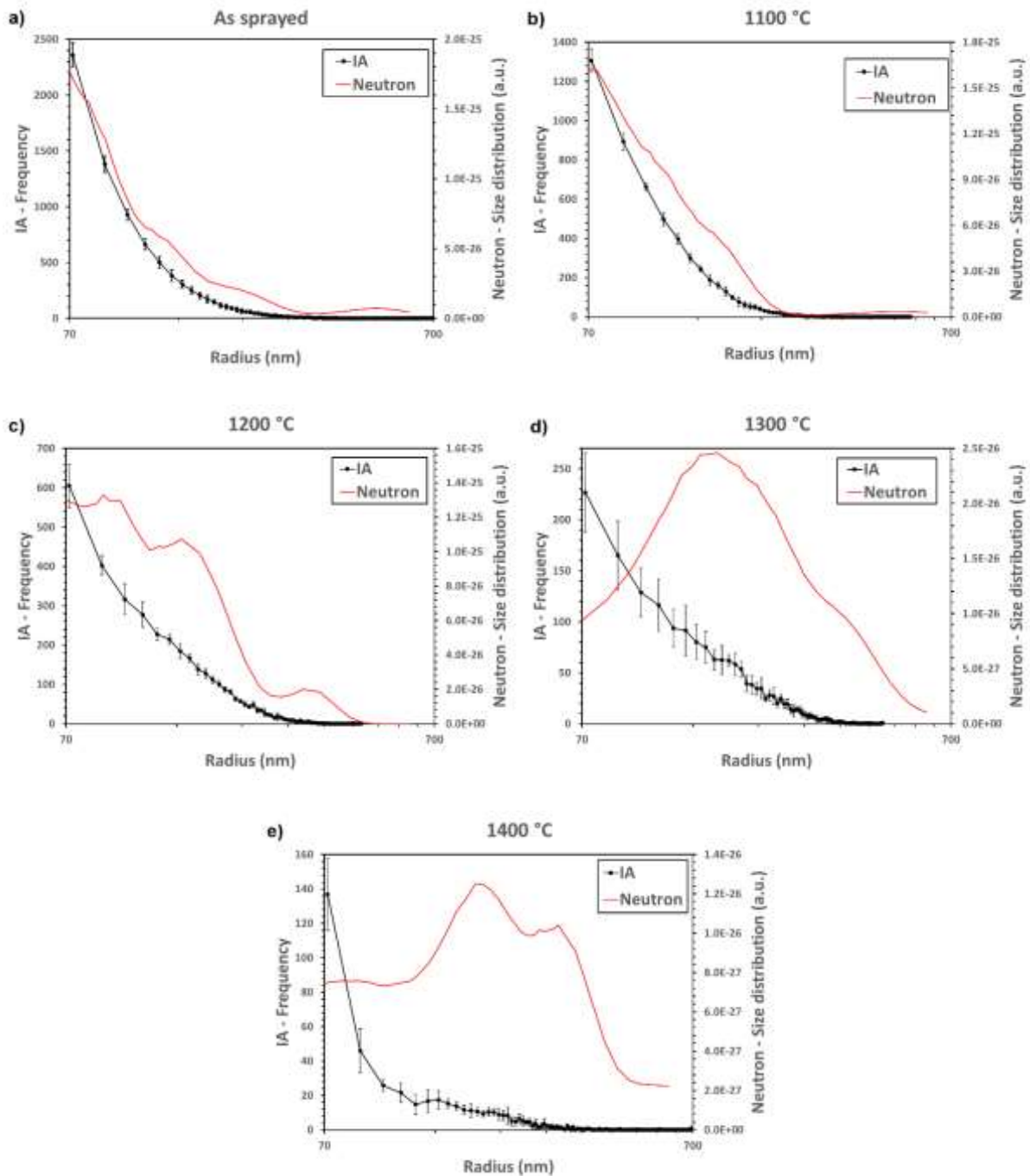


Figure 46: Size distribution of the porosity measured using SEM-BSE cross-section images (black) and neutron scattering (red). The results show good agreement on pore size distribution for the as-sprayed samples, with diverging profiles as the heat treatment temperature is increased, inducing microstructure changes not captured by IA

Pore size distribution data show good agreement within the available range (70 – 700 nm) between IA and neutron scattering for the as-sprayed samples. Once the samples are heat

treated, microstructural changes take place. The differences between IA and neutron scattering become more apparent as the temperature is increased, particularly at 1300 °C and 1400 °C, where the local maximum does not match for both techniques. This phenomenon is discussed in depth in section 4.4.1 “Porosity measurement: neutron scattering versus image analysis techniques”.

Neutron scattering and IA also provide information on the total porosity of the coating. The results from both techniques can be seen in Figure 47, where the total porosity, measured with both neutron scattering and IA techniques, is presented.

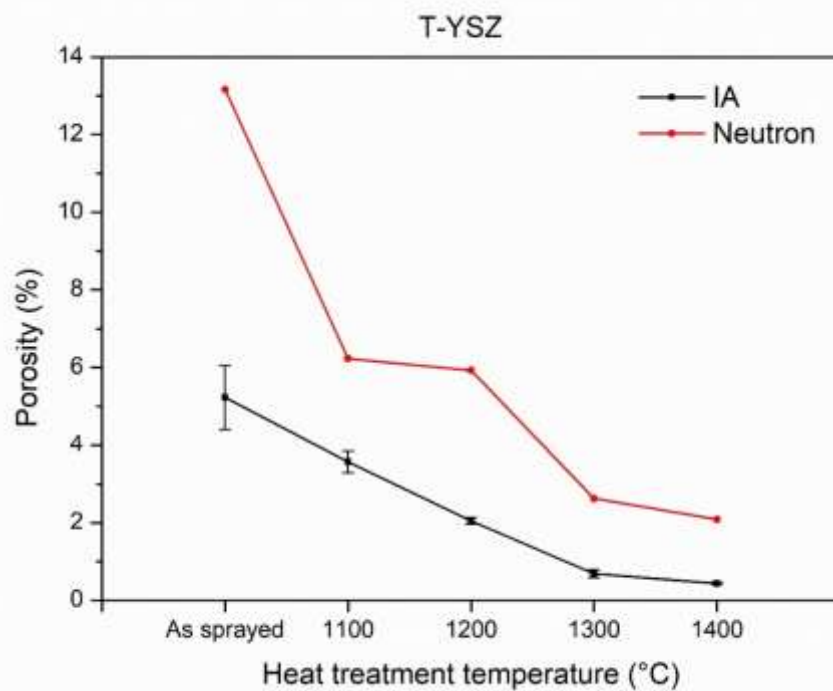
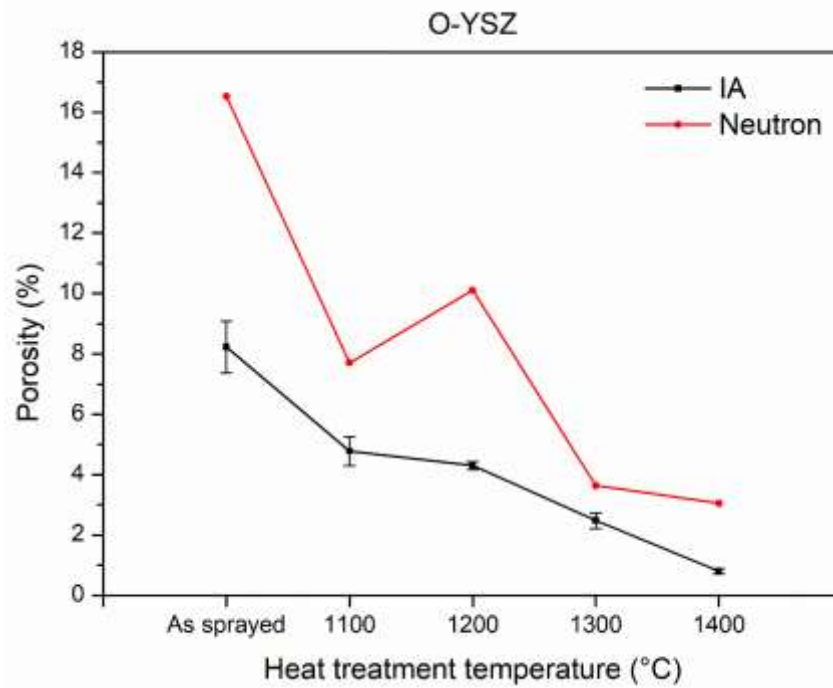


Figure 47: Total porosity in the as-sprayed as well as heat-treated samples for O-YSZ and T-YSZ coatings, measured using image analysis (black) and neutron scattering (red). The results show an overall reduction in porosity as the heat treatment temperature is increased. Neutron scattering measurements produce a higher porosity when compared to IA measurements

The data in Figure 47 indicates that, for both coatings, neutron scattering measures a higher total porosity when compared to IA. This difference is particularly notable in the as-sprayed samples. A complementary porosity measurement technique, such as the Archimedes method, could be used to provide another data point for these samples. Regarding the O-YSZ coatings, there is a sharp increase in the porosity measured using neutron scattering in the sample heat-treated at 1200 °C, contrary to the observed tendency of a reduction in the total porosity as the heat treatment temperature is increased. When measured using IA, the porosity decreases between 1100 °C and 1200 °C 10%, a much lower value compared to the 40 – 60% reduction experienced for the rest of the temperatures. The data seems to indicate that there is an unknown phenomenon in sample O-YSZ 1200 °C that neutron scattering data is reflecting, but IA is not fully capturing. As for the T-YSZ 1200 °C sample, there could be signs of a similar phenomenon, although neutron scattering does not show an increased porosity. Regardless, the reduction in porosity at 1200 °C is 5%, being notably lower than the 20 – 50% reduction in the rest of temperatures. IA data does not show any distinctive feature, suggesting that if T-YSZ is experiencing a similar process than O-YSZ, its magnitude is lower, and in any case below the detection limit of the IA technique.

#### **4.3.2. Phase composition**

To understand the different behaviour of the coatings when heat treated at 1200 °C, the phase content was investigated using XRD measurements. It is a generally well-known fact that 8YSZ undergoes phase transformation when exposed to high temperatures. During prolonged heat treatment above 1200 °C [190,213], the initial metastable tetragonal phase (*t'*-YSZ) decomposes into yttria-lean tetragonal phase (*t*-YSZ) and yttria-rich cubic phase (*c*-YSZ). If the decomposition process continues, the coating will reach a state where monoclinic (*m*-YSZ) and cubic are the only two phases present. The phase transformation process is as follows:



Due to the similarities between the two tetragonal phases,  $t\text{'-YSZ}$  and  $t\text{-YSZ}$ , with only a difference in yttria content but the same crystalline structure [213], phase identification on the XRD must be done attending to the peaks present in the  $2\theta$   $72^\circ$  to  $76^\circ$  range, as presented in Figure 48. The cubic phase, also identifiable in the same  $2\theta$  range, is generally considered to be detrimental due to its lower fracture toughness when compared to the metastable tetragonal phase [176]. The transformation from tetragonal to monoclinic should be avoided as well, as it implies a volume expansion of 4% [214] that can induce failure in the coating. The presence of monoclinic phase is best identified on XRD measurement focused on the  $2\theta$   $28^\circ$  to  $32^\circ$  range, as shown in Figure 49.

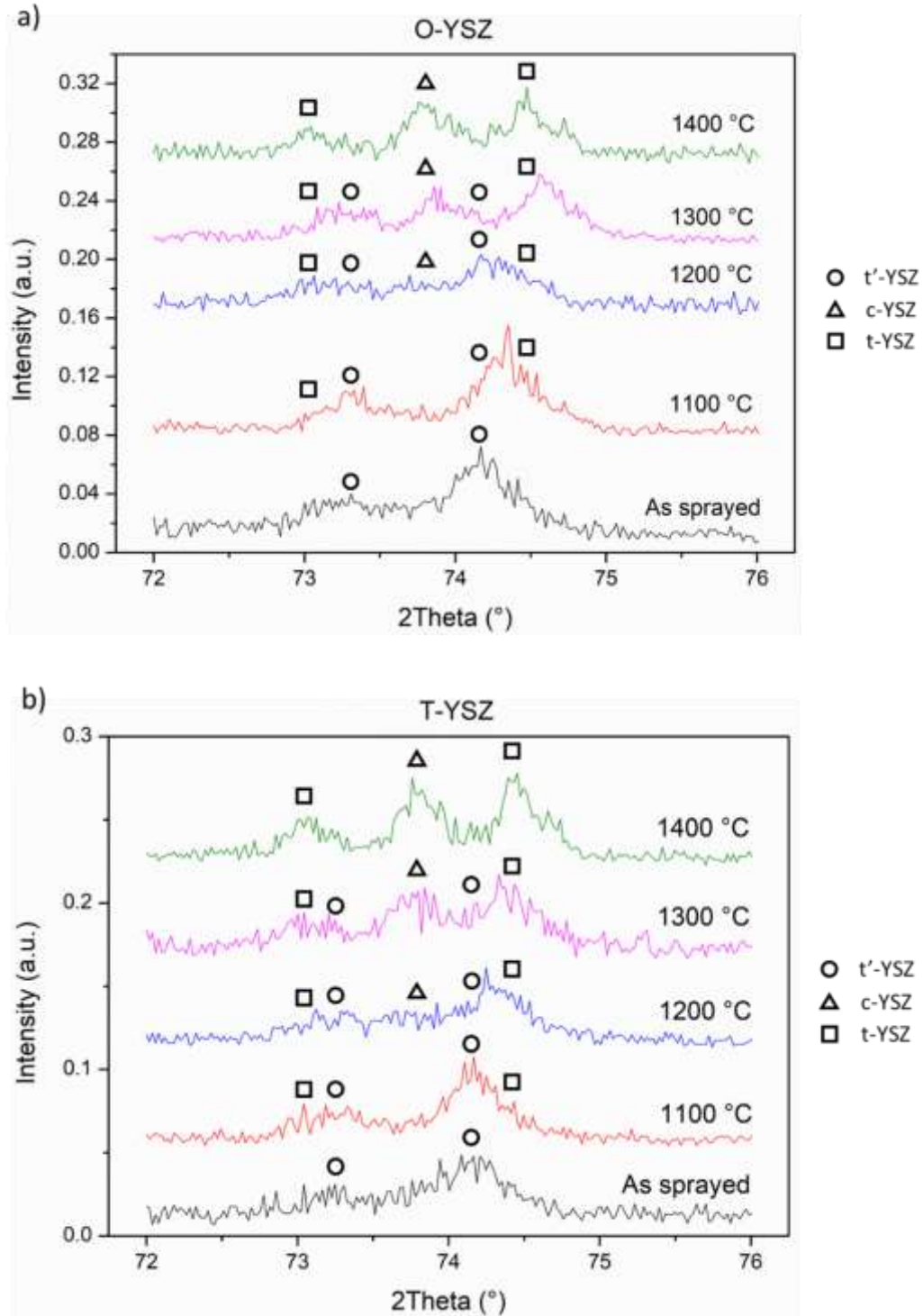


Figure 48: XRD spectra for both O-YSZ (plot a) and T-YSZ (plot b) as-sprayed and heat-treated coatings. Both plots show a detailed view of the range of interest for phase identification. The 72° - 76° scans show for both coatings that the transformation from the initial  $t'$  phase (circles) into a mixture of  $t$  (squares) and  $c$  (triangles) phases starts at 1100 °C and is only fully completed after 72 h at 1400 °C

The data indicates that for both O-YSZ and T-YSZ samples, the phase composition of the as-sprayed coatings is only metastable tetragonal phase (i.e.  $t'$ -YSZ). Due to the close proximity between the main  $t'$ -YSZ peak ( $\sim 74.1^\circ$ ) and the main  $t$ -YSZ peak ( $\sim 74.4^\circ$ ), the determination of the phases is a challenging task. The data presented in Figure 48 seems to suggest that a small amount of decomposition is taking place at 1100 °C; however, since no evidence of  $c$ -YSZ peaks ( $\sim 73.8^\circ$ ) could be identified, it could be due to the noise in the measurement. At 1200 °C both samples show clear signs of  $t$ -YSZ and  $c$ -YSZ peaks, although the decomposition is not completed yet, as the  $t'$ -YSZ peak is still quite predominant. A heat treatment at 1300 °C seems to mostly complete the  $t'$ -YSZ decomposition into  $t$ -YSZ and  $c$ -YSZ, with only traces of the initial  $t'$ -YSZ peak. The heat treatment at the higher temperature, 1400 °C, shows no evident signs of  $t'$ -YSZ phase, which would indicate that the decomposition is completed at or below this temperature. Even after 72 h at 1400 °C no evidence of monoclinic  $m$  phase could be detected, as shown in Figure 49.

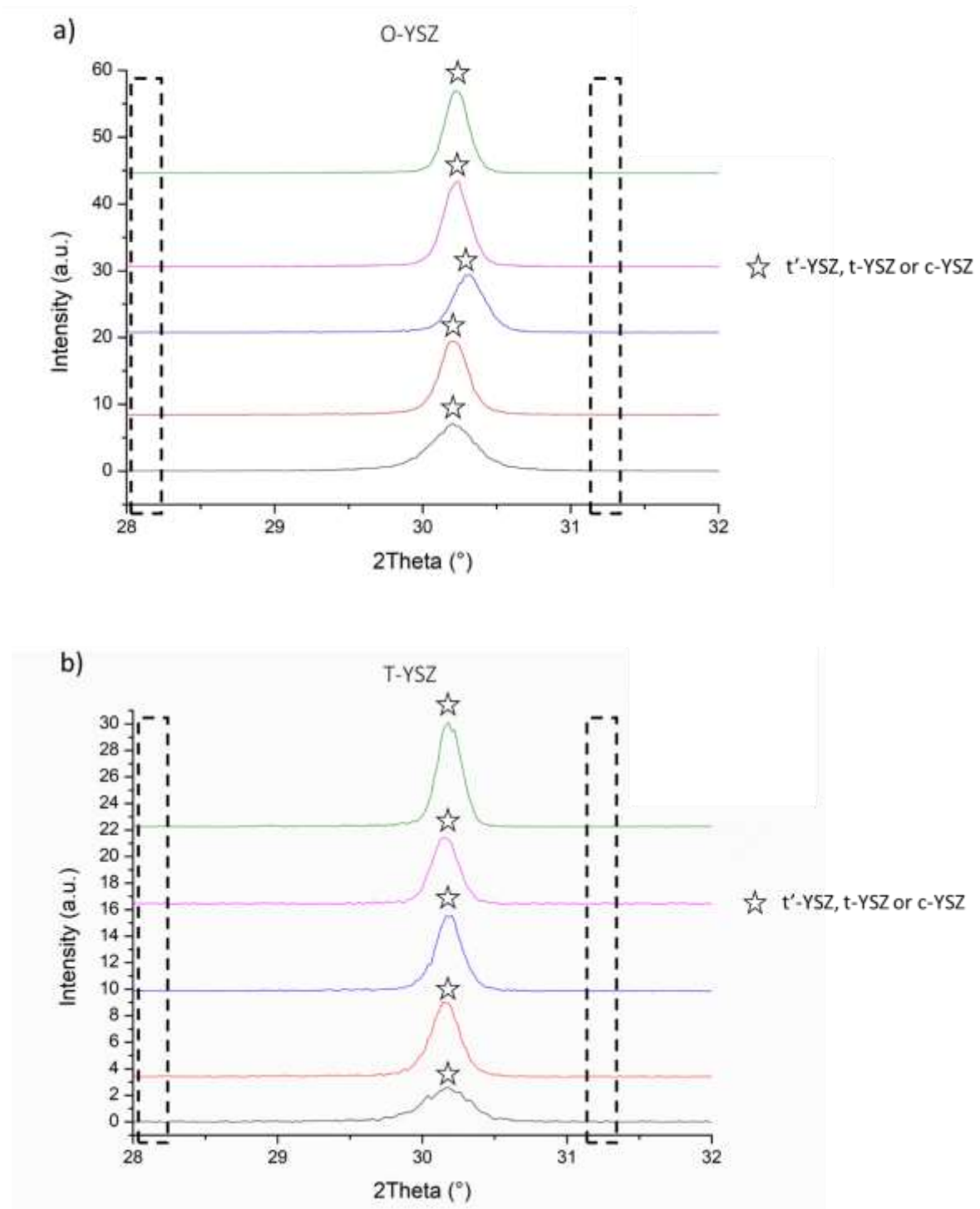


Figure 49: XRD measurements for O-YSZ and T-YSZ as-sprayed and heat-treated coatings. Both coatings show a detailed view of the range of interest for phase identification. The 28° - 32° scans show no evidence of cubic monoclinic phase (relevant peaks would appear inside the areas marked with dashed lines). The peak present at ~30.1° is not suitable for identification as it is caused by the overlap of three phases (t'-YSZ, t-YSZ and c-YSZ)

To further investigate the effect that this phase transformation has on the heat-treated coatings, Rietveld refinement was conducted to calculate the tetragonality, as it is shown in Figure 50. Ilavsky *et al.* [190] has determined the cell parameter variations  $c/a\sqrt{2}$  as a function of the amount of  $YO_{1.5}$  in mol % ( $x$ ) as the following equation over the concentration of  $YO_{1.5}$  up to about 7 mol %, as shown in Equation 14 (data was retrieved from the original plot and linear fitted with  $R^2 = 1$ ):

$$c/a\sqrt{2} = 1.02257 - 0.0032x \quad (14)$$

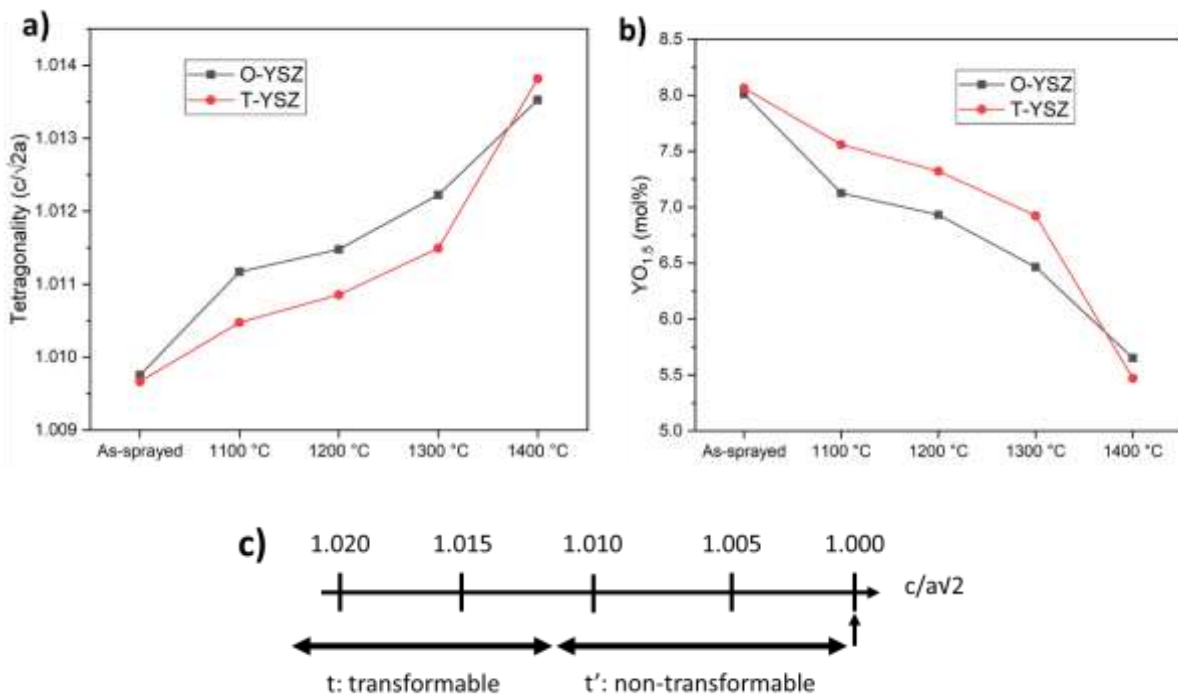


Figure 50: a) Tetragonality and b)  $YO_{1.5}$  composition (mol %) of O-YSZ and T-YSZ coatings as-sprayed and after various heat treatments, c) tetragonal forms of YSZ based on the tetragonality value [215]. Tetragonality increases in both coatings as the heat treatment temperature is increased, but T-YSZ presents a lower value, requiring a higher temperature to reach the threshold between transformable and non-transformable phases

As it can be seen, the tetragonality of both as-sprayed coatings is approximately 1.0096, corresponding to the  $t'$  non-transformable phase region as indicated in Figure 50c. As the

temperature of the heat treatment is increased, starting at 1100 °C, the tetragonality increases, reaching a value of ~1.011 in the case of O-YSZ. As the heat treatment temperature is increased, so does the tetragonality value, reaching the *t* transformable phase region, and leading to the appearance of the corresponding peaks in the XRD spectra presented in Figure 48. This same trend can be seen as the temperature is increased, with a noticeable increase in the tetragonality once the heat treatment temperature is 1400 °C. The same effect, although with the reduction of YO<sub>1.5</sub> composition can be seen in Figure 50, as expected. From the Rietveld refinement, it can also be calculated the crystallite size and the micro-strain of the coatings, as it is shown in Figure 51.

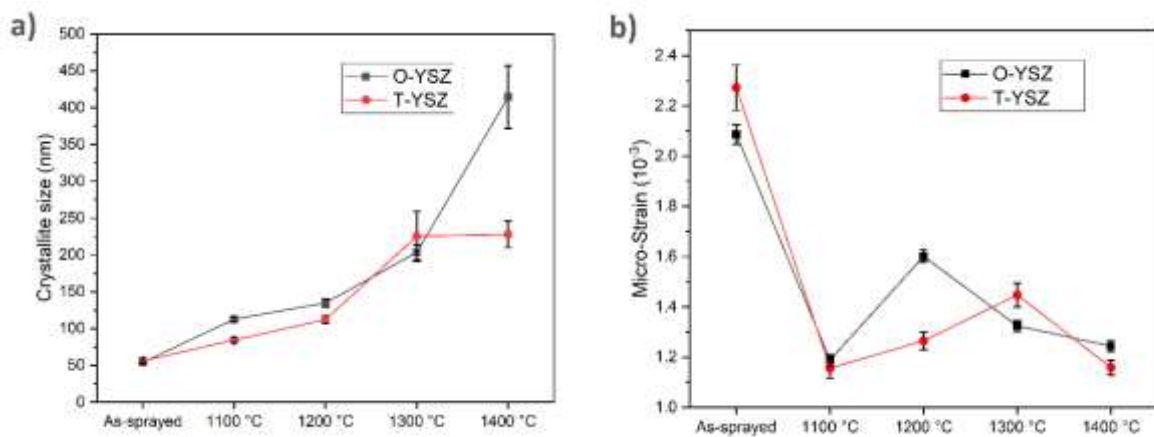


Figure 51: a) Crystallite size and micro-strain for both O-YSZ and T-YSZ coatings on the as-sprayed condition and after various heat treatments. O-YSZ shows almost a two-fold increase in crystallite size at 1400 °C compared to T-YSZ. b) Micro-strain is reduced in both cases from the as-sprayed condition. O-YSZ presents a sharp peak at 1200 °C whereas T-YSZ shows a smaller peak, with a smoother transition at 1300 °C

The initial crystallite size for both coatings is approximately 50 nm, with a slow increase in crystallite size up to ~125 nm at 1200 °C. There is a further increase in size up to ~200 nm at 1300 °C for both coatings, but from this point the behaviour is different for each coating. In the case of O-YSZ, heat treatment at 1400 °C causes the crystallite size to increase up to ~400 nm,

whereas for T-YSZ the same temperature produces no change with respect to 1300 °C. When considering the micro-strain, both coatings show a high level of micro-strain in the as-sprayed condition ( $\sim 2.2 \times 10^{-3}$ ), phenomenon expected on thermal sprayed coatings due to the rapid cooling experienced upon impact [106]. The micro-strain is reduced once the heat treatment at the lowest temperature, 1100 °C, is conducted ( $\sim 1.2 \times 10^{-3}$ ), suggesting an annealing-like process. From this point, the two coatings once more differ in their behaviour. The O-YSZ coating presents a micro-strain peak at 1200 °C, being the values at 1300 °C and 1400 °C lower. In the case of T-YSZ, the peak occurs at 1300 °C, and its magnitude is less than the one in O-YSZ. Both coatings have a low micro-strain value ( $\sim 1.2 \times 10^{-3}$ ) at 1400 °C.

As well as the phase content and porosity are related to the heat treatment temperature, such process has an impact on the mechanical properties of the coating, such as micro-hardness. Aiming to further understand the implications of the evolution of porosity within heat-treated 8YSZ coatings, the micro-hardness of the as-sprayed and heat-treated, free-standing coatings was measured. The relationship between micro-hardness and porosity, measured using both neutron scattering and IA, can be seen in Figure 52.

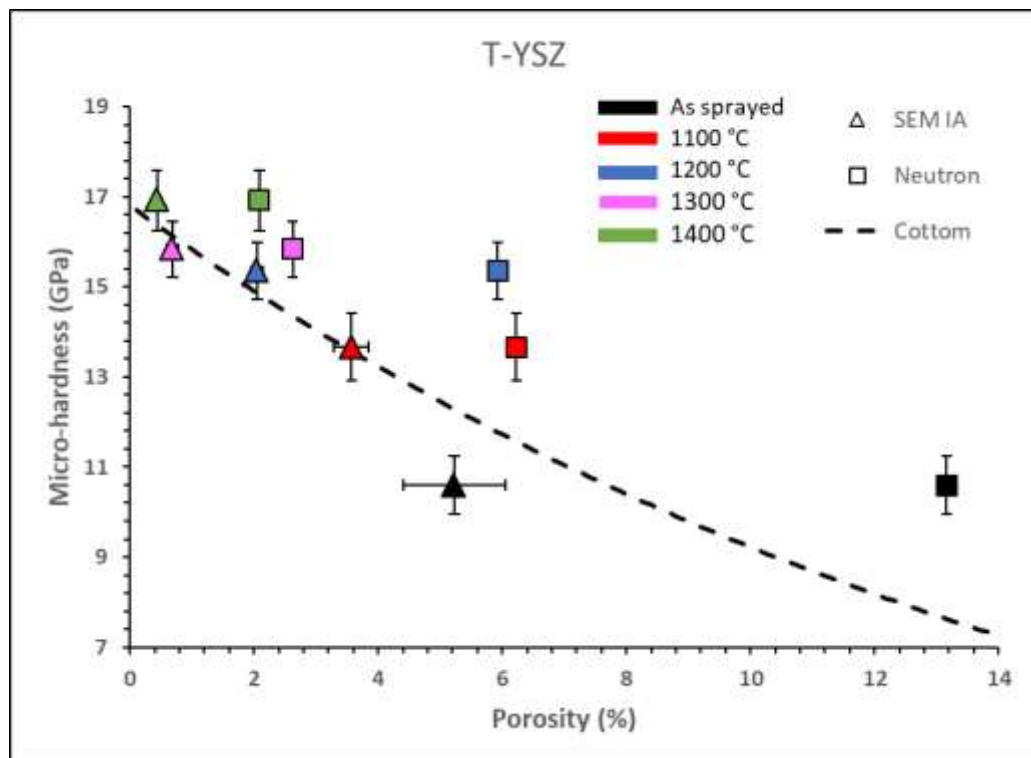
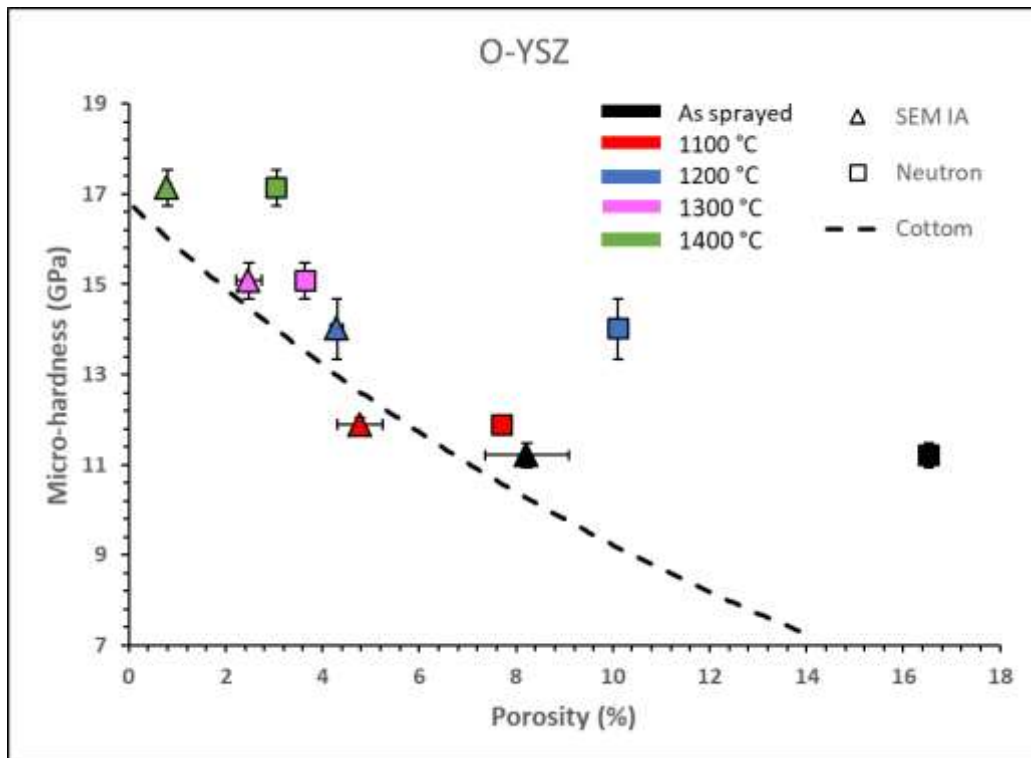


Figure 52: Plot of the micro-hardness versus the measured porosity using neutron scattering (square) and image analysis (triangle). The dashed line corresponds to the empirical curve reported by Cottom

et al. [216]

In addition to the micro-hardness measurements, Figure 52 also shows a dashed line corresponding to the empirical curve reported by Cottom *et al.* [216], being derived from measurements of the porosity on sintered YSZ using IA. The results show a good agreement between the empirical curve and the measurements performed using IA. In the case of the neutron scattering data points, they all show a shift to the right, due to the higher porosity measured with this technique. There is also a similar trend in the relationship between micro-hardness and porosity, except for the points corresponding to the as-sprayed coating and 1200 °C, which will be further discussed in the next section.

## **4.4. Discussion**

### **4.4.1. Porosity measurement: neutron scattering versus image analysis techniques**

Both neutron scattering and IA techniques can be successfully applied to study the porosity present within thermal sprayed coatings, but some considerations should be taken first. Three main differences were observed in this work, namely, the pore size range measurable, the inclusion of “handling cracks” as porosity features and the need for pore shape assumption.

First, as it was shown in Figure 43, the combination of SANS and USANS techniques allows the study of pores with a radius between ~1 nm and ~10 µm. In the case of IA, the lower limit for the radius was ~70 nm, with the largest feature observed being around ~700 nm. Due to the use of suspension HVOF thermal spraying as the deposition technique, pores with a radius below ~70 nm play a considerable role. Even after heat treatment at 1300 °C for 72 h, there is a considerable contribution of such porosity, which is not detectable using IA. This is one of the key factors contributing to the persistent higher value for the total porosity when measured through neutron scattering versus IA, particularly for heat treatment temperatures below 1300 °C, as it can be seen in Figure 47. In the comparison between SANS and IA reported by

Deshpande *et al.* [66] the results consistently showed a porosity 1.25 times higher when measured using IA, being the opposite in this work. However, in their work, coatings were produced using powder-based thermal spray techniques. Secondly, “handling cracks” influence the total porosity measured using neutron scattering, as this technique exposes the whole sample to the neutron beam, without the possibility of the user avoiding unwanted features. Nevertheless, neutron scattering is sensitive to interfacial surface. Pores, due to their size and volume fraction have a significantly high interface and so give rise to significantly high scattering. Scattering from non-spherical features and cracks would be significantly lower and, although this will contribute to the overall scattering, it should be low. Neutron scattering provides a more complete picture, whereas IA allows for the determination of the amount of porosity and cracks. Thirdly, as it was described in Appendix A, the shape of the pores had to be established for the analysis, which in this case corresponded to spheres. As it could be seen in the SEM-BSE cross-section images in Figure 44, this assumption was the less accurate for the as-sprayed samples. Given the large difference when compared to the IA porosity value, the initial hypothesis would be that neutron scattering techniques overestimate this value. This is further corroborated by the observed deviation from the empirical curve in the micro-hardness versus porosity plot (Figure 52). As the micro-hardness value is independent from the data modelling, to have the as-sprayed data point closer to the empirical relationship, the porosity value should be smaller. Therefore, it can be concluded that the porosity of the as-sprayed coatings is being overestimated when using neutron scattering techniques.

Regarding the differences between neutron scattering and IA size distributions, the first thing that should be considered is that only the range from 70 to 700 nm could be compared, although for neutron scattering there is much more information outside these limits. Secondly, the IA profile is obtained as the average of the five individual areas imaged. This has the effect of “smoothing out” outliers and individual features only present in one area. As a result, the black

profiles in Figure 46 show the overall tendency of the pores with radius between 70 and 700 nm. In the case of neutron scattering, a single measurement per coating, which included the whole area submerged on the neutron beam, was performed. This allowed for a more detailed view of unique occurrences or populations of features. Such difference can be clearly seen in Figure 46a, b and c, showing the as-sprayed coating and heat treatments with temperatures up to 1200 °C. On these three instances, both techniques present a very similar picture, with differences arising as the heat treatment temperature is increased. Despite the already mentioned difference experienced at 1200 °C between the porosity measurement for neutron scattering and IA, the size distribution shown in Figure 46c is still fairly consistent. This is due to the range investigated (70 to 700 nm), which doesn't include the majority of the features observed in the neutron scattering volume distribution, as it can be seen in Figure 43. In the case of 1300 °C and 1400 °C the tendency changes, mainly due to detection of features by the neutron scattering techniques, which translate into a signal with an associated radius values between 70 and 700 nm.

#### **4.4.2. Porosity evolution**

The porosity was studied attending to three main characteristics: pore shape, pore volume distribution and total porosity present in the coating. These three characteristics presented an evolution as the samples were heat treated. First, pore shape was highly irregular in the as-sprayed coatings, presenting a combination of elongated, inter-splat pores and globular pores, as represented in Figure 44. Heat treatment even at the lowest temperature (1100 °C) produced the consolidation of the porosity as globular pores, with only small traces of non-spherical pores. This effect could be seen to continue at higher heat treatment temperatures.

The porosity volume distribution obtained from the neutron scattering curves for both the 8YSZ coatings, presented in Figure 43, clearly shows how heat treatment at any temperature has a

considerable impact on the porosity of the coatings. As it can be seen, porosity with a radius below 20 nm is greatly reduced at heat treatment temperatures as low as 1100 °C. If the heat treatment temperature is 1300 °C or above, this effect is extended to porosity with a radius below 100 nm, although to a lesser degree. One of the possible explanations for this very efficient reduction of porosity with a radius below 20 nm can be found when considering the crystallite size. The crystallite size of the as-sprayed coatings was determined to be ~50 nm for both coatings, as shown in Figure 51. During heat treatment, pores with a radii below 20 nm are reduced due to a densification process, which is favoured for pores smaller than the crystallite size [217]. In general, an increase in the heat treatment temperature had the effect of reducing the amount of fine pores in favour of porosity with a larger radius, producing an overall shift of the pore volume distribution to the right, as represented in Figure 43.

The effect on the total porosity is represented in Figure 47, with a reduction in the total porosity as the heat treatment temperature is increased. A different behaviour is observed at 1200 °C, with the porosity remaining the same, as in the T-YSZ coating, or even increasing as seen in the O-YSZ coating. A contribution to this phenomenon can be found in the SEM-BSE cross-section images taken during the study. As the image in Figure 53a shows, the O-YSZ coating heat treated at 1100 °C presented areas where the porosity was distributed along a line. The origin on this lined porosity is unknown at the moment, with more research being needed. Once the O-YSZ coating were heat treated above 1100 °C, these features were no longer present, and only micro-cracks (cracks with a length lower than 100 µm and not connected to the coating surface or the substrate interface) could be detected. This could indicate that lined porosity acted as a precursor of cracks, as seen in Figure 53b. This feature could not be found in any of the T-YSZ samples imaged, but was present in one out of three O-YSZ samples imaged, indicating that it is a rather uncommon occurrence.

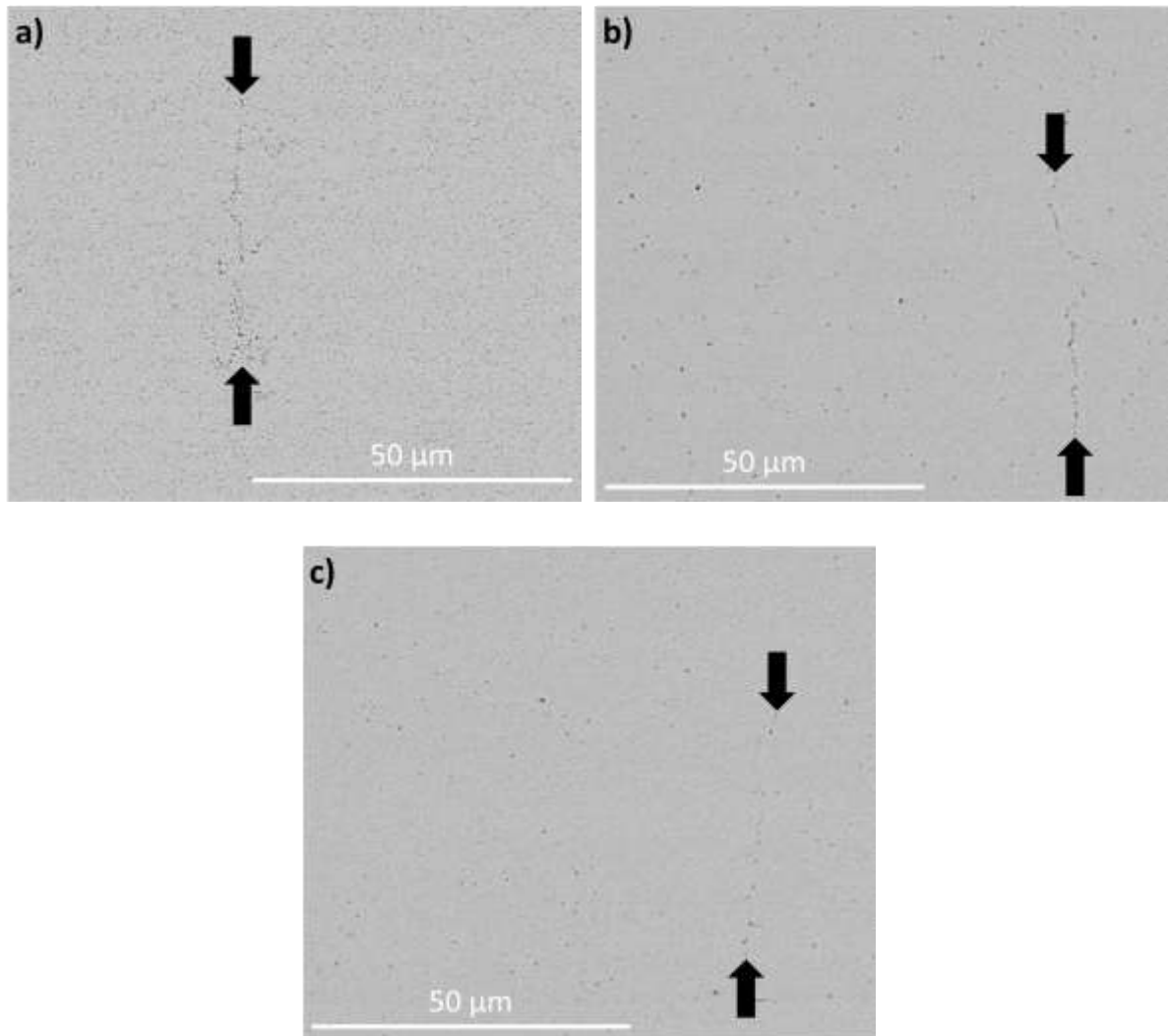


*Figure 53: SEM-BSE images of the cross-section of O-YSZ coating heat treated at a) 1100 °C and b) 1400 °C. Image b shows an example of a full crack, whereas image c shows a crack with reduced intensity due to heat treatment. The arrows mark the beginning and end of the lined porosity and the crack*

#### **4.4.3. Phase transformation**

Heat treatment will have an effect on the phase composition of the 8YSZ coatings, particularly as the temperature approaches 1200 °C, which is traditionally considered as the threshold for the decomposition of pure metastable tetragonal to tetragonal plus cubic phase, as discussed in section 4.3.2 “Phase composition”. As it could be appreciated in the XRD spectra in Figure 48, heat treatment at 1200 °C causes the initiation of the phase transformation from pure metastable

tetragonal to tetragonal plus cubic phase. This temperature is consistent with the literature, with an established temperature of 1200 °C as the upper limit for the presence of metastable tetragonal phase. A shift in the metastable tetragonal phase peak at  $2\Theta \sim 74^\circ$  is also observed, which has been associated with a decrease of the yttria content in the *t* phase and an increase in the *c* phase [190]. These phase transformation and yttria content reduction were confirmed through Rietveld refinement, as it can be seen in Figure 50 and Figure 51.

The tetragonality of both coatings is almost identical on the as-sprayed samples, but once the heat treatment at 1100 °C is conducted, O-YSZ presents a higher tetragonality value. At this temperature, the tetragonality value is  $\sim 1.011$ , almost at the transition point between the initial *t'* non-transformable phase region and the *t* transformable phase region, as reported by Ilavsky *et al.* [190]. As the heat treatment temperature is increased to 1200 °C, there is a further reduction in the  $YO_{1.5}$  composition, accompanied by another increase in the tetragonality. This additional increase is enough to enable the phase decomposition from metastable tetragonal to stable tetragonal and cubic phase, although only in the case of O-YSZ. The tetragonality value for T-YSZ at 1200 °C is still below 1.011. This threshold value is passed at 1300 °C in the case of T-YSZ. This phase transformation has implications regarding the micro-strains present within the coating. As observed by Witz *et al.* [213], the micro-strain present on thermal-sprayed YSZ coatings after heat treatment at 1100 °C for 100 h is  $\sim 0.4\%$ ; however, the micro-strain on the coating after heat treatment at 1200 °C for 100 h was measured to be  $\sim 0.7\%$ , due to the reduction in the metastable tetragonal phase content. This increase in the micro-strain as the phase decomposition takes place can be seen in Figure 51. In the case of O-YSZ, as mentioned before, there is a sharp increase at 1200 °C, coinciding with the transition from *t'* non-transformable to *t* transformable, whereas for T-YSZ the peak is located at 1300 °C. Both the sharpness and the maximum magnitude of the peak are less than for O-YSZ. Nevertheless,

the increase in micro-strain caused by the phase transformation is not believed to be the sole origin of the increase in porosity observed at 1200 °C.

This phase transformation is believed to be the cause for the appearance of the previously mentioned micro-cracks. The presence of aligned porosity, as it could be seen in Figure 53a, acts as preferential sites for micro-cracks to form once the thermal stresses accumulate within the coating. Such micro-cracks would correspond to the features observed in the scattering profiles above 100 nm and at 800 – 900 nm. The reason why this phenomenon has a higher effect on the O-YSZ coating could be due to the differences observed in the micro-strain profile in the T-YSZ, reaching at 1300 °C a lower micro-strain value ( $\sim 1.4 \times 10^{-3}$ ) than the O-YSZ coating at 1200 °C ( $\sim 1.6 \times 10^{-3}$ ). In addition, O-YSZ suspension showed a larger particle size distribution, as well as a higher content of larger pores in the as-sprayed sample, when compared to T-YSZ. This increase in pores of larger size could lead to more aligned pores, producing micro-crack initiators.

Once the heat treatment temperature is further increased to 1300 °C or 1400 °C, the phase transformation from pure metastable tetragonal to tetragonal plus cubic phases seems to be mostly completed. The appearance of the cubic phase at this temperature produced a reduction of  $\sim 1.7\%$  in the micro-strain of the coating. In addition, the higher temperatures, once they had completed the phase transformation, produced a relaxation of the accumulated micro-strain. These phenomena contributed to the reduction of micro-cracks to some degree, as it was appreciated during SEM imaging shown in Figure 53. In no case presence of monoclinic phase could be detected, which indicates that in both coatings a heat treatment of 1400 °C for 72 h is not enough to promote the transformation from tetragonal to monoclinic phase. This corroborates the results reported by Ilavsky *et al.* [190] where plasma sprayed YSZ coating heat treated at 1400 °C for 100 h did not show appreciable traces of monoclinic phase. Presence of monoclinic phase was detected by Witz *et al.* [213] after 1000 h at 1300 °C, which indicates

that longer exposures at lower temperature can cause the formation of monoclinic phase. A general schematic showing the evolution observed in 8YSZ coatings during heat treatment up to 1400 °C for 72 h is presented in Figure 54.

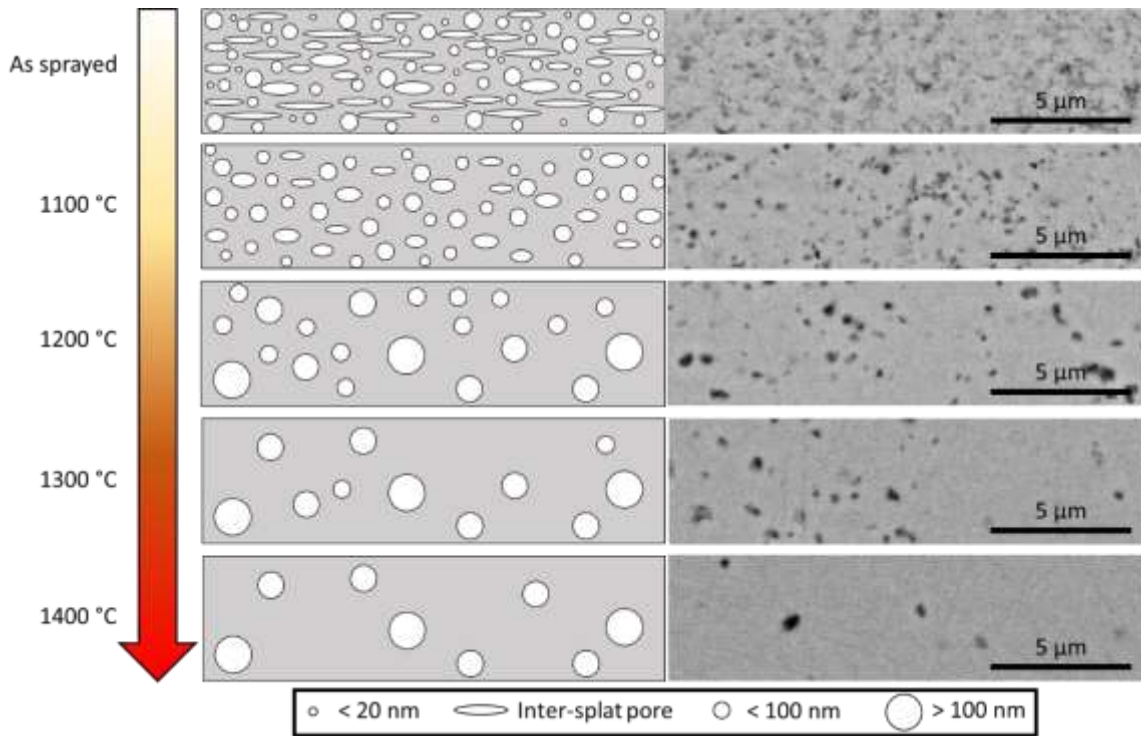


*Figure 54: Schematic representation of the evolution of porosity on thermal sprayed 8YSZ coatings (left) along with the corresponding BSE images of the cross-section of the coatings (right)*

The schematic show in Figure 54 represents the evolution of porosity on thermal sprayed 8YSZ coatings, at the as-sprayed condition and after heat treatment at several temperatures for 72 h. The 1100 °C heat treatment reduces porosity below 20 nm, almost all non-globular porosity and aligned porosity can be seen. Heat treatment at 1200 °C further reduces porosity below 100 nm. Higher temperatures produce a reduction of the finer pores, causing an overall reduction of the porosity level.

## 4.5. Conclusions

In this work, we have demonstrated that 8YSZ coatings deposited using SHVOF thermal spray present a large amount of nano-sized porosity, contrary to more traditional powder-based thermal spray techniques such as APS, and a mixture of elongated, inter-splat pores and spherical pores. SANS & USANS and IA techniques were used to investigate the evolution of porosity after heat treatment at 1100 °C, 1200 °C, 1300 °C and 1400 °C for 72 h. Both techniques were capable of measuring the pore size distribution and total porosity; however, for suspension thermal sprayed coatings, due to the presence of nano-sized pores, neutron scattering is needed to study the entire range of porosity present. IA is needed to visually inspect the microstructure of the porosity, assessing artefacts and shape, information required for an accurate modelling of the SANS and USANS data.

The results show that heat treatment at 1100 °C reduces the presence of nano-pores and overall porosity, with a transition from elongated pores into spherical pores. Heat treatment at 1200 °C induced, in addition to a continuation of the evolution of the microstructure, a phase transformation from the original metastable tetragonal into stable tetragonal and cubic phases. This process, which was accompanied by a raise in the micro-strain, led to the formation of micro-cracks within the coating. Heat treatments at higher temperatures (1300 and 1400 °C) completed the phase transformation, without the formation of monoclinic phase, limiting the accumulation of thermal stresses, further reducing the presence of fines pores.

## 4.6. Appendix A

The SANS technique is based on the different scattering length densities (SLD) present within a heterogeneous material, being in this case assumed that the pores have SLD equal to zero, and the 8YSZ coating has a SLD of  $5.4 \times 10^{-10} \text{ cm}^{-2}$ . The contrast in SLD between the coating and the pores gives rise to the coherent elastic scattering of the monochromatic neutron beam,

which can be detected and quantified. A general schematic of the scattering process is shown in Figure A.1.

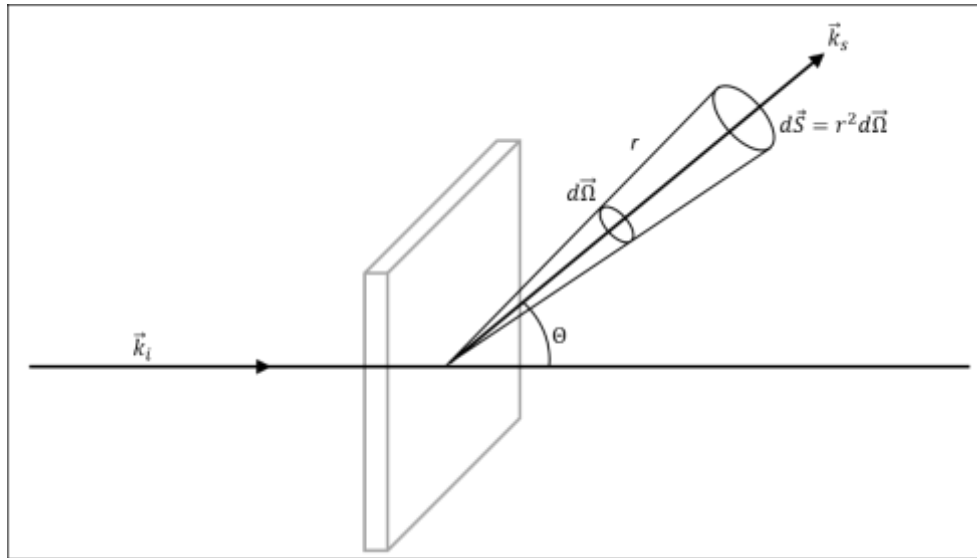


Figure A.1: Schematic representation of the neutron scattering process of an incident neutron beam ( $\vec{k}_i$ ) with a rectangular sample, producing a scattered neutron beam ( $\vec{k}_s$ ) with an angle  $\theta$  inside a solid angle  $d\vec{\Omega}$ , resulting in a microscopic differential scattering cross-section  $d\vec{S}$

In the case of the USANS technique, the core concept remains the same as with SANS, being the scattering of a monochromatic neutron beam due to difference on the SLD of the material. Nevertheless, in order to be able to detect lower scattering angles (corresponding to larger physical features in the sample) smaller wavelengths and shorter flight paths are used. Two sets of five Si (311) single crystals are placed in front and behind the sample, using the diffraction of the neutrons to highly collimate the beam, creating a strong correlation between scattering angles and wavelengths. This improves the flux on the sample while allowing detailed angular resolution.

The differential scattering cross-section can be defined as described in Equation A.1.

$$\frac{d\Sigma}{d\Omega}(Q) = \frac{\text{number of neutrons scattered per second into } d\Omega}{\Phi d\Omega} \quad (\text{A.1})$$

Where  $\vec{Q}$  is the scattering vector (or momentum transfer)  $\vec{k}_s - \vec{k}_i$  with magnitude  $Q = \left(4\pi/\lambda\right)\sin\Theta$  and being  $\Phi$  the flux. The differential scattering cross-section has units of  $\text{cm}^2$ .

This is what the detectors pick up during the experiment, being necessary a reduction step, where the data is normalised over the sample volume. After said step the normalised differential scattering cross-section  $I(Q)$  is obtained, with units of  $\text{cm}^{-1}$ .

To model the scattering data collected,  $I(Q)$ , two factors are used: a form factor (which in this work has been chosen to be a sphere) and a size distribution (for the analysis a normal Gaussian distribution was used). The form factor of a sphere can be expressed as shown in Equation A.2.

$$I_{sphere}(Q, R, \Delta\eta) = \left[ \frac{4}{3}\pi R^3 \Delta\eta^3 \frac{\sin QR - QR \cos QR}{(QR)^3} \right]^2 \quad (\text{A.2})$$

Whereas the Gaussian size distribution is characterised by Equation A.3.

$$Gauss(x, N, s, x_0) = \frac{N}{c} e^{-\frac{(x-x_0)^2}{2s^2}} \quad (\text{A.3})$$

Where  $N$  is a scaling factor of the size distribution,  $x$  is the radius of the pores,  $x_0$  is the mean of the distribution and  $s$  is the standard deviation of the distribution.  $c$  is chosen so that  $\int Gauss(x, s, x_0) dR = N$ . Therefore, the Gaussian size distribution can be rewritten as  $Gauss = N \times p(x)$  where  $\int p(x) dx = 1$ . The combination of both the form factor and the size distribution can be used as a model for the analysis of the neutron scattering data, as shown in Equation A.4.

$$I_{model}(Q) = \int_0^\infty Np(R)I_{sphere}dR \rightarrow I_{model}(Q) = N \int_0^\infty I_{sphere}dR \quad (\text{A.4})$$

In Equation A.4,  $N$  has an additional physical meaning, being the number density of scatterers per unit volume. Therefore, this value can be used to both calculate the volume distribution as  $N(R) \times R^3$ , and the volume fraction of spheres within the sample volume, as detailed in Equation A.5.

$$f_p = \int_0^{\infty} n(R) \frac{4}{3} \pi R^3 dR = N \frac{4}{3} \pi \langle R^3 \rangle \quad (\text{A.5})$$

The modelling was done using the SASfit software [208], version 0.94.10. It follows a non-linear least square fitting routine. Several populations of spheres were added, each one of them following the  $I_{\text{model}}(Q)$  equation described above, until the combined signal matched the measured data. Once the fitting was performed, the values of  $N(R)$  and  $\langle R^3 \rangle$  were exported from SASfit to calculate the volume distribution and volume fraction for each population of spheres. The complete curve of the volume distribution was constructed following the convolution of the individual curves from each population of spheres, while the total volume fraction was calculated as the sum of each volume fractions, multiplied by 100 to express the value as a percentage.

#### **4.7. Acknowledgements**

This work was supported by the Engineering and Physical Sciences Research Council (EPSRC) (grant number EP/L016206/1) as well as by an Innovation Placement from the EPSRC Centre for Doctoral Training in Innovative Metal Processing (IMPACT). The authors thank ANSTO for the awarded beam time proposal number 7216 that allowed the neutron scattering experiments to be conducted. The authors would like to thank John Kirk for his assistance during the SHVOF thermal spray, Dr Acacio Rincon Romero for the fruitful discussions regarding densification of YSZ and to the Nanoscale and Microscale Research Centre (nmRC) at the University of Nottingham for providing access to microscopy facilities.

## **Chapter 5: Interaction of CMAS on Thermal Sprayed Ytterbium Disilicate Environmental Barrier Coatings: A Story of Porosity**

The main body of this section is reproduced from the paper:

*D. Tejero-Martin, A. R. Romero, R. G. Wellman, T. Hussain, Interaction of CMAS on thermal sprayed ytterbium disilicate environmental barrier coatings: a story of porosity, Ceram. Int.*

Article in press <https://doi.org/10.1016/j.ceramint.2021.12.033>

### **Abstract**

Molten calcium magnesium alumina-silicates (CMAS) represent a challenge for the current generation of rare earth silicates environmental barrier coatings (EBCs). Their interaction with ytterbium disilicate ( $\text{Yb}_2\text{Si}_2\text{O}_7$ ) free-standing coatings deposited using thermal spraying technique has been studied to further understand the reaction mechanisms. Three coatings, deposited with different porosity levels and thickness, representing traditional EBCs (< 3 % porosity and ~350  $\mu\text{m}$  thickness) and abrasible coatings (~20% porosity and 500 – 1000  $\mu\text{m}$  thickness) were exposed to CMAS at 1350 °C. The results show that higher porosity levels facilitates CMAS infiltration in the first hour of exposure, in combination with infiltration through the inter-splat boundaries. Preferential dissolution of ytterbium monosilicate ( $\text{Yb}_2\text{SiO}_5$ ) takes place, forming a 10 – 15  $\mu\text{m}$   $\text{Ca}_2\text{Yb}_8(\text{SiO}_4)_6\text{O}_2$  apatite layer as the reaction product, producing a network of fine porosity (< 10  $\mu\text{m}$ ) as the inter-splat boundary material is consumed. After exposure for 48 h, CMAS has completely infiltrated all three coatings, with apatite crystals present across the coatings, up to a depth of ~550  $\mu\text{m}$ . Despite the extensive CMAS infiltration and apatite formation, no damage could be observed in any of the coatings, providing a promising first step for environmental barrier abrasible coatings.

## 5.1. Introduction

SiC/SiC ceramic matrix composites (CMCs) are expected to unlock the next breakthrough in gas turbine engines for aerospace and energy generation. Their increased service temperature and superior strength at high temperatures compared to Ni-based super-alloys, today's standard for components in the hot section of gas turbines, present a promising prospect in terms of efficiency and weight reduction [5]. Under a clean, dry oxygen atmosphere, CMCs show adequate oxidation and corrosion resistance due to the formation of a protective SiO<sub>2</sub> layer [67]. Nevertheless, under the presence of steam [70] (a naturally occurring combustion product) or corrosive species [68,76], CMCs can show accelerated corrosion. The presence of these corrosive species is caused by the ingestion of debris during take-off and landing, when flying over arid environments or due to the presence of airborne volcanic ash. Due to the varied nature and composition of these corrosive species, generally containing CaO, MgO, Al<sub>2</sub>O<sub>3</sub> and SiO<sub>2</sub> in different proportions, the term CMAS (calcium magnesium aluminosilicates) was coined as an umbrella designation for these corrosive species [218].

In order to provide CMCs with reliable protection during service, environmental barrier coatings (EBCs) were introduced. The goal of a successful EBC is to hinder the access of the corrosive species to the CMC component underneath while maintaining its integrity to protect during extended periods of time. The current generation of EBCs is formed by a rare earth silicate as the top layer, being the one in direct contact with molten CMAS during service. From the plethora of rare earth silicates currently identified [219], ytterbium disilicate (Yb<sub>2</sub>Si<sub>2</sub>O<sub>7</sub>, referred to as YbDS in this work) stands as a promising candidate due to its close CTE match to that of SiC (3.6 – 4.5 x 10<sup>-6</sup> K<sup>-1</sup> for YbDS [83] and 4.5 – 5.5 x 10<sup>-6</sup> K<sup>-1</sup> for SiC [82]), absence of phase transformation at high temperature, adequate silica volatilisation under steam environments and low thermal conductivity at high temperatures (~2 W m K<sup>-1</sup> at 1000 °C) [86].

Several studies have reported the interaction between YbDS and CMAS of varying compositions. The protocol followed varied between each study: two sintered bodies of YbDS and CMAS in contact at high temperatures [128], CMAS on top of sintered YbDS [130] or thermal sprayed YbDS coatings [135,136], and mixed YbDS and CMAS powders [124,133]. Several factors play a role in the study of the interaction between YbDS and CMAS: temperature and duration of the exposure, environment, phase purity, CMAS composition, production method for the YbDS and microstructure of the YbDS.

Little reaction at 1300 °C between YbDS pellets and CMAS was reported by Stolzenburg *et al.* [133], although extensive infiltration of the CMAS into the YbDS pellet was observed. CMAS was present 1 mm away from the YbDS/CMAS interface after 96 h. Limited reaction and formation of Yb-apatite was reported after 1 h at 1500 °C by Turcer *et al.* [130], with extensive infiltration once more after 24 h. The infiltration of CMAS caused the so-called “blister” damage, also reported by Zhao *et al.* [135] after 100 h at 1300 °C, although the presence of YbDS and ytterbium monosilicate (YbMS) in the thermal sprayed coating caused the combination of apatite formation and blister damage. Liu *et al.* [128], on the other hand, reported considerable reaction between YbDS and CMAS without the appearance of large apatite crystals, showing pore formation instead, although the test was conducted at 1400 °C under steam environment, making it difficult to draw clear conclusions. Stokes *et al.* [124] reported the preferential formation of apatite as the temperature is increased from 1200 °C to 1400 °C, also exploring the effect of leaner Ca compositions, with no reaction detected with a ~7 mol.% of CaO.

Despite the plethora of studies looking at the interaction between CMAS and rare earth silicates, there is a lack of literature where thermal sprayed coatings (which have varying levels of porosity and rarely present phase purity), and not powder or sintered bodies, are studied [135,136]. Due to this scarcity of publications, there is little knowledge on the desirable

microstructure and phase composition, since studies typically present the effect of one coating with a given microstructure and phase composition, being difficult to draw general conclusions.

Porosity, in particular, is a parameter that is worth studying in more detail since certain applications of these materials require certain levels of porosity, such as abradable coatings [145]. However, in order to provide gas-tight protection against the ingress of steam in water-containing environments, low porosity has been preferred when depositing EBCs [107]. Nevertheless, no study has been conducted on the effect that varying porosity levels have on the thermal sprayed YbDS/CMAS interaction. If EBC abradable coatings are to be considered for service, further research into this correlation is needed.

Due to the prevalence of thermal spraying methods for the deposition of environmental barrier coatings in the aerospace industry, this work aims to study the interaction of molten CMAS with three different free-standing coatings, all of them being produced using air plasma spraying (APS) but showing varying porosity levels (low porosity for EBC and high porosity for abradable). To evaluate the effect molten CMAS has on these thermal sprayed YbDS, exposure to CMAS at 1350 °C in air was conducted for 1 h and 48 h. This study, therefore, seeks to investigate the CMAS on thermal sprayed coatings produced in accordance with standards for commercial applications.

## **5.2. Experimental methods**

### **5.2.1. Free-standing coatings**

Three different free-standing YbDS coatings were studied in this work, all of them produced using air plasma spraying (APS). Free-standing coatings were chosen to study the interaction between the YbDS and the CMAS without the interaction of a Si bond coat or SiC substrate. The first one, labelled in this work as EBC SG-100, was a ~350 µm thick ytterbium disilicate (YbDS) environmental barrier coating which had a 1 wt.% of alumina powder added to the

feedstock prior to spraying. The coating was produced using Treibacher Industrie AG (Austria) YbDS powder through a Praxair Surface Technology (USA) SG-100 plasma spray gun. The second free-standing coating, labelled as ABR SG-100, was a ~500  $\mu\text{m}$  thick YbDS abrasible coating which had a ~1.5 wt.% of polyester powder added to the feedstock prior to spraying. The coating was also deposited using a Praxair Surface Technology (USA) SG-100 plasma spray gun, but this time the YbDS powder was provided by Oerlikon Metco AG (Switzerland). The third free-standing coating, labelled here as ABR F4, was a ~1000  $\mu\text{m}$  thick YbDS abrasible coating which also had a ~1.5 wt.% of polyester powder added to the feedstock prior to spraying. The coating was deposited using an Oerlikon Metco F4 plasma spray gun using the same Oerlikon Metco YbDS powder as with ABR SG-100. Both the Treibacher and Oerlikon YbDS powders were manufactured to conform to a nominal composition of 22 – 24 wt.%  $\text{SiO}_2$  and balance of  $\text{Yb}_2\text{O}_3$ , with a maximum of 5 vol.% of unreacted  $\text{Yb}_2\text{O}_3$  and YbMS. All three free-standing coatings were cut to produce samples with dimensions of 2.5 x 1.5  $\text{cm}^2$ . Previous to any CMAS exposure, all samples were heat treated in order to crystallise the amorphous content. Samples were annealed at 1200  $^\circ\text{C}$  for 2 h in air, with a heating rate of 5  $^\circ\text{C}/\text{min}$ .

### **5.2.2. CMAS exposure**

The CMAS powder used for the exposure tests was manufactured by Oerlikon Metco with a nominal composition of 35 CaO – 10 MgO – 7  $\text{Al}_2\text{O}_3$  – 48  $\text{SiO}_2$  in mol %. CMAS powder was mixed with deionised water in a 1:5 ratio by weight and thoroughly homogenised using a roller mixer. For the application of the CMAS slurry to the free-standing coatings, first, the surface area of the samples was measured to ensure a coverage of approximately 15  $\text{mg}/\text{cm}^2$ . The CMAS concentration was chosen according to OEM protocol which is also in line with the guidance from the high temperature community. Then, in order to facilitate the evaporation of the deionised water on the CMAS slurry, the samples were placed on a hot plate at ~100  $^\circ\text{C}$ .

While the samples were being heated, the CMAS slurry was placed on a Fisherbrand (UK) Isotemp hot plate stirrer at ~60 °C to further facilitate evaporation upon deposition and to ensure that the slurry remains well mixed. Once the samples were hot, a brush was dipped in the CMAS slurry and used to deposit a thin layer on top of the coatings. Once the water had completely evaporated, the sample was weighted and another pass of the brush was done if needed, slowly building up the CMAS concentration to the desired 15 mg/cm<sup>2</sup> concentration.

Two sets of CMAS-coated samples were heat treated at 1350 °C in air, using a heating rate of 10 °C/min, on an Elite Thermal Systems Ltd. (UK) BRF14/5 box furnace. All the samples were placed on top of 22 mm sapphire discs (PI-KEM, UK) to prevent any reaction between the samples and the furnace. The first set of samples was maintained at said temperature for 1 h before cooling down inside the furnace at a rate of 10 °C/min. The second set of samples was heat treated for 48 h, maintaining the rest of the parameters equal.

### **5.2.3. Material characterisation**

Phase identification of the feedstock powder, free-standing coatings and CMAS-exposed samples was performed using a D8 Advance Da Vinci diffractometer (Bruker, Germany) with Cu cathode (wavelength of 1.5406 Å) using Bragg-Brentano scanning mode. The angular range investigated was from 10° to 70° with a step size set to 0.02° and a dwell time of 0.3 s for all the measurements.

To investigate the microstructure of the free-standing coatings, the samples were cold mounted through vacuum impregnation using EpoFix resin and hardener (Struers, Denmark). Once the resin was fully cured, the samples were cut using a low speed saw and remounted using the same method as already described. The now exposed cross-section of the coatings was then ground and polished to a 1 µm finish using SiC grinding papers (Buehler, Germany).

Scanning electron microscope (SEM) images were taken using a Quanta 600 (FEI Europe, Netherlands). Porosity was calculated as the average measurement across three backscattered electron (BSE) images of representative regions of the coating. All the images were taken with a magnification of 400x, accelerating voltage of 15 kV and spot size of 5 nm. To do the porosity measurement, the open source software “ImageJ” with the image processing package “Fiji” was used [212]. To do so, BSE images were converted into black and white maps upon setting a threshold. Then, the automated function “Analyze particle” was employed, which measured the area percentage of the image covered by porosity, returning an overall value per image. An average of the three images of each coating was calculated, being the standard deviation used as the error. BSE images were also used to measure the thickness of the reaction and infiltration layers. The reaction layer was defined as the area at the CMAS/coating interface where reaction products (apatite crystals in this case) could be detected. The CMAS infiltration layer was defined as the area of the coating in which CMAS could be detected, be it through Ca mapping or BSE imaging.

Thermogravimetric analysis (TGA) and differential scanning calorimetry (DSC) was conducted in a TA Instruments SDT-Q600 thermobalance (Australia) in order to determine the melting point of the CMAS powder. A temperature profile of 10 °C/min from room temperature up to 1400 °C in static air was applied.

## **5.3. Results**

### **5.3.1. Powder and coating characterisation**

SEM imaging of the feedstock powder for the EBC and ABR coatings was conducted in order to better understand the microstructure of the deposited coatings and CMAS interaction. Figure 55 shows a backscattered image of the two powders.

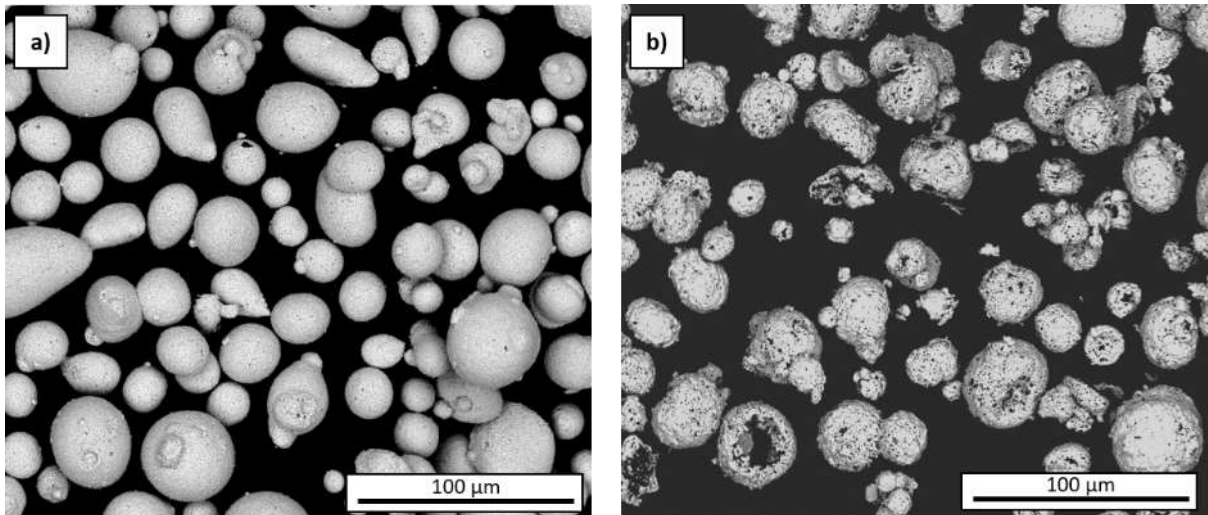


*Figure 55: BSE images of the powders used in this work: a) corresponds to sample EBC, b) corresponds to samples ABR*

As shown in Figure 55a, the EBC powder is mostly spherical, with few defects and a smooth surface on all of the particulates. ABR powder, as shown in Figure 55b, also has a mostly spherical morphology; however, in this case, the particulates show porosity in the surface, even with some of them appearing to have a hollow core.

As mentioned in the Experimental Methods section, the three coatings were annealed to crystallise the amorphous content, with the annealed sample visible in the SEM images presented in Figure 56.

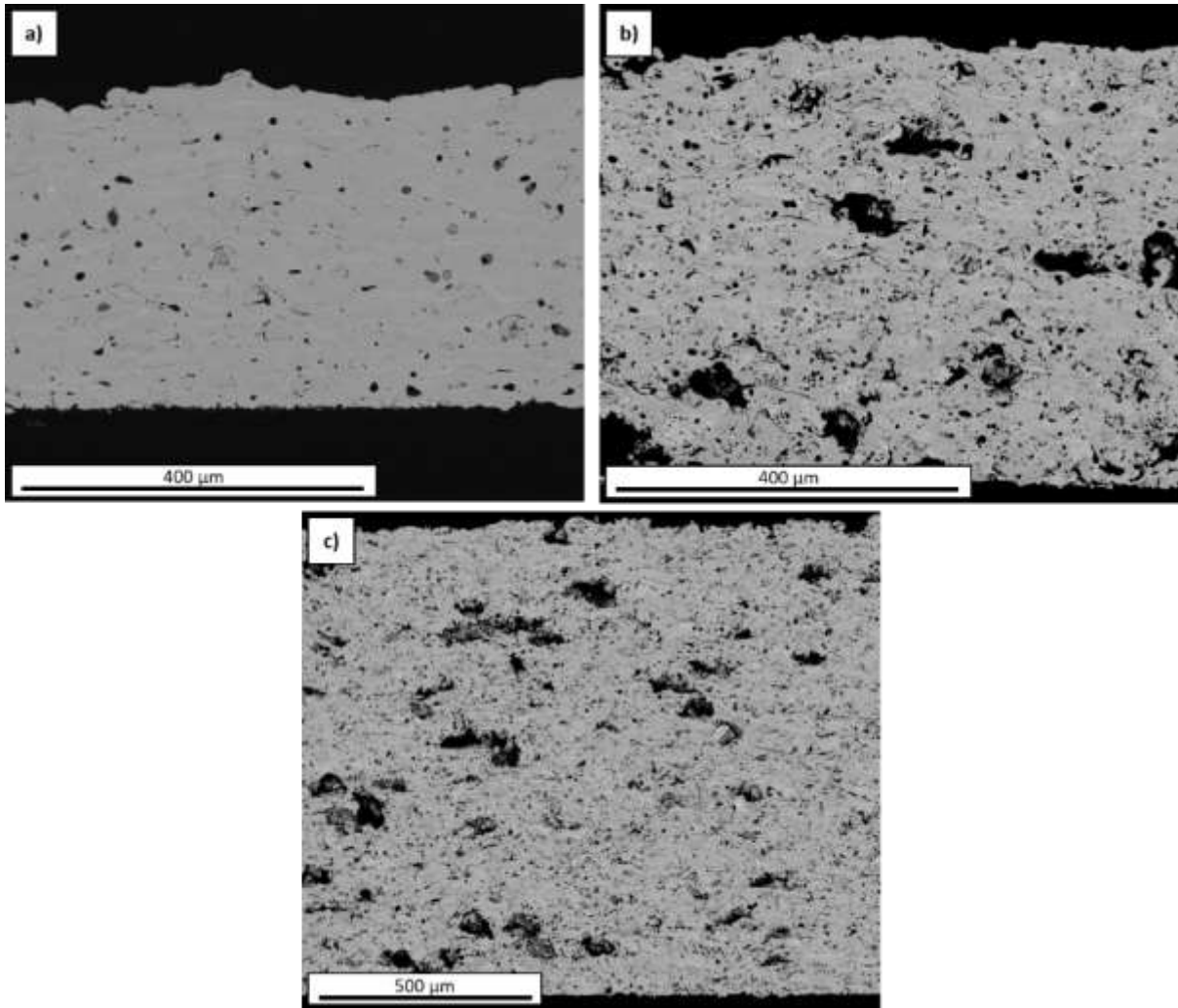


*Figure 56: BSE images of the three free-standing coatings after annealing. Image a) shows EBC SG-100, b) ABR SG-100 and c) ABR F4*

From the SEM images in Figure 56, it can be seen that the sample EBC SG-100 has a lower porosity and thickness than the two ABR coatings. This qualitative observation is confirmed by the porosity measurements, indicating that coating EBC SG-100 has a porosity of  $2.4 \pm 0.3$  %, with ABR SG-100 having a value of  $21.3 \pm 1.1$  % and ABR F4 being  $19.4 \pm 4.0$  %. This higher porosity level in the ABR samples was expected, as the addition of polyester to the feedstock powder and subsequent burn off stage during the annealing was meant to produce porosity within the coatings. For the thickness, the values measured for each coating were  $368.6 \pm 10.4$   $\mu\text{m}$  for the EBC SG-100 coating,  $509.9 \pm 9.2$   $\mu\text{m}$  for ABR SG-100 and  $1099.7 \pm 12.7$

$\mu\text{m}$  for ABR F4. Thickness for the EBC SG-100 sample was selected in line with traditional EBCs, whereas the two abrasible coatings were chosen to present one thickness closer to EBCs (ABR SG-100 sample) and one with a higher thickness (ABR F4).

Regarding the phase composition of both the feedstock powders, the as-sprayed coatings and the annealed coatings, Figure 57 shows the XRD diffractogram for each set of samples.

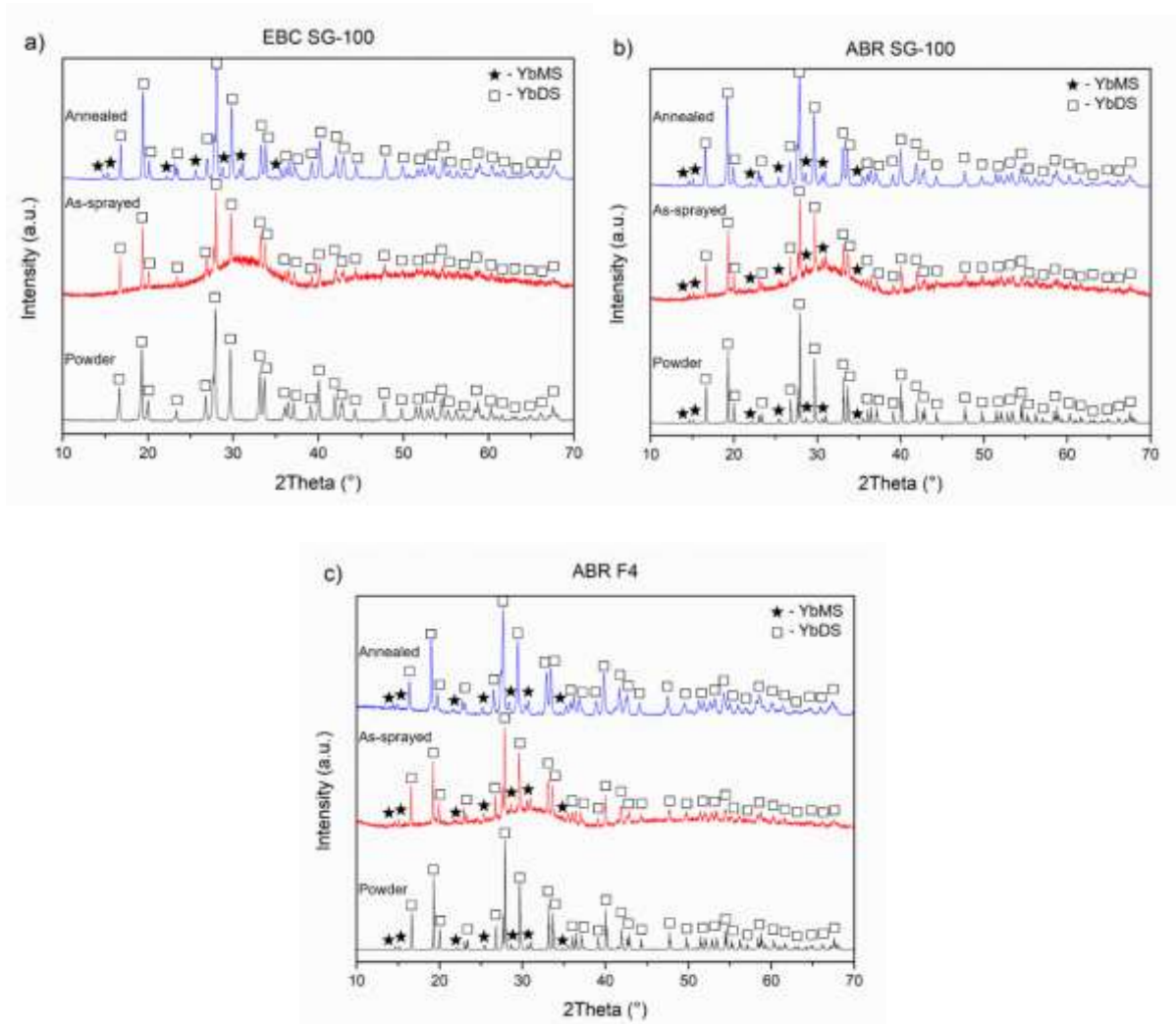


Figure 57: XRD measurements for a) EBC SG-100, b) ABR SG-100 and c) ABR F4. On each graph, bottom plot corresponds to the powder, middle to the as-sprayed coating and top to the annealed coating. Phases have been identified with a star (★) for YbMS and a square (□) for YbDS

In the case of the EBC powder (Figure 57a), only peaks corresponding to the YbDS phase (PDF card number 00-082-0734) could be detected. For the ABR powder (Figure 57b and c), there is a small amount of YbMS phase (PDF card number 00-040-0386) as indicated by the small double peaks at  $\sim 15^\circ$ . In the as-sprayed samples, EBC SG-100 coating shows only presence of YbDS, whereas ABR SG-100 and ABR F4 are mostly YbDS with a small amount of YbMS. In addition to the mentioned crystalline peaks, all the three as-sprayed coatings present two broad amorphous humps, centred on  $\sim 30^\circ$  and  $\sim 55^\circ$ . Once the coatings have been annealed, the amorphous content evolved by crystallisation, and the samples can be considered to be fully crystalline. All three samples now show peaks indicating mostly YbDS with a small quantity of YbMS.

### **5.3.2. 1 h CMAS exposure**

The cross-section of the 1 h CMAS exposed samples can be seen in Figure 58.

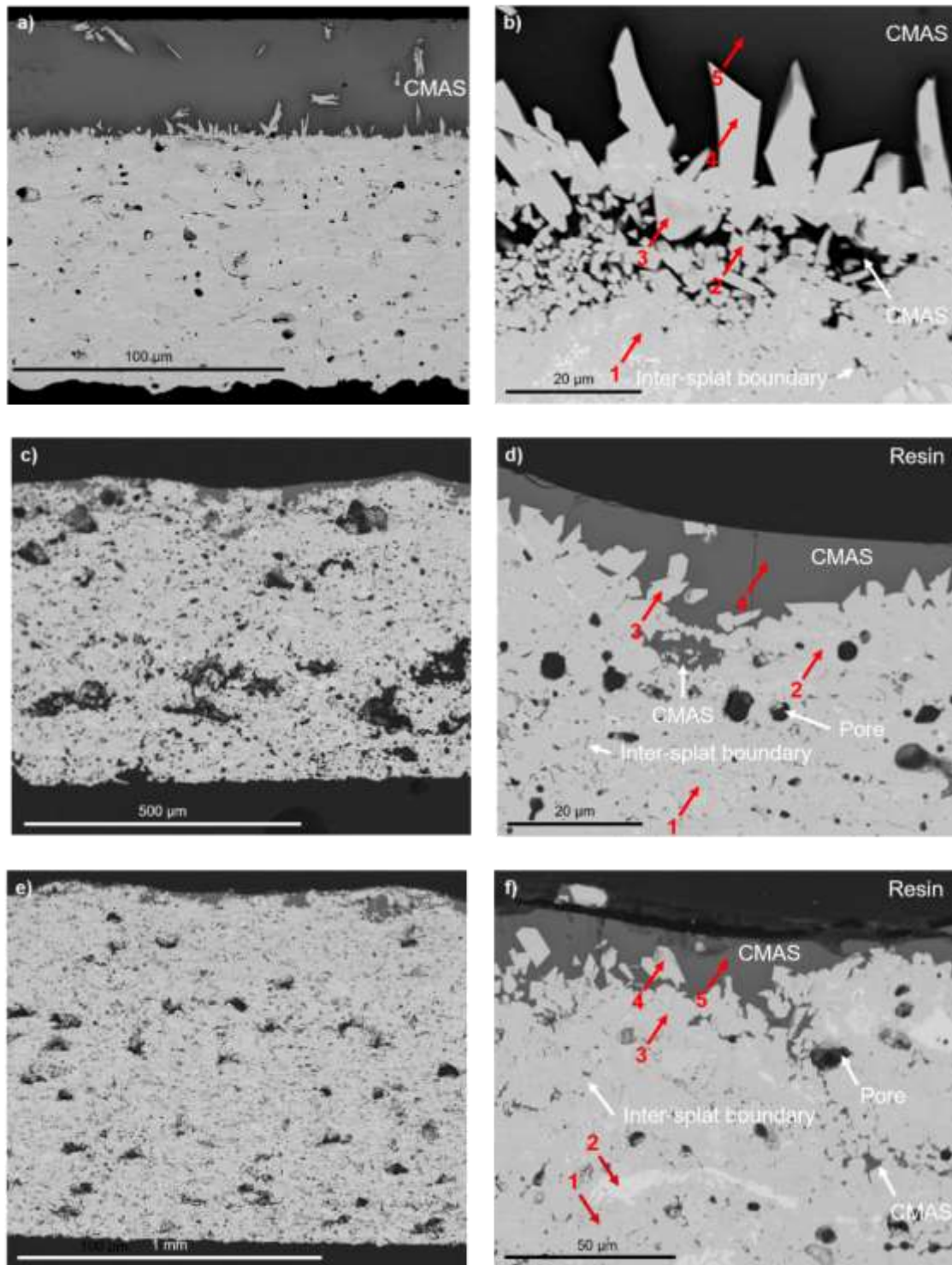


Figure 58: BSE images of the cross-section of the coatings exposed to 15 mg/cm<sup>2</sup> of CMAS for 1 h. Images a) and b) correspond to sample EBC SG-100, images c) and d) to ABR SG-100 and e) and f) to ABR F4. Arrows with numbers indicate where EDS analysis was performed, with the quantification shown in Table 4. To facilitate identification, CMAS, pores, inter-splat boundaries and mounting resin have been labelled with arrows

The CMAS powder used here has a melting point of  $\sim 1250$  °C, as determined from the DSC measurements, as shown in Figure 59. Since the exposure temperature was 1350 °C, the CMAS is expected to be fully molten.

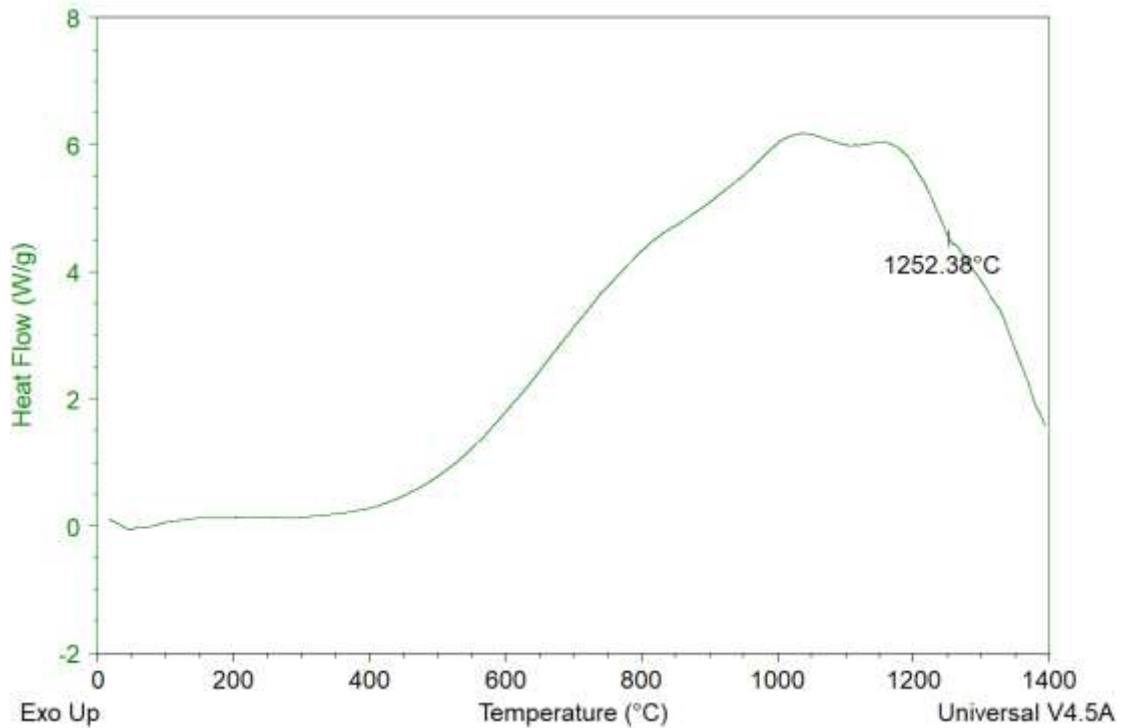


Figure 59: DSC measurement of the CMAS, with the melting point labelled

From the images presented in Figure 58, clear differences can be seen between the various coatings. Sample EBC SG-100 shows little consumption of the CMAS deposited in the surface, as shown in Figure 58a, where a layer of  $\sim 170$   $\mu\text{m}$  of CMAS is still present on top of the coating. A more detailed view of the CMAS/coating interface is depicted in Figure 58b, where the limited reaction between the CMAS and the coating can be observed. This reaction layer was measured to have a thickness of approximately  $\sim 15$   $\mu\text{m}$ . Needle-like crystals are present at the surface, with a CMAS deposit seen underneath with smaller crystals embedded. Such reaction products can be associated with Yb-containing apatite, as shown in Table 4. This type of microstructure has also been reported on APS YbDS coatings by Zhao *et al.* [135]. In order to determine how far the CMAS had penetrated within the coating and to distinguish CMAS

from porosity, EDS elemental mapping was conducted on all three samples, and the Ca map over the BSE image is shown in Figure 60. Ca mapping was chosen as it is a good indication of the presence of CMAS within the coating. From the Ca distribution in Figure 60a, it can be seen that only a small amount of Ca is detected within the EBC SG-100 coating. The CMAS infiltration layer was estimated to have a thickness of approximately  $\sim 50 \mu\text{m}$ .

In the case of ABR SG-100, depicted in Figure 58c and d, there is barely any CMAS remaining on top of the coating, with some areas even showing no presence of CMAS. Despite this absence of CMAS, there is little evidence of reaction between the CMAS and the coating, as shown in Figure 58d. Some apatite crystals are present, but the reaction is quite limited. This observation is confirmed by the thickness of the reaction layer, which is approximately  $\sim 10 \mu\text{m}$ . Regarding CMAS infiltration, shown in Figure 58b, and contrary to sample EBC SG-100, ABR SG-100 shows a higher degree of Ca present within the coating. Since Figure 60 superimposes the Ca map with the BSE image, it can be seen that this infiltrated CMAS is located where fine porosity is present. This higher degree of infiltration is reflected in the thickness of the CMAS infiltration layer, which was  $\sim 150 \mu\text{m}$ .

The behaviour of the ABR F4 coating is quite similar to that of ABR SG-100. Only a thin layer of CMAS is present at the surface of the coating (as shown in Figure 58e), and despite the presence of apatite crystal at the CMAS/coating interface, the reaction can be described as limited after 1 h. Indeed, the thickness of the reaction layer is approximately  $\sim 12 \mu\text{m}$ . The EDS performed in the spots marked in Figure 58f confirms the presence of YbMS, seen as a brighter phase in the BSE images, and measured in spot 2 in the ABR F4 coating shown in Table 4. From the Ca map shown in Figure 60c, there can be seen once more evidence of CMAS infiltration following along the fine porosity present in the coating. The degree of infiltration of CMAS is similar to that of ABR SG-100, measured to have a thickness of approximately  $\sim 200 \mu\text{m}$ .

Table 4: EDS measurements (in weight %) of the CMAS exposed samples for 1 h. The spots correspond to the arrows in Figure 58

	Spot	Yb	Si	O	Ca	Mg	Al
EBC SG-100	1	21.8	18.2	60.0	---	---	---
	2	21.0	18.5	60.0	0.5	---	---
	3	18.9	19.1	60.5	1.5	---	---
	4	21.1	18.1	60.3	0.5	---	---
	5	2.6	19.6	58.6	11.5	2.7	5.0
ABR SG-100	1	22.0	17.7	60.3	---	---	---
	2	22.2	17.7	60.1	---	---	---
	3	21.4	17.8	60.6	< 0.5	---	---
	4	2.3	19.2	59.0	11.8	3.0	4.7
ABR F4	1	22.6	17.5	59.9	---	---	---
	2	29.2	11.7	59.1	---	---	---
	3	19.2	17.3	60.8	2.2	< 0.5	---
	4	20.0	17.5	62.3	< 0.5	---	---
	5	2.1	19.1	59.5	11.7	3.0	4.6

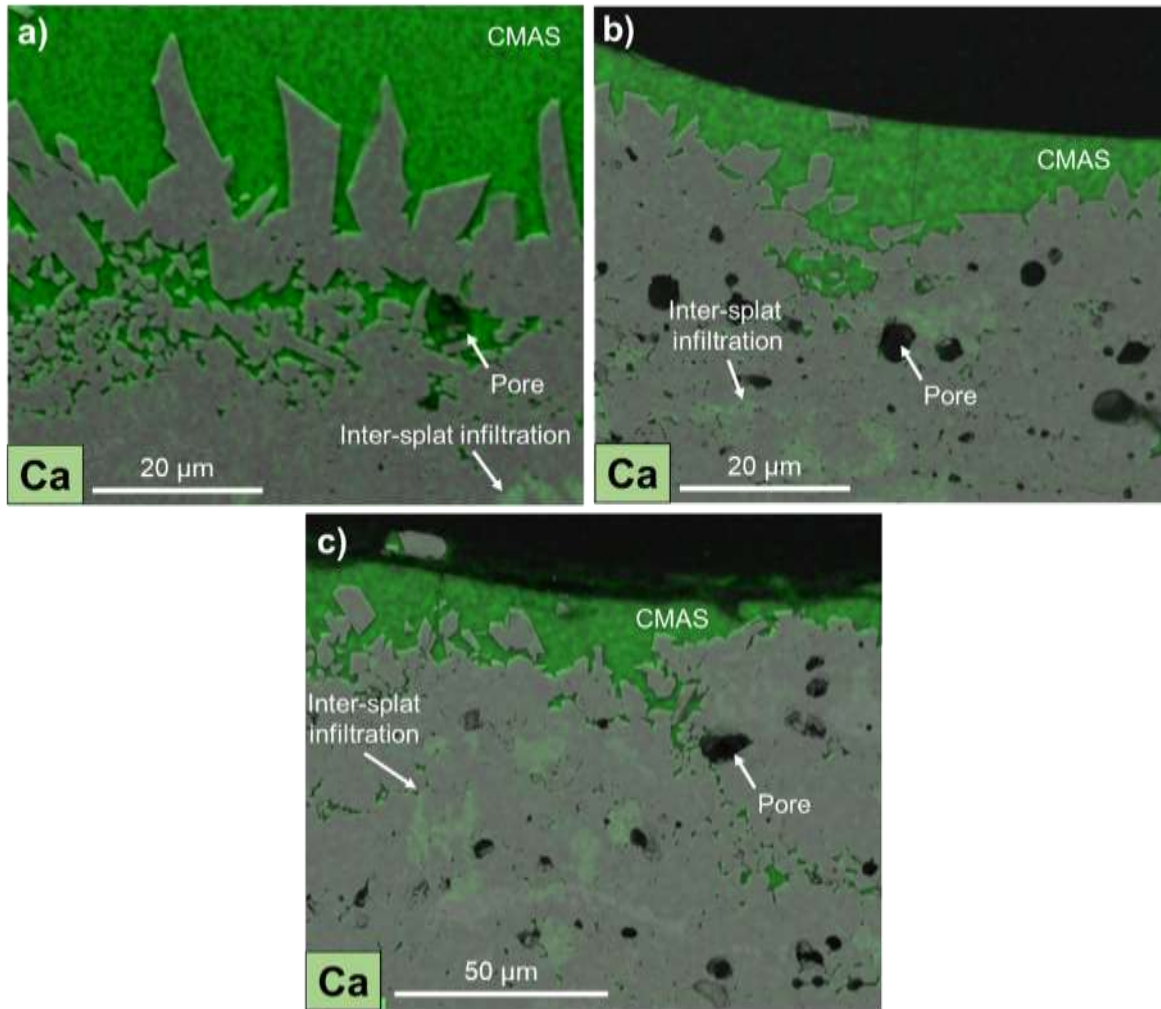


Figure 60: Ca maps superposed with BSE image of coatings a) EBC SG-100, b) ABR SG-100 and c) ABR F4 exposed to CMAS for 1 h

### 5.3.3. 48 h CMAS exposure

The cross-section images of the exposed samples are shown in Figure 61, along with the superimposition of the BSE image with the Ca map.

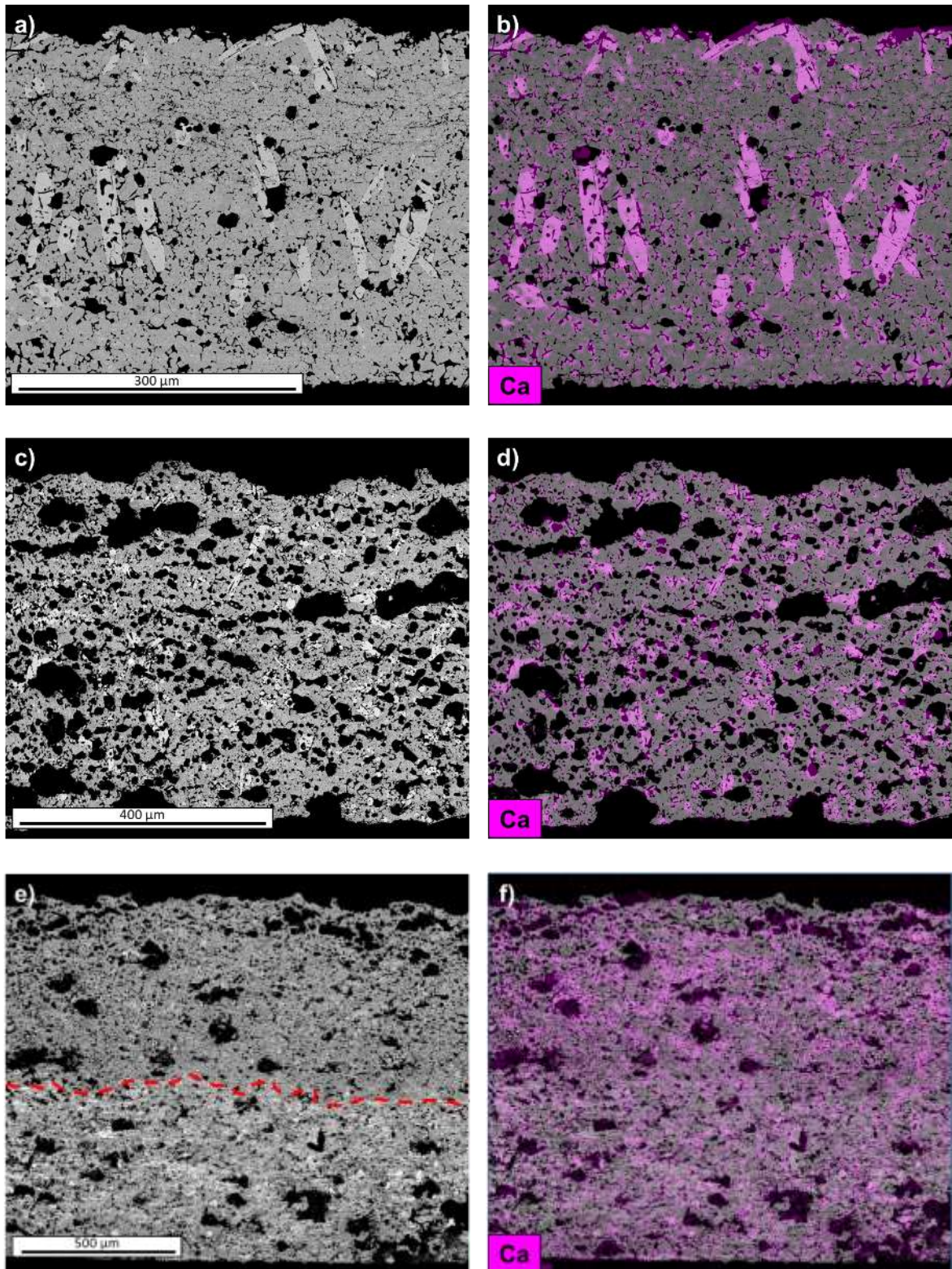
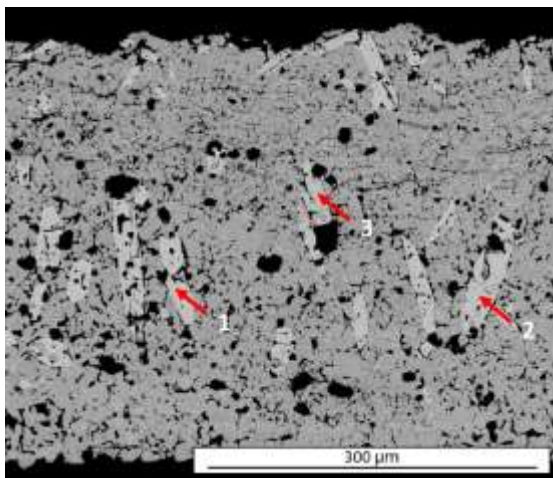


Figure 61: BSE images and superposed Ca maps for a-b) EBC SG-100, c-d) ABR SG-100 and e-f) ABR F4 exposed to CMAS for 48 h. The dotted line in Figure 6e marks the point where YbMS could still be found

The BSE image of the cross section of sample EBC SG-100 after CMAS exposure for 48 h, depicted in Figure 61a, clearly shows the presence of large (~150  $\mu\text{m}$ ) crystals scattered across the entire thickness of the coating. Both the reaction and CMAS infiltration layers can be described as covering the entire thickness of the coating. EDS measurements of these crystals, shown in Figure 62, along with the Ca mapping present in Figure 61b determine these structures to be Yb-containing apatite, as seen in the 1 h samples.



Spot	Yb	Si	O	Ca
1	70.8	7.1	18.4	3.7
2	71.4	7.1	17.8	3.7
3	71.1	7.2	17.9	3.8

*Figure 62: BSE image of sample EBC SG-100 after CMAS exposure for 48 h, along with EDS analysis of the crystals observed*

Another evident effect of the CMAS exposure is the increase in the porosity level, with the appearance of both fine porosity (< 10  $\mu\text{m}$ ) and larger pores (>10  $\mu\text{m}$ ). This is confirmed by the porosity measurements, which shows a porosity level of  $13.3 \pm 0.9 \%$  for EBC SG-100 after CMAS exposure for 48 h, in comparison with the initial  $2.4 \pm 0.3 \%$  of the annealed sample. A more detailed study of the Ca map in Figure 61b reveals infiltrated CMAS along with the finer porosity (< 10  $\mu\text{m}$ ) all across the coating, whereas larger pores generally do not present any Ca signal. Secondary electron SEM images were used to confirm that all the features identified as pores in the BSE images were indeed porosity, as shown in Figure 63.

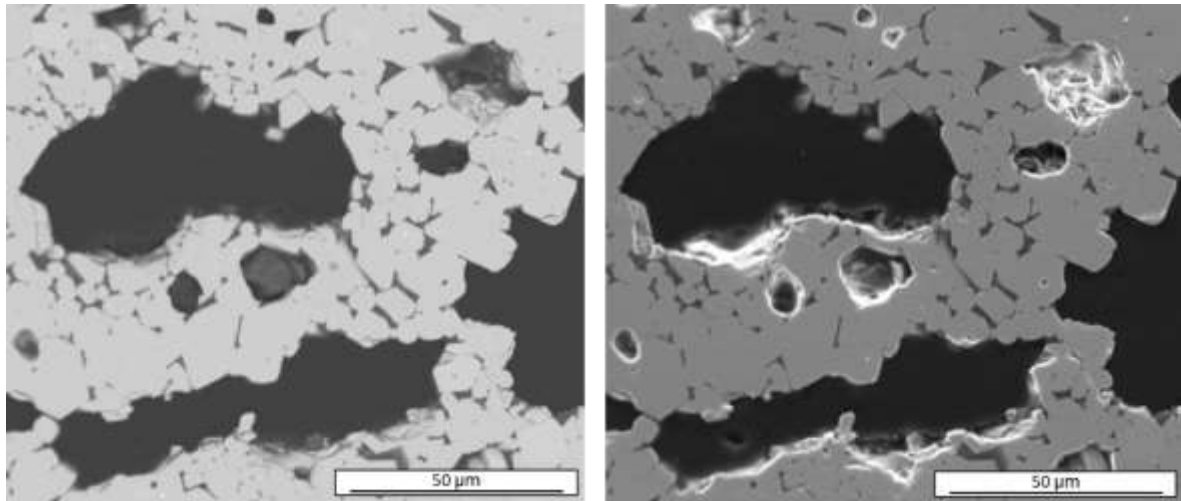


*Figure 63: SEM images of sample SG-100 exposed to CMAS for 48 h. Image on the left corresponds to backscattered electron imaging and image to the right to secondary electron imaging. As shown, empty pores appear as such regardless of the imaging mode, with features present within pores also visible no matter the imaging mode*

Those that showed Ca signal within the pore also presented CMAs presence were imaged using secondary electron SEM. A final observation, not clearly visible in Figure 61 due to the contrast/brightness chosen to identify the apatite crystals, is the absence of YbMS phase, although this affirmation is further discussed following the XRD measurements.

In the case of ABR SG-100, seen in Figure 61c and d, the phenomena observed are similar to those described for EBC SG-100. There is a presence of large apatite crystal scattered across the entirety of the coating, visible in Figure 61c, although their size is slightly smaller than those found on EBC SG-100, perhaps due to the increased level of porosity of this coating, acting as a physical constrain to the crystal growth. Once more, both the reaction and CMAS infiltration layers are as thick as the coating. The total porosity of the coating is also increased after the 48 h CMAS exposure, being measured at  $33.5 \pm 2.4 \%$ , compared to  $21.3 \pm 1.1 \%$  of the annealed sample. As with the EBC SG-100, there was no discernible presence of YbMS phase.

Finally, the BSE image and Ca map of sample ABR F4 shown in Figure 61e and f, present a different picture. As shown in Figure 61e and marked with a dotted line, the lower half of the coating still shows the presence of a brighter phase that did not correspond with apatite crystals. EDS measurements (not shown here) confirm that this phase is YbMS that has not reacted with CMAS. The upper half of the coating still presents apatite crystals, with a size and distribution similar to those seen in ABR SG-100. In this case, the reaction layer was measured to be approximately  $\sim 550 \mu\text{m}$ , whereas the infiltration layer still corresponds to the entire thickness of the coating ( $\sim 1 \text{ mm}$ ).

XRD measurements were performed on both sets of samples, those exposed to CMAS for 1 h, and those exposed for 48 h. The results can be seen in Figure 64. For better identification of the phases, a detailed view of the  $20^\circ - 35^\circ$  range has been plotted.

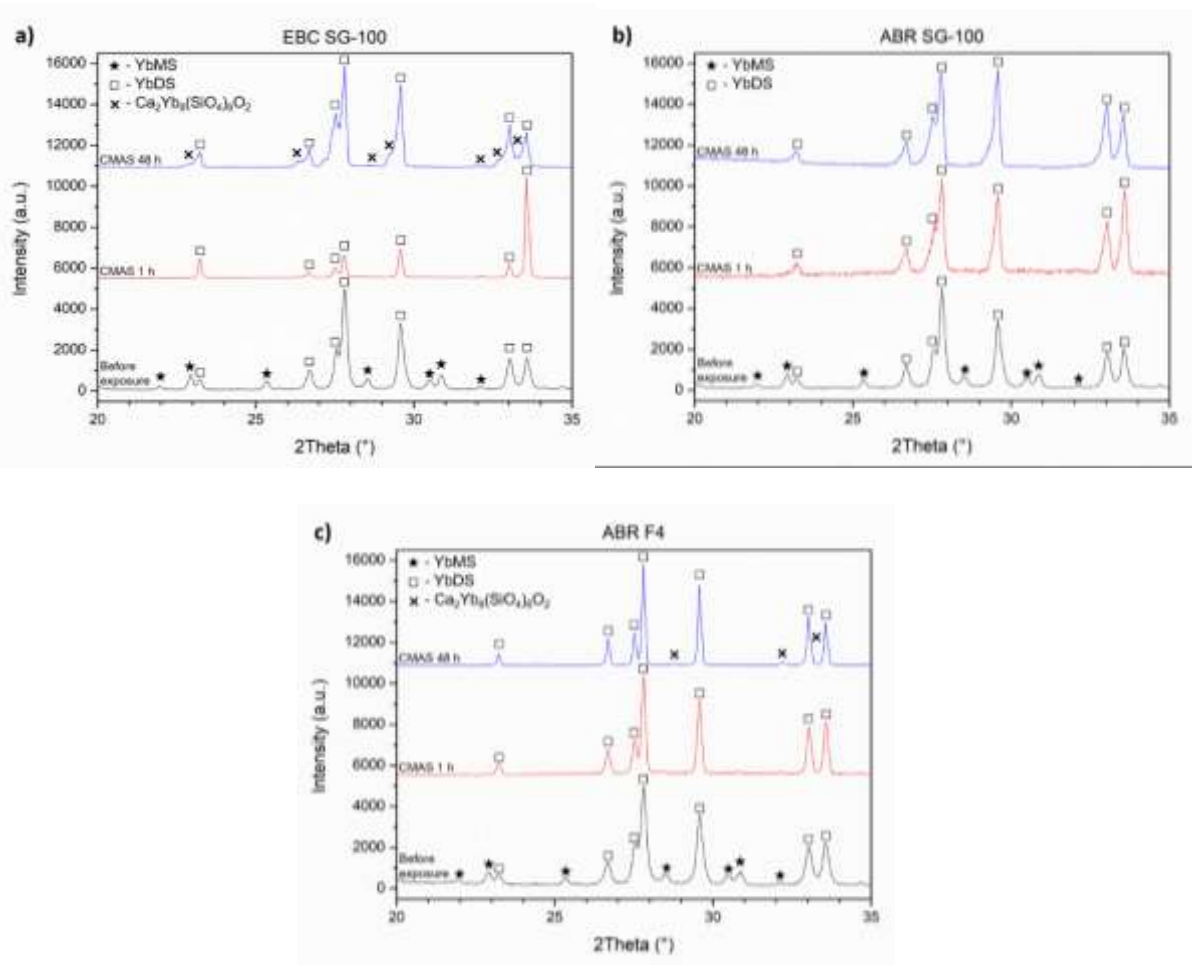


Figure 64: XRD measurements of the coatings before exposure (bottom), exposed to CMAS for 1 h (middle) and exposed to CMAS for 48 h (top) of samples a) EBC SG-100, b) ABR SG-100 and c) ABR

F4

The XRD diffractograms for the annealed coatings, bottom plots in Figure 64, shows that in all of the three samples the initial phase composition is mainly made of YbDS with a small amount of YbMS. Once the samples have been exposed to CMAS for 1 h, none of the three diffractograms shows peaks corresponding to the YbMS phase, with only YbDS detected. In sample EBC SG-100, peak intensity at 27 - 28° is reduced compared to the non-exposed sample and the 1 h exposed abrasable samples, with peak intensity at ~34° being increased, as can be seen in Figure 64a. This effect may be attributed to the presence of a thicker CMAS layer on top of sample EBC SG-100 as shown in Figure 58. When the CMAS exposure was extended

to 48 h, the EBC SG-100 sample showed clear evidence of the presence of a new phase, as marked in Figure 64a. This phase can be associated with the reaction product of the CMAS/YbDS interaction, corresponding to a hexagonal silicate oxyapatite,  $\text{Ca}_2\text{Yb}_8(\text{SiO}_4)_6\text{O}_2$ , with ICDD PDF card 04-006-0320. Some of the peaks associated with this new phase can be detected in the ABR F4 sample, as seen in Figure 64c, but they were not found in the ABR SG-100 sample. The reason for the lack of apatite peaks in ABR SG-100 after 48 h can be observed in Figure 61d. Although apatite crystals are clearly present, their presence close to the surface is minimal. XRD penetration for coatings with this composition is approximately 10 – 15  $\mu\text{m}$  [220], being the apatite content in this region below the detection limit for this technique.

#### 5.4. Discussion

CMAS interaction with rare earth silicates is often studied based on composition alone; however, porosity also plays an important role, particularly if abrasion resistant coatings are to be considered. The three coatings studied here presented mostly YbDS after the annealing process, as shown in Figure 57. This result was to be expected since the feedstock powder used for deposition had high phase purity. In the case of the ABR powder, a small amount of YbMS could be detected, which resulted in a small amount of YbMS in the as-sprayed ABR coatings. Additionally, due to the environment experienced during APS deposition, preferential volatilisation of  $\text{SiO}_2$  leads to the formation of a small amount of an amorphous phase with YbMS stoichiometry [221], in amorphous form due to the rapid cooling experienced by the splats upon impact with the substrate [106]. The annealing process removes the amorphous content, leading to highly crystalline coatings. In terms of microstructure, the differentiating factor between the coatings was the level of porosity present. Sample EBC SG-100 had a low level of porosity,  $2.4 \pm 0.3 \%$ , in line with the requirements of optimised EBCs, where gas-tight protection against the environment is required [219]. In the case of samples ABR SG-100 and ABR F4, polyester was added to the feedstock powder to act as a pore former once burnt

off, which resulted in porosity levels of  $21.3 \pm 1.1 \%$  and  $19.4 \pm 4.0 \%$ , respectively. This higher porosity content, not generally seen in EBC coatings, is a requirement for abradable coatings to ensure correct abrasion and the creation of a successful seal.

The reduced porosity of sample EBC SG-100 might explain the hindered infiltration of CMAS seen in samples exposed for 1 h. As shown in Figure 58, EBC SG-100 presented a thick layer of CMAS still located on top of the coating, contrary to the abradable samples, where CMAS showed a higher degree of infiltration. It seems that the initial stage of the interaction between the YbDS coatings and molten CMAS was the infiltration of molten CMAS into the coating following existing porosity. This can be observed in Figure 58b and c, where pores were filled with CMAS (labelled accordingly in the figure), but no reaction products were visible. Nevertheless, as it has already been reported in the literature, porosity is not the preferential path for infiltration of CMAS into YbDS [124,128,130,133]. Here, evidence of inter-splat boundary infiltration could be found on all three samples, as shown in Figure 58, although it was more predominant in the two abradable coatings. Evidence of inter-splat boundary infiltration can be seen after exposure for 1 h in Figure 58 and 48 h in Figure 61. In the latter, the longer exposure times created a network of finer porosity ( $< 10 \mu\text{m}$ ) caused by the consumption of the inter-splat material by the infiltrated CMAS. The presence of residual CMAS after 48 h can be detected in the Ca maps presented in Figure 61a, b and c. It could be suggested that open porosity facilitates the infiltration of molten CMAS in the early stages of the interaction, but it is replaced by inter-splat boundary diffusion as the interaction continues. This mechanism is supported by the absence of CMAS in larger pores after 48 h, contrary to the already mentioned CMAS in the inter-splat boundaries. The thickness of the CMAS infiltration layer after 1 h also supports this observation, being  $\sim 50 \mu\text{m}$  for EBC SG-100,  $\sim 150 \mu\text{m}$  for ABR SG-100 and  $\sim 200 \mu\text{m}$  for ABR F4.

After the initial stage of CMAS infiltration, the CMAS reacts with the YbMS present within the coatings to form apatite due to its higher CMAS reactivity compared to YbDS [124,128,130,133]. The reaction product was identified as hexagonal silicate oxyapatite,  $\text{Ca}_2\text{Yb}_8(\text{SiO}_4)_6\text{O}_2$ , as confirmed by EDS measurements (Table 4) and XRD analysis (Figure 64) of the coatings exposed for 48 h. The thickness of this reaction layer also shows different values for EBC and abrasible coatings. In EBC SG-100, the reaction layer after 1 h is  $\sim 15 \mu\text{m}$ ; whereas for ABR SG-100 and ABR F4 is  $\sim 10 \mu\text{m}$  and  $\sim 12 \mu\text{m}$ , respectively. Although the difference in thickness is less predominant here and could be due to experimental error, it could also be caused by the presence of a thicker layer of CMAS remaining on top of the EBC SG-100 coating. All three coatings were exposed to the same surface concentration of CMAS (initially the CMAS thickness was identical) which suggests a reduced infiltration rate in EBC SG-100. The reduced infiltration caused the CMAS/coating interface to experience a higher degree of reaction, leading to more apatite being formed. Another indication of this possibility can be found on the EDS measurements of the CMAS present in the surface (spot 5 for EBC SG-100, spot 4 for ABR SG-100 and spot 5 for ABR F4 in Table 4). It has been reported that the Ca:Si ratio in CMAS is directly linked to the formation of apatite [124,126], and since in all of the three samples the initial CMAS composition was the same, a difference in the Ca:Si ratio in the final CMAS could provide information of the degree of interaction that has taken place. The Ca:Si for EBC SG-100 after 1 h is 0.59, whereas for both ABR SG-100 and ABR F4 is 0.61. Although the difference, once more, is small, this could suggest that more Ca has reacted to form apatite, and it has been consumed, supporting a higher degree of surface reactivity than the abrasible samples, where infiltration was higher.

The samples exposed for 48 h show a very different behaviour, as can be seen in Figure 61. In the case of samples EBC SG-100 and ABR SG-100, the CMAS reaction layer and the infiltration depth were equal to the thickness of the coatings ( $\sim 350 \mu\text{m}$  for EBC SG-100 and

~500  $\mu\text{m}$  for ABR SG-100). On the other hand, sample ABR F4 presented a CMAS reaction layer of ~550  $\mu\text{m}$  with an infiltration depth equal to the thickness of the coating (~1000  $\mu\text{m}$ ). A similar degree of CMAS infiltration has been reported by Stolzenburg *et al.* [133], where bulk YbDS (with a porosity level of ~10%) was exposed to CMAS at 1300 °C for up to 96 h. In their work, small particles of YbMS can only be detected 1 mm away from the surface, suggesting a reaction layer with a thickness of 1 mm, in line with the levels of infiltration observed here.

It is worth noting that in all the samples, the CMAS reaction layer and the infiltration depth had different values. An exception to this was EBC SG-100 and ABR SG-100 after 48 h since the thickness of the coating was the limiting factor. This seems to indicate that the presence of infiltrated CMAS along YbMS does not warrant the immediate formation of apatite. This reaction seems to present slow kinetics, which would explain why in Figure 61f, showing ABR F4 after 48 h, there is the abundant presence of YbMS in the lower sections of the coatings, even if CMAS has infiltrated the entirety of the coating. In addition to the reaction kinetics, apatite formation is also dependent on the Ca:Si ratio, as previously mentioned. It is to be expected that the formation of the abundant quantities of apatite seen after 48 h will consume some of the Ca content of the infiltrated CMAS, which would slow down the reaction.

From the BSE images, shown in Figure 61, and XRD measurements, shown in Figure 64, it can be concluded that no traces of the YbMS phase are present in EBC SG-100 and ABR SG-100, and enough quantity of apatite has been formed to appear as distinct peaks in the XRD diffractograms. The infiltration of CMAS along grain boundaries and consumption of YbMS created both fine porosity and larger pores, particularly evident in the case of EBC SG-100 due to the initial low porosity of this coating. Despite this increase in porosity, the appearance of large apatite crystals and the infiltration of CMAS along the grain boundaries throughout the entire coating, none of the samples showed any sign of damage or indication of failure. The so-

called blister damage, attributed to the slow infiltration of CMAS along grain boundaries, creating the build-up of a dilation gradient [130], was not present in this study. The reason why blister damage was not seen in this case could be due to two factors. First, the higher porosity of thermal sprayed coatings compared to the sintered bodies used by Turcer *et al.* [130] may have facilitated the CMAS infiltration in the early stages of the exposure, as discussed above. Secondly, sintered pellets were high phase purity, with virtually no presence of YbMS. As discussed here, CMAS readily reacts with YbMS to form apatite, which created porosity along the grain boundaries and resulting in paths for further CMAS infiltration. The fact that EBC SG-100, with its initial lower porosity compared to the abradable coatings, still presented complete infiltration after 48 h, suggests that the presence of YbMS played a more relevant role compared to open porosity.

Particularly relevant is the comparison with the work of Zhao *et al.* [135], since, to the best of the author's knowledge, it was the only example of APS deposited YbDS coating exposed to CMAS that reported details on the coating/CMAS interaction, present in the literature. Their work reports limited CMAS infiltration and little reaction between the coating and CMAS, with the presence of unreacted areas on a ~100  $\mu\text{m}$  thick coating, after 200 h at 1300  $^{\circ}\text{C}$ . Two main factors could explain this apparently different behaviour. First, as discussed before, porosity plays a key role. Although there is no porosity measurement provided, cross-section images allow determining a lower porosity level than in this work. This provides access pathways for molten CMAS in the early stages of the exposure, whereas very low porosity coatings hinder the penetration of CMAS, forcing it to react and form apatite crystals at the surface. Secondly, the amount of YbMS phase present in the coating affects how quickly CMAS can infiltrate. If the YbMS content is high, the formation of apatite further aids the formation of this protective layer described above. Contrary, a low YbMS content prevents the

formation of a protective layer, and promotes the infiltration of CMAS through grain boundaries deeper into the coating.

The different interactions between thermally sprayed YbDS and CMAS, depending on the porosity levels present, are schematically shown in Figure 65.

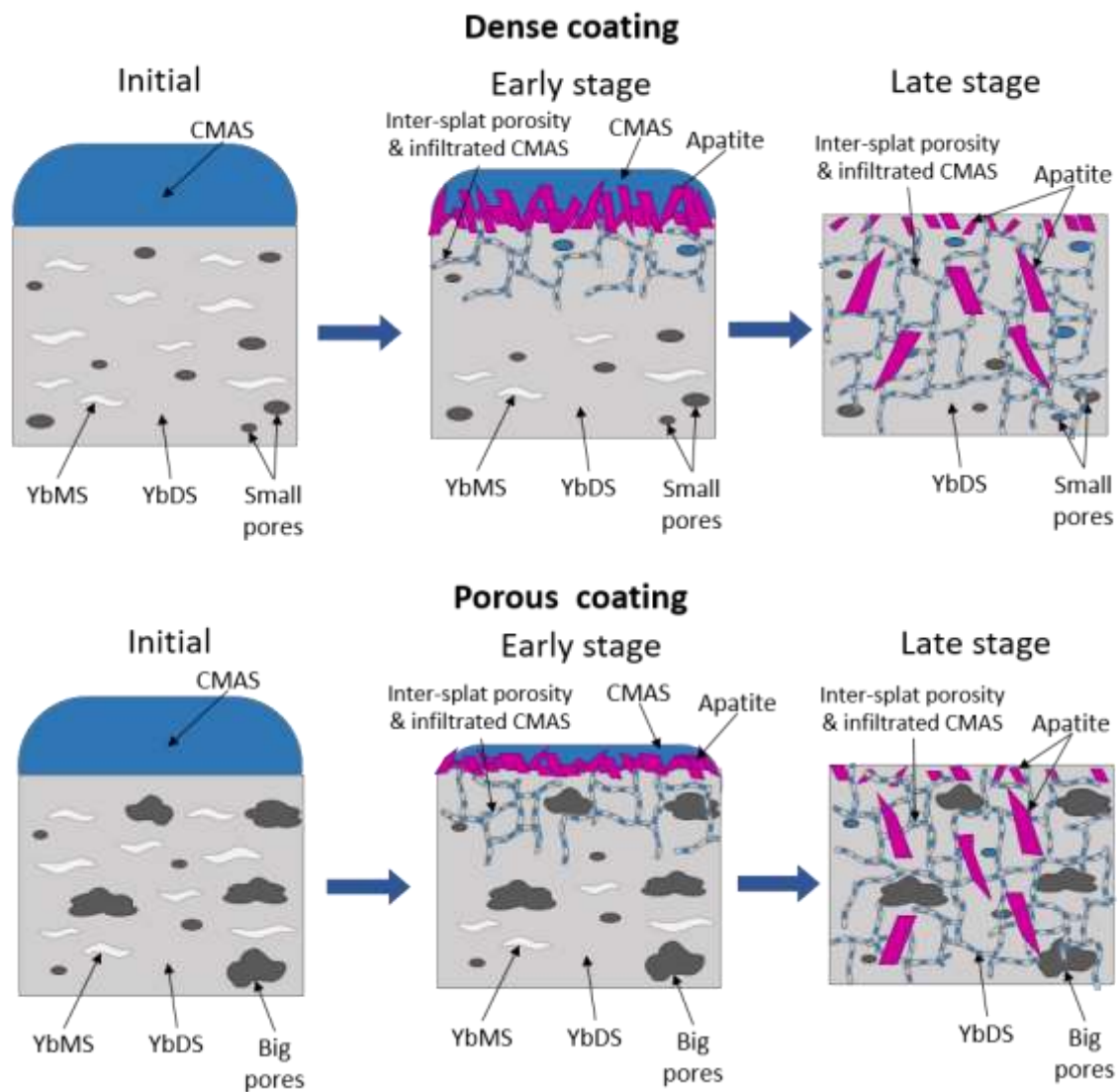


Figure 65: Schematic of the CMAS attack on APS-deposited YbDS coatings for dense coatings (top) and porous coatings (bottom). Early stages show deeper CMAS infiltration and reduced apatite formation for porous coatings. Late stages present complete CMAS infiltration with large apatite crystals across the coating. Fine porosity, infiltrated with CMAS, is present due to the consumption of material at the inter-splat boundaries

From Figure 65 it can be seen how the same CMAS loading ( $\sim 15 \text{ mg/cm}^2$ ) affects dense and porous thermal sprayed YbDS coatings. The initial state in both cases presents a small amount of YbMS along the YbDS matrix and equal CMAS presence. After 1 h at  $1350 \text{ }^\circ\text{C}$ , molten CMAS infiltrates the coating. At this early stage, CMAS infiltration is aided by porosity, being more extensive in the case of the porous coating. Molten CMAS reacts with the YbMS present in the coating, producing two phenomena. First, apatite is formed at the surface, to a higher degree in the case of the dense coating due to the higher availability of non-infiltrated CMAS at the surface. Infiltrated CMAS also reacts with the YbMS present within the coating, particularly along the inter-splat boundaries, creating a network of fine pores infiltrated with CMAS. The consumption of YbMS creates a YbMS-depleted layer at the surface of the coating. Further exposure sees the coatings entirely infiltrated with CMAS, showing fine porosity across the entire thickness. At this late stage, only a minority of large pores appear filled with CMAS, contrary to the network of fine pores described above, indicating a transition to inter-splat boundary as the preferential pathway for CMAS infiltration. Large apatite crystals appear across the coatings, and the YbMS-depleted layer now extends to the entire thickness of the coatings.

## 5.5. Conclusions

CMAS attack on thermally sprayed ytterbium disilicate coatings is a serious phenomenon that needs to be studied and addressed adequately for the successful implementation of EBC. In this work, three free-standing ytterbium disilicate coatings, deposited using APS were exposed to  $\sim 15 \text{ mg/cm}^2$  of CMAS, with composition  $35 \text{ CaO} - 10 \text{ MgO} - 7 \text{ Al}_2\text{O}_3 - 48 \text{ SiO}_2$  in mol%, at  $1350 \text{ }^\circ\text{C}$  for 1 h and 48 h. Two of the coatings were produced with a high level of porosity ( $\sim 20 \%$ ) in accordance with industry standards for abrasible coatings. The third coating had a lower porosity,  $< 3 \%$ , closer to typical EBCs. All three coatings had small amounts of ytterbium monosilicate as a secondary phase after then heat treatment.

The results show a limited reaction after 1 h, particularly in the abradable coatings, with the formation of apatite at the surface due to the reaction between molten CMAS and YbMS. The difference observed in CMAS infiltration, greater in abradable coatings, is attributed to the higher porosity level. If the CMAS exposure is maintained for 48 h, the entire coating thickness shows CMAS infiltration, causing the consumption of the YbMS phase, along with the formation of apatite crystals distributed across the coating. Apart from an increase in the porosity, no damage or defects were found after CMAS exposure for 48 h. The absence of blister damage, commonly reported for YbDS, was avoided due to the rapid infiltration of the molten CMAS, which is suggested to be caused by the low YbMS content and presence of porosity in the coating. It could be suggested that a higher porosity content is beneficial (for abradable coatings) in order to ensure fast infiltration of CMAS and avoiding blister damage, although this could lead to other issues such as faster degradation during short exposures, particularly for thinner coatings.

In long term exposures, no detrimental effect of a higher level of porosity could be observed, although care should be taken in short term exposures as it can lead to higher CMAS infiltration. Overall, the results indicate that YbDS is a promising material for the development of both traditional environmental barrier and abradable coatings. Further research is needed to evaluate the effect that the complete infiltration of CMAS and growth of apatite crystals might have on multi-layered EBCs, deposited on top of a CMC substrate.

## **5.6. Acknowledgements**

This work was supported by the Engineering and Physical Sciences Research Council (EPSRC) (grant number EP/L016206/1). The authors thank Kah Leng for his assistance in performing the TGA/DSC measurements of the CMAS powder, Richard Homer for helping with the

vacuum impregnation and cutting of the samples and to the Nanoscale and Microscale Research Centre (nmRC) at the University of Nottingham for providing access to microscopy facilities.

## **Chapter 6: Steam Degradation of Ytterbium Disilicate Environmental Barrier Coatings: Effect of Composition, Microstructure and Temperature**

The main body of this section is reproduced from the paper:

*D. Tejero-Martin, M. Bai, A. R. Romero, R. G. Wellman, T. Hussain, Steam degradation of ytterbium disilicate environmental barrier coatings: effect of composition, microstructure and temperature. Manuscript submitted for publication.*

### **Abstract**

Recession of environmental barrier coatings (EBC) in environments containing steam is a pressing concern that requires further research before their implementation in gas turbine engines can be realized. In this work, free-standing plasma sprayed  $\text{Yb}_2\text{Si}_2\text{O}_7$  coatings were exposed to flowing steam at 1350 °C and 1400 °C for 96 h. Three samples were investigated, one coating with a low porosity level (< 3 %) and 1 wt.%  $\text{Al}_2\text{O}_3$  representing traditional EBCs; and two coatings with higher porosity levels (~20 %) representing abradable EBCs. Phase composition and microstructural evolution were studied in order to reveal the underlying mechanism for the interaction between high temperature steam and ytterbium disilicate. The results show depletion of  $\text{Yb}_2\text{SiO}_5$  near the surface and formation of ytterbium garnet ( $\text{Yb}_3\text{Al}_5\text{O}_{12}$ ) on top of all three coatings due to the reaction with gaseous Al-containing impurities coming from the alumina furnace tubes. The 1 wt.%  $\text{Al}_2\text{O}_3$  added to the EBC sample exacerbated the formation of garnet at 1400 °C compared to the abradable samples, which presented lower quantities of garnet. Additionally, inter-splat boundaries were visible after

exposure, indicating preferential ingress of gaseous Al-containing impurities through the splat boundaries.

## 6.1. Introduction

Nickel-based super-alloys have allowed the current generation of gas turbine engines for aerospace and energy generation to reach extraordinary levels of efficiency. Despite advances in protective coatings and active cooling, the service temperature is ultimately limited to the melting point of the nickel-based super-alloy substrate. SiC/SiC ceramic matrix composites (CMCs) have been identified as a suitable replacement as the material to be used in the hot section for the next generation of gas turbines. Their increased service temperature and superior strength/weight ratio at high temperatures compared to nickel-based super-alloys [5,7] are regarded as the key to improving the performance and weight of future gas turbine engines.

Before nickel-based super-alloys can be effectively replaced with CMCs [8], an effective and reliable protection against corrosion and degradation during service must be developed. CMCs exposed to service conditions face two main degradation mechanisms. Firstly, the presence of calcium magnesium alumina-silicates corrosive species (generally labelled as CMAS for convenience [77,78,134]) can cause molten deposits that interact with the components, shortening their service life. CMAS can be present by the ingestion of debris during take-off and landing, as well as when flying over arid environments or due to the presence of airborne volcanic ash [68,76]. Secondly, CMCs exposed to high temperatures under clean, dry oxygen form a protective SiO<sub>2</sub> scale that provides protection against corrosion and recession [67]. Under the presence of steam, a naturally occurring combustion product [70,222], the CMCs components show increased oxidation [223–225] and accelerated corrosion due to the volatilization of the SiO<sub>2</sub> scale to form gaseous Si-O-H species, such as Si(OH<sub>4</sub>) [71], as shown below:



This silica volatilisation causes the recession of the surface of the component, which has been estimated to be as high as  $\sim 1 \mu\text{m/h}$  under normal gas turbine operating conditions [75,226]. Since such components are expected to withstand at least 30,000 h of service without maintenance, this level of corrosion is unacceptable.

Environmental barrier coatings (EBCs) were then developed to negate the pernicious effects that CMAS and steam have on CMCs components [219]. The current generation of EBCs generally presents a rare earth silicate top layer, providing direct protection against CMAS attack and silica volatilisation. Several compositions have been suggested and thoroughly studied [219], each one with its own set of advantages and disadvantages. Among those compositions, ytterbium disilicate (referred to as YbDS in this work) presents several promising characteristics. Its coefficient of thermal expansion is closely matched to that of SiC substrates ( $3.6 - 4.5 \times 10^{-6} \text{ K}^{-1}$  for YbDS [83] and  $4.5 - 5.5 \times 10^{-6} \text{ K}^{-1}$  for SiC [82]), it presents no phase transformation at high temperatures [227], adequate silica volatilisation and low thermal conductivity at high temperatures ( $\sim 2 \text{ W}\cdot\text{m/K}$  at  $1000 \text{ }^\circ\text{C}$ ) [86].

Several studies have reported the interaction between heated steam and YbDS, although currently, there is no standard that allows easy and direct comparison. Additionally, the presence of alumina tubes in most testing rings influences the results through the presence of Al-containing contamination [88,220,228,229]. Presentation of the YbDS testing material is varied, ranging from cold pressed pellets [88,114], hot pressed pellets [80,92,109], coatings formed through oxidation bonded by reaction sintering (OBRS) [113] or coatings deposited using air plasma spraying (APS) [101,102]. Different deposition techniques result in differences in phase composition, microstructure, and porosity levels. Porosity, in particular,

presents an interesting dilemma. Traditional EBCs aim for low levels of porosity to prevent steam reaching the substrate through connected pores; however, certain applications require higher levels of porosity. Abradable coatings, for instance, are designed to present porosity as high as 20 % in order to be eroded and allow the turbine blades to create a tight seal without risking damage due to friction [145]. Despite the interest in abradable EBCs, no study has reported the effect that porosity has on the resistance to steam exposure of rare earth silicates.

In this work, three free-standing YbDS coatings deposited using air plasma spraying (APS), with three varying levels of porosity content, were studied. To evaluate the degree of degradation experienced, all three coatings were exposed to a flowing atmosphere of 90 vol.% H<sub>2</sub>O/10 vol.% O<sub>2</sub> with a flow velocity of ~ 100 mm/s, atmospheric pressure and exposure time of 96 h. Two different tests were conducted, at 1350 °C and 1400 °C, to investigate the effect that temperature has on the corrosion from steam with presence of gaseous Al-containing impurities. Temperatures and exposure duration were chosen in line with OEM testing protocols and according to guidance from the high temperature community.

## **6.2. Experimental methods**

### **6.2.1. Materials and steam exposure**

Three different free-standing YbDS coatings were studied in this work, all of them produced using air plasma spraying. The first one, labelled in this work as EBC SG-100 (EBC stands for environmental barrier coating), was a ~350 µm thick YbDS environmental barrier coating, which had a 1 wt.% of alumina powder added to the feedstock prior to spraying. The coating was produced using Treibacher Industrie AG (Althofen, Austria) YbDS powder through a Praxair Surface Technology (Danbury, Connecticut, USA) SG-100 plasma spray gun. The second free-standing coating, labelled as ABR SG-100 (ABR is short for abradable), was a ~500 µm thick YbDS abradable coating which had a ~1.5 wt.% of polyester powder added to

the feedstock prior to spraying. The coating was also deposited using a Praxair Surface Technology SG-100 plasma spray gun, but this time the YbDS powder was provided by Oerlikon Metco AG (Pfäffikon, Freienbach, Switzerland). The third free-standing coating, labelled here as ABR F4, was a ~1000  $\mu\text{m}$  thick YbDS abradable coating which also had a ~1.5 wt.% of polyester powder added to the feedstock prior to spraying. The coating was deposited using an Oerlikon Metco F4 plasma spray gun using the same Oerlikon Metco YbDS powder as with ABR SG-100. Both the Treibacher and Oerlikon YbDS powders were manufactured to conform to a nominal composition of 22 – 24 wt.%  $\text{SiO}_2$  and balance of  $\text{Yb}_2\text{O}_3$ , with a maximum of 5 vol.% of unreacted  $\text{Yb}_2\text{O}_3$ , YbMS and  $\text{SiO}_2$ . Compositions were in-line with commercial applications in future gas turbine engines. All three free-standing coatings were cut to produce samples with dimensions of 2.5 x 1.5  $\text{cm}^2$ . Previous to any steam exposure, all of the as-sprayed samples were heat treated in order to crystallize the amorphous content. Samples were annealed at 1200  $^\circ\text{C}$  for 2 h in air, with a heating rate of 5  $^\circ\text{C}/\text{min}$ .

For the steam exposure, a custom steam rig was designed and built, comprised of the different components shown in Figure 66. The base of the steam rig is an Elite Thermal Systems Ltd (Market Harborough, UK) TSH15/25/180 tube furnace with an alumina tube with an internal diameter of 25 mm. An oxygen bottle is connected to one of the open ends of the tube, being the oxygen flow controlled with a MKS Instruments Inc. (Andover, Massachusetts, USA) type 247 mass flow controller. Deionized water is introduced in the furnace via a Watson-Marlow (Falmouth, UK) 120S peristaltic pump with 0.63 mm bore PVC tubing. The deionized water is first passed through a Grant Instruments (Shepreth, UK) Optima TC120 heated circulating bath kept at 60  $^\circ\text{C}$  to facilitate the evaporation once inside the furnace. Both the oxygen and water line are connected through a T connector outside the furnace, being the mixture introduced into the tube furnace using an alumina tube (99.7 % purity) with an internal diameter of 1.5 mm, supplied by Almath Crucibles Ltd. (Newmarket, UK), reaching until the start of the hot zone.

The other end of the tube furnace was kept open to maintain atmospheric pressure. Oxygen and water flow were set to obtain a flowing atmosphere at the hot zone with a content of 90 vol.% H<sub>2</sub>O/10 vol.% O<sub>2</sub>, and a gas velocity of ~100 mm/s. Oxygen and water flow were started once the furnace reached the desired temperature. Samples were placed on top of an alumina plate in the order shown in Figure 66.

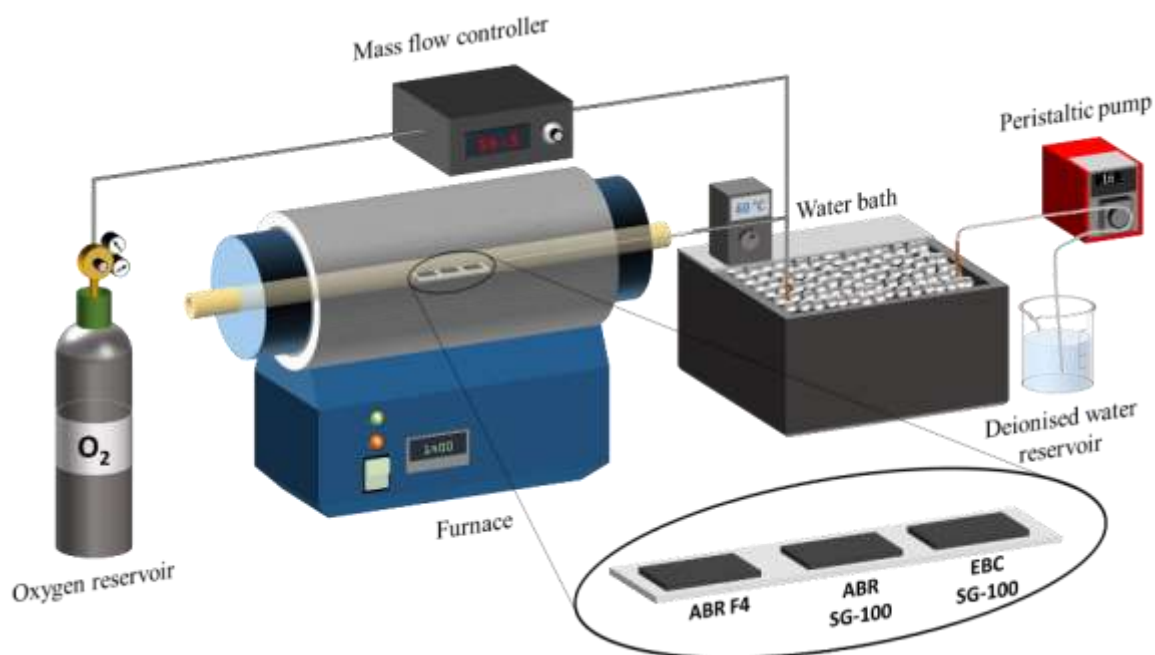


Figure 66: Schematic of the custom steam rig designed and built for the steam exposure

Two different exposures were conducted, the first one at 1350 °C and the second one at 1400 °C, all the other parameters were kept constant between the two experiments.

### 6.2.2. Materials characterisation

Phase identification of the feedstock powder and free-standing coatings was performed using a Bruker D8 Advance Da Vinci diffractometer (Billerica, Massachusetts, USA) with Cu cathode (wavelength of 1.5406 Å) using Bragg-Brentano geometry. The angular range investigated was from 10° to 70° with a step size set to 0.02° and a dwell time of 0.3 s for all

the measurements. Quantitative Rietveld refinement (TOPAS V5, Bruker, Germany) was employed to determine the quantity of each phase [210].

To investigate the microstructure of the free-standing coatings, the samples were cold mounted using Struers EpoFix resin and hardener (Copenhagen, Denmark), then ground and polished to a 1  $\mu\text{m}$  finish using Buehler SiC grinding papers (Leinfelden-Echterdingen, Germany). Scanning electron microscope (SEM) images were taken using a FEI Europe Quanta 600 (Eindhoven, Netherlands). Porosity was calculated as the average measurement across three backscattered electron (BSE) images of representative regions of the coating. All the images were taken with a magnification of 400x, accelerating voltage of 15 kV and spot size of 5 nm. To do the porosity measurement, the open source software “ImageJ” with the image processing package “Fiji” was used [212]. To do so, BSE images were converted into black and white maps upon setting a threshold. Then, the automated function “Analyze particle” was employed, which measured the area percentage of the image covered by porosity, returning an overall value per image. An average of the three images of each coating was calculated, being the standard deviation used as the error.

## **6.3. Results**

### **6.3.1. Powder and coating characterisation**

Powder morphology was investigated through SEM imaging to better understand the microstructure of the produced coatings. Figure 67 shows a backscattered image of the two powders used in this study.

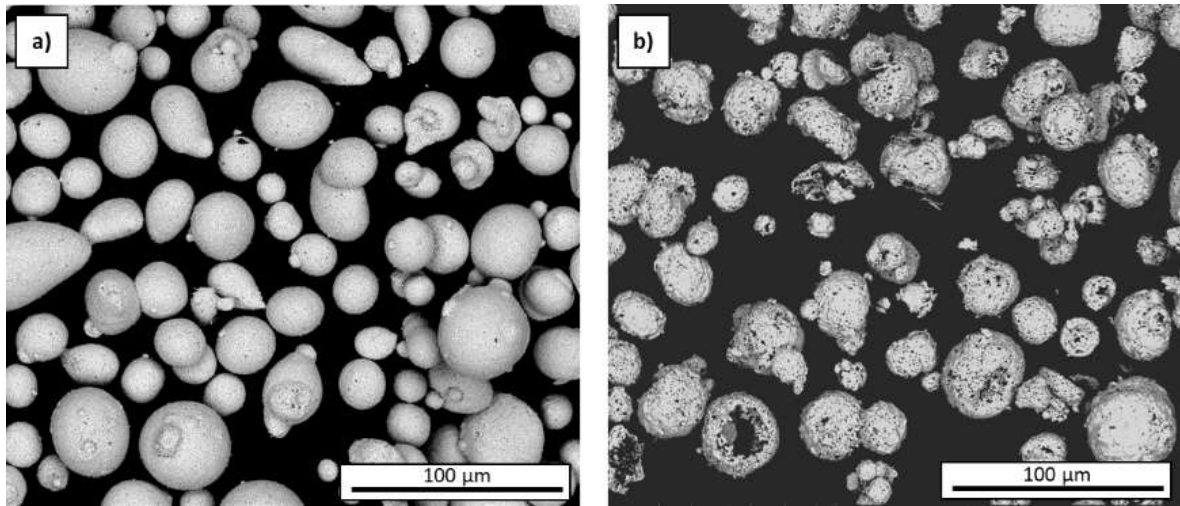


*Figure 67: BSE images of the powders used in this work: a) corresponds to sample EBC, b) corresponds to samples ABR*

The morphology of the EBC powder, as shown in Figure 67a, is spherical in shape with a smooth surface, mostly lacking any defects or inclusion. On the other hand, ABR powder, as shown in Figure 67b, presents a more irregular shape, still mostly spherical, but with a rough surface and the presence of pores and visible hollow cores.

In order to crystallise the amorphous content of the three as-sprayed coatings, they were annealed; the cross-section of the annealed coatings are shown in Figure 68.

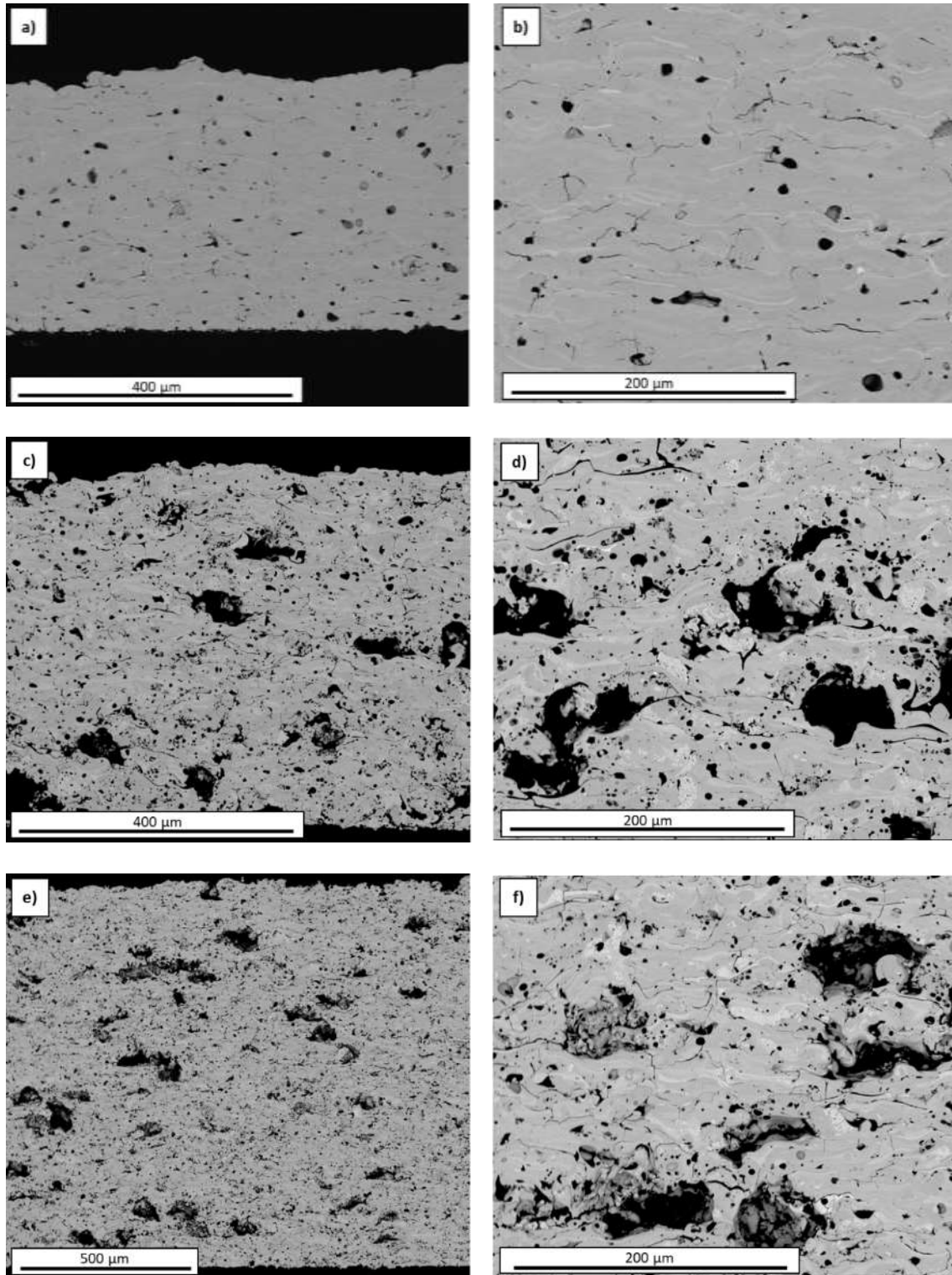
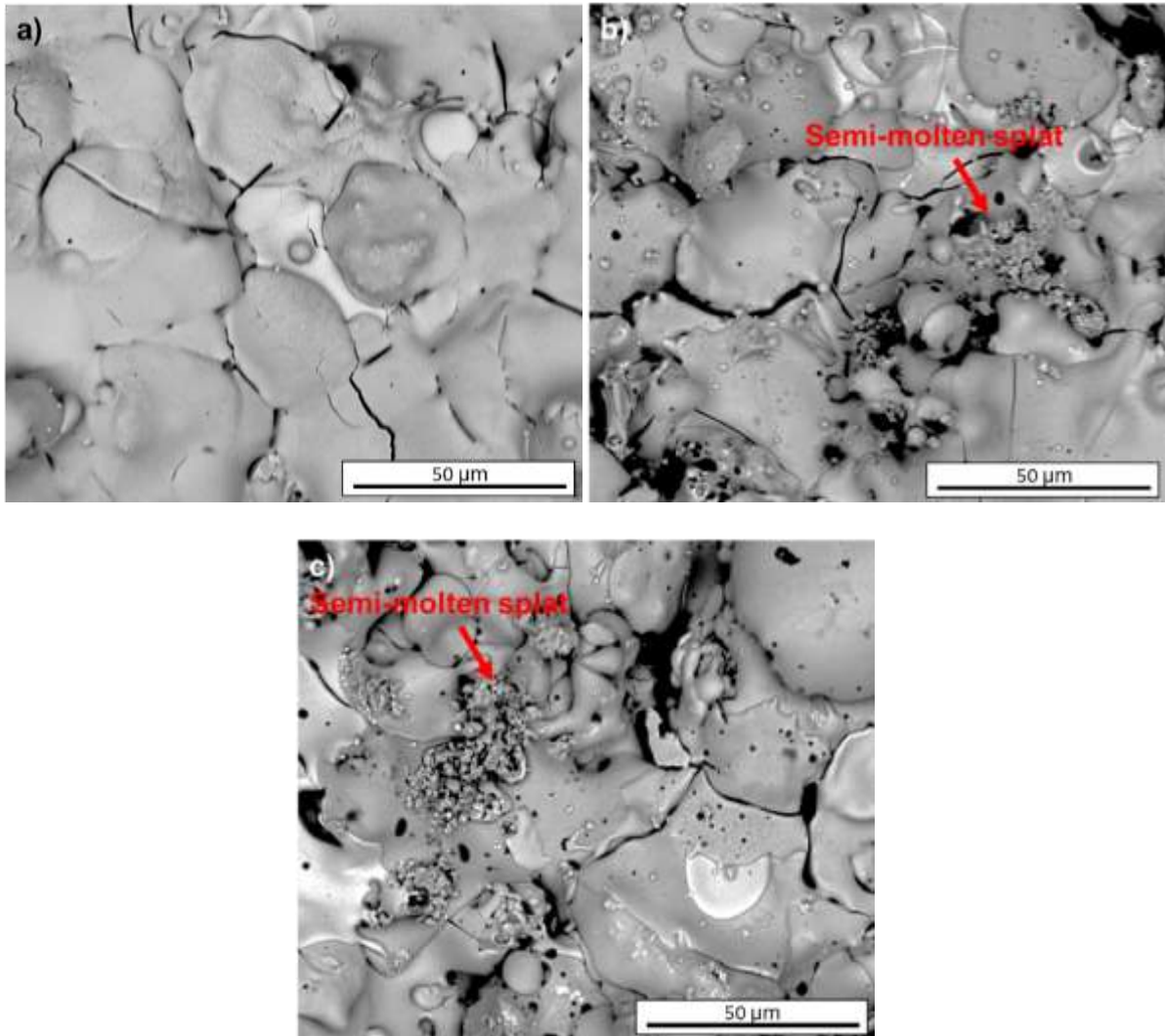


Figure 68: BSE images of the three free-standing coatings after annealing. Images a) and b) show sample EBC SG-100, c) and d) ABR SG-100 and e) and f) ABR F4

The cross-section SEM images shown in Figure 68 reveal that sample EBC SG-100 has a lower porosity level and thickness when compared to the two ABR coatings. This is confirmed by the porosity measurements, showing a porosity level of  $2.4 \pm 0$ .



*Figure 69: BSE images of the top surface of the annealed samples. Image a) corresponds to sample EBC SG-100, image b) to ABR SG-100 and image c) to ABR F4*

From the images of the top surface shown in Figure 69, it can be seen that sample EBC SG-100 presents a smooth surface with well-molten splats, along with cracks distributed across the surface. In the case of the two abrasible samples, ABR SG-100 and ABR F4, Figure 69b and c respectively, the surface presents a combination of well molten and semi-molten splats, the latter being labelled in the images.

The phase composition of the annealed coatings was also studied. The XRD diffractogram for the feedstock powder, as-sprayed and annealed conditions are shown in Figure 70 for each of the three coatings.

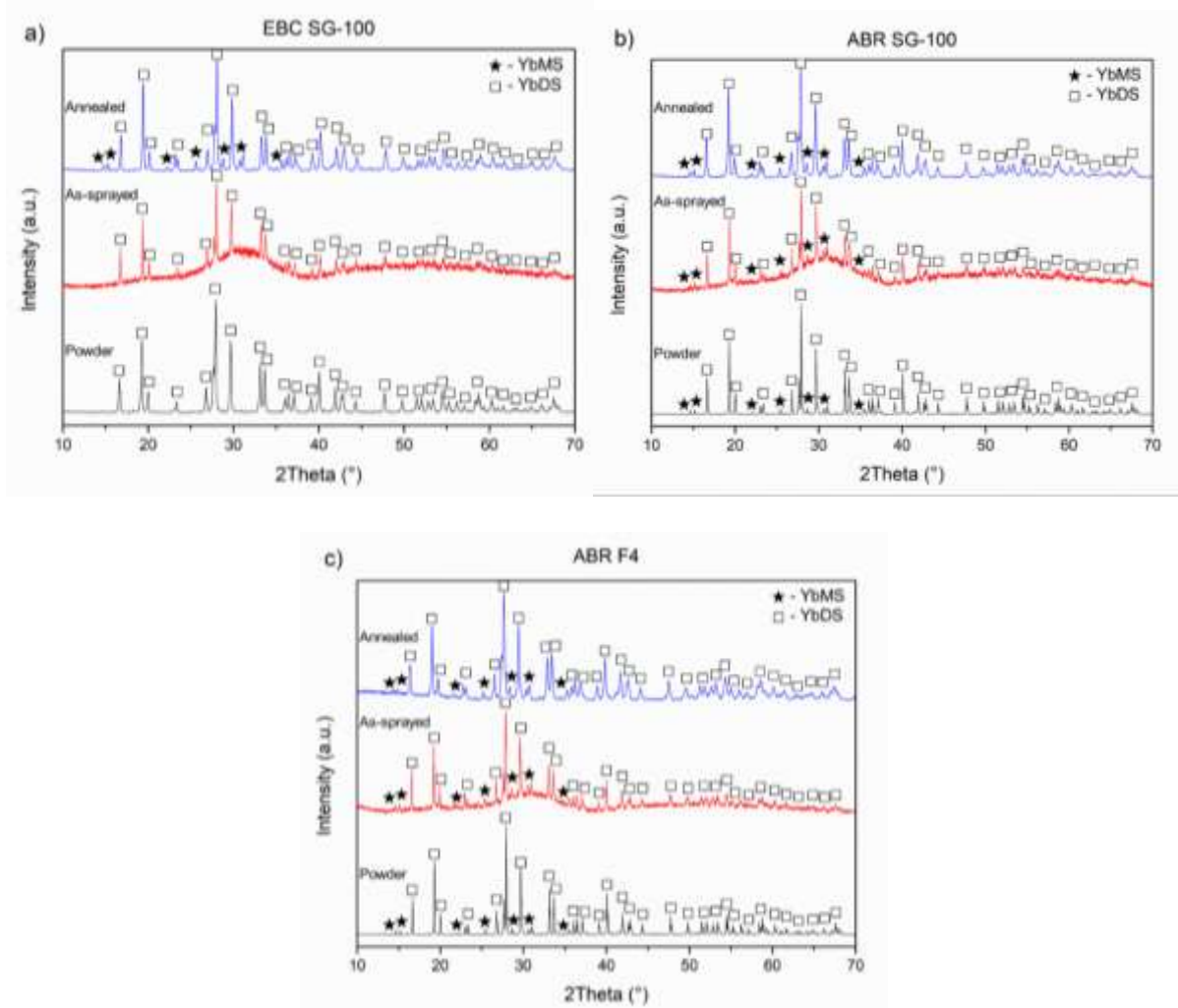


Figure 70: XRD measurements for a) EBC SG-100, b) ABR SG-100 and c) ABR F4. On each graph, the bottom plot corresponds to the powder, middle to the as-sprayed coating and top to the annealed coating. Phases have been identified with a star (★) for YbMS and a square (□) for YbDS

The XRD measurements show that the EBC powder, Figure 70a, presents only peaks from the YbDS phase (PDF card number 00-082-0734), although Rietveld refinement identified a small quantity of YbMS (5.4 wt.%). The powder used to spray the abrasible samples, Figure 70b and c, shows the presence of a higher quantity of YbMS (PDF card number 00-040-0386),

measured as 18.7 wt.%. In the as-sprayed condition, EBC SG-100 only shows the presence of YbDS peaks with a 63.6 % of amorphous content , whereas samples ABR SG-100 and ABR F4 show YbMS peaks accounting for ~25 wt.%. In addition to the crystalline peaks, all of the three as-sprayed coatings show two broad amorphous humps, centred on  $\sim 30^\circ$  and  $\sim 55^\circ$ . The annealing process removes the presence of these amorphous humps, showing all of the three samples consist mainly of YbDS, with approximately ~30 wt.% of YbMS. The detailed phase content as measured through Rietveld refinement is presented in Figure 77.

Particular attention was paid to the potential presence of  $\text{SiO}_2$  in the annealed samples. As it will be discussed in section 6.4 “Discussion”,  $\text{SiO}_2$  has been reported to play a critical role in the steam behaviour of thermal sprayed YbDS samples. The XRD measurements of the three annealed samples is presented in Figure 71, where the  $\text{SiO}_2$  peaks, as well as the YbDS and YbMS, have been included.

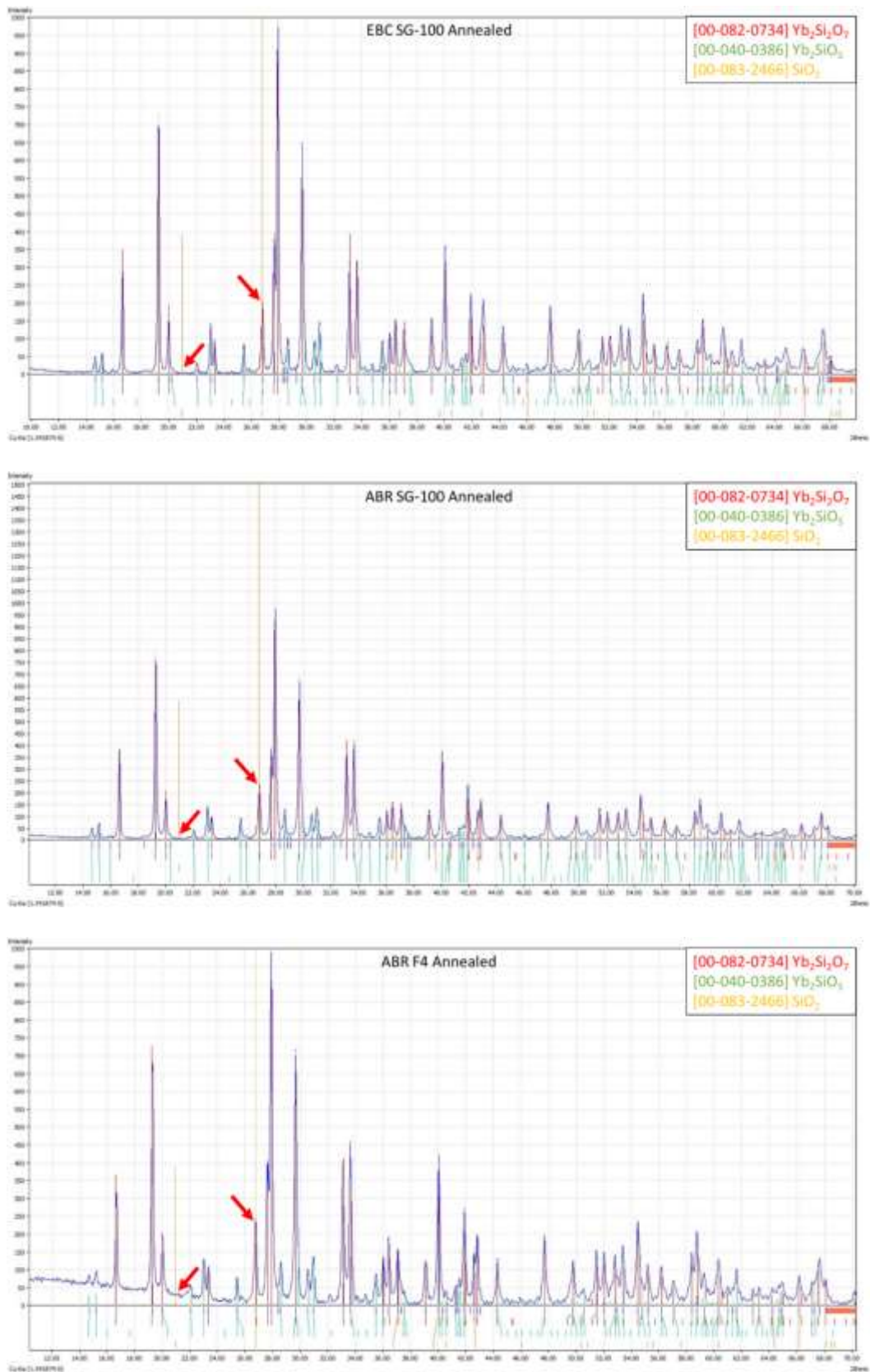


Figure 71: XRD measurements of the three annealed samples with peaks for YbDS, YbMS and  $\text{SiO}_2$  shown. Red arrows indicate the two main peaks for  $\text{SiO}_2$

The strongest reflection for SiO<sub>2</sub> is present at ~27°, which overlaps with a YbDS peak, not being possible to use this peak for identification. The second strongest peak in SiO<sub>2</sub> can be found at ~21°. In this case, none of the three samples show presence of SiO<sub>2</sub>.

### **6.3.2. Steam exposure to 1350 °C**

The cross-section of the samples exposed to steam at 1350 °C for 96 h is shown in Figure 72.

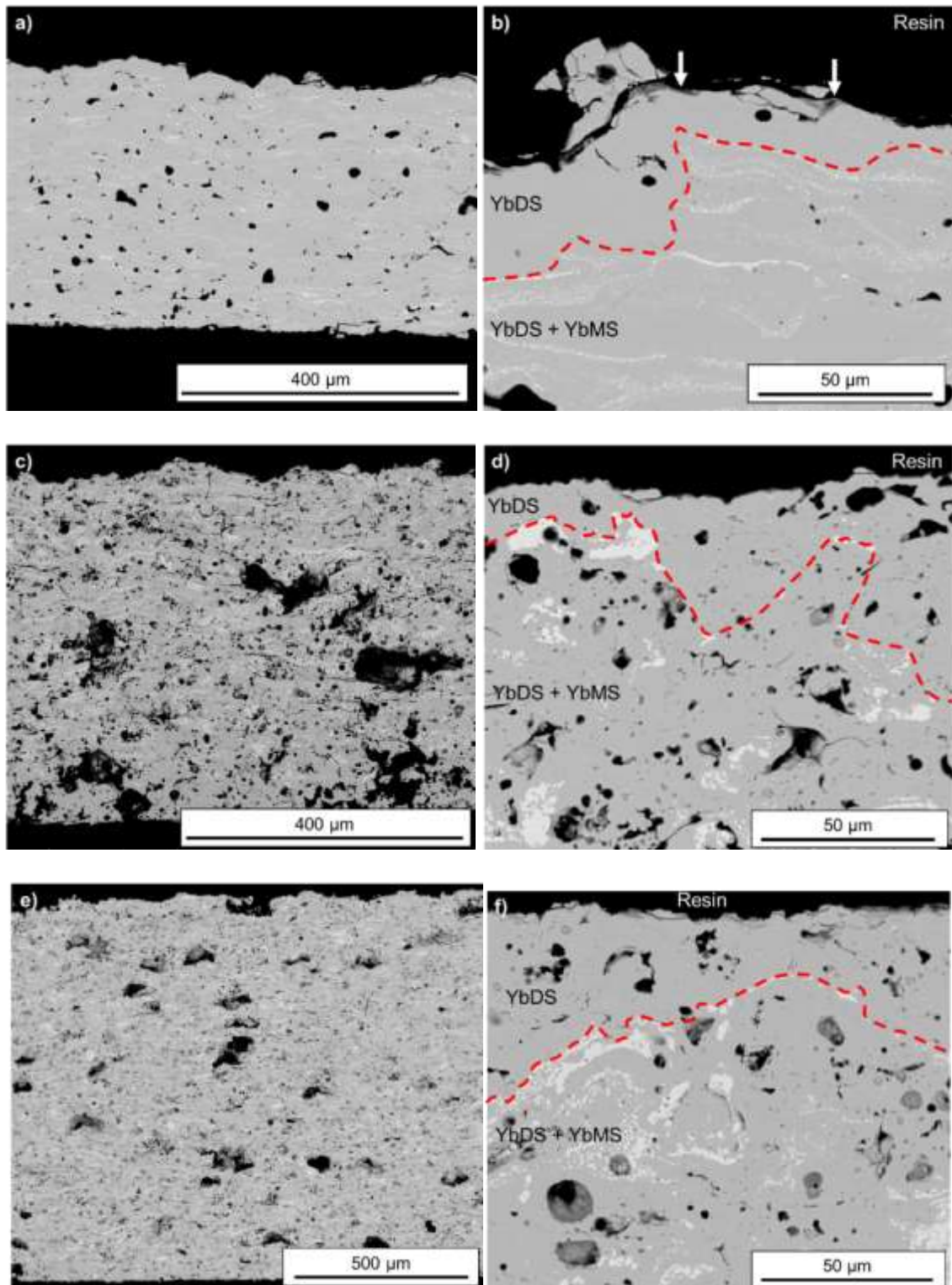
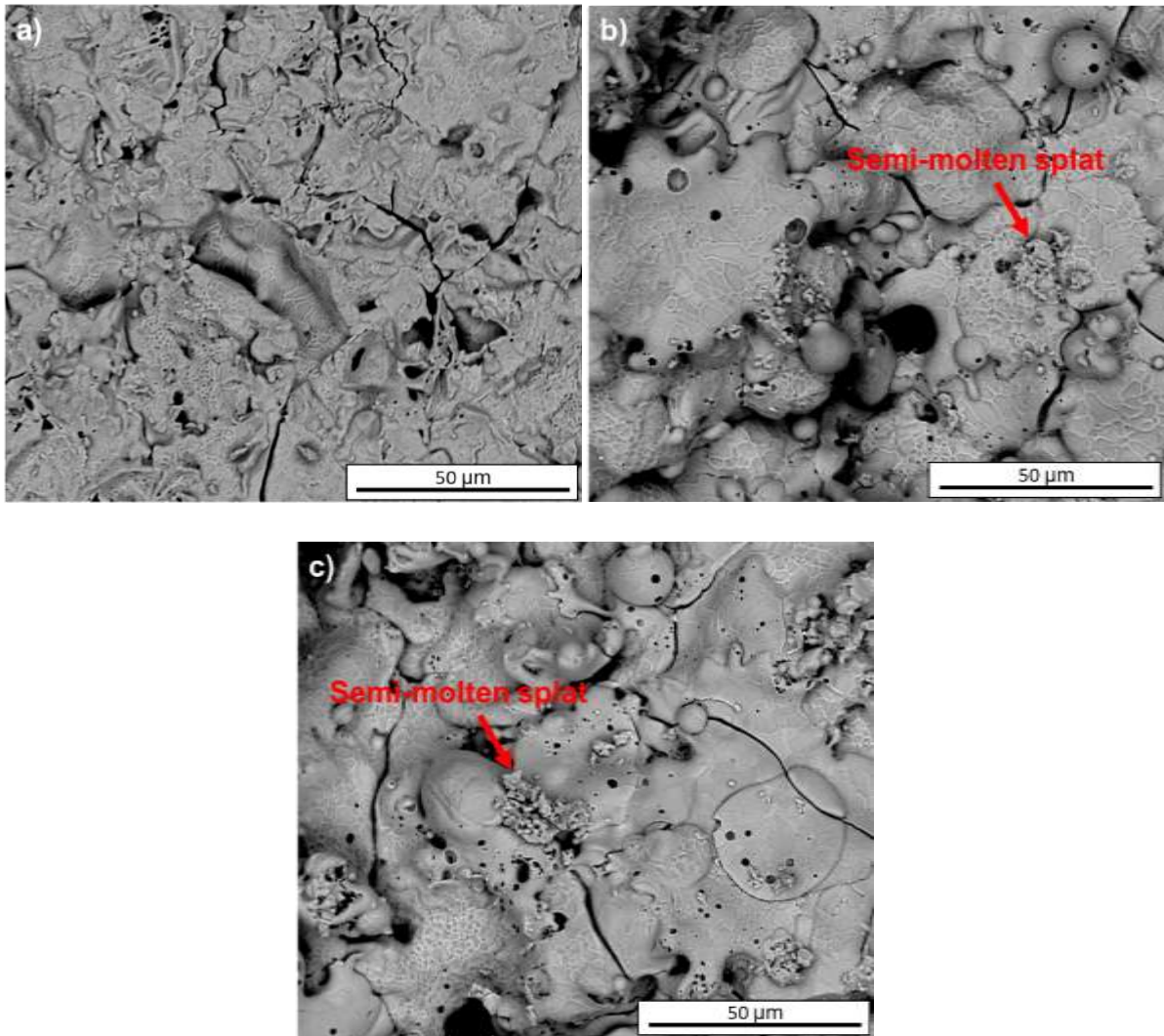


Figure 72: Low and high magnification BSE images of the cross-section of the samples exposed to steam for 96 h at 1350 °C. Images a) and b) correspond to sample EBC SG-100, images c) and d) to ABR SG-100 and images e) and f) to ABR F4. The red dashed line marks where no more YbMS could be found. White arrows in image b) indicate where a new phase was detected

From the SEM images shown in Figure 72, it can be seen that exposure to steam at 1350 °C caused the depletion of the YbMS closest to the surface, leaving behind a YbMS depleted layer. In the case of sample EBC SG-100, the high magnification image in Figure 72b shows small amounts of a new phase (marked with arrows) present at the surface of the coating. Due to the size of these features and the overlap between the Al-K<sub>α</sub> and Yb-M<sub>α</sub> lines, EDS quantification proved to be challenging. More details and identification are provided in section 6.3.3 “Steam exposure at 1400 °C”.

In addition to the cross-section, the top surface of the exposed samples was also imaged. The images are shown in Figure 73.



*Figure 73: BSE images of the top surface of the samples exposed to steam at 1350 °C for 96 h. Image a) corresponds to sample EBC SG-100, image b) to ABR SG-100 and image c) to ABR F4*

From the images of the top surface shown in Figure 73, it can be seen that sample EBC SG-100, Figure 73a, has a smoother aspect, meaning the individual splats are more difficult to distinguish. On the other hand, samples ABR SG-100 and ABR F4, Figure 73b and c, still show the presence of individual splats, both molten and semi-molten. All of the three samples show the effects of steam exposure; the grain boundary attack on the splats is clearly visible. Multiple cracks, both intra- and inter-splat, are also visible on the three samples.

### **6.3.3. Steam exposure at 1400 °C**

SEM images of the cross-section of the three coatings exposed to steam at 1400 °C for 96 h are presented in Figure 74.

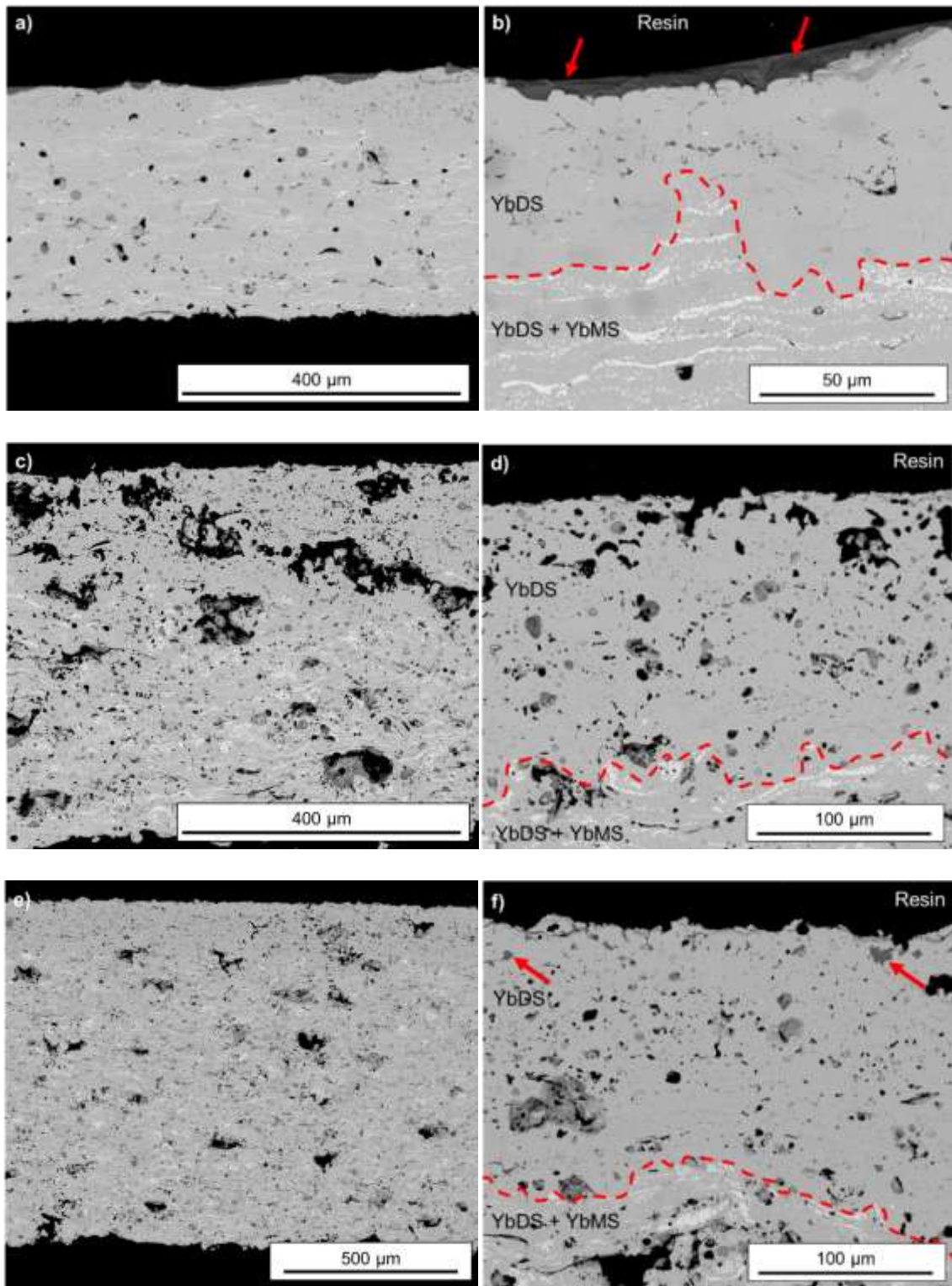
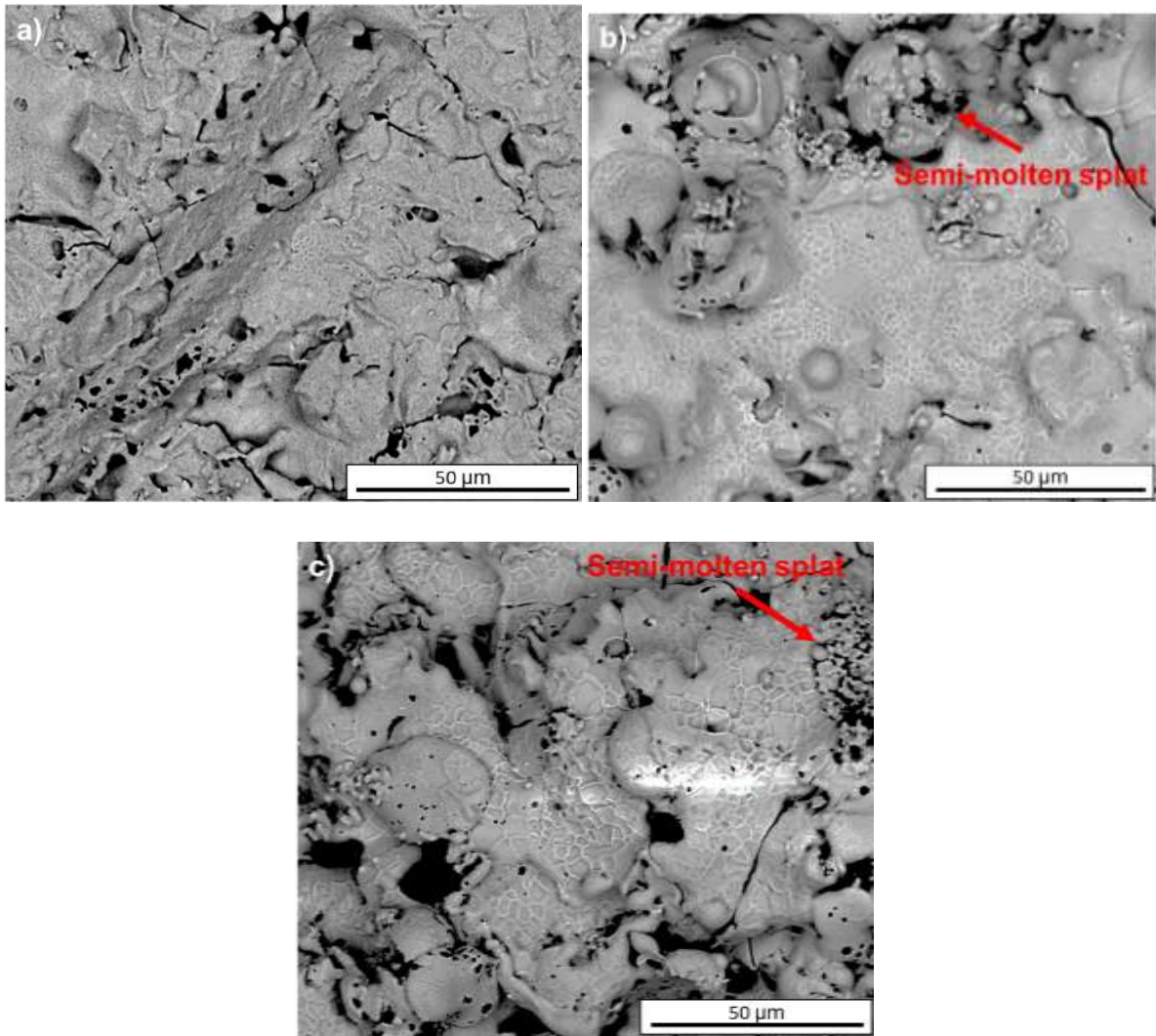


Figure 74: Low and high magnification BSE images of the cross-section of the samples exposed to steam for 96 h at 1400 °C. Images a) and b) correspond to sample EBC SG-100, images c) and d) to ABR SG-100 and images e) and f) to ABR F4. The red dashed line marks where no more YbMS could be found. Red arrows in images b) and f) indicate where a new phase was detected

From the low and high magnification images of the three coatings exposed to steam at 1400 °C, as shown in Figure 74, some differences can be appreciated. First, there is a clear new phase on the surface of sample EBC SG-100, marked with red arrows in Figure 74b. This scale, visible even at low magnification, was only present to such an extent on this sample. Smaller traces could be found on the two abradable samples, especially in ABR F4, as marked with red arrows in Figure 74f. In the case of the abradable samples, this new phase was not seen as a homogenous scale on top of the surface but as small patches and within filled pores. EDS identification was tried, but the results were unreliable due to the already mentioned issue of overlapping peaks between the Al-K $\alpha$  and Yb-M $\alpha$  lines, which is why XRD measurements were used for identification, as shown in Figure 76.

Another feature observed was the previously mentioned YbMS depleted layer near the surface of the coating. The thickness of the depleted layer is thinner in the case of sample EBC SG-100, approximately 50  $\mu\text{m}$ , whereas the thickness of the depleted layer on the abradable samples is closer to  $\sim 125 \mu\text{m}$ . In addition, the top area of the depleted layer presents visible inter-splat boundaries, not present in the samples exposed to steam at 1350 °C, as it can be seen in Figure 72. These newly formed pores were located at the inter-splat boundaries and can be more clearly seen in sample EBC SG-100 due to the initial low level of porosity. This newly formed feature were located at the inter-splat boundaries and can be more clearly seen in sample EBC SG-100 due to the initial low level of porosity. The top surface of the three coatings exposed to steam at 1400 °C was imaged, as shown in Figure 75.



*Figure 75: BSE images of the top surface of the samples exposed to steam at 1400 °C for 96 h. Image a) corresponds to sample EBC SG-100, image b) to ABR SG-100 and image c) to ABR F4*

From the SEM images of the top surface, the grain boundary attack is less visible in the EBC SG-100 sample exposed to 1400 °C (Figure 75a) compared to 1350 °C (Figure 73a). Individual splats are difficult to identify, whereas cracks are visible. The top surface of the two abrasible coatings, ABR SG-100 (Figure 75b) and ABR F4 (Figure 75c), show very similar features, with presence of semi-molten splats. Individual splats affected by grain boundary corrosion can be seen, as well as cracks.

XRD measurements were performed to study the phase content of the three coatings. Figure 76 shows the XRD measurements of the three coatings on the three different conditions studied: before exposure, after exposure at 1350 °C and after exposure after 1400 °C.

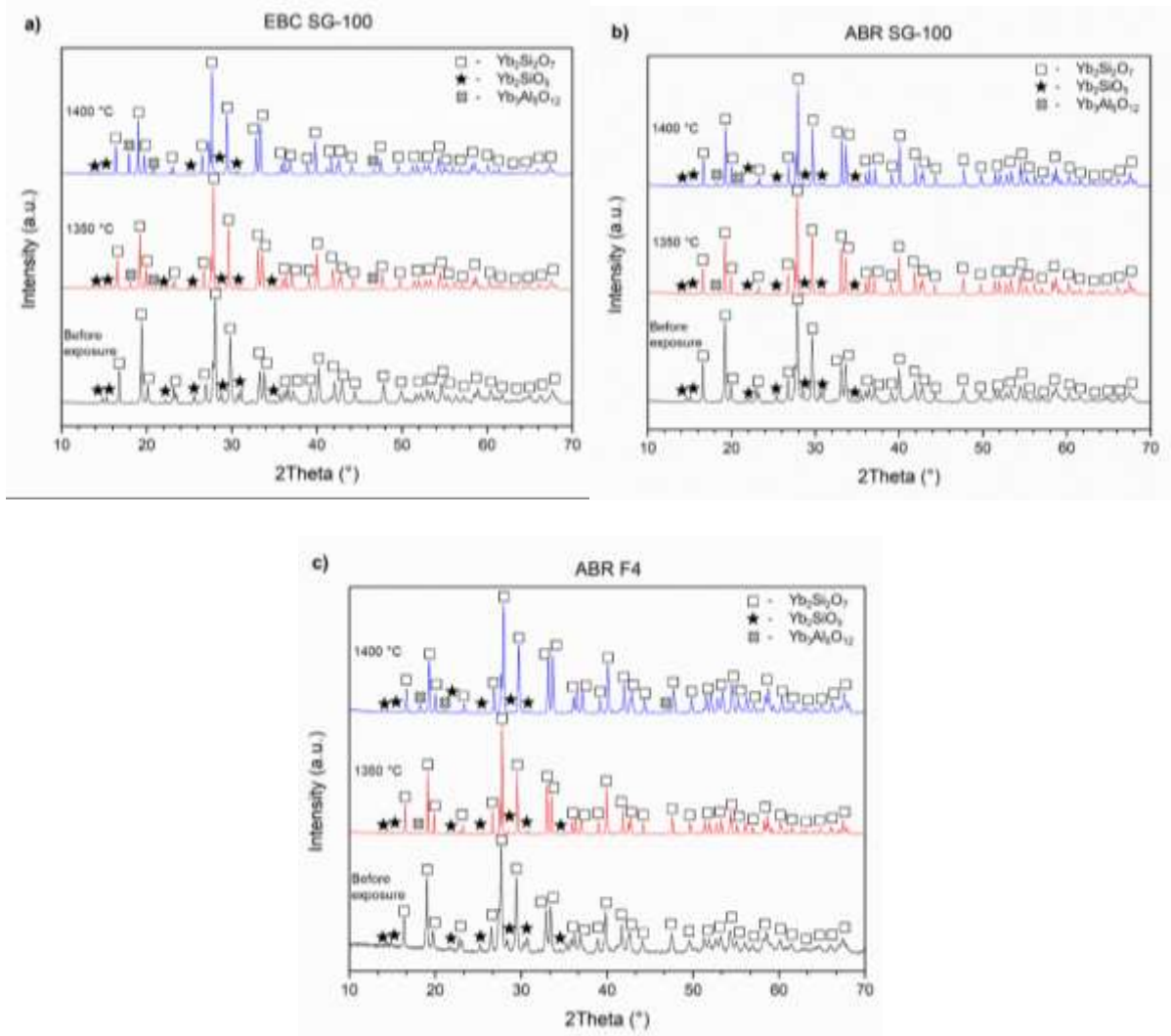


Figure 76: XRD measurements for a) EBC SG-100, b) ABR SG-100 and c) ABR F4. On each graph, bottom plot corresponds to the coating before steam exposure, middle to the 1350 °C steam exposure and top to the 1400 °C steam exposure. Phases have been identified with a square ( $\square$ ) for YbDS, a star ( $\star$ ) for YbMS and a cross ( $\times$ ) for the garnet

The XRD measurements for sample EBC SG-100, Figure 76a, show how once the sample is exposed to steam at 1350 °C, there is a reduction in the intensity of the YbMS peaks. For EBC

SG-100, this means a reduction from a YbMS content of 29.3 wt.% down to 8.1%, as shown in Figure 77. In the case of the two abradable samples, ABR SG-100 and ABR F4, the reduction is from ~29 wt.% to ~12 wt.%. At the same time, a new phase can be seen, identified as ytterbium garnet ( $\text{Yb}_3\text{Al}_5\text{O}_{12}$ , PDF card number 00-023-1476). This new phase was seen on the SEM images of the cross-section, Figure 72 and Figure 74. The presence of garnet is most predominant on EBC SG-100, with a 7.0 wt.%, whereas the two abradable samples present a garnet phase content around or below 1 wt.%. This trend continues for the samples exposed at 1400 °C. EBC SG-100 experiences a further reduction in the YbMS content, down to 3.9 wt.%, with garnet content rising to 17.6 wt.%. Regarding ABR SG-100, exposure to steam at 1400 °C did increase the amount of garnet formed (2.6 wt.%) compared to exposure at 1350 °C (0.1 wt.%). This change is most notable in ABR F4, having a garnet content of 1.0 wt.% when exposed at 1350 °C, rising to 7.2 wt.% when exposed at 1400 °C. It should be noted that the phase content only takes into account the top 10 -15  $\mu\text{m}$  of the coatings due to the penetration depth of x-rays for this composition [220].

The phase content as quantified through Rietveld refinement for all the samples here studied can be found in Figure 77.

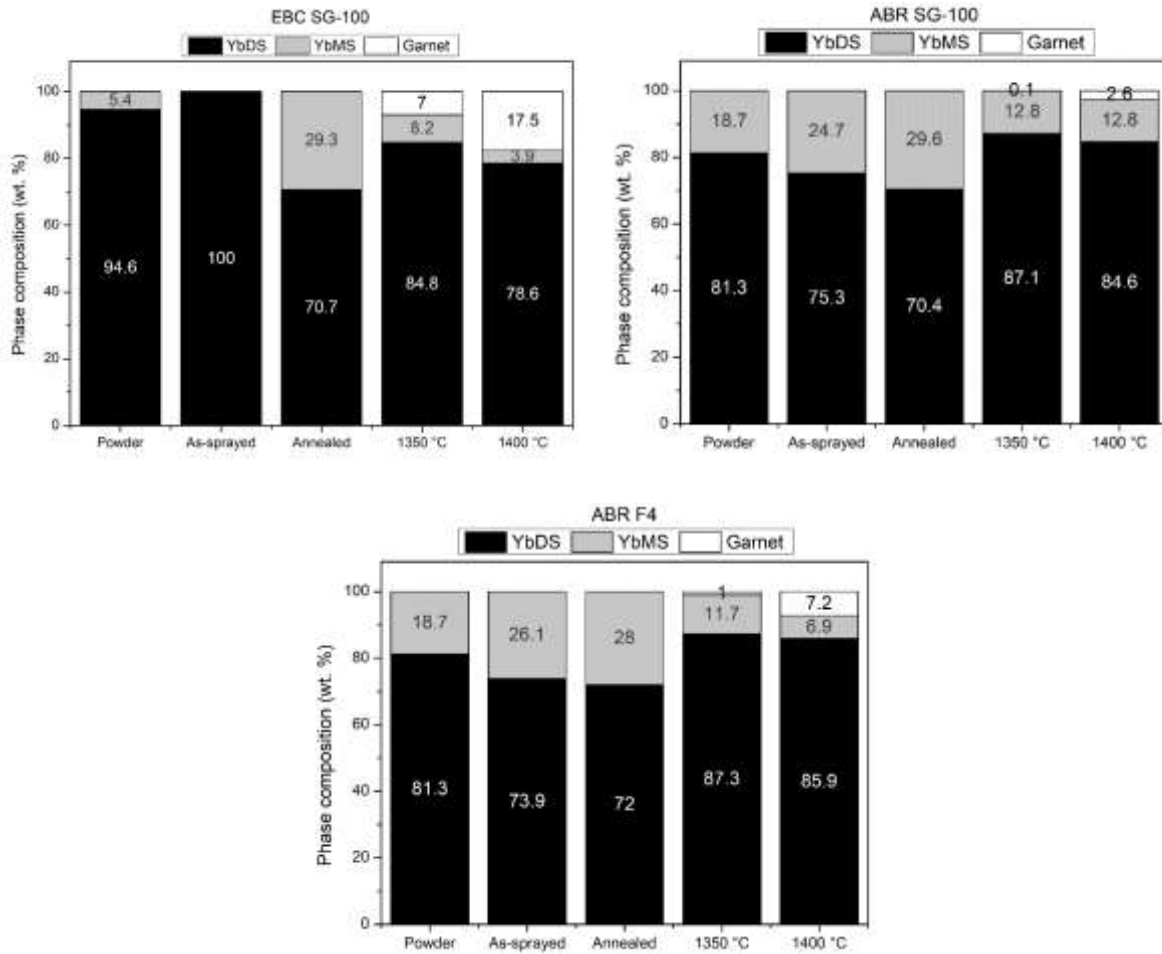


Figure 77: Crystalline phase content quantified using Rietveld refinement for coatings EBC SG-100, ABR SG-100 and ABR F4

## 6.4. Discussion

Steam degradation is correlated with several factors, such as coating phase composition, microstructure, temperature and steam velocity [219]. The three coatings studied here present a similar composition, as revealed by the XRD measurements in Figure 70. EBC powder was mainly composed of YbDS, whereas ABR powder had traces of YbMS phase. During APS deposition, preferential volatilisation of  $\text{SiO}_2$  takes place due to the in-flight conditions, leading to the formation of small quantities of YbMS [221]. This phase is in an amorphous state due to the rapid cooling experienced by the splats upon impact [106]. This would explain why no distinguishable YbMS peaks can be found on the as-sprayed EBC SG-100 sample (Figure 70a),

where the amorphous content is as high as 63.6 %. Once the annealing treatment is completed, the amorphous content is crystallised, leading to only crystalline peaks for YbDS as the main phase and small quantities of YbMS.

Despite this very similar starting composition of the annealed coatings, microstructure presents a differentiating factor between the EBC SG-100 sample and the two ABR coatings. As shown in the cross-section SEM images in Figure 68, EBC SG-100 presented a lower porosity level ( $2.4 \pm 0.3$  %) which can be explained by the absence of pores and defects in the feedstock powder as well as the lack of added polyester as pore former, as seen in Figure 67a. On the other hand, both the abradable coatings, ABR SG-100 and ABR F4, present much higher levels of porosity,  $21.3 \pm 1.1$  % and  $19.4 \pm 4.0$  %, respectively. This is due to the presence of porosity and hollow cores in the feedstock powder (Figure 67b) and the addition of polyester as a pore former. When comparing the top surface of the annealed samples, there is also a clear difference between the EBC samples and the abradable ones, as can be seen in Figure 69. EBC SG-100 presents a smoother surface caused by well-molten splats that flattened upon impact. The abradable samples show the presence of semi-molten, but not completely flat splats, giving rise to a rougher surface where individual splats are easily identifiable. In all of the three samples, intra- and inter-splat cracks could be found.

From the SEM images of the top surface of the three steam exposed coatings, shown in Figure 73, it can be seen that the interaction between the steam and the coatings takes place preferentially at the grain boundaries, a phenomenon also reported by Maier *et al.* [88] and Rohbeck *et al.* [228]. Exposure to steam at 1350 °C caused the appearance of a YbMS depleted layer on all of the three coatings, as shown in Figure 72, being particularly visible in the high magnification images. In addition to the depletion of YbMS from the top layers near the surface, XRD measurements indicate the formation of a new phase, identified as ytterbium garnet. Figure 77 shows the evolution of the quantitative phase content for each of the three

coatings here studied. In all three coatings, a reduction in the YbMS content could be observed as the content of garnet increased.

Exposure of YbDS to flowing, high temperature steam has been reported to cause SiO<sub>2</sub> volatilisation and YbMS formation through the reaction shown in Equation 17 [101,102,118,229–231].



Nevertheless, in this work, no presence of a YbMS layer could be observed. Instead, a reduction in the YbMS content, including a YbMS depleted layer at the surface of the coatings, along with the appearance of garnet is detected. The appearance of garnet on steam exposure testing conducted using high purity alumina tubes is expected and has been extensively reported in the literature [88,220,228]. In particular, Kane *et al.* [220] report the formation of a YbMS depleted layer on a multi-layer YbDS/Si EBC exposed to steam at 1300 °C. Their system, containing a Si bond-coat, presented YbMS depletion both near the surface and at the Si – YbDS interface, suggesting the involvement of Si/SiO<sub>2</sub> in the YbMS depletion process, but they reported no presence of garnet at this temperature. As can be seen in Figure 76, XRD measurements confirmed the presence of garnet at 1350 °C in all of the three samples, although sample EBC SG-100 showed the highest content. This seems to suggest two things: first, the formation of garnet is temperature dependent, with 1300 °C not high enough for the reaction to take place. Secondly, the 1 wt.% of alumina added to the feedstock EBC powder could explain why this sample shows the highest content of garnet at 1350 °C. Whereas the abrasable samples rely on the Al-containing impurities from the furnace tubes to form the garnet via gas phase transport, the EBC SG-100 sample has the additional alumina within the coating.

Regarding the consumption of the YbMS phase to form garnet, similar results have been reported by Kane *et al.* [220] and Rohbeck *et al.* [228]. Although Rohbeck *et al.* did not specify

the steam velocity used in their experimental setup, Kane *et al.* measured their steam velocity to be 1.5 cm/s. It is suggested that steam velocity plays a key role in the corrosion mechanism observed [229], with low-velocity flowing steam not causing YbDS volatilisation.

The mechanism behind the depletion of YbMS is not fully understood yet, although two mechanisms have been proposed in the literature. The first one involves the consumption of the YbMS as it reacts with the Al-containing impurities (or the alumina present within the coating in the case of sample EBC SG-100) to form the garnet phase. Kane *et al.* [220] suggested that YbMS is more reactive than YbDS regarding alumina, which would explain why YbDS is unaffected in the steam exposure. This mechanism is temperature dependent, as the lowest eutectic point of the Yb-Al-Si-O system is 1500 °C [232], although the presence of alkali impurities from the furnace may unlock the formation of aluminosilicate compounds at a lower temperature [220]. This temperature dependence would explain the increase in YbMS depletion in all the samples in the 1400 °C steam exposure. When considering the 1400 °C exposure of sample EBC SG-100, it is worth noting that this sample was the one where the splat boundaries were more clearly visible, as presented in Figure 74b. For the two abradable coatings, this feature in the depleted layer was more difficult to detect due to the initial higher level of porosity. Similar to the infiltration of CMAS into YbDS [124,128,130,133], splat boundaries seem to be the preferential path for the ingress of Al-containing impurities, which would explain this phenomenon. Therefore, it can be suggested that this mechanism is prevalent in the case of sample EBC SG-100, where the extensive formation of garnet is observed. Once a dense scale of garnet is formed on the surface of the coating at 1400 °C, the ingress of Al-containing impurities is hindered, which slowed the expansion of the YbMS depleted layer compared to the abradable samples.

The second mechanism for the depletion of YbMS is based on the reaction between YbMS and SiO<sub>2</sub> to form YbDS. The presence of two YbMS depleted layers in work by Kane *et al.* [220],

one near the surface and one near the Si bond coat after steam exposure at 1300 °C, supports the idea of a low temperature Si/SiO<sub>2</sub> mediated mechanism for the depletion of YbMS. The presence of SiO<sub>2</sub> could not be confirmed through XRD measurements, as shown in Figure 71, which could indicate that the quantity present is below the detection limit of the technique. The high content of ytterbium on the coatings limits x-ray penetration to below 10 - 15 μm [220], limiting the amount of SiO<sub>2</sub> available for detection. Additionally, the overlap between the YbDS/YbMS and SiO<sub>2</sub> peaks might have masked the presence of traces amounts of SiO<sub>2</sub>. Nevertheless, since the system here studied was a free-standing coating without the presence of a Si bond coat, and presence of SiO<sub>2</sub> could not be observed, this mechanism cannot be robustly argued to explain the phenomenon detected here. A schematic representing the interaction between high-temperature steam and both EBC YbDS coating and abrasion-resistant (ABR) YbDS coatings is presented in Figure 78.

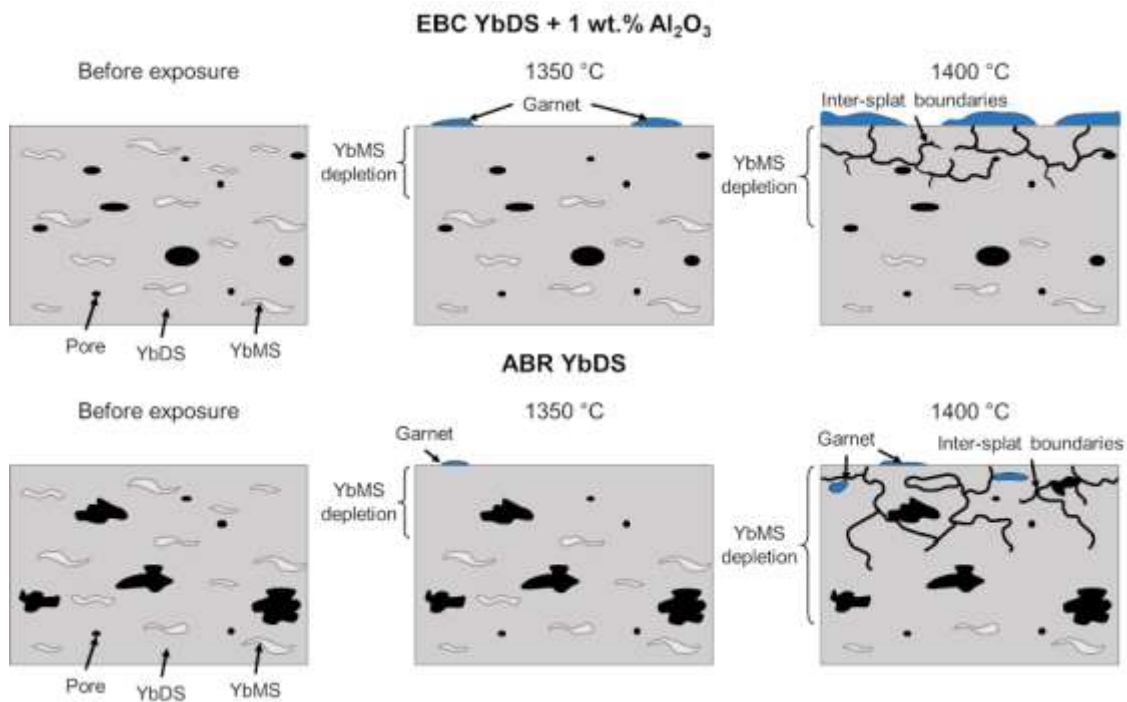


Figure 78: Schematic with the different behaviour of EBC YbDS + 1 wt.% Al<sub>2</sub>O<sub>3</sub> and abrasion-resistant YbDS coatings when exposed to steam at high temperature

From Figure 78, it can be seen how EBC SG-100 presents depletion of YbMS once exposed to steam at 1350 °C, while forming small quantities of garnet located at the top surface. At 1400 °C, the formation of garnet is more extensive, leading to a scale at the surface and a slightly larger depleted layer. Inter-splat boundaries can be observed in the depleted layer. In the case of the abradable samples, exposure to steam at 1350 °C also produces a YbMS depleted layer, although lower quantities of garnet are formed due to the absence of added alumina to the coatings. At 1400 °C, however, evidence of garnet formation can be observed, both at the surface and inside pores located near the surface. The depletion layer is considerably larger, containing finer pores aligned with the splat boundaries, along with larger pores. As previously mentioned, the presence of these fine pores within the inter-splat boundaries indicates that splat boundary is the preferential ingress path of gaseous Al-containing impurities.

## **6.5. Conclusions**

Degradation of ytterbium disilicate EBCs under steam conditions is one of the main considerations for the successful implementation of SiC CMC components into the current generation of gas turbine engines. In this work, three free-standing YbDS coatings deposited using APS were exposed to steam at 1350 °C and 1400 °C for 96 h. The results show that sample EBC SG-100, with a low porosity level and 1 wt.% of Al<sub>2</sub>O<sub>3</sub> added to the feedstock powder, presented moderate depletion of YbMS near the surface with the formation of ytterbium garnet. At 1400 °C, the garnet formed a dense scale at the surface and inter-splat porosity formed within the YbMS depleted layer. The mechanism for the YbMS depletion is believed to be a reaction with gaseous Al-containing impurities from the alumina furnace tubes and the alumina present within the coating, leading to the formation of the garnet.

The two abradable samples, with 1.5 wt.% polyester added to the feedstock powder as a pore former, behaved in a similar fashion at 1350 °C, with the appearance of a YbMS depletion

layer and traces amount of garnet detected. At 1400 °C, the size of the depleted layer grew considerably larger than in the case of the EBC sample, with less garnet phase forming. Porosity also increased within the depleted layer; however, its effect was more difficult to clearly identify due to the higher level of porosity. The mechanism for the formation of the YbMS depleted layer is associated with the gaseous Al-containing impurities from the furnace. Since the abradable coatings did not contain added alumina, less garnet phase formed compared to the EBC coating.

In both cases, the exposure to flowing steam for 96 h at high temperature did not produce any evidence that the integrity of the coatings might be compromised, both in terms of cracking or loss of mass. Nevertheless, Al-containing impurities coming from the furnace tubes played a key role in the steam degradation of the coatings, requiring further investigation using experimental setups where external contributions are not a factor.

## **6.6. Acknowledgements**

This work was supported by the Engineering and Physical Sciences Research Council (EPSRC) (grant number EP/L016206/1). The authors would like to thank Dr Hannah Constantin for her assistance in performing the XRD measurements and to the Nanoscale and Microscale Research Centre (nmRC) at the University of Nottingham for providing access to microscopy facilities.

## Appendix

The purpose of this section is to provide further information on the thermal spraying setup used in this thesis to deposit ceramic coatings. These details are pertinent to the coatings deposited and studied in Chapter 3 and Chapter 4.

Figure 79 presents a schematic representation of the HVOF spraying system used to deposit coatings using liquid feedstock (both suspension and solution precursor).

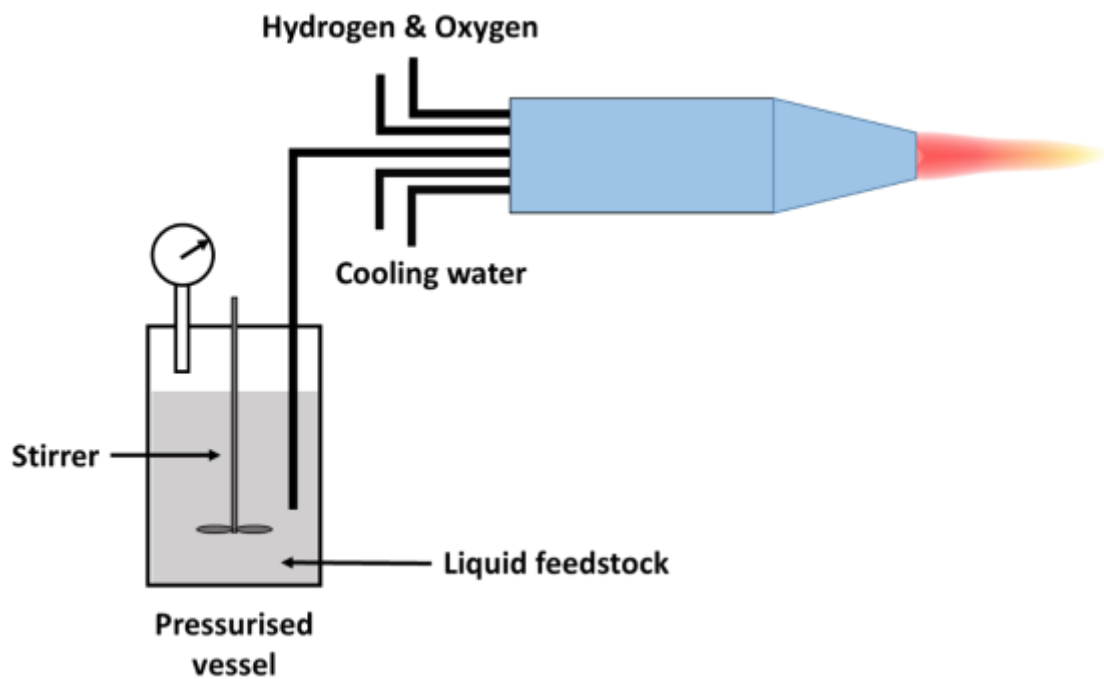


*Figure 79: Schematic of the HVOF setup used for suspension and solution precursor*

Once the suspension or solution precursor is prepared and ready for spraying, it is placed in a pressurised vessel with a mechanical stirrer, aiming to maintain a homogenous mixing of the liquid. The feedstock flow being introduced into the spray gun can be controlled through the pressure. The spray gun, a modified GTV TopGun thermal spray gun, has five inlets. The first two are for the injection of the oxygen and the fuel (hydrogen in this case) with two more for

the circulation of cooling water. The final inlet connects directly into the centre of the combustion chamber, as shown in Figure 80, to deliver the feedstock through axial injection.

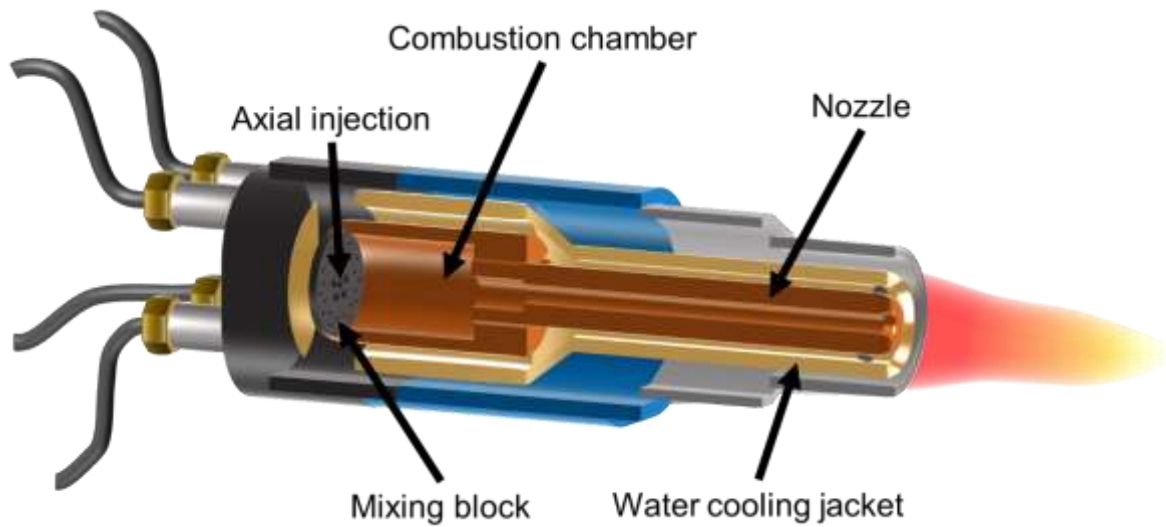


*Figure 80: Schematic of the modified GTV TopGun spray gun used for all the suspension and solution precursor HVOF thermal spraying. Schematic drawn by Dr Acacio Romero Rincon. Reproduced here with permission*

In addition to the flow of oxygen, hydrogen and flow of feedstock delivered into the combustion chamber, the stand-off distance (distance from the end of the nozzle to the substrate) and the number of passes were the main parameters modified to alter the characteristics of the deposited coating. Samples were placed on a rotating carousel, as shown in Figure 81, with an optimised rotating speed of 73 rpm (corresponding to a surface speed of 1 m/s). To cover the entirety of the surface of the substrate, the gun had a traverse movement along the vertical direction with a speed of 5 mm/s.



*Figure 81: Photo of the spraying setup where the spray gun (left) is visible along with the sample carousel (right)*

## Chapter 7: General discussion

The overall goal of this thesis was the detailed study of the properties and performance of thermal sprayed coatings, deposited using a variety of feedstock presentations (powder, suspension or solution precursor). Each of the four experimental chapters has presented and discussed the results in depth, and therefore, the purpose of this chapter is not to reiterate the technical details described there. This chapter aims to present an overview of the totality of the findings of this thesis, combining the most relevant results and detailing the novelty and achievements of the work, as schematically represented in Figure 82.

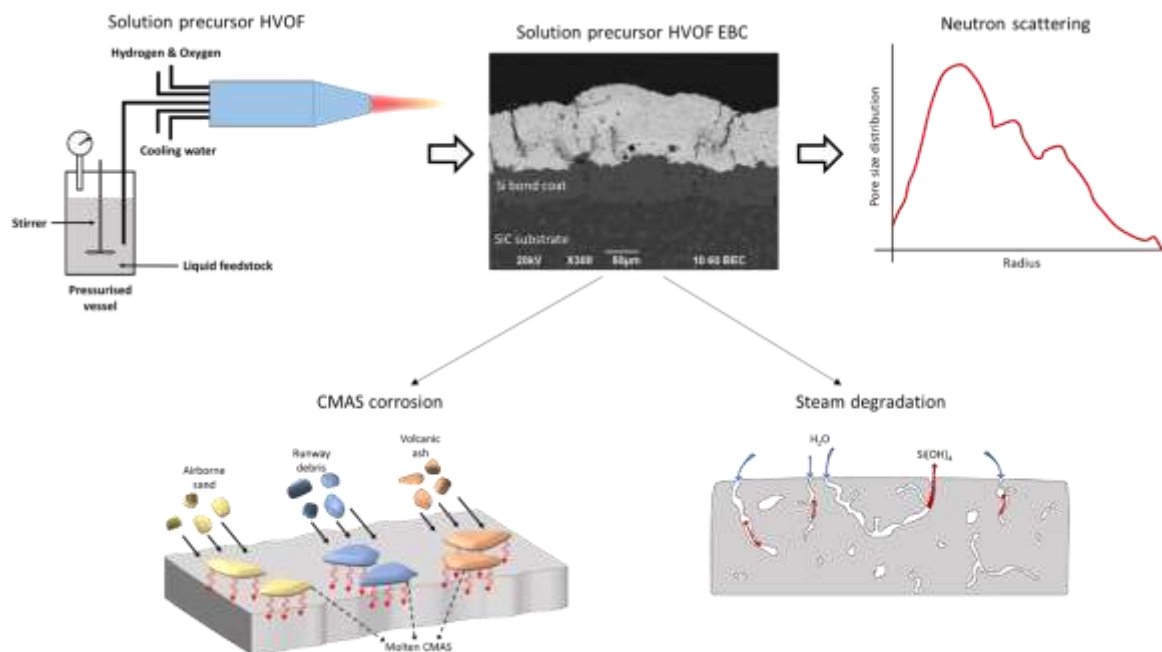


*Figure 82: Schematic showing the overall findings of this thesis and the relationship between the four experimental chapters*

Figure 82 shows how the finding regarding solution precursor HVOF are currently being applied for the deposition of novel EBCs. These novel coatings, both in terms of composition and microstructure, will need to be thoroughly investigated to understand the differences present when compare to traditional powder-based EBCs. Neutron scattering, a powerful

technique for the measurement of porosity, can be applied to research in detail the pore characteristics and high temperature evolution. Once the deposition process has been optimised and the microstructure of the produced coating are fully understood, novel EBCs need to be tested under simulated service conditions. The performance of such coatings under molten CMAS attack and steam degradation will dictate the path forward towards the introduction in gas turbine engines.

### **7.1. Solution precursor HVOF thermal spray**

The use of solution precursor HVOF (SP-HVOF) thermal spraying to produce doped ceramic coatings was the focus of Chapter 3. Although the material selected for this study was Nb-doped TiO<sub>2</sub>, the understanding of the deposition process is fundamental enough to warrant its application to other ceramic compositions, doped or not. Three main discussing points arise from this chapter. The first one is the ability of SP-HVOF thermal spraying to deposit ceramic coatings without the need for powder or suspended material as feedstock, contrary to traditional powder-based or suspension-based thermal spraying. This line of work has prompted very interesting research questions, such as the possibility of solution precursor thermal sprayed EBCs. As discussed in the literature review in section 2.3 “Environmental barrier coatings”, current research efforts are focused mainly on powder-based thermal spraying techniques, as also evidenced in Chapters 5 and 6.

The discoveries presented in this thesis regarding the transformation of solution precursor as it is injected into the combustion chamber and travels along the flame (for more details the reader is encouraged to re-visit Figure 40) have been the founding blocks for on-going research regarding solution precursor EBCs currently being developed at the University of Nottingham. The work, currently in progress and that will be published in the public domain once completed, shows promising results regarding the use of ytterbium (III) nitrate hydrate (Yb(NO<sub>3</sub>)<sub>3</sub>·5-6H<sub>2</sub>O)

and Ludox colloidal silica ( $\text{SiO}_2$ ) suspended in water to produce high-phase purity YbDS environmental barrier coatings. Preliminary results, shown in Figure 83, show deposition of mostly YbDS coatings, with traces of YbMS and good adherence to the silicon bond coat underneath.

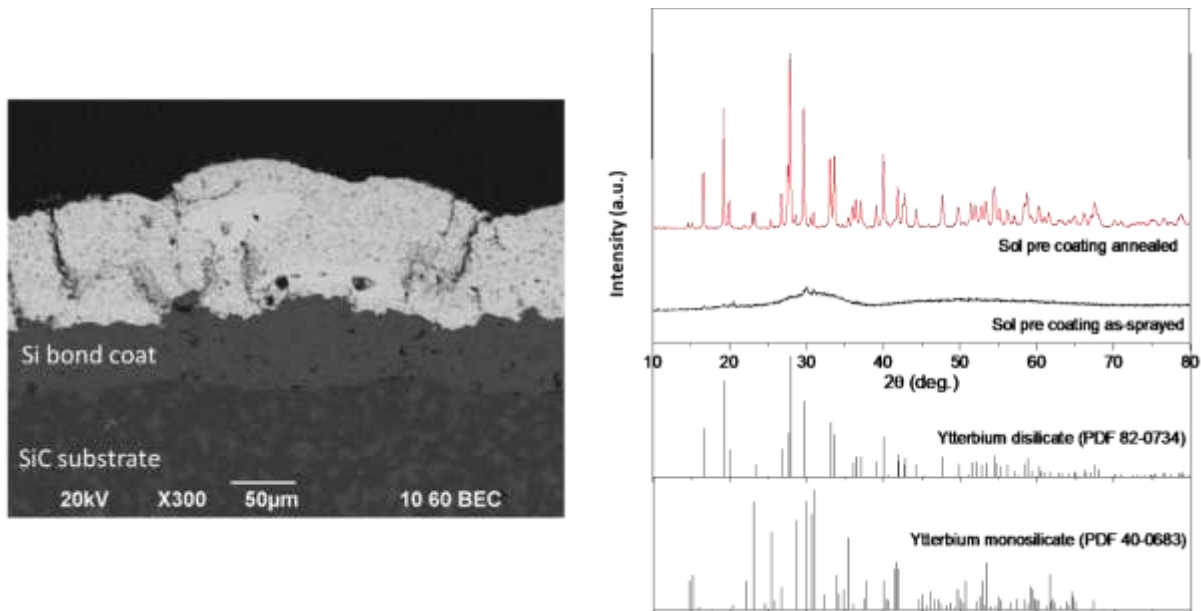


*Figure 83: SEM-BSE image of the cross section of a SP-HVOF YbDS coating deposited on top of a Si bond coat on a SiC substrate (left) and XRD measurement of the coating as-sprayed and after annealing at 1200 °C for 1 h (right). All the data here presented was kindly provided by Dr Acacio Rincon Romero and reproduced with permission*

The second discussion point regarding SP-HVOF thermal spray is its proven capability to produce homogeneously doped ceramic coatings. Current research indicates that instead of the use of a single rare earth element for the composition of EBCs, it might be beneficial to incorporate varying quantities of two rare earth elements [86]. Once such doped composition,  $\text{Y}_x\text{Yb}_{(2-x)}\text{Si}_2\text{O}_7$ , could be easily produced following the SP-HVOF thermal spraying deposition route mentioned above, with the addition of varying quantities of yttrium (III) nitrate hexahydrate ( $\text{Y}(\text{NO}_3)_3 \cdot 6\text{H}_2\text{O}$ ) to achieve the desired level of doping. This approach would represent a leap in terms of testing and evaluation of new EBC compositions, which currently

relies on slow and expensive sintering process to produce enough amount of powder to either spray directly, or disperse in a liquid medium as suspension feedstock.

Finally, the third result to discuss regarding SP-HVOF thermal spray is the easy tailoring of the microstructure of the coating by altering the spraying parameters. Combining the already produced SP-HVOF YbDS EBC with the possibility to deposit high porosity coatings, the research possibilities expand. As presented in Chapters 5 and 6, abradable EBCs require higher levels of porosity in order to form an adequate seal. The use of SP-HVOF would allow to test traditional as well as abradable EBCs, including the addition of novel compositions, to evaluate the optimal microstructure and chemical composition. These novel EBCs can be tested against the most common corrosive environments, CMAS and steam, being the protocols and results presented in Chapters 5 and 6 an ideal starting point to test performance.

## **7.2. Porosity measurement of SP-HVOF thermal sprayed coatings**

The use of novel deposition techniques, such as SP-HVOF thermal spray, for the deposition of the next generation of EBCs requires an in-depth study of the properties of the produced coatings. As discussed in Chapter 4, the study of the porosity present within thermal sprayed coatings, both in terms of overall content and characteristics of the pores, is crucial for the introduction of new coatings into service. Traditional powder-based thermal sprayed coatings have been thoroughly researched in the past, leading to their successful implementation in gas turbine engines. For these well-established deposition techniques, Image Analysis has been proven as an effective and cost-efficient technique to evaluate the porosity within coatings. Nevertheless, as detailed in Chapter 4, the transition into suspension and solution precursor feedstock requires careful research to ensure that all the new features are properly captured and studied. The sub-micron characteristics of the solid material present in suspensions, and formed in-flight during solution precursor thermal spray, creates sub-micron porosity, not accessible

using traditional Image Analysis. Taking into account this challenge, alternative techniques need to be considered to fully comprehend the microstructure of these novel coatings.

With this goal in mind, neutron scattering was selected as a powerful technique that can increase the information obtained from a coating, particularly in terms of pore size range studied. Although neutron scattering presents some drawbacks (primarily the difficulty of access to a synchrotron or nuclear source and the increased complexity in data analysis), its benefits are particularly appealing when dealing with novel deposition techniques. The detailed porosity evolution on a suspension HVOF thermal sprayed coating presented in Chapter 4 provides a wealth of information that is required for novel deposition techniques, such as suspension HVOF or SP-HVOF thermal spray.

Once these novel EBCs have been thoroughly researched and the characteristics and high temperature evolution of the porosity are understood, complementary porosity measurement techniques more accessible to researchers all over the world (such as Image Analysis, Archimedes method or mercury intrusion porosimetry) can be introduced. No experimental technique is perfect, which requires a good understanding of the limitations and drawbacks of the chosen technique and, when possible, the addition of a complementary technique to overcome some of the shortcomings present.

### **7.3. Performance testing of novel EBCs**

The deposition of novel EBCs making use of SP-HVOF thermal spray, including their thorough characterisation using techniques such as neutron scattering, is only the first step in the search for the next generation of EBCs. Testing of the coatings under laboratory simulated conditions is required to assess the capability that the coatings possess to withstand the harsh conditions expected to experience during service.

The new compositions produced taking advantage of the flexibility offered by SP-HVOF thermal spray, as well as the knowledge acquired regarding porosity within the coating, can inform and clarify the behaviour observed during performance testing. For instance, in this thesis two main corrosion mechanisms have been studied: CMAS attack and steam degradation. In both cases, grain boundaries were a central element of the mechanisms observed. When depositing coatings using SP-HVOF thermal spray instead of powder-based techniques, grain boundaries will be affected, which should be taken into account when analysing the produced data.

The data collected during the performance testing, as well as the conclusions reached after the pertinent analysis, can inform the spraying parameters used for the coating deposition, aiming to optimise the coating deposition and performance behaviour. In addition, not only the deposition process can be improved in order to optimise the system. As shown in Chapter 6, useful conclusions regarding the steam rig used for the performance testing were gathered after the analysis of the experimental data. All this information can be fed back into the development loop, producing better coatings and testing procedures, as schematically demonstrated in Figure 84.

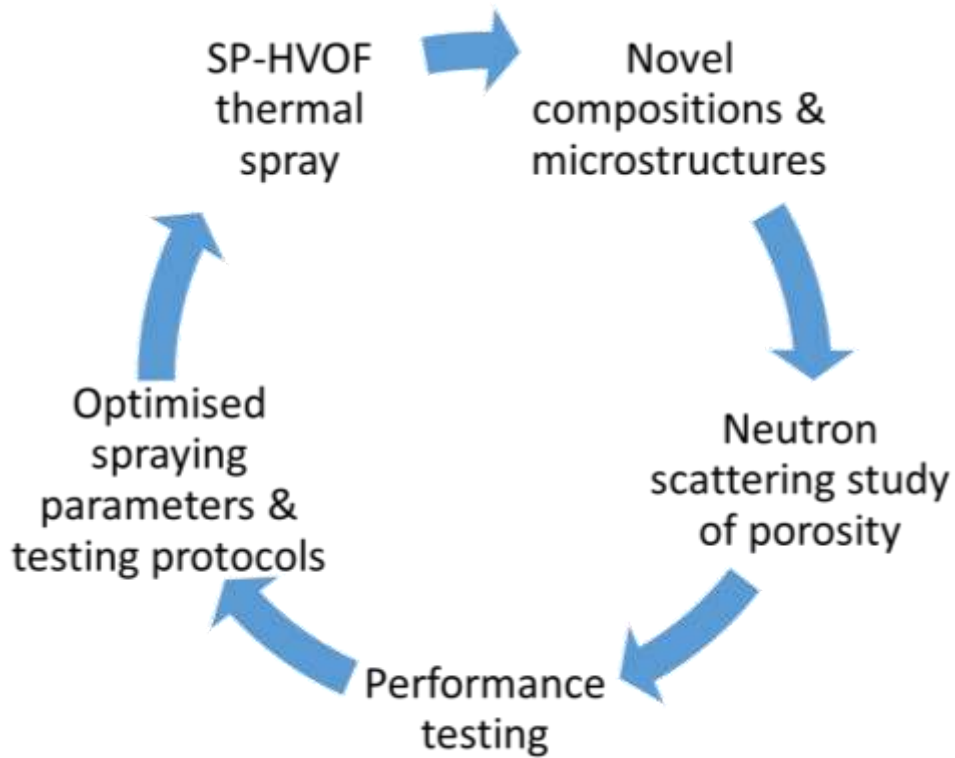


*Figure 84: Schematic development loop for the use of novel deposition techniques. In this case, SP-HVOF thermal spray can be used to produce coatings with novel compositions and microstructures, which require extensive study using advanced techniques such as neutron scattering. The data collected can be used to better tailor the conditions of the performance tests, which produce information that can be used to better inform the choice of spraying parameters and testing protocols*

## **Chapter 8: General conclusions and Future work**

### **8.1. General conclusions**

In this thesis, the relationship between the feedstock presentation, as well as the spraying parameters, and the microstructure and performance of thermal sprayed ceramic coatings has been investigated. The results here presented can be used to extract a series of conclusions, which can be summarised as follows.

Solution precursor is a powerful and flexible feedstock for thermal spray, capable of producing functional ceramic coatings with different compositions, making use of doping. The easy addition of doping elements facilitates the deposition of coatings with tailored compositions aimed at different functionalities. Niobium, a popular element for the improvement of the electrical properties of TiO<sub>2</sub> was used here, but the possibilities are not limited to electrical properties. In addition to the compositional changes, varied microstructures were produced, as shown in Chapter 3, proving that porosity can be tailored to the application in mind. In particular, a deeper understanding of the mechanism behind coating deposition was presented for solution precursor high velocity oxy-fuel thermal spray. Although solution precursor thermal spraying has been investigated in the past, most of the focus had been placed on solution precursor plasma spraying. This work demonstrates the capabilities of SP-HVOF to produce ceramic coatings, homogeneously doped and capable of varying levels of porosity. The deep knowledge of the in-flight transformation also provides a roadmap for the development of future functional coatings.

Feedstock, be it powder, suspension or solution precursor, plays a key role in the final microstructure of the deposited coating. One specific parameter heavily influenced by this is the porosity of the coating. Although porosity is generally recognised as a critical characteristic of ceramic coatings, the importance of this feature is paramount in thermal barrier coatings.

The direct correlation between porosity and hardness, distribution of thermal residual stress and thermal conductivity, makes its measurement a topic of the utmost importance. Porosity in thermal sprayed coatings can be generally described attending to three characteristics: total porosity, pore size distribution and pore morphology. Total porosity and pore morphology are influenced not only by the feedstock presentation, but by the spraying parameters as well. Pore size distribution, however, is strongly correlated to the feedstock selected. As seen in Chapter 4, suspension thermal spraying presents porosity with pore sizes well below 10  $\mu\text{m}$ , which are not present in coatings deposited using powder feedstock. This requires a change in the traditional frameworks developed for the measurement of porosity in coatings, as certain mainstream techniques (such as image analysis) cannot measure porosity of such small size, providing an incomplete picture of the porosity of the coating. Neutron scattering techniques, capable of detecting sub-micron pores as well as being non-destructive, are more suitable for porosity measurements, including pores with size below 10  $\mu\text{m}$ . This work proves their suitability to precisely measure porosity content as well as pore size distribution, key factors in thermal barrier coatings.

Finally, once a suitable feedstock and spraying parameters have been chosen to deposit a coating with the desired microstructure, it should be considered how the microstructure will affect the performance during service. In the case of environmental barrier coatings, CMAS and steam degradation are the two main concerns regarding the implementation of said coatings into commercial gas engine turbines. Regarding CMAS, this work proves that even when notable differences in porosity levels are present, CMAS corrosion experienced is fairly comparable. Although higher porosity promotes quicker penetration of molten CMAS in the first stages of the exposure (with times below 1 h), the long-term effect is mainly driven by inter-splat boundary infiltration, leading to similar levels of apatite formation and CMAS infiltration after 48 h. Another important aspect shown here is that no damage or evidence of

coating failure could be detected despite the extensive reaction and infiltration. Moreover, faster infiltration is preferred if “blister damage” is to be avoided. When considering steam degradation, once more the porosity content proved to present no difference regarding the corrosion mechanism or degree of degradation. The reaction with gaseous Al-containing impurities coming from the furnace tubes was the predominant effect observed, which was exacerbated by the presence of added alumina into the low-porosity coating. The formation of garnet and depletion of ytterbium monosilicate within the coating, once more showed no detrimental effect to the physical integrity of the coatings, which is promising. These results represent a first stepping stone into the introduction of abradable environmental barrier coatings, presenting higher levels of porosity but still providing adequate protection against CMAS and steam degradation.

In conclusion, this thesis has proved the capability of solution precursor thermal spray to produce homogeneously doped ceramic coatings with tailored levels of porosity. Since traditional porosity measurement techniques (such as image analysis) cannot measure pores below  $\sim 10 \mu\text{m}$  (present in solution precursor and suspension thermal sprayed thermal barrier coatings), neutron scattering was studied and presented as a suitable technique. The capability of neutron scattering to measure pores below  $10 \mu\text{m}$  was demonstrated, as well as presenting a non-destructive alternative, suitable if multiple investigations must be conducted with the exact same sample. Finally, environmental barrier coatings with distinctive levels of porosity were studied to assess their resistance to the two most common degradation mechanisms: CMAS attack and steam corrosion. This work demonstrates that higher porosity levels, never evaluated before, present similar degradation behaviour, with no evidence of failure. This result is instrumental in the future development of abradable environmental barrier coatings deposited using thermal spray, a field barely developed as of yet.

## 8.2. Future work

Future work would be beneficial to answer some of the pending questions created by the research presented in this thesis. As a summary, two main paths are suggested to further develop this research.

- The application of the knowledge acquired regarding the use of solution precursor and suspension thermal spray to produce environmental barrier coatings. Currently, the majority of the performance investigations are based on powder-based deposited coatings. The flexibility and control provided by solution precursor, as presented in Chapter 3, would allow to tailor the porosity, both in total content and pore size distribution as well as the composition through the use doping. The introduction of nano-sized porosity, properly investigated through the appropriate porosity measurement techniques (as discussed in Chapter 4), and the inclusion of doping element in varying concentrations could drastically alter the behaviour of the current generation of environmental barrier coatings
- The research presented in this thesis has been conducted using either stainless steel substrates (on the solution precursor study) or free-standing coatings. This is convenient for the initial stages of research, but it is hardly representative of the real service conditions. The introduction of the appropriate substrate, including potential bond coats, would allow for more representative studies on the CMAS and steam degradation. Additionally, the steam rig could be optimise to minimise the amount of reaction with Al-containing impurities (discussed in Chapter 6), providing a more detailed picture of the mechanisms behind steam degradation during service

## References

- [1] D. Tejero-Martin, M. Rezvani Rad, A. McDonald, T. Hussain, Beyond Traditional Coatings: A Review on Thermal-Sprayed Functional and Smart Coatings, *J. Therm. Spray Technol.* 28 (2019) 598–644. <https://doi.org/10.1007/s11666-019-00857-1>.
- [2] K.N. Lee, Protective Coatings for Gas Turbines, in: *Gas Turbine Handb.*, 2006: pp. 419–437.
- [3] R. Darolia, Thermal barrier coatings technology: critical review, progress update, remaining challenges and prospects, *Int. Mater. Rev.* 58 (2013) 315–348. <https://doi.org/10.1179/1743280413Y.0000000019>.
- [4] N.P. Padture, Environmental degradation of high-temperature protective coatings for ceramic-matrix composites in gas-turbine engines, *Npj Mater. Degrad.* 3 (2019) 11. <https://doi.org/10.1038/s41529-019-0075-4>.
- [5] N.P. Padture, Advanced structural ceramics in aerospace propulsion, *Nat. Mater.* 15 (2016) 804–809. <https://doi.org/10.1038/nmat4687>.
- [6] L.B. Chen, Ytria-stabilized Zirconia Thermal Barrier Coatings — A Review, *Surf. Rev. Lett.* 13 (2006) 535–544. <https://doi.org/10.1142/S0218625X06008670>.
- [7] M. van Roode, Ceramic Gas Turbine Development: Need for a 10 Year Plan, *J. Eng. Gas Turbines Power.* 132 (2010) 1–8. <https://doi.org/10.1115/1.3124669>.
- [8] J. Steibel, Ceramic matrix composites taking flight at GE Aviation, *Am. Ceram. Soc. Bull.* 98 (2019) 30–33.
- [9] U. Schulz, B. Saruhan, K. Fritscher, C. Leyens, Review on Advanced EB-PVD Ceramic Topcoats for TBC Applications, *Int. J. Appl. Ceram. Technol.* 1 (2005) 302–315.

<https://doi.org/10.1111/j.1744-7402.2004.tb00182.x>.

- [10] M. Peters, C. Leyens, U. Schulz, W.A. Kaysser, EB-PVD Thermal Barrier Coatings for Aeroengines and Gas Turbines, *Adv. Eng. Mater.* 3 (2001) 193–204. [https://doi.org/10.1002/1527-2648\(200104\)3:4<193::AID-ADEM193>3.0.CO;2-U](https://doi.org/10.1002/1527-2648(200104)3:4<193::AID-ADEM193>3.0.CO;2-U).
- [11] H. Herman, S. Sampath, R. McCune, Thermal Spray: Current Status and Future Trends, *MRS Bull.* 25 (2000) 17–25. <https://doi.org/10.1557/mrs2000.119>.
- [12] A. Vardelle, C. Moreau, J. Akedo, H. Ashrafizadeh, C.C. Berndt, J.O. Berghaus, M. Boulos, J. Brogan, A.C. Bourtsalas, A. Dolatabadi, M. Dorfman, T.J. Eden, P. Fauchais, G. Fisher, F. Gaertner, M. Gindrat, R. Henne, M. Hyland, E. Irissou, E.H. Jordan, K.A. Khor, A. Killinger, Y.C. Lau, C.J. Li, L. Li, J. Longtin, N. Markocsan, P.J. Masset, J. Matejicek, G. Mauer, A. McDonald, J. Mostaghimi, S. Sampath, G. Schiller, K. Shinoda, M.F. Smith, A.A. Syed, N.J. Themelis, F.-L. Toma, J.P. Trelles, R. Vaßen, P. Vuoristo, The 2016 Thermal Spray Roadmap, *J. Therm. Spray Technol.* 25 (2016) 1376–1440. <https://doi.org/10.1007/s11666-016-0473-x>.
- [13] K.N. Lee, D. Zhu, R.S. Lima, Perspectives on Environmental Barrier Coatings (EBCs) Manufactured via Air Plasma Spray (APS) on Ceramic Matrix Composites (CMCs): A Tutorial Paper, *J. Therm. Spray Technol.* 2021 301. 30 (2021) 40–58. <https://doi.org/10.1007/S11666-021-01168-0>.
- [14] D.E. Crawmer, Thermal Spray Processes, in: *Handb. Therm. Spray Technol.*, ASM International, 2013: pp. 54–76.
- [15] D.E. Crawmer, Introduction to Coatings, Equipment, and Theory, *Handb. Therm. Spray Technol.* (2008) 43–46.
- [16] J.R. Davis, Introduction to Thermal Spray Processing, in: *Handb. Therm. Spray*

- Technol., 2004: pp. 3–13.
- [17] M. Oksa, E. Turunen, T. Suhonen, T. Varis, S.-P. Hannula, Optimization and Characterization of High Velocity Oxy-fuel Sprayed Coatings: Techniques, Materials, and Applications, *Coatings*. 1 (2011) 17–52. <https://doi.org/10.3390/coatings1010017>.
- [18] P. Fauchais, M. Vardelle, A. Vardelle, S. Goutier, What Do We Know, What are the Current Limitations of Suspension Plasma Spraying?, *J. Therm. Spray Technol.* 24 (2015) 1120–1129. <https://doi.org/10.1007/s11666-015-0286-3>.
- [19] R. Vaßen, H. Kaßner, G. Mauer, D. Stöver, Suspension Plasma Spraying: Process Characteristics and Applications, *J. Therm. Spray Technol.* 19 (2010) 219–225. <https://doi.org/10.1007/s11666-009-9451-x>.
- [20] A. Killinger, P. Müller, R. Gadow, What Do We Know, What are the Current Limitations of Suspension HVOF Spraying?, *J. Therm. Spray Technol.* 24 (2015) 1130–1142. <https://doi.org/10.1007/s11666-015-0264-9>.
- [21] J. Oberste Berghaus, B.R. Marple, High-velocity oxy-fuel (HVOF) suspension spraying of mullite coatings, *J. Therm. Spray Technol.* 17 (2008) 671–678. <https://doi.org/10.1007/s11666-008-9219-8>.
- [22] A. Killinger, R. Gadow, G. Mauer, A. Guignard, R. Vaßen, D. Stöver, Review of New Developments in Suspension and Solution Precursor Thermal Spray Processes, *J. Therm. Spray Technol.* 20 (2011) 677–695. <https://doi.org/10.1007/s11666-011-9639-8>.
- [23] J. Puranen, J. Laakso, M. Kylmälahti, P. Vuoristo, Characterization of High-Velocity Solution Precursor Flame-Sprayed Manganese Cobalt Oxide Spinel Coatings for Metallic SOFC Interconnectors, *J. Therm. Spray Technol.* 22 (2013) 622–630.

<https://doi.org/10.1007/s11666-013-9922-y>.

- [24] M. Mahrukh, A. Kumar, S. Gu, Experimental Study of the Effects of Using Different Precursor Concentrations, Solvent Types, and Injection Types on Solution Precursor High-Velocity Oxygen Fuel (HVOF) Nanostructured Coating Formation, *Ind. Eng. Chem. Res.* 56 (2017) 4957–4969. <https://doi.org/10.1021/acs.iecr.6b04857>.
- [25] D. Chen, E.H. Jordan, M. Gell, Solution precursor high-velocity oxy-fuel spray ceramic coatings, *J. Eur. Ceram. Soc.* 29 (2009) 3349–3353. <https://doi.org/10.1016/j.jeurceramsoc.2009.07.010>.
- [26] P. Fauchais, J.V.R. Heberlein, M.I. Boulos, *Thermal Spray Fundamentals*, Springer US, Boston, MA, 2014. <https://doi.org/10.1007/978-0-387-68991-3>.
- [27] L. Pawlowski, Suspension and solution thermal spray coatings, *Surf. Coatings Technol.* 203 (2009) 2807–2829. <https://doi.org/10.1016/j.surfcoat.2009.03.005>.
- [28] D. Tejero-Martin, Z. Pala, S. Rushworth, T. Hussain, Splat formation and microstructure of solution precursor thermal sprayed Nb-doped titanium oxide coatings, *Ceram. Int.* 46 (2020) 5098–5108. <https://doi.org/10.1016/j.ceramint.2019.10.253>.
- [29] D. Chen, E.H. Jordan, M. Gell, Effect of solution concentration on splat formation and coating microstructure using the solution precursor plasma spray process, *Surf. Coatings Technol.* 202 (2008) 2132–2138. <https://doi.org/10.1016/j.surfcoat.2007.08.077>.
- [30] A. Fujishima, K. Honda, Electrochemical Photolysis of Water at a Semiconductor Electrode, *Nature.* 238 (1972) 37–38. <https://doi.org/10.1038/238037a0>.
- [31] Y. Kikuchi, K. Sunada, T. Iyoda, K. Hashimoto, A. Fujishima, Photocatalytic bactericidal effect of TiO<sub>2</sub> thin films: dynamic view of the active oxygen species responsible for the effect, *J. Photochem. Photobiol. A Chem.* 106 (1997) 51–56.

[https://doi.org/10.1016/S1010-6030\(97\)00038-5](https://doi.org/10.1016/S1010-6030(97)00038-5).

- [32] B. Jeffery, M. Pepler, R.S. Lima, A. McDonald, Bactericidal effects of HVOF-sprayed nanostructured TiO<sub>2</sub> on *Pseudomonas aeruginosa*, *J. Therm. Spray Technol.* 19 (2010) 344–349. <https://doi.org/10.1007/s11666-009-9369-3>.
- [33] A. Teleki, S.E. Pratsinis, K. Kalyanasundaram, P.I. Gouma, Sensing of organic vapors by flame-made TiO<sub>2</sub> nanoparticles, *Sensors Actuators B Chem.* 119 (2006) 683–690. <https://doi.org/10.1016/j.snb.2006.01.027>.
- [34] M.C. Carotta, M. Ferroni, D. Gnani, V. Guidi, M. Merli, G. Martinelli, M.C. Casale, M. Notaro, Nanostructured pure and Nb-doped TiO<sub>2</sub> as thick film gas sensors for environmental monitoring, *Sensors Actuators B Chem.* 58 (1999) 310–317. [https://doi.org/10.1016/S0925-4005\(99\)00148-3](https://doi.org/10.1016/S0925-4005(99)00148-3).
- [35] B. Fleming, S. Rushworth, Investigation of glyme additives to metalorganic ink systems, *J. Sol-Gel Sci. Technol.* 82 (2017) 308–314. <https://doi.org/10.1007/s10971-017-4302-6>.
- [36] Y. Sato, H. Akizuki, T. Kamiyama, Y. Shigesato, Transparent conductive Nb-doped TiO<sub>2</sub> films deposited by direct-current magnetron sputtering using a TiO<sub>2</sub>-x target, *Thin Solid Films.* 516 (2008) 5758–5762. <https://doi.org/10.1016/j.tsf.2007.10.047>.
- [37] Y. Wang, B.M. Smarsly, I. Djerdj, Niobium doped TiO<sub>2</sub> with mesoporosity and its application for lithium insertion, *Chem. Mater.* 22 (2010) 6624–6631. <https://doi.org/10.1021/cm1020977>.
- [38] M. Fehse, S. Cavaliere, P.E. Lippens, I. Savych, A. Iadecola, L. Monconduit, D.J. Jones, J. Rozière, F. Fischer, C. Tessier, L. Stievano, Nb-Doped TiO<sub>2</sub> Nanofibers for Lithium Ion Batteries, *J. Phys. Chem. C.* 117 (2013) 13827–13835.

<https://doi.org/10.1021/jp402498p>.

- [39] J. Arbiol, J. Cerdà, G. Dezanneau, A. Cirera, F. Peiró, A. Cornet, J.R. Morante, Effects of Nb doping on the TiO<sub>2</sub> anatase-to-rutile phase transition, *J. Appl. Phys.* 92 (2002) 853–861. <https://doi.org/10.1063/1.1487915>.
- [40] S. Phanichphant, C. Liewhiran, K. Wetchakun, A. Wisitsoraat, A. Tuantranont, Flame-Made Nb-Doped TiO<sub>2</sub> Ethanol and Acetone Sensors, *Sensors*. 11 (2011) 472–484. <https://doi.org/10.3390/s110100472>.
- [41] A. Teleki, N. Bjelobrk, S. Pratsinis, Flame-made Nb- and Cu-doped TiO<sub>2</sub> sensors for CO and ethanol, *Sensors Actuators B Chem.* 130 (2008) 449–457. <https://doi.org/10.1016/j.snb.2007.09.008>.
- [42] N.L.H. Hoang, N. Yamada, T. Hitosugi, J. Kasai, S. Nakao, T. Shimada, T. Hasegawa, Low-temperature Fabrication of Transparent Conducting Anatase Nb-doped TiO<sub>2</sub> Films by Sputtering, *Appl. Phys. Express.* 1 (2008) 115001. <https://doi.org/10.1143/APEX.1.115001>.
- [43] G. Wan, S. Wang, X. Zhang, M. Huang, Y. Zhang, W. Duan, L. Yi, Transparent conductive Nb-doped TiO<sub>2</sub> films deposited by RF magnetron co-sputtering, *Appl. Surf. Sci.* 357 (2015) 622–625. <https://doi.org/10.1016/j.apsusc.2015.09.080>.
- [44] T. Hitosugi, A. Ueda, S. Nakao, N. Yamada, Y. Furubayashi, Y. Hirose, T. Shimada, T. Hasegawa, Fabrication of highly conductive Ti<sub>1-x</sub>Nb<sub>x</sub>O<sub>2</sub> polycrystalline films on glass substrates via crystallization of amorphous phase grown by pulsed laser deposition, *Appl. Phys. Lett.* 90 (2007) 212106. <https://doi.org/10.1063/1.2742310>.
- [45] S. Lee, J.H. Noh, H.S. Han, D.K. Yim, D.H. Kim, J.-K. Lee, J.Y. Kim, H.S. Jung, K.S. Hong, Nb-Doped TiO<sub>2</sub>: A New Compact Layer Material for TiO<sub>2</sub> Dye-Sensitized Solar

- Cells, *J. Phys. Chem. C*. 113 (2009) 6878–6882. <https://doi.org/10.1021/jp9002017>.
- [46] J.-P. Niemelä, H. Yamauchi, M. Karppinen, Conducting Nb-doped TiO<sub>2</sub> thin films fabricated with an atomic layer deposition technique, *Thin Solid Films*. 551 (2014) 19–22. <https://doi.org/10.1016/j.tsf.2013.11.043>.
- [47] A. V. Manole, M. Dobromir, M. Gîrtan, R. Mallet, G. Rusu, D. Luca, Optical properties of Nb-doped TiO<sub>2</sub> thin films prepared by sol–gel method, *Ceram. Int.* 39 (2013) 4771–4776. <https://doi.org/10.1016/j.ceramint.2012.11.066>.
- [48] D.S. Bhachu, S. Sathasivam, G. Sankar, D.O. Scanlon, G. Cibin, C.J. Carmalt, I.P. Parkin, G.W. Watson, S.M. Bawaked, A.Y. Obaid, S. Al-Thabaiti, S.N. Basahel, Solution Processing Route to Multifunctional Titania Thin Films: Highly Conductive and Photocatalytically Active Nb:TiO<sub>2</sub>, *Adv. Funct. Mater.* 24 (2014) 5075–5085. <https://doi.org/10.1002/adfm.201400338>.
- [49] P. Ctibor, V. Stengl, Z. Pala, Structural and photocatalytic characteristics of TiO<sub>2</sub> coatings produced by various thermal spray techniques, *J. Adv. Ceram.* 2 (2013) 218–226. <https://doi.org/10.1007/s40145-013-0063-z>.
- [50] M. Gardon, J.M. Guilemany, Milestones in Functional Titanium Dioxide Thermal Spray Coatings: A Review, *J. Therm. Spray Technol.* 23 (2014) 577–595. <https://doi.org/10.1007/s11666-014-0066-5>.
- [51] D. Chen, E.H. Jordan, M. Gell, Porous TiO<sub>2</sub> coating using the solution precursor plasma spray process, *Surf. Coatings Technol.* 202 (2008) 6113–6119. <https://doi.org/10.1016/j.surfcoat.2008.07.017>.
- [52] D. Chen, E.H. Jordan, M. Gell, X. Ma, Dense TiO<sub>2</sub> Coating Using the Solution Precursor Plasma Spray Process, *J. Am. Ceram. Soc.* 91 (2008) 865–872.

<https://doi.org/10.1111/j.1551-2916.2007.02225.x>.

- [53] M. Gell, E.H. Jordan, M. Teicholz, B.M. Cetegen, N.P. Padture, L. Xie, D. Chen, X. Ma, J. Roth, Thermal Barrier Coatings Made by the Solution Precursor Plasma Spray Process, *J. Therm. Spray Technol.* 17 (2008) 124–135. <https://doi.org/10.1007/s11666-007-9141-5>.
- [54] W. Fan, Y. Bai, Review of suspension and solution precursor plasma sprayed thermal barrier coatings, *Ceram. Int.* 42 (2016) 14299–14312. <https://doi.org/10.1016/j.ceramint.2016.06.063>.
- [55] M. Gell, L. Xie, E.H. Jordan, N.P. Padture, Mechanisms of spallation of solution precursor plasma spray thermal barrier coatings, *Surf. Coatings Technol.* 188–189 (2004) 101–106. <https://doi.org/10.1016/j.surfcoat.2004.08.004>.
- [56] E.H. Jordan, L. Xie, M. Gell, N.P. Padture, B. Cetegen, A. Ozturk, J. Roth, T.D. Xiao, P.E.C. Bryant, Superior Thermal Barrier Coatings Using Solution Precursor Plasma Spray, *J. Therm. Spray Technol.* 13 (2004) 57–65. <https://doi.org/10.1361/10599630418121>.
- [57] A. Jadhav, N.P. Padture, F. Wu, E.H. Jordan, M. Gell, Thick ceramic thermal barrier coatings with high durability deposited using solution-precursor plasma spray, *Mater. Sci. Eng. A.* 405 (2005) 313–320. <https://doi.org/10.1016/j.msea.2005.06.023>.
- [58] A. Kulkarni, A. Vaidya, A. Goland, S. Sampath, H. Herman, Processing effects on porosity-property correlations in plasma sprayed yttria-stabilized zirconia coatings, *Mater. Sci. Eng. A.* 359 (2003) 100–111. [https://doi.org/10.1016/S0921-5093\(03\)00342-3](https://doi.org/10.1016/S0921-5093(03)00342-3).
- [59] D. Tejero-Martin, M. Bai, J. Mata, T. Hussain, Evolution of porosity in suspension

- thermal sprayed YSZ thermal barrier coatings through neutron scattering and image analysis techniques, *J. Eur. Ceram. Soc.* 41 (2021) 6035–6048. <https://doi.org/10.1016/j.jeurceramsoc.2021.04.020>.
- [60] J.G. Odhiambo, W. Li, Y. Zhao, C. Li, Porosity and Its Significance in Plasma-Sprayed Coatings, *Coatings*. 9 (2019) 460. <https://doi.org/10.3390/coatings9070460>.
- [61] Y. Yuan, R. Rezaee, Comparative Porosity and Pore Structure Assessment in Shales: Measurement Techniques, Influencing Factors and Implications for Reservoir Characterization, *Energies*. 12 (2019) 2094. <https://doi.org/10.3390/en12112094>.
- [62] B. Hammouda, Probing Nanoscale Structure - SANS Toolbox, 2016. [http://www.ncnr.nist.gov/staff/hammouda/the\\_SANS\\_toolbox.pdf](http://www.ncnr.nist.gov/staff/hammouda/the_SANS_toolbox.pdf).
- [63] H. Du, J.H. Shin, S.W. Lee, Study on Porosity of Plasma-Sprayed Coatings by Digital Image Analysis Method, *J. Therm. Spray Technol.* 14 (2005) 453–461. <https://doi.org/10.1361/105996305X76450>.
- [64] ASTM International, ASTM E2109–01: Test Methods of Determining Area Percentage Porosity in Thermal Sprayed Coatings, *Stand. Test Methods Determin. Area Percent. Porosity Therm. Sprayed Coatings*. 01 (2014) 1–8.
- [65] J. Ilavsky, C.C. Berndt, J. Karthikeyan, Mercury intrusion porosimetry of plasma-sprayed ceramic, *J. Mater. Sci.* 32 (1997) 3925–3932. <https://doi.org/10.1023/A:1018612815364>.
- [66] S. Deshpande, A. Kulkarni, S. Sampath, H. Herman, Application of image analysis for characterization of porosity in thermal spray coatings and correlation with small angle neutron scattering, *Surf. Coatings Technol.* 187 (2004) 6–16. <https://doi.org/10.1016/j.surfcoat.2004.01.032>.

- [67] N. Al Nasiri, N. Patra, N. Ni, D.D. Jayaseelan, W.E. Lee, Oxidation behaviour of SiC/SiC ceramic matrix composites in air, *J. Eur. Ceram. Soc.* 36 (2016) 3293–3302. <https://doi.org/10.1016/j.jeurceramsoc.2016.05.051>.
- [68] N.S. Jacobson, J.L. Smialek, D.S. Fox, *Molten Salt Corrosion of SiC and Si<sub>3</sub>N<sub>4</sub>*, 1988. <https://ntrs.nasa.gov/archive/nasa/casi.ntrs.nasa.gov/19890002541.pdf>.
- [69] K.N. Lee, Key Durability Issues With Mullite-Based Environmental Barrier Coatings for Si-Based Ceramics, *Trans. ASME.* 122 (2000) 632–636. <https://doi.org/doi:10.1115/99-GT-443>.
- [70] E.J. Opila, R.E. Hann, Paralinear Oxidation of CVD SiC in Water Vapor, *J. Am. Ceram. Soc.* 80 (1997) 197–205. <https://doi.org/10.1111/j.1151-2916.1997.tb02810.x>.
- [71] E.J. Opila, D.S. Fox, N.S. Jacobson, Mass Spectrometric Identification of Si-O-H(g) Species from the Reaction of Silica with Water Vapor at Atmospheric Pressure, *J. Am. Ceram. Soc.* 80 (2005) 1009–1012. <https://doi.org/10.1111/j.1151-2916.1997.tb02935.x>.
- [72] K.L. More, P.F. Tortorelli, M.K. Ferber, J.R. Keiser, Observations of Accelerated Silicon Carbide Recession by Oxidation at High Water-Vapor Pressures, *J. Am. Ceram. Soc.* 83 (2000) 211–13. <https://doi.org/10.1111/j.1151-2916.2000.tb01172.x>.
- [73] D.C. Faucett, S.R. Choi, Strength Degradation of Oxide/Oxide and SiC/SiC Ceramic Matrix Composites in CMAS and CMAS/Salt Exposures, in: *Vol. 1 Aircr. Engine; Ceram. Coal, Biomass Altern. Fuels; Wind Turbine Technol.*, ASMEDC, 2011: pp. 497–504. <https://doi.org/10.1115/GT2011-46771>.
- [74] N.S. Jacobson, D.S. Fox, J.L. Smialek, E.J. Opila, C. Dellacorte, K.N. Lee, Performance of Ceramics in Severe Environments, in: *Corros. Mater.*, ASM International, 2005: pp.

- 565–578. <https://doi.org/10.31399/asm.hb.v13b.a0003842>.
- [75] S.L. dos Santos e Lucato, O.H. Sudre, D.B. Marshall, A Method for Assessing Reactions of Water Vapor with Materials in High-Speed, High-Temperature Flow, *J. Am. Ceram. Soc.* 94 (2011) s186–s195. <https://doi.org/10.1111/j.1551-2916.2011.04556.x>.
- [76] J. Kim, M.G. Dunn, A.J. Baran, D.P. Wade, E.L. Tremba, Deposition of Volcanic Materials in the Hot Sections of Two Gas Turbine Engines, in: Vol. 3 Coal, Biomass Altern. Fuels; Combust. Fuels; Oil Gas Appl. Cycle Innov., American Society of Mechanical Engineers, 1992: pp. 641–651. <https://doi.org/10.1115/92-GT-219>.
- [77] K.M. Grant, S. Krämer, J.P.A. Löfvander, C.G. Levi, CMAS degradation of environmental barrier coatings, *Surf. Coatings Technol.* 202 (2007) 653–657. <https://doi.org/10.1016/j.surfcoat.2007.06.045>.
- [78] K.M. Grant, S. Krämer, G.G.E. Seward, C.G. Levi, Calcium-Magnesium Alumino-Silicate Interaction with Yttrium Monosilicate Environmental Barrier Coatings, *J. Am. Ceram. Soc.* 93 (2010) 3504–3511. <https://doi.org/10.1111/j.1551-2916.2010.03916.x>.
- [79] K.N. Lee, M. van Roode, Environmental barrier coatings enhance performance of SiC/SiC ceramic matrix composites, *Am. Ceram. Soc. Bull.* 98 (2019) 46–53.
- [80] K.N. Lee, D.S. Fox, N.P. Bansal, Rare earth silicate environmental barrier coatings for SiC/SiC composites and Si<sub>3</sub>N<sub>4</sub> ceramics, *J. Eur. Ceram. Soc.* 25 (2005) 1705–1715. <https://doi.org/10.1016/j.jeurceramsoc.2004.12.013>.
- [81] J. Felsche, Polymorphism and crystal data of the rare-earth disilicates of type R.E.<sub>2</sub>Si<sub>2</sub>O<sub>7</sub>, *J. Less Common Met.* 21 (1970) 1–14. [https://doi.org/10.1016/0022-5088\(70\)90159-1](https://doi.org/10.1016/0022-5088(70)90159-1).
- [82] Y. Xu, X. Hu, F. Xu, K. Li, Rare earth silicate environmental barrier coatings: Present

- status and prospective, *Ceram. Int.* 43 (2017) 5847–5855.  
<https://doi.org/10.1016/j.ceramint.2017.01.153>.
- [83] A.J. Fernández-Carrión, M. Allix, A.I. Becerro, Thermal Expansion of Rare-Earth Pyrosilicates, *J. Am. Ceram. Soc.* 96 (2013) 2298–2305.  
<https://doi.org/10.1111/jace.12388>.
- [84] N. Al Nasiri, N. Patra, D. Horlait, D.D. Jayaseelan, W.E. Lee, Thermal Properties of Rare-Earth Monosilicates for EBC on Si-Based Ceramic Composites, *J. Am. Ceram. Soc.* 99 (2016) 589–596. <https://doi.org/10.1111/jace.13982>.
- [85] M.D. Dolan, B. Harlan, J.S. White, M. Hall, S.T. Misture, S.C. Bancheri, B. Bewlay, Structures and anisotropic thermal expansion of the  $\alpha$ ,  $\beta$ ,  $\gamma$ , and  $\delta$  polymorphs of  $Y_2Si_2O_7$ , *Powder Diffr.* 23 (2008) 20–25. <https://doi.org/10.1154/1.2825308>.
- [86] L.R. Turcer, N.P. Padture, Towards multifunctional thermal environmental barrier coatings (TEBCs) based on rare-earth pyrosilicate solid-solution ceramics, *Scr. Mater.* 154 (2018) 111–117. <https://doi.org/10.1016/j.scriptamat.2018.05.032>.
- [87] P.J. Meschter, E.J. Opila, N.S. Jacobson, Water Vapor–Mediated Volatilization of High-Temperature Materials, *Annu. Rev. Mater. Res.* 43 (2013) 559–588.  
<https://doi.org/10.1146/annurev-matsci-071312-121636>.
- [88] N. Maier, K.G. Nickel, G. Rixecker, High temperature water vapour corrosion of rare earth disilicates (Y,Yb,Lu) $_2Si_2O_7$  in the presence of  $Al(OH)_3$  impurities, *J. Eur. Ceram. Soc.* 27 (2007) 2705–2713. <https://doi.org/10.1016/j.jeurceramsoc.2006.09.013>.
- [89] R.A. Golden, E.J. Opila, A method for assessing the volatility of oxides in high-temperature high-velocity water vapor, *J. Eur. Ceram. Soc.* 36 (2016) 1135–1147.  
<https://doi.org/10.1016/j.jeurceramsoc.2015.11.016>.

- [90] Y. Wang, J. Liu, First-principles investigation on the corrosion resistance of rare earth disilicates in water vapor, *J. Eur. Ceram. Soc.* 29 (2009) 2163–2167. <https://doi.org/10.1016/j.jeurceramsoc.2009.02.005>.
- [91] N.S. Jacobson, Silica Activity Measurements in the Y<sub>2</sub>O<sub>3</sub> - SiO<sub>2</sub> System and Applications to Modeling of Coating Volatility, *J. Am. Ceram. Soc.* 97 (2014) 1959–1965. <https://doi.org/10.1111/jace.12974>.
- [92] G.C.C. Costa, N.S. Jacobson, Mass spectrometric measurements of the silica activity in the Yb<sub>2</sub>O<sub>3</sub>–SiO<sub>2</sub> system and implications to assess the degradation of silicate-based coatings in combustion environments, *J. Eur. Ceram. Soc.* 35 (2015) 4259–4267. <https://doi.org/10.1016/j.jeurceramsoc.2015.07.019>.
- [93] H.E. Eaton, G.D. Linsey, Accelerated oxidation of SiC CMC's by water vapor and protection via environmental barrier coating approach, *J. Eur. Ceram. Soc.* 22 (2002) 2741–2747. [https://doi.org/10.1016/S0955-2219\(02\)00141-3](https://doi.org/10.1016/S0955-2219(02)00141-3).
- [94] H.E. Eaton, W.P. Allen, N.S. Jacobson, K.N. Lee, E.J. Opila, J.L. Smialek, H. Wang, P.J. Meschter, K.L. Luthra, Silicon Based Substrate With Yttrium Silicate Environmental/Thermal Barrier Layer, 6296941 B1, 2001.
- [95] N. Maier, G. Rixecker, K.G. Nickel, Formation and stability of Gd, Y, Yb and Lu disilicates and their solid solutions, *J. Solid State Chem.* 179 (2006) 1630–1635. <https://doi.org/10.1016/j.jssc.2006.02.019>.
- [96] A. Lange, R. Braun, P. Mechnich, C.C. Büttner, U. Schulz, L. Portebois, S. Mathieu, M. Vilasi, S. Drawin, Y<sub>2</sub>SiO<sub>5</sub> environmental barrier coatings for niobium silicide based materials, *Mater. High Temp.* 32 (2015) 74–80. <https://doi.org/10.1179/0960340914Z.00000000079>.

- [97] B.T. Richards, H.N.G. Wadley, Plasma spray deposition of tri-layer environmental barrier coatings, *J. Eur. Ceram. Soc.* 34 (2014) 3069–3083. <https://doi.org/10.1016/j.jeurceramsoc.2014.04.027>.
- [98] B.T. Richards, H. Zhao, H.N.G. Wadley, Structure, composition, and defect control during plasma spray deposition of ytterbium silicate coatings, *J. Mater. Sci.* 50 (2015) 7939–7957. <https://doi.org/10.1007/s10853-015-9358-5>.
- [99] B.T. Richards, M.R. Begley, H.N.G. Wadley, Mechanisms of Ytterbium Monosilicate/Mullite/Silicon Coating Failure during Thermal Cycling in Water Vapor, *J. Am. Ceram. Soc.* 98 (2015) 4066–4075. <https://doi.org/10.1111/jace.13792>.
- [100] B.T. Richards, S. Sehr, F. De Francqueville, M.R. Begley, H.N.G. Wadley, Fracture mechanisms of ytterbium monosilicate environmental barrier coatings during cyclic thermal exposure, *Acta Mater.* 103 (2016) 448–460. <https://doi.org/10.1016/j.actamat.2015.10.019>.
- [101] E. Bakan, Y.J. Sohn, W. Kunz, H. Klemm, R. Vaßen, Effect of processing on high-velocity water vapor recession behavior of Yb-silicate environmental barrier coatings, *J. Eur. Ceram. Soc.* 39 (2019) 1507–1513. <https://doi.org/10.1016/j.jeurceramsoc.2018.11.048>.
- [102] E. Bakan, M. Kindelmann, W. Kunz, H. Klemm, R. Vaßen, High-velocity water vapor corrosion of Yb-silicate: Sprayed vs. sintered body, *Scr. Mater.* 178 (2020) 468–471. <https://doi.org/10.1016/j.scriptamat.2019.12.019>.
- [103] J. Han, Y. Wang, R. Liu, Y. Cao, Thermal shock behavior of mixed ytterbium disilicates and ytterbium monosilicates composite environmental barrier coatings, *Surf. Coatings Technol.* 352 (2018) 348–353. <https://doi.org/10.1016/j.surfcoat.2018.08.041>.

- [104] H. -I. Ryu, S.-M. Lee, Y.-S. Han, K. Choi, G.S. An, S. Nahm, Y.-S. Oh, Preparation of crystalline ytterbium disilicate environmental barrier coatings using suspension plasma spray, *Ceram. Int.* 45 (2019) 5801–5807. <https://doi.org/10.1016/J.CERAMINT.2018.12.048>.
- [105] E. Garcia, H. Lee, S. Sampath, Phase and microstructure evolution in plasma sprayed Yb<sub>2</sub>Si<sub>2</sub>O<sub>7</sub> coatings, *J. Eur. Ceram. Soc.* 39 (2019) 1477–1486. <https://doi.org/10.1016/j.jeurceramsoc.2018.11.018>.
- [106] S. Sampath, H. Herman, Rapid solidification and microstructure development during plasma spray deposition, *J. Therm. Spray Technol.* 5 (1996) 445–456. <https://doi.org/10.1007/BF02645275>.
- [107] E. Bakan, D. Marcano, D. Zhou, Y.J. Sohn, G. Mauer, R. Vaßen, Yb<sub>2</sub>Si<sub>2</sub>O<sub>7</sub> Environmental Barrier Coatings Deposited by Various Thermal Spray Techniques: A Preliminary Comparative Study, *J. Therm. Spray Technol.* 26 (2017) 1011–1024. <https://doi.org/10.1007/s11666-017-0574-1>.
- [108] E. Bakan, G. Mauer, Y.J. Sohn, D. Koch, R. Vaßen, Application of High-Velocity Oxygen-Fuel (HVOF) Spraying to the Fabrication of Yb-Silicate Environmental Barrier Coatings, *Coatings*. 7 (2017) 55. <https://doi.org/10.3390/coatings7040055>.
- [109] N. Al Nasiri, N. Patra, D.D. Jayaseelan, W.E. Lee, Water vapour corrosion of rare earth monosilicates for environmental barrier coating application, *Ceram. Int.* 43 (2017) 7393–7400. <https://doi.org/10.1016/j.ceramint.2017.02.123>.
- [110] E. Courcot, F. Rebillat, C. Louchet-Pouillerie, Relation between Synthesis Process, Microstructure and Corrosion Resistance of Two Yttrium Silicates, *Mater. Sci. Forum.* 595–598 (2008) 923–931. <https://doi.org/10.4028/www.scientific.net/MSF.595-598.923>.

- [111] J. Liu, L. Zhang, F. Hu, J. Yang, L. Cheng, Y. Wang, Polymer-derived yttrium silicate coatings on 2D C/SiC composites, *J. Eur. Ceram. Soc.* 33 (2013) 433–439. <https://doi.org/10.1016/j.jeurceramsoc.2012.08.032>.
- [112] N. Al Nasiri, N. Patra, M. Pezoldt, J. Colas, W.E. Lee, Investigation of a single-layer EBC deposited on SiC/SiC CMCs: Processing and corrosion behaviour in high-temperature steam, *J. Eur. Ceram. Soc.* (2018). <https://doi.org/10.1016/j.jeurceramsoc.2018.12.019>.
- [113] S. Ueno, D.D. Jayaseelan, T. Ohji, Comparison of water vapor corrosion behavior of silicon nitride with various EBC layers, *J. Ceram. Process. Res.* 5 (2004) 355–359.
- [114] S. Ueno, D.D. Jayaseelan, T. Ohji, Development of Oxide-Based EBC for Silicon Nitride, *Int. J. Appl. Ceram. Technol.* 1 (2004) 362–373. <https://doi.org/10.1111/j.1744-7402.2004.tb00187.x>.
- [115] S. Ueno, D.D. Jayaseelan, T. Ohji, Water vapor corrosion behavior of lutetium silicates at high temperature, *Ceram. Int.* 32 (2006) 451–455. <https://doi.org/10.1016/j.ceramint.2005.03.022>.
- [116] J.A. Duffy, M.D. Ingram, An interpretation of glass chemistry in terms of the optical basicity concept, *J. Non. Cryst. Solids.* 21 (1976) 373–410. [https://doi.org/10.1016/0022-3093\(76\)90027-2](https://doi.org/10.1016/0022-3093(76)90027-2).
- [117] J.A. Duffy, Acid-Base Reactions of Transition Metal Oxides in the Solid State, *J. Am. Ceram. Soc.* 80 (2005) 1416–1420. <https://doi.org/10.1111/j.1151-2916.1997.tb02999.x>.
- [118] B.T. Richards, K.A. Young, F. De Francqueville, S. Sehr, M.R. Begley, H.N.G. Wadley, Response of ytterbium disilicate-silicon environmental barrier coatings to thermal

- cycling in water vapor, *Acta Mater.* 106 (2016) 1–14.  
<https://doi.org/10.1016/j.actamat.2015.12.053>.
- [119] C.G. Levi, J.W. Hutchinson, M.-H. Vidal-Sétif, C.A. Johnson, Environmental degradation of thermal-barrier coatings by molten deposits, *MRS Bull.* 37 (2012) 932–941. <https://doi.org/10.1557/mrs.2012.230>.
- [120] A.R. Krause, H.F. Garces, G. Dwivedi, A.L. Ortiz, S. Sampath, N.P. Padture, Calcia-magnesia-alumino-silicate (CMAS)-induced degradation and failure of air plasma sprayed yttria-stabilized zirconia thermal barrier coatings, *Acta Mater.* 105 (2016) 355–366. <https://doi.org/10.1016/j.actamat.2015.12.044>.
- [121] S. Krämer, S. Faulhaber, M. Chambers, D.R. Clarke, C.G. Levi, J.W. Hutchinson, A.G. Evans, Mechanisms of cracking and delamination within thick thermal barrier systems in aero-engines subject to calcium-magnesium-alumino-silicate (CMAS) penetration, *Mater. Sci. Eng. A.* 490 (2008) 26–35. <https://doi.org/10.1016/j.msea.2008.01.006>.
- [122] A.R. Krause, B.S. Senturk, H.F. Garces, G. Dwivedi, A.L. Ortiz, S. Sampath, N.P. Padture, 2ZrO<sub>2</sub> · Y<sub>2</sub>O<sub>3</sub> Thermal Barrier Coatings Resistant to Degradation by Molten CMAS: Part I, Optical Basicity Considerations and Processing, *J. Am. Ceram. Soc.* 97 (2014) 3943–3949. <https://doi.org/10.1111/jace.13210>.
- [123] A.R. Krause, H.F. Garces, B.S. Senturk, N.P. Padture, 2ZrO<sub>2</sub> · Y<sub>2</sub>O<sub>3</sub> Thermal Barrier Coatings Resistant to Degradation by Molten CMAS: Part II, Interactions with Sand and Fly Ash, *J. Am. Ceram. Soc.* 97 (2014) 3950–3957. <https://doi.org/10.1111/jace.13209>.
- [124] J.L. Stokes, B.J. Harder, V.L. Wiesner, D.E. Wolfe, High-Temperature thermochemical interactions of molten silicates with Yb<sub>2</sub>Si<sub>2</sub>O<sub>7</sub> and Y<sub>2</sub>Si<sub>2</sub>O<sub>7</sub> environmental barrier coating materials, *J. Eur. Ceram. Soc.* 39 (2019) 5059–5067. <https://doi.org/10.1016/j.jeurceramsoc.2019.06.051>.

- [125] J.L. Stokes, B.J. Harder, V.L. Wiesner, D.E. Wolfe, Effects of crystal structure and cation size on molten silicate reactivity with environmental barrier coating materials, *J. Am. Ceram. Soc.* 103 (2020) 622–634. <https://doi.org/10.1111/jace.16694>.
- [126] W.D. Summers, D.L. Poerschke, D. Park, J.H. Shaw, F.W. Zok, C.G. Levi, Roles of composition and temperature in silicate deposit-induced recession of yttrium disilicate, *Acta Mater.* 160 (2018) 34–46. <https://doi.org/10.1016/j.actamat.2018.08.043>.
- [127] D.L. Poerschke, J.H. Shaw, N. Verma, F.W. Zok, C.G. Levi, Interaction of yttrium disilicate environmental barrier coatings with calcium-magnesium-iron alumino-silicate melts, *Acta Mater.* 145 (2018) 451–461. <https://doi.org/10.1016/j.actamat.2017.12.004>.
- [128] J. Liu, L. Zhang, Q. Liu, L. Cheng, Y. Wang, Calcium–magnesium–aluminosilicate corrosion behaviors of rare-earth disilicates at 1400°C, *J. Eur. Ceram. Soc.* 33 (2013) 3419–3428. <https://doi.org/10.1016/j.jeurceramsoc.2013.05.030>.
- [129] N.L. Ahlborg, D. Zhu, Calcium–magnesium aluminosilicate (CMAS) reactions and degradation mechanisms of advanced environmental barrier coatings, *Surf. Coatings Technol.* 237 (2013) 79–87. <https://doi.org/10.1016/j.surfcoat.2013.08.036>.
- [130] L.R. Turcer, A.R. Krause, H.F. Garces, L. Zhang, N.P. Padture, Environmental-barrier coating ceramics for resistance against attack by molten calcia-magnesia-aluminosilicate (CMAS) glass: Part II,  $\beta$ -Yb<sub>2</sub>Si<sub>2</sub>O<sub>7</sub> and  $\beta$ -Sc<sub>2</sub>Si<sub>2</sub>O<sub>7</sub>, *J. Eur. Ceram. Soc.* 38 (2018) 3914–3924. <https://doi.org/10.1016/j.jeurceramsoc.2018.03.010>.
- [131] W.D. Summers, D.L. Poerschke, M.R. Begley, C.G. Levi, F.W. Zok, A computational modeling framework for reaction and failure of environmental barrier coatings under silicate deposits, *J. Am. Ceram. Soc.* (2020) jace.17187. <https://doi.org/10.1111/jace.17187>.

- [132] W.D. Summers, D.L. Poerschke, A.A. Taylor, A.R. Ericks, C.G. Levi, F.W. Zok, Reactions of molten silicate deposits with yttrium monosilicate, *J. Am. Ceram. Soc.* 103 (2020) 2919–2932. <https://doi.org/10.1111/jace.16972>.
- [133] F. Stolzenburg, M.T. Johnson, K.N. Lee, N.S. Jacobson, K.T. Faber, The interaction of calcium–magnesium–aluminosilicate with ytterbium silicate environmental barrier materials, *Surf. Coatings Technol.* 284 (2015) 44–50. <https://doi.org/10.1016/j.surfcoat.2015.08.069>.
- [134] D.L. Poerschke, D.D. Hass, S. Eustis, G.G.E. Seward, J.S. Van Sluytman, C.G. Levi, Stability and CMAS Resistance of Ytterbium-Silicate/Hafnate EBCs/TBC for SiC Composites, *J. Am. Ceram. Soc.* 98 (2015) 278–286. <https://doi.org/10.1111/jace.13262>.
- [135] H. Zhao, B.T. Richards, C.G. Levi, H.N.G. Wadley, Molten silicate reactions with plasma sprayed ytterbium silicate coatings, *Surf. Coatings Technol.* 288 (2016) 151–162. <https://doi.org/10.1016/j.surfcoat.2015.12.053>.
- [136] F. Stolzenburg, P. Kenesei, J. Almer, K.N. Lee, M.T. Johnson, K.T. Faber, The influence of calcium–magnesium–aluminosilicate deposits on internal stresses in Yb<sub>2</sub>Si<sub>2</sub>O<sub>7</sub> multilayer environmental barrier coatings, *Acta Mater.* 105 (2016) 189–198. <https://doi.org/10.1016/j.actamat.2015.12.016>.
- [137] L.R. Turcer, A.R. Krause, H.F. Garces, L. Zhang, N.P. Padture, Environmental-barrier coating ceramics for resistance against attack by molten calcia-magnesia-aluminosilicate (CMAS) glass: Part I, YAlO<sub>3</sub> and  $\gamma$ -Y<sub>2</sub>Si<sub>2</sub>O<sub>7</sub>, *J. Eur. Ceram. Soc.* 38 (2018) 3905–3913. <https://doi.org/10.1016/j.jeurceramsoc.2018.03.021>.
- [138] V.L. Wiesner, D. Scales, N.S. Johnson, B.J. Harder, A. Garg, N.P. Bansal, Calcium–magnesium aluminosilicate (CMAS) interactions with ytterbium silicate environmental

- barrier coating material at elevated temperatures, *Ceram. Int.* 46 (2020) 16733–16742.  
<https://doi.org/10.1016/j.ceramint.2020.03.249>.
- [139] F. Jiang, L. Cheng, Y. Wang, Hot corrosion of RE<sub>2</sub>SiO<sub>5</sub> with different cation substitution under calcium–magnesium–aluminosilicate attack, *Ceram. Int.* 43 (2017) 9019–9023. <https://doi.org/10.1016/j.ceramint.2017.04.045>.
- [140] V.L. Wiesner, B.J. Harder, N.P. Bansal, High-temperature interactions of desert sand CMAS glass with yttrium disilicate environmental barrier coating material, *Ceram. Int.* 44 (2018) 22738–22743. <https://doi.org/10.1016/j.ceramint.2018.09.058>.
- [141] R. Naraparaju, J.J. Gomez Chavez, U. Schulz, C. V. Ramana, Interaction and infiltration behavior of Eyjafjallajökull, Sakurajima volcanic ashes and a synthetic CMAS containing FeO with/in EB-PVD ZrO<sub>2</sub>-65 wt% Y<sub>2</sub>O<sub>3</sub> coating at high temperature, *Acta Mater.* 136 (2017) 164–180. <https://doi.org/10.1016/j.actamat.2017.06.055>.
- [142] U. Kueppers, C. Cimarelli, K.-U. Hess, J. Taddeucci, F.B. Wadsworth, D.B. Dingwell, The thermal stability of Eyjafjallajökull ash versus turbine ingestion test sands, *J. Appl. Volcanol.* 3 (2014) 4. <https://doi.org/10.1186/2191-5040-3-4>.
- [143] R.J. Clarkson, E.J.E. Majewicz, P. Mack, A re-evaluation of the 2010 quantitative understanding of the effects volcanic ash has on gas turbine engines, *Proc. Inst. Mech. Eng. Part G J. Aerosp. Eng.* 230 (2016) 2274–2291. <https://doi.org/10.1177/0954410015623372>.
- [144] D.L. Poerschke, R.W. Jackson, C.G. Levi, Silicate Deposit Degradation of Engineered Coatings in Gas Turbines: Progress Toward Models and Materials Solutions, *Annu. Rev. Mater. Res.* 47 (2017) 297–330. <https://doi.org/10.1146/annurev-matsci-010917-105000>.

- [145] D. Qin, Y. Niu, H. Li, X. Zhong, X. Zheng, J. Sun, Fabrication and characterization of Yb<sub>2</sub>Si<sub>2</sub>O<sub>7</sub>-based composites as novel abradable sealing coatings, *Ceram. Int.* 47 (2021) 23153–23161. <https://doi.org/10.1016/j.ceramint.2021.05.029>.
- [146] L. Kavan, M. Grätzel, J. Rathouský, A. Zukalb, Nanocrystalline TiO<sub>2</sub> (Anatase) Electrodes: Surface Morphology, Adsorption, and Electrochemical Properties, *J. Electrochem. Soc.* 143 (1996) 394. <https://doi.org/10.1149/1.1836455>.
- [147] N. Negishi, T. Iyoda, K. Hashimoto, A. Fujishima, Preparation of Transparent TiO<sub>2</sub> Thin Film Photocatalyst and Its Photocatalytic Activity, *Chem. Lett.* 24 (1995) 841–842. <https://doi.org/10.1246/cl.1995.841>.
- [148] S. Ito, T. Takeuchi, T. Katayama, M. Sugiyama, M. Matsuda, T. Kitamura, Y. Wada, S. Yanagida, Conductive and Transparent Multilayer Films for Low-Temperature-Sintered Mesoporous TiO<sub>2</sub> Electrodes of Dye-Sensitized Solar Cells, *Chem. Mater.* 15 (2003) 2824–2828. <https://doi.org/10.1021/cm021051t>.
- [149] S. Sathasivam, D.S. Bhachu, Y. Lu, N. Chadwick, S.A. Althabaiti, A.O. Alyoubi, S.N. Basahel, C.J. Carmalt, I.P. Parkin, Tungsten Doped TiO<sub>2</sub> with Enhanced Photocatalytic and Optoelectrical Properties via Aerosol Assisted Chemical Vapor Deposition, *Sci. Rep.* 5 (2015) 10952. <https://doi.org/10.1038/srep10952>.
- [150] D.H. Dawson, G.S. Henshaw, D.E. Williams, Description and characterization of a hydrogen sulfide gas sensor based on Cr<sub>2-y</sub>Ti<sub>y</sub>O<sub>3+x</sub>, *Sensors Actuators B Chem.* 26 (1995) 76–80. [https://doi.org/10.1016/0925-4005\(94\)01560-5](https://doi.org/10.1016/0925-4005(94)01560-5).
- [151] F. Bregani, C. Casale, L.E. Depero, I. Natali-Sora, D. Robba, L. Sangaletti, G.P. Toledo, Temperature effects on the size of anatase crystallites in Mo-TiO<sub>2</sub> and W-TiO<sub>2</sub> powders, *Sensors Actuators B Chem.* 31 (1996) 25–28. [https://doi.org/10.1016/0925-4005\(96\)80011-6](https://doi.org/10.1016/0925-4005(96)80011-6).

- [152] E. Comini, V. Guidi, C. Frigeri, I. Riccò, G. Sberveglieri, CO sensing properties of titanium and iron oxide nanosized thin films, *Sensors Actuators B Chem.* 77 (2001) 16–21. [https://doi.org/10.1016/S0925-4005\(01\)00666-9](https://doi.org/10.1016/S0925-4005(01)00666-9).
- [153] A.M. Ruiz, A. Cornet, J.R. Morante, Study of La and Cu influence on the growth inhibition and phase transformation of nano-TiO<sub>2</sub> used for gas sensors, *Sensors Actuators B Chem.* 100 (2004) 256–260. <https://doi.org/10.1016/j.snb.2003.12.043>.
- [154] H. Usui, S. Yoshioka, K. Wasada, M. Shimizu, H. Sakaguchi, Nb-Doped Rutile TiO<sub>2</sub> : a Potential Anode Material for Na-Ion Battery, *ACS Appl. Mater. Interfaces.* 7 (2015) 6567–6573. <https://doi.org/10.1021/am508670z>.
- [155] Y. Furubayashi, T. Hitosugi, Y. Yamamoto, K. Inaba, G. Kinoda, Y. Hirose, T. Shimada, T. Hasegawa, A transparent metal: Nb-doped anatase TiO<sub>2</sub>, *Appl. Phys. Lett.* 86 (2005) 252101. <https://doi.org/10.1063/1.1949728>.
- [156] E. Traversa, M.L. Di Vona, S. Licoccia, M. Sacerdoti, M.C. Carotta, M. Gallana, G. Martinelli, Sol-gel nanosized semiconducting titania-based powders for thick-film gas sensors, *J. Sol-Gel Sci. Technol.* 19 (2000) 193–196. <https://doi.org/10.1023/A:1008723902604>.
- [157] N. Bonini, M.C. Carotta, A. Chiorino, V. Guidi, C. Malagù, G. Martinelli, L. Paglialonga, M. Sacerdoti, Doping of a nanostructured titania thick film: structural and electrical investigations, *Sensors Actuators B Chem.* 68 (2000) 274–280. [https://doi.org/10.1016/S0925-4005\(00\)00444-5](https://doi.org/10.1016/S0925-4005(00)00444-5).
- [158] D.A.H. Hanaor, C.C. Sorrell, Review of the anatase to rutile phase transformation, *J. Mater. Sci.* 46 (2011) 855–874. <https://doi.org/10.1007/s10853-010-5113-0>.
- [159] E.H. Jordan, C. Jiang, M. Gell, The Solution Precursor Plasma Spray (SPPS) Process:

- A Review with Energy Considerations, *J. Therm. Spray Technol.* 24 (2015) 1153–1165.  
<https://doi.org/10.1007/s11666-015-0272-9>.
- [160] Y. Cai, T.W. Coyle, G. Azimi, J. Mostaghimi, Superhydrophobic Ceramic Coatings by Solution Precursor Plasma Spray, *Sci. Rep.* 6 (2016) 24670.  
<https://doi.org/10.1038/srep24670>.
- [161] M. Bai, R. Khammas, L. Guan, J.W. Murray, T. Hussain, Suspension high velocity oxy-fuel spraying of a rutile TiO<sub>2</sub> feedstock: Microstructure, phase evolution and photocatalytic behaviour, *Ceram. Int.* 43 (2017) 15288–15295.  
<https://doi.org/10.1016/j.ceramint.2017.08.068>.
- [162] M. Bai, H. Maher, Z. Pala, T. Hussain, Microstructure and phase stability of suspension high velocity oxy-fuel sprayed yttria stabilised zirconia coatings from aqueous and ethanol based suspensions, *J. Eur. Ceram. Soc.* 38 (2018) 1878–1887.  
<https://doi.org/10.1016/j.jeurceramsoc.2017.10.026>.
- [163] N. Berger-Keller, G. Bertrand, C. Filiatre, C. Meunier, C. Coddet, Microstructure of plasma-sprayed titania coatings deposited from spray-dried powder, *Surf. Coatings Technol.* 168 (2003) 281–290. [https://doi.org/10.1016/S0257-8972\(03\)00223-8](https://doi.org/10.1016/S0257-8972(03)00223-8).
- [164] C.-J. Li, G.-J. Yang, Y.-Y. Wang, C.-X. Li, F.-X. Ye, A. Ohmori, Phase Formation during Deposition of TiO<sub>2</sub> Coatings through High Velocity Oxy-Fuel Spraying, *Mater. Trans.* 47 (2006) 1690–1696. <https://doi.org/10.2320/matertrans.47.1690>.
- [165] G.-J. Yang, C.-J. Li, Y.-Y. Wang, Phase Formation of Nano-TiO<sub>2</sub> Particles during Flame Spraying with Liquid Feedstock, *J. Therm. Spray Technol.* 14 (2005) 480–486.  
<https://doi.org/10.1361/105996305X76487>.
- [166] S. Chadha, R. Jefferson-Loveday, T. Hussain, Effect of nozzle geometry on the gas

- dynamics and evaporation rates of Suspension High Velocity Oxy Fuel (SHVOF) thermal spray: A numerical investigation, *Surf. Coatings Technol.* 371 (2019) 78–89. <https://doi.org/10.1016/j.surfcoat.2018.10.085>.
- [167] Y. Sun, T. Egawa, L. Zhang, X. Yao, High Anatase-Rutile Transformation Temperature of Anatase Titania Nanoparticles Prepared by Metalorganic Chemical Vapor Deposition, *Jpn. J. Appl. Phys.* 41 (2002) L945–L948. <https://doi.org/10.1143/JJAP.41.L945>.
- [168] H. Zhang, J.F. Banfield, Phase transformation of nanocrystalline anatase-to-rutile via combined interface and surface nucleation, *J. Mater. Res.* 15 (2000) 437–448. <https://doi.org/10.1557/JMR.2000.0067>.
- [169] J. Arbiol, J. Cerdà, G. Dezanneau, A. Cirera, F. Peiró, A. Cornet, J.R. Morante, Effects of Nb doping on the TiO<sub>2</sub> anatase-to-rutile phase transition, *J. Appl. Phys.* 92 (2002) 853–861. <https://doi.org/10.1063/1.1487915>.
- [170] S. Hishita, I. Mutoh, K. Koumoto, H. Yanagida, Inhibition mechanism of the anatase-rutile phase transformation by rare earth oxides, *Ceram. Int.* 9 (1983) 61–67. [https://doi.org/10.1016/0272-8842\(83\)90025-1](https://doi.org/10.1016/0272-8842(83)90025-1).
- [171] Y. Li, T. Ishigaki, Thermodynamic analysis of nucleation of anatase and rutile from TiO<sub>2</sub> melt, *J. Cryst. Growth.* 242 (2002) 511–516. [https://doi.org/10.1016/S0022-0248\(02\)01438-0](https://doi.org/10.1016/S0022-0248(02)01438-0).
- [172] J.A. Gan, C.C. Berndt, Nanocomposite coatings: thermal spray processing, microstructure and performance, *Int. Mater. Rev.* 60 (2015) 195–244. <https://doi.org/10.1179/1743280414Y.0000000048>.
- [173] M. Jadidi, S. Moghtadernejad, A. Dolatabadi, A Comprehensive Review on Fluid

- Dynamics and Transport of Suspension/Liquid Droplets and Particles in High-Velocity Oxygen-Fuel (HVOF) Thermal Spray, *Coatings*. 5 (2015) 576–645. <https://doi.org/10.3390/coatings5040576>.
- [174] D.R. Guildenbecher, C. López-Rivera, P.E. Sojka, Secondary atomization, *Exp. Fluids*. 46 (2009) 371–402. <https://doi.org/10.1007/s00348-008-0593-2>.
- [175] A.J. Atanacio, T. Bak, J. Nowotny, Niobium Segregation in Niobium-Doped Titanium Dioxide (Rutile), *J. Phys. Chem. C*. 118 (2014) 11174–11185. <https://doi.org/10.1021/jp4110536>.
- [176] E. Bakan, R. Vaßen, Ceramic Top Coats of Plasma-Sprayed Thermal Barrier Coatings: Materials, Processes, and Properties, *J. Therm. Spray Technol.* 26 (2017) 992–1010. <https://doi.org/10.1007/s11666-017-0597-7>.
- [177] A. Kulkarni, A. Goland, H. Herman, A.J. Allen, T. Dobbins, F. DeCarlo, J. Ilavsky, G.G. Long, S. Fang, P. Lawton, Advanced neutron and X-ray techniques for insights into the microstructure of EB-PVD thermal barrier coatings, *Mater. Sci. Eng. A*. 426 (2006) 43–52. <https://doi.org/10.1016/j.msea.2006.03.070>.
- [178] X. Qiao, Y.M. Wang, W.X. Weng, B.L. Liu, Q. Li, Influence of pores on mechanical properties of plasma sprayed coatings: Case study of YSZ thermal barrier coatings, *Ceram. Int.* 44 (2018) 21564–21577. <https://doi.org/10.1016/j.ceramint.2018.08.220>.
- [179] A. Keyvani, M. Saremi, M. Heydarzadeh Sohi, Z. Valefi, A comparison on thermomechanical properties of plasma-sprayed conventional and nanostructured YSZ TBC coatings in thermal cycling, *J. Alloys Compd.* 541 (2012) 488–494. <https://doi.org/10.1016/j.jallcom.2012.06.062>.
- [180] H.B. Guo, R. Vaßen, D. Stöver, Atmospheric plasma sprayed thick thermal barrier

- coatings with high segmentation crack density, *Surf. Coatings Technol.* 186 (2004) 353–363. <https://doi.org/10.1016/j.surfcoat.2004.01.002>.
- [181] S. V. Shinde, E.J. Gildersleeve V, C.A. Johnson, S. Sampath, Segmentation crack formation dynamics during air plasma spraying of zirconia, *Acta Mater.* 183 (2020) 196–206. <https://doi.org/10.1016/j.actamat.2019.10.052>.
- [182] A. Portinha, V. Teixeira, J. Carneiro, M.G. Beghi, C.E. Bottani, N. Franco, R. Vassen, D. Stoeber, A.D. Sequeira, Residual stresses and elastic modulus of thermal barrier coatings graded in porosity, *Surf. Coatings Technol.* 188–189 (2004) 120–128. <https://doi.org/10.1016/j.surfcoat.2004.08.014>.
- [183] J. Ekberg, A. Ganvir, U. Klement, S. Creci, L. Nordstierna, The Influence of Heat Treatments on the Porosity of Suspension Plasma-Sprayed Yttria-Stabilized Zirconia Coatings, *J. Therm. Spray Technol.* 27 (2018) 391–401. <https://doi.org/10.1007/s11666-017-0682-y>.
- [184] A. Ganvir, N. Curry, N. Markocsan, P. Nylén, F.-L. Toma, Comparative study of suspension plasma sprayed and suspension high velocity oxy-fuel sprayed YSZ thermal barrier coatings, *Surf. Coatings Technol.* 268 (2015) 70–76. <https://doi.org/10.1016/j.surfcoat.2014.11.054>.
- [185] J. Wang, J. Sun, H. Zhang, S. Dong, J. Jiang, L. Deng, X. Zhou, X. Cao, Effect of spraying power on microstructure and property of nanostructured YSZ thermal barrier coatings, *J. Alloys Compd.* 730 (2018) 471–482. <https://doi.org/10.1016/j.jallcom.2017.09.323>.
- [186] F. Tarasi, E. Alebrahim, A. Dolatabadi, C. Moreau, A Comparative Study of YSZ Suspensions and Coatings, *Coatings.* 9 (2019) 188. <https://doi.org/10.3390/coatings9030188>.

- [187] A. Ganvir, N. Curry, S. Björklund, N. Markocsan, P. Nylén, Characterization of Microstructure and Thermal Properties of YSZ Coatings Obtained by Axial Suspension Plasma Spraying (ASPS), *J. Therm. Spray Technol.* 24 (2015) 1195–1204. <https://doi.org/10.1007/s11666-015-0263-x>.
- [188] B. Siebert, C. Funke, R. Vaßen, D. Stöver, Changes in porosity and Young's Modulus due to sintering of plasma sprayed thermal barrier coatings, *J. Mater. Process. Technol.* 92–93 (1999) 217–223. [https://doi.org/10.1016/S0924-0136\(99\)00243-5](https://doi.org/10.1016/S0924-0136(99)00243-5).
- [189] A. Ganvir, N. Markocsan, S. Joshi, Influence of Isothermal Heat Treatment on Porosity and Crystallite Size in Axial Suspension Plasma Sprayed Thermal Barrier Coatings for Gas Turbine Applications, *Coatings.* 7 (2016) 4. <https://doi.org/10.3390/coatings7010004>.
- [190] J. Ilavsky, J.K. Stalick, Phase composition and its changes during annealing of plasma-sprayed YSZ, *Surf. Coatings Technol.* 127 (2000) 120–129. [https://doi.org/10.1016/S0257-8972\(00\)00562-4](https://doi.org/10.1016/S0257-8972(00)00562-4).
- [191] A. Cipitria, I.O. Golosnoy, T.W. Clyne, A sintering model for plasma-sprayed zirconia TBCs. Part I: Free-standing coatings, *Acta Mater.* 57 (2009) 980–992. <https://doi.org/10.1016/j.actamat.2008.10.024>.
- [192] A. Cipitria, I.O. Golosnoy, T.W. Clyne, A sintering model for plasma-sprayed zirconia thermal barrier coatings. Part II: Coatings bonded to a rigid substrate, *Acta Mater.* 57 (2009) 993–1003. <https://doi.org/10.1016/j.actamat.2008.10.058>.
- [193] K. Wang, H. Peng, H. Guo, S. Gong, Effect of Sintering on Thermal Conductivity and Thermal Barrier Effects of Thermal Barrier Coatings, *Chinese J. Aeronaut.* 25 (2012) 811–816. [https://doi.org/10.1016/S1000-9361\(11\)60449-4](https://doi.org/10.1016/S1000-9361(11)60449-4).

- [194] U. Klement, J. Ekberg, S.T. Kelly, 3D Analysis of Porosity in a Ceramic Coating Using X-ray Microscopy, *J. Therm. Spray Technol.* 26 (2017) 456–463. <https://doi.org/10.1007/s11666-017-0532-y>.
- [195] A. Bacciochini, G. Montavon, J. Ilavsky, A. Denoirjean, P. Fauchais, Porous Architecture of SPS Thick YSZ Coatings Structured at the Nanometer Scale (~50 nm), *J. Therm. Spray Technol.* 19 (2010) 198–206. <https://doi.org/10.1007/s11666-009-9429-8>.
- [196] A. Ganvir, N. Curry, N. Markocsan, P. Nylén, S. Joshi, M. Vilemova, Z. Pala, Influence of Microstructure on Thermal Properties of Axial Suspension Plasma-Sprayed YSZ Thermal Barrier Coatings, *J. Therm. Spray Technol.* 25 (2016) 202–212. <https://doi.org/10.1007/s11666-015-0355-7>.
- [197] F. Xia, J. Zhao, B.E. Etschmann, J. Brugger, C.J. Garvey, C. Rehm, H. Lemmel, J. Ilavsky, Y.S. Han, A. Pring, Characterization of porosity in sulfide ore minerals: A USANS/SANS study, *Am. Mineral.* 99 (2014) 2398–2404. <https://doi.org/10.2138/am-2014-4845>.
- [198] P. Strunz, G. Schumacher, R. Vaßen, A. Wiedenmann, V. Ryukhtin, In situ small-angle neutron scattering study of La<sub>2</sub>Zr<sub>2</sub>O<sub>7</sub> and SrZrO<sub>3</sub> ceramics for thermal barrier coatings, *Scr. Mater.* 55 (2006) 545–548. <https://doi.org/10.1016/j.scriptamat.2006.05.022>.
- [199] W. Wagner, J.A. Eastman, Characterization of yttria-stabilized zirconia coatings with controlled nanometer-sized porosity by SANS, *Appl. Phys. A Mater. Sci. Process.* 74 (2002) s1007–s1009. <https://doi.org/10.1007/s003390101176>.
- [200] P. Strunz, G. Schumacher, R. Vaßen, A. Wiedenmann, In situ SANS study of pore microstructure in YSZ thermal barrier coatings, *Acta Mater.* 52 (2004) 3305–3312. <https://doi.org/10.1016/j.actamat.2004.03.026>.

- [201] J. Ilavsky, G.G. Long, A.J. Allen, C.C. Berndt, Evolution of the void structure in plasma-sprayed YSZ deposits during heating, *Mater. Sci. Eng. A.* 272 (1999) 215–221. [https://doi.org/10.1016/S0921-5093\(99\)00450-5](https://doi.org/10.1016/S0921-5093(99)00450-5).
- [202] A. Kulkarni, Z. Wang, T. Nakamura, S. Sampath, A. Goland, H. Herman, A.J. Allen, J. Ilavsky, G. Long, J. Frahm, R.W. Steinbrech, Comprehensive microstructural characterization and predictive property modeling of plasma-sprayed zirconia coatings, *Acta Mater.* 51 (2003) 2457–2475. [https://doi.org/10.1016/S1359-6454\(03\)00030-2](https://doi.org/10.1016/S1359-6454(03)00030-2).
- [203] A.J. Allen, J. Ilavsky, G. Long, J.S. Wallace, C.C. Berndt, H. Herman, Microstructural characterization of yttria-stabilized zirconia plasma-sprayed deposits using multiple small-angle neutron scattering, *Acta Mater.* 49 (2001) 1661–1675. [https://doi.org/10.1016/S1359-6454\(00\)00393-1](https://doi.org/10.1016/S1359-6454(00)00393-1).
- [204] J. Marthe, E. Meillot, G. Jeandel, F. Enguehard, J. Ilavsky, Enhancement of scattering and reflectance properties of plasma-sprayed alumina coatings by controlling the porosity, *Surf. Coatings Technol.* 220 (2013) 80–84. <https://doi.org/10.1016/j.surfcoat.2012.05.048>.
- [205] A. Bacciochini, J. Ilavsky, G. Montavon, A. Denoirjean, F. Ben-ettouil, S. Valette, P. Fauchais, K. Wittmann-teneze, Quantification of void network architectures of suspension plasma-sprayed (SPS) yttria-stabilized zirconia (YSZ) coatings using Ultra-small-angle X-ray scattering (USAXS), *Mater. Sci. Eng. A.* 528 (2010) 91–102. <https://doi.org/10.1016/j.msea.2010.06.082>.
- [206] K. Wood, J.P. Mata, C.J. Garvey, C.-M. Wu, W.A. Hamilton, P. Abbeywick, D. Bartlett, F. Bartsch, P. Baxter, N. Booth, W. Brown, J. Christoforidis, D. Clowes, T. D’Adam, F. Darmann, M. Deura, S. Harrison, N. Hauser, G. Horton, D. Federici, F. Franceschini, P. Hanson, E. Imamovic, P. Imperia, M. Jones, S. Kennedy, S. Kim, T. Lam, W.T. Lee, M.

- Lasha, D. Mannicke, T. Noakes, S.R. Olsen, J.C. Osborn, D. Penny, M. Perry, S.A. Pullen, R.A. Robinson, J.C. Schulz, N. Xiong, E.P. Gilbert, QUOKKA, the pinhole small-angle neutron scattering instrument at the OPAL Research Reactor, Australia: design, performance, operation and scientific highlights, *J. Appl. Crystallogr.* 51 (2018) 294–314. <https://doi.org/10.1107/S1600576718002534>.
- [207] C. Rehm, L. de Campo, A. Brûlé, F. Darmann, F. Bartsch, A. Berry, Design and performance of the variable-wavelength Bonse–Hart ultra-small-angle neutron scattering diffractometer KOOKABURRA at ANSTO, *J. Appl. Crystallogr.* 51 (2018) 1–8. <https://doi.org/10.1107/S1600576717016879>.
- [208] I. Breßler, J. Kohlbrecher, A.F. Thünemann, SASfit : a tool for small-angle scattering data analysis using a library of analytical expressions, *J. Appl. Crystallogr.* 48 (2015) 1587–1598. <https://doi.org/10.1107/S1600576715016544>.
- [209] L.B. McCusker, R.B. Von Dreele, D.E. Cox, D. Louër, P. Scardi, Rietveld refinement guidelines, *J. Appl. Crystallogr.* 32 (1999) 36–50. <https://doi.org/10.1107/S0021889898009856>.
- [210] P. Scardi, M. Leoni, Whole powder pattern modelling, *Acta Crystallogr. Sect. A Found. Crystallogr.* 58 (2002) 190–200. <https://doi.org/10.1107/S0108767301021298>.
- [211] H.M. Rietveld, The Rietveld method, *Phys. Scr.* 89 (2014) 098002. <https://doi.org/10.1088/0031-8949/89/9/098002>.
- [212] J. Schindelin, I. Arganda-Carreras, E. Frise, V. Kaynig, M. Longair, T. Pietzsch, S. Preibisch, C. Rueden, S. Saalfeld, B. Schmid, J.-Y. Tinevez, D.J. White, V. Hartenstein, K. Eliceiri, P. Tomancak, A. Cardona, Fiji: an open-source platform for biological-image analysis, *Nat. Methods.* 9 (2012) 676–682. <https://doi.org/10.1038/nmeth.2019>.

- [213] G. Witz, V. Shklover, W. Steurer, S. Bachegowda, H.-P. Bossmann, Phase Evolution in Yttria-Stabilized Zirconia Thermal Barrier Coatings Studied by Rietveld Refinement of X-Ray Powder Diffraction Patterns, *J. Am. Ceram. Soc.* 90 (2007) 2935–2940. <https://doi.org/10.1111/j.1551-2916.2007.01785.x>.
- [214] G.-J. Yang, Z.-L. Chen, C.-X. Li, C.-J. Li, Microstructural and Mechanical Property Evolutions of Plasma-Sprayed YSZ Coating During High-Temperature Exposure: Comparison Study Between 8YSZ and 20YSZ, *J. Therm. Spray Technol.* 22 (2013) 1294–1302. <https://doi.org/10.1007/s11666-013-9986-8>.
- [215] C. Viazzi, J.-P. Bonino, F. Ansart, A. Barnabé, Structural study of metastable tetragonal YSZ powders produced via a sol–gel route, *J. Alloys Compd.* 452 (2008) 377–383. <https://doi.org/10.1016/j.jallcom.2006.10.155>.
- [216] B.A. Cottom, M.J. Mayo, Fracture toughness of nanocrystalline ZrO<sub>2</sub>-3mol% Y<sub>2</sub>O<sub>3</sub> determined by Vickers indentation, *Scr. Mater.* 34 (1996) 809–814. [https://doi.org/10.1016/1359-6462\(95\)00587-0](https://doi.org/10.1016/1359-6462(95)00587-0).
- [217] D. Hotza, D.E. García, R.H.R. Castro, Obtaining highly dense YSZ nanoceramics by pressureless, unassisted sintering, *Int. Mater. Rev.* 60 (2015) 353–375. <https://doi.org/10.1179/1743280415Y.0000000005>.
- [218] M.P. Borom, C.A. Johnson, L.A. Peluso, Role of environment deposits and operating surface temperature in spallation of air plasma sprayed thermal barrier coatings, *Surf. Coatings Technol.* 86–87 (1996) 116–126. [https://doi.org/10.1016/S0257-8972\(96\)02994-5](https://doi.org/10.1016/S0257-8972(96)02994-5).
- [219] D. Tejero-Martin, C. Bennett, T. Hussain, A review on environmental barrier coatings: History, current state of the art and future developments, *J. Eur. Ceram. Soc.* 41 (2021) 1747–1768. <https://doi.org/10.1016/j.jeurceramsoc.2020.10.057>.

- [220] K.A. Kane, E. Garcia, S. Uwanyuze, M. Lance, K.A. Unocic, S. Sampath, B.A. Pint, Steam oxidation of ytterbium disilicate environmental barrier coatings with and without a silicon bond coat, *J. Am. Ceram. Soc.* 104 (2021) 2285–2300. <https://doi.org/10.1111/jace.17650>.
- [221] E. Garcia, O. Sotelo-Mazon, C.A. Poblano-Salas, G. Trapaga, S. Sampath, Characterization of Yb<sub>2</sub>Si<sub>2</sub>O<sub>7</sub>–Yb<sub>2</sub>SiO<sub>5</sub> composite environmental barrier coatings resultant from in situ plasma spray processing, *Ceram. Int.* 46 (2020) 21328–21335. <https://doi.org/10.1016/j.ceramint.2020.05.228>.
- [222] N.S. Jacobson, Corrosion of Silicon-Based Ceramics in Combustion Environments, *J. Am. Ceram. Soc.* 76 (1993) 3–28. <https://doi.org/10.1111/j.1151-2916.1993.tb03684.x>.
- [223] E.J. Opila, Variation of the Oxidation Rate of Silicon Carbide with Water-Vapor Pressure, *J. Am. Ceram. Soc.* 82 (1999) 625–636. <https://doi.org/10.1111/j.1151-2916.1999.tb01810.x>.
- [224] E.J. Opila, Oxidation Kinetics of Chemically Vapor-Deposited Silicon Carbide in Wet Oxygen, *J. Am. Ceram. Soc.* 77 (1994) 730–736. <https://doi.org/10.1111/j.1151-2916.1994.tb05357.x>.
- [225] K. Kane, E. Garcia, P. Stack, M. Lance, C. Parker, S. Sampath, B.A. Pint, Evaluating steam oxidation kinetics of environmental barrier coatings, *J. Am. Ceram. Soc.* 105 (2022) 590–605. <https://doi.org/10.1111/jace.18093>.
- [226] E.J. Opila, J.L. Smialek, R.C. Robinson, D.S. Fox, N.S. Jacobson, SiC Recession Caused by SiO<sub>2</sub> Scale Volatility under Combustion Conditions: II, Thermodynamics and Gaseous-Diffusion Model, *J. Am. Ceram. Soc.* 82 (1999) 1826–1834. <https://doi.org/10.1111/j.1151-2916.1999.tb02005.x>.

- [227] J. Felsche, The crystal chemistry of the rare-earth silicates, in: 1973: pp. 99–197.  
[https://doi.org/10.1007/3-540-06125-8\\_3](https://doi.org/10.1007/3-540-06125-8_3).
- [228] N. Rohbeck, P. Morrell, P. Xiao, Degradation of ytterbium disilicate environmental barrier coatings in high temperature steam atmosphere, *J. Eur. Ceram. Soc.* 39 (2019) 3153–3163. <https://doi.org/10.1016/j.jeurceramsoc.2019.04.034>.
- [229] M. Ridley, E.J. Opila, Thermochemical stability and microstructural evolution of Yb<sub>2</sub>Si<sub>2</sub>O<sub>7</sub> in high-velocity high-temperature water vapor, *J. Eur. Ceram. Soc.* 41 (2021) 3141–3149. <https://doi.org/10.1016/j.jeurceramsoc.2020.05.071>.
- [230] S. Ueno, T. Ohji, H.-T. Lin, Recession behavior of Yb<sub>2</sub>Si<sub>2</sub>O<sub>7</sub> phase under high speed steam jet at high temperatures, *Corros. Sci.* 50 (2008) 178–182.  
<https://doi.org/10.1016/j.corsci.2007.06.014>.
- [231] E. Bakan, D.E. Mack, S. Lobe, D. Koch, R. Vaßen, An investigation on burner rig testing of environmental barrier coatings for aerospace applications, *J. Eur. Ceram. Soc.* 40 (2020) 6236–6240. <https://doi.org/10.1016/j.jeurceramsoc.2020.06.016>.
- [232] Y. Murakami, H. Yamamoto, Phase Equilibria and Properties of Glasses in the Al<sub>2</sub>O<sub>3</sub>-Yb<sub>2</sub>O<sub>3</sub>-SiO<sub>2</sub> System, *J. Ceram. Soc. Japan.* 101 (1993) 1101–1106.  
<https://doi.org/10.2109/jcersj.101.1101>.